Open heavy-flavour measurements via muons in proton-proton and nucleus-nucleus collisions with the ALICE detector at the CERN-LHC

Zuman Zhang

To cite this version:

Zuman Zhang. Open heavy-flavour measurements via muons in proton-proton and nucleus-nucleus collisions with the ALICE detector at the CERN-LHC. Accelerator Physics [physics.acc-ph]. Université Clermont Auvergne [2017-2020]; Central China Normal University, 2018. English. NNT : 2018CLFAC077 . tel-02137482

HAL Id: tel-02137482
https://theses.hal.science/tel-02137482

Submitted on 23 May 2019

CENTRAL CHINA NORMAL UNIVERSITY
UNIVERSITÉ CLERMONT AUVERGNE

PHD THESIS

présentée pour obtenir le grade de

DOCTOR OF UNIVERSITY

Spécialité : Physique des Particules

Par

Zuman ZHANG

Open heavy-flavour measurements via muons in proton-proton and nucleus-nucleus collisions with the ALICE detector at the CERN-LHC

defended on November 22, 2018

Jury :

Examinateurs:	A. BALDISSERI	-	DSM/IRFU, CEA, Saclay
	A. GRELLI	-	University of Utrecht, Utrecht
	Y. MA	-	SINAP, Shanghai
	Z. YIN	-	CCNU, Wuhan
	X. LI	-	CIAE, Beijing
Directeurs de thèse:	N. BASTID	-	LPC, Clermont-Ferrand
	P. CROCHET	-	LPC, Clermont-Ferrand
	D. ZHOU	-	CCNU, Wuhan
	X. ZHANG	-	CCNU, Wuhan

分类号______ 密级______

UDC ______ 编号______

华中师范大学

博士学位论文

LHC/ALICE 实验向前区重味强子衰变半单轻子物理的研究

学位申请人姓名：张祖满

申请学位学生类别：全日制博士

申请学位学科专业：粒子物理与原子核物理

指导教师姓名：周代翠 教授

张晓明 副教授

Philippe Crochet 研究员

Nicole Bastid 教授

博士学位论文
DOCTORAL DISSERTATION

博士学位论文

LHC/ALICE 实验向前区重味强子衰变半单轻子物理的研究

论文作者：张祖满

指导教师：周代翠　　　　教授
张晓明　　　　副教授
菲利普•胡克　资深研究员
妮可•巴斯蒂　教授

学科专业：粒子物理与原子核物理

研究方向：高能重离子碰撞实验

华中师范大学物理科学与技术学院

2018 年 11 月

博士学位论文
DOCTORAL DISSERTATION

Dissertation

Open heavy-flavour measurements via muons in proton-proton and nucleus-nucleus collisions with the ALICE detector at the CERN-LHC

By

Zuman Zhang

Supervisors: Pr. Daicui Zhou
Pr. Xiaoming Zhang
Dr. Philippe Crochet
Pr. Nicole Bastid

Specialty: Particle Physics and Nuclear Physics

Research Area: Heavy-Ion Collision Experiment

College of Physical Science and Technology

Central China Normal University

11, 2018

华中师范大学学位论文原创性声明和使用授权说明

原创性声明

本人郑重声明：所呈交的学位论文，是本人在导师指导下，独立进行研究工作所取得的研究成果。除文中已经标明引用的内容外，本论文不包含任何其他个人或集体已经发表或撰写过的研究成果。对本文的研究做出贡献的个人和集体，均已在文中以明确方式标明。本声明的法律结果由本人承担。

作者签名：　　　　　　　　　　　　日期：　　年　　月　　日

学位论文版权使用授权书

学位论文作者完全了解华中师范大学有关保留、使用学位论文的规定，即：研究生在校攻读学位期间论文工作的知识产权单位属华中师范大学。学校有权保留并向国家有关部门或机构送交论文的复印件和电子版，允许学位论文被查阅和借阅；学校可以公布学位论文的全部或部分内容，可以允许采用影印、缩印或其它复制手段保存、汇编学位论文。（保密的学位论文在解密后遵守此规定）

保密论文注释：本学位论文属于保密，在 ____年解密后适用本授权书。

非保密论文注释：本学位论文不属于保密范围，适用本授权书。

作者签名：　　　　　　　　　　　　导师签名：

日期：　　年　　月　　日　　　　　日期：　　年　　月　　日

本人已经认真阅读“CALIS 高校学位论文全文数据库发布章程”，同意将本人的学位论文提交“CALIS 高校学位论文全文数据库”中全文发布，并可按“章程”中的规定享受相关权益。同意论文提交后滞后：□半年；□一年；□二年发布。

作者签名：　　　　　　　　　　　　导师签名：

日期：　　年　　月　　日　　　　　日期：　　年　　月　　日

摘 要

自然界中可见物质的结构探索，可追溯到英国物理学家约瑟夫·约翰·汤姆逊（Joseph John Thomson）1897 年通过测量阴极射线的荷质比发现电子。1932 年詹姆斯·查德威克（James Chadwick）在用α粒子轰击核的实验中发现了中子，之后人们认识到原子核是由质子和中子构成的，从而形成所有物质都是由基本的结构单元：质子 、中子、电子构成的统一的世界图像。19 世纪初开始，现代的基本粒子概念也逐渐形成，研究比基本结构单元更深层次的微观世界中物质的结构性质，和在很高的能量下，这些物质相互作用的现象。人们利用粒子加速器，进行粒子高能碰撞实验，从而生产和侦测这些基本粒子，研究基本粒子，以及它们之间相互作用的原因和规律。

根据描述自然界中可见物质由那些基本粒子组成，以及基本粒子间相互作用特性的标准模型（SM），构成物质的基本粒子分为三代夸克，三代轻子和它们的反粒子，且这些基本粒子间通过传递胶子、$W^{\pm}$ 和 Z^0 玻色子及光子发生对应的强、弱和电磁相互作用。一种解释基本粒子质量之源的粒子－希格斯玻色子，于 2012 年在欧洲核子研究中心(CERN)的大型强子对撞机(LHC)实验中发现。夸克胶子(部分子)间发生的强相互作用通过量子色动力学(QCD)来描述，QCD 具有三个特殊性质：渐近自由、手征对称性动力学破缺和色禁闭。由于色禁闭，夸克和胶子被禁闭在强子中。格点量子色动力学(LQCD)的理论计算预言在高温和/或高密条件下，禁闭在普通强子内的部分子将发生退禁闭形成一种由处于渐近自由状态的夸克和胶子组成的新物质相:夸克胶子等离子体（QGP）。目前，QGP 被认为存在于自然界中正在塌陷的中子星内部（高重子数密度）和宇宙大爆炸后数μs 的初期（极高温）。研究 QGP 不仅帮助理解多粒子体系的强相互用特性和使物理学的研究疆域拓展至接近宇宙诞生初始，而且对考察宇宙的起源、物质的本性以及对验证现有的粒子物理标准模型等都有重要意义。如何在现有实验条件下通过实验产生 QGP 这种新物质相一直是科学家们思考的问题。

通过高能重离子碰撞，制造高温高密极端环境，是现有的探寻禁闭解除的 QGP，研究 QGP 特性的可行途径。被剥离带电的两入射原子核被加速到接近于光速实现猛烈对撞，深度非弹性过程导致两核的巨大动能转化为热能沉积在碰撞中心区，在一个有限空间范围内形成极端高温或高重子密度环境，诱导强子物质解

除夸克禁闭，形成夸克胶子等离子体这种新物质形态。随着时间的推移，夸克物质体系的膨胀和冷却，QGP 物质相又冻结为强子相，发射出末态可观测的粒子。我们利用高能重离子探测器侦测到的粒子研究 QGP 特性。上世纪七十年代以来国际上相继建造了一系列高能重离子加速器，包括欧洲核子研究中心（CERN）的超级质子同步加速器（SPS）、美国布鲁海文国家实验室（BNL）的交变梯度加速器（AGS）和相对重离子对撞机（RHIC），在发现强作用 QGP 信号及其性质上取得了很好的成果和进展：1. SPS 能区， 奇异粒子产额明显增强，被解释为手征对称性在退禁闭物质相中得到恢复，而使得奇异夸克在 QGP 物质中产生阈值的降低；J/ψ 粒子产额压低，被认为是粲夸克偶素（cc）在 QGP 物质中 Debye 屏蔽势作用下熔解而致。2. RHIC 能区，不同种类带电强子椭圆流的组分夸克数目的标度特性，揭示了部分子在 QGP 内的热化自由度；高横动量区域强子谱压低以及喷注强子背向关联的减弱，反映了高能部分子在穿越 QGP 热密介质时发生强相互作用，诱导部分子辐射能量损失所致。上述实验观测结果与相应理论描述一致，证明了 QGP 物质的存在。

为了系统的深入地研究 QGP 物质性质，世界上最大的大型强子对撞机（LHC）于 2009 年在 CERN 正式运行。大型重离子碰撞实验（ALICE），作为 LHC 上四大实验（ALICE、ATLAS、CMS 和 LHCb）之一，专门致力于高能重离子碰撞的夸克物质信号探测及其性质的研究。ALICE 在 2010 年底首次获取质心能量 2.76 TeV 铅-铅碰撞数据。 该能量相当于 RHIC 最高碰撞能量（金-金碰撞，$\sqrt{s_{NN}}=200$ GeV）的～14 倍，因此碰撞所形成的 QGP 物质相比于 RHIC 能区将持续时间更长且体积更大，这为全面而深入地研究 QGP 物质的特性提供了更加优越的条件。

在众多反映 QGP 性质的末态探针中，重夸（粲夸克和美夸克）十分重要。由于重夸克质量大，重夸克主要产生于碰撞初期的硬散射过程，且重夸克具有更短的形成时间和更硬的碎裂函数。因此，重夸克早于 QGP 物质形成，并穿越随后形成的 QGP 物质体系，记录了 QGP 系统各演化阶段的信息；其运动学分布又能很好的被其碎裂末态强子所反映。

核子-核子（pp）碰撞中，对重夸克末态产物的测量蕴涵着丰富的物理，不仅为核子-核（pA）碰撞和重离子碰撞提供了归一化基准，同时，也是检测微扰量子色动力学（pQCD）的有利工具。在核-核（AA）碰撞中，重夸克穿越 QGP 体系时

与其内部部分子相互作用，而导致的能量损失体现了强相互作用的特性。根据QCD理论预言，胶子的辐射能量损失大于夸克。而较之轻夸克，重夸克的胶子辐射会在与其夸克质量相关的锥角内压低，从而导致重夸克辐射能量损失比轻夸克小，这一效应被称为死角效应。基于重夸克辐射能量损失的死角效应，重味强子与其内部部分子相互作用的能量损失应该小于轻强子。随横动量分布的核修正因子（R_{AA}）是反映部分子能量损失的实验观测量，R_{AA}定义为同一能量的核-核（如金-金、铅-铅和氙-氙）碰撞中约化为一对核子碰撞产生的粒子产额与核子-核子（如质子-质子）碰撞中的粒子产额之比。若没有核效应，R_{AA}值为单位一；R_{AA}值小于单位一，可能是由部分子能量损失和其它核效应导致。在p-A碰撞中，R_{pA}是了解各种冷核效应（核遮蔽、内禀横动量增宽以及胶子饱和等）的有力工具，特别是在实验的向前快度区间，它能使对冷核效应的测量达到及小的Bjorken-x值区间（2013年，ALICE，p-Pb在质心系能量 $\sqrt{s_{NN}}$ = 5.02 TeV的碰撞，向前区Bjorken-x ~ 10^{-6}，处于核遮蔽区间）。

本文的工作基于ALICE实验向前区μ子谱仪采集的实验数据，通过重味夸克半轻子衰变道研究pp碰撞和A-A碰撞中重味产额的物理性质。分析步骤包括重建粒子径迹和反应事件，测量最小无偏碰撞的单举μ子横动量谱，扣除K/π、J/ψ和$W/Z,\gamma^*$衰变μ背景贡献，计算μ子重建效率，研究系统误差，得到pp碰撞和A-A碰撞中重味夸克半轻衰变道μ子的产物，计算A-A碰撞中重夸克衰变μ子的产额的核修正因子R_{AA}，比较模型预言，研究AA碰撞中的重夸克产生是否存在压低行为，检验热核效应。

第一章对QGP相变，高能重离子碰撞的QGP测量结果做简要介绍，LHC能区实验相对于SPS和RHIC实验有更好的QGP测量结果。pp、pA和AA碰撞中重味产生也做了简要介绍，重夸克是十分重要的QGP性质的末态探针。第二章介绍ALICE探测器特别是向前区μ子谱仪的结构、原理和性能。还简要的介绍ALICE探测器升级，并对ALICE实验数据获取以及在线和离线分析环境进行进行描述。本文还介绍本工作对重夸克半轻μ子道测量所开发的数据分析和校正的软件和分析代码框架。

第三、四、五、六章着重讨论数据分析方法、内容和物理结果。第三章，重点讨论质心能量$\sqrt{s}=5.02$ TeV、2.76 TeV和5.44 TeV pp碰撞中的重夸克衰变μ子的产生截面，为计算质心能量$\sqrt{s_{NN}}=5.02$ TeV和2.76 TeV的铅-铅（Pb-Pb）碰撞

和 $\sqrt{s_{NN}} = 5.44$ TeV 氙-氙（Xe-Xe）碰撞中的 $R_{\rm AA}$ 测量计算提供基准（reference）。我们还比较了实验测量与理论模型预言，结果显示，在误差范围内，我们的测量结果很好的符合了次领头阶的 pQCD 计算的预言，这一结果是首次在新能区 $\sqrt{s} = 5.02$ TeV 下对 pQCD 理论预言的重夸克产生截面的检验。

在第四章，我们讨论质心能量 $\sqrt{s_{NN}} = 5.02$ TeV（2015 年数据）和 $\sqrt{s_{NN}} = 2.76$ TeV（2011 年数据）Pb-Pb 碰撞实验中重夸克衰变 μ 子的 $R_{\rm AA}$ 的实验分析方法。第五章展示和讨论第四章的物理结果。其数据样本较之前发表的质心能量 $\sqrt{s_{NN}} = 2.76$ TeV（2010 年数据）Pb-Pb 碰撞结果有更高的统计量。本分析选择了高横动量阈值的触发样本，因此本分析工作能测到更宽更高横动量（p_T）区间的 $R_{\rm AA}$。结果显示，2015 年数据的结果比 2010 年数据的结果有更高的精度；$\sqrt{s_{NN}} = 5.02$ TeV 和 2.76 TeV Pb-Pb 碰撞中重夸克衰变 μ 子的 $R_{\rm AA}$ 值小于单位一，且两者的结果在误差范围内相同；质心能量 $\sqrt{s_{NN}} = 5.02$ TeV（2013 年数据）表明冷核效应对核修正因子的影响较小（$R_{\rm pA} \sim 1$），因此 Pb-Pb 碰撞实验结果证实，在核-核对心碰撞中观测到的重夸克衰变 子谱在高 p_T 区间的明显压低现象，主要由热核效应导致；在向前区重味强子衰变 μ 子与中心快度区重味强子衰变电子的结果在不确定度范围内一致；实验测量与理论模型预言在误差范围内保持一致。

第六章介绍 $\sqrt{s_{NN}} = 5.44$ TeV Xe-Xe 碰撞实验中重夸克衰变 μ 子的 $R_{\rm AA}$ 的实验分析方法、误差，其分析方法和 Pb-Pb 碰撞中的分析方法一致。对这一章的结果也做了讨论，在向前区，相对于 $\sqrt{s_{NN}} = 5.02$ TeV 10-20%中心度的 Pb-Pb 碰撞，$\sqrt{s_{NN}} = 5.02$ TeV 0-10%中心度的 Xe-Xe 碰撞有相似的带电粒子平均多重数，且两者的 $R_{\rm AA}$ 结果在误差范围内相同。此外，与 Pb-Pb 结果相比，Xe-Xe 碰撞系统中 $R_{\rm AA}$ 的测量还可以首次在实验结果中测试能量损失的路径长度依赖性。

本文第七章对前六章的介绍和讨论以及结果进行了总结，并对进一步的相关研究内容提出了展望。

关键词：夸克胶子等离子体（QGP）；大型强子对撞机（LHC）；大型重离子碰撞实验（ALICE）；质子-质子（pp）和核-核（AA）碰撞；冷核效应和热核效应；重味夸克产生的单举 μ 子谱；核修正因子（$R_{\rm AA}$）

Abstract

In nature, the interaction of particles and microscopic structure of matter have historically been concerned by human being. The Standard Model (SM) widely accepted by the theory of particle physics, describes that the fundamental particles are three generation of quarks, three generation of leptons and their anti-particles. The bosons, including photons (γ), gluons (g), $W^{\pm}$, Z^{0}, are the force carriers of the electromagnetic, strong and weak interactions. In 2012 the ATLAS (A Toroidal LHC ApparatuS) and CMS (Compact Muon Solenoid) experiments at the LHC (Large Hadron Collider) observed the Higgs boson, which explains the origin of mass.

According to Quantum ChromoDynamics (QCD) calculations on the lattice, a state of strongly-interacting matter at high energy density and temperature where quarks and gluons are deconfined, the Quark-Gluon Plasma (QGP), is produced. This state of matter would have existed in the core of neutron stars at high baryonic densities and few microseconds after the Big Bang where extremely high temperatures were reached. High-energy heavy-ion collisions provide a unique opportunity for the QGP formation and for characterizing its properties. Since the 1970's, several facilities have been built to produce and study of the QGP by means of heavy-ion collisions at various energies. The results from different experiments improved our understanding of the QGP. The LHC started operated in 2009 and delivered until 2013 (run-1) pp ($\sqrt{s}$ = 0.9-8 TeV), p-Pb ($\sqrt{s_{\rm NN}}$ = 5.02 TeV) and Pb-Pb ($\sqrt{s_{\rm NN}}$ = 2.76 TeV) collisions. By delivering Pb-Pb collisions at $\sqrt{s_{\rm NN}}$ = 5.02 TeV with a significantly higher luminosity compared to the run-1, the LHC run-2 (2015-2018) provides new conditions for the study of the QGP. During the run-2, the LHC delivered also pp ($\sqrt{s}$ = 5.03, 13 TeV) and p-Pb ($\sqrt{s_{\rm NN}}$ = 5.02 and 8.16 TeV) collisions. Finally, a short Xe-Xe run at $\sqrt{s_{\rm NN}}$ = 5.44 TeV was performed to investigate the system-size dependence of various observables.

ALICE is the experiment designed and optimized for the study of heavy-ion collisions at the LHC. ALICE also takes part in the pp program which provides the mandatory reference for p-Pb, Xe-Xe and Pb-Pb collisions, and allows to us to test perturbative QCD-based calculations.

Amongst the most important probes of the properties of the QGP, heavy quarks (charm and beauty) are of particular interest since they are predominantly produced in initial hard scattering processes and experience the full evolution of the hot and dense QCD medium. During their propagation through the medium, they lose energy via radiative and collisional processes. Quarks are expected to lose less energy than gluons due to the colour-charge dependence of the strong interactions, and due to the dead-cone effect the heavy-quark energy loss is reduced compared to that of light quarks. Further processes such as collisional energy loss, fragmentation, recombination and coalescence can also modified the particle yields. . These in-medium effects can be quantified using the nuclear modification factor $R_{\rm AA}$ which compares the $p_{\rm T}$-differential particle yields in nucleus-nucleus collisions and binary-scaled pp collisions.

This thesis presents measurements of the production of open heavy flavours at forward rapidity ($2.5 < y < 4$) via the semi-muonic channel in pp collisions at a centre-of-mass energy $\sqrt{s} = 5.02$ TeV, Pb-Pb collisions at a nucleon-nucleon centre-of-mass energy $\sqrt{s_{\mathrm{NN}}} = 2.76$ and 5.02 TeV, and in Xe-Xe collisions at $\sqrt{s_{\mathrm{NN}}} = 5.44$ TeV with the ALICE (A Large Ion Collider Experiment) detector at the CERN Large Hadron Collider (LHC). The document is organized as follows. The first chapter consists in a general introduction on heavy-ion collisions and QCD phase transitions, and summarizes the motivations for the study of open heavy flavours in pp, p-A and A-A collisions. Chapter 2 gives an overview of the ALICE experiment with a particular emphasis on the description of the forward muon spectrometer. The online and offline systems are also presented. The analysis framework and in particular the software developed for the study of open heavy flavours are presented. The ALICE upgrade project is also discussed. Chapter 3 is dedicated to the measurement of the production of muons from heavy-flavour hadron decays in pp collisions at $\sqrt{s} = 5.02$ TeV. The analysis strategy is detailed. The experimental results are obtained in wide transverse momentum interval, $2 < p_{\mathrm{T}} < 20$ GeV/c, and with an improved precision compared to the published run-1 measurements. They are compared with perturbative QCD (pQCD)-based calculations. That concerns the p_{T}- and y-differential production cross sections and ratios between different centre-of-mass energies and rapidities. The needed pp references at $\sqrt{s} = 2.76$ and 5.44 TeV are also presented. Chapter 4 consists of a detailed description of the analysis strategy implemented for the measurements of the production of muons from heavy-flavour hadron decays in Pb-Pb collisions at $\sqrt{s_{\mathrm{NN}}} = 5.02$ TeV. The procedure to perform same measurements at $\sqrt{s_{\mathrm{NN}}} = 2.76$ TeV is also discussed. Chapter 5 presents the Pb-Pb results at $\sqrt{s_{\mathrm{NN}}} = 5.02$ TeV (production cross sections and nuclear modification factor as function of p_{T} and collision centrality). They are compared with same measurements performed at $\sqrt{s_{\mathrm{NN}}} = 2.76$ TeV. Comparisons with results obtained in a different kinematic region by ALICE and other experiments are also shown. Finally, comparisons with model predictions are discussed. Chapter 6 addresses the measurement of heavy-flavour hadron decay muons in Xe-Xe collisions at $\sqrt{s_{\mathrm{NN}}} = 5.44$ TeV. The analysis strategy is described and the results (R_{AA}) are compared with the ones obtained in Pb-Pb collisions at $\sqrt{s_{\mathrm{NN}}} = 5.02$ TeV and with model calculations. Finally, a summary and outlooks are given in Chapter 7.

Keywords: Quark-Gluon Plasma (QGP); A Large Ion Collider Experiment (ALICE); Large Hadron Collider (LHC); proton-proton (pp) and nucleus-nucleus (A-A) collisions; Cold and hot nuclear matter effects; Open heavy-flavour production via single muons; Nuclear modification factor (R_{AA})

Contents

List of Figures

List of Tables

Chapter 1

Introduction

Since a long time, a variety of questions such as what is the matter made of led to the development of elementary particle physics. Its goals are to understand what are the elementary particles of the matter and how they interact with each others. The aim of ultra-relativistic heavy-ion physics is to study strongly-interacting matter under extreme conditions of temperature and energy density, where Quantum ChromoDynamics (QCD), the theory of strong interactions within the Standard Model (SM), predicts a transition to a new phase of matter, the Quark-Gluon Plasma (QGP).

In this chapter we introduce the basic notions of the Standard Model of particle physics and a theory describing the strong interaction of colored quarks and color gluons, QCD in Sec. 1.1. We also describe the hadronic matter phase diagram and QGP formation in heavy-ion collisions in Sec. 1.2. Among the many probes presented in Sec. 1.3 which are used to study the medium formed in heavy-ion collisions, we mainly focus on heavy favours in Sec. 1.4, since this is the main subject of this thesis.

1.1 Standard Model and Quantum ChromoDynamics

The Standard Model [1, 2] of particle physics is the theory describing three of the four known fundamental forces (the electromagnetic, weak, and strong interactions, but not the gravitational force) in the universe, as well as classifying all known elementary particles. The elementary particles are characterised by their mass, spin and charge. A summary of elementary particles is shown in Fig. 1.1. The spin allows us to classify the elementary particles into two basic types, the fermions and the bosons.

The basic components of matter are fermions and the mediators of the fundamental interactions are bosons. The fermions consist of three generations of quarks: (u, d), (c, s), (t, b) and their anti-quarks; and three generations of leptons: (ν_{e}, e), (ν_μ, μ), (ν_τ, τ) and their anti-leptons. The bosons, including photons (γ), gluons (g), $\mathrm{W}^{\pm}$ and Z^0 , carry the electromagnetic, strong and weak fundamental interactions shown in Fig. 1.2.

The SU(3)×SU(2)×U(1) gauge symmetry [3] is an internal symmetry that essentially defines the SM, which roughly corresponds to the symmetries of one of the three forces. U(1) represents the electromagnetic interaction, SU(2) represents the weak interaction while the strong interaction is represented by SU(3).

The electromagnetic and weak interactions are unified in the electroweak theory [2] (U(1)×SU(2)). The mechanism that breaks electroweak symmetry, implies the

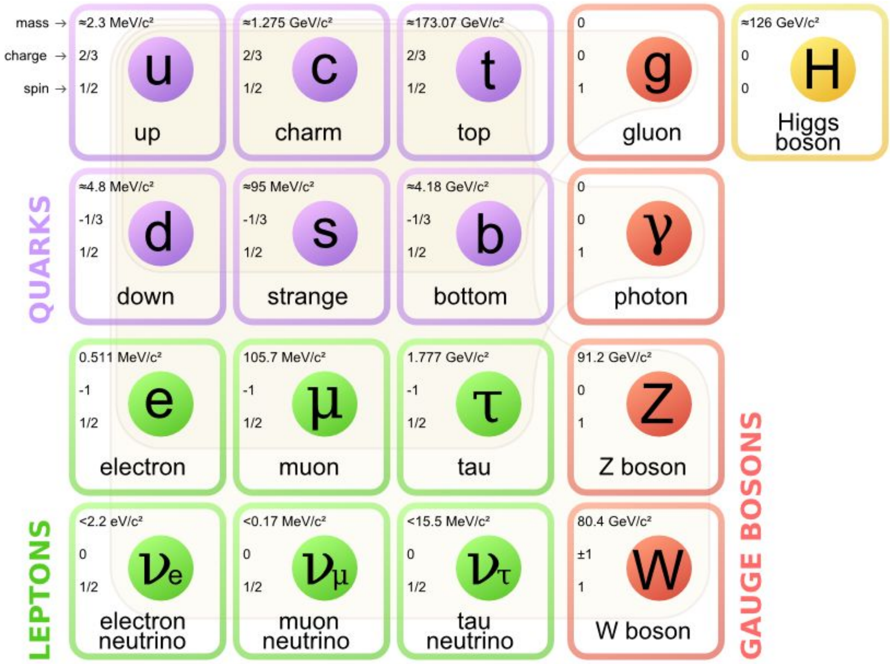

Figure 1.1: The SM of elementary particles, with the three generations of matter, gauge bosons in the fourth column, and the Higgs boson in the fifth column. Figure taken from Ref. [3]

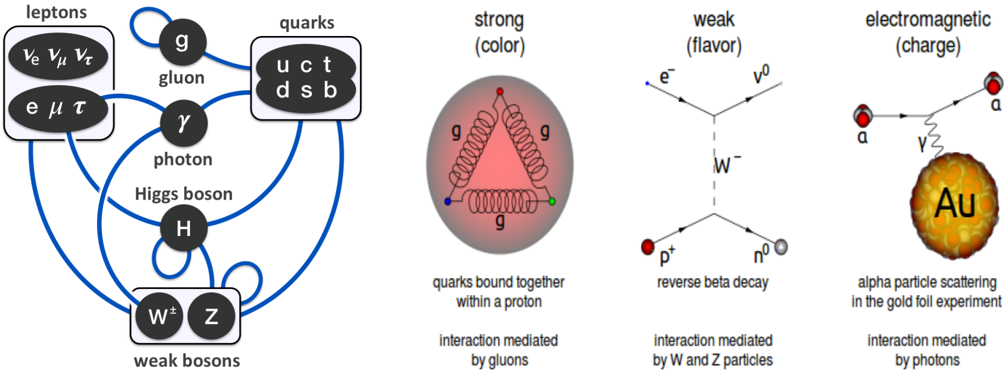

Figure 1.2: Summary of interactions between particles (left), and example of strong, weak and electromagnetic interactions from middle to right. Figure taken from Ref. [3].

existence of a scalar particle, the Higgs boson (H), which leads to the generation of the $W^{\pm}$ and Z^0 masses. The Higgs boson was discovered by A Toroidal LHC ApparatuS (ATLAS) [135] and Compact Muon Solenoid (CMS) [136], see Fig. 1.3. The 2013 Nobel Prize in Physics was awarded jointly to F. Englert and P. W. Higgs for the prediction of this fundamental particle.

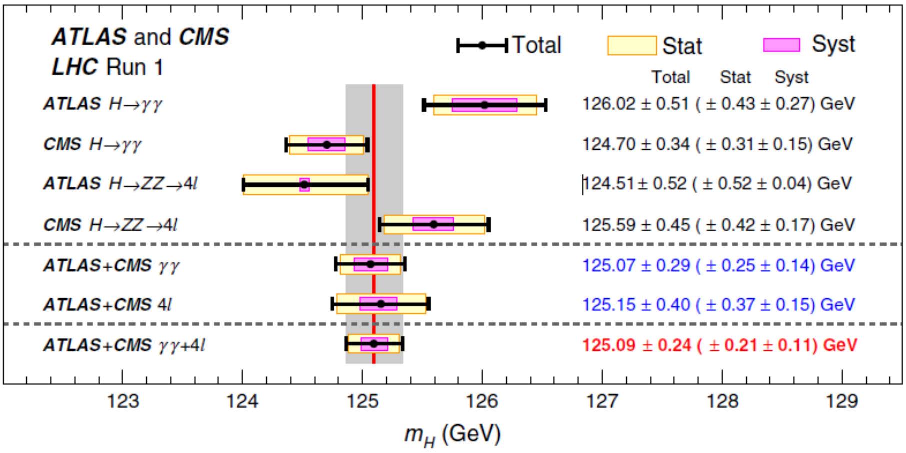

Figure 1.3: Summary of Higgs-boson mass measurements from the analyses of ATLAS and CMS collaborations. The systematic (narrower, magenta-shaded bands), statistical (wider, yellow-shaded bands), and total (black error bars) uncertainties are indicated. The (red) vertical line and corresponding (gray) shaded column indicate the central value and the total uncertainty of the combined measurement, respectively. Figure taken from Ref. [6].

Particles consisting of quarks are called hadrons. The hadrons are categorized into two families: baryons (qqq), made of three quarks, and mesons ($q\bar{q}$), made of one quark and one antiquark. Quarks and gluons are color-charged particles. Color-charged particles cannot be found individually. For this reason, the color-charged quarks are confined in hadrons with other quarks. These composites are color neutral. Just as electrically-charged particles interact by exchanging photons, colored-charged particles exchange gluons in strong interactions. QCD is a theory that describes the properties of the strong interaction between color (namely red, blue and green) quarks and color gluons. The QCD theory defines the interactions between quarks and gluons with SU(3) symmetry. QCD is the gauge field theory, in which quarks and gluons are collectively called partons.

QCD Lagrangian

As a part of SM, QCD is the gauge field theory to describe the properties of strong interaction between quarks and gluons. The Lagrangian of QCD is written as [7]

$$\mathcal{L}_{\mathrm{QCD}} = \sum_{q} \overline{\psi}_{\mathrm{q,a}}(i\gamma^{\mu}\partial_{\mu}\delta_{\mathrm{ab}} - g_{\mathrm{s}}\gamma^{\mu}t^{\mathrm{C}}_{\mathrm{ab}}\mathcal{A}^{\mathrm{C}}_{\mu} - m_{\mathrm{q}}\delta_{\mathrm{ab}})\psi_{\mathrm{q,b}} - \frac{1}{4}F^{\mathrm{A}}_{\mu\nu}F^{\mathrm{A},\mu\nu}. \tag{1.1}$$

In Eq. (1.1), $\psi_{\mathrm{q,b}}$ is the Dirac spinors of the quark field, where, q and a are the quark flavour and color indexes, (red, green, blue), running from a $= 1$ to $N_{\mathrm{c}} = 3$; γ^{μ} are Dirac γ-matrices which expresses the vector nature of the strong interaction with μ being a Lorentz vector index; $\mathcal{A}^{\mathrm{C}}_{\mu}$ corresponds to the gluon fields with C varying between $C = 1$ to $N_{\mathrm{c}}^2 - 1 = 8$; $t^{\mathrm{C}}_{\mathrm{ab}}$ are 8 generators of the SU(3) group; m_{q} are quark masses generated via the Higgs mechanism and g_{s} (or $\alpha_{\mathrm{s}} = g_{\mathrm{s}}/4\pi$) is the QCD coupling constant.

The field tensor $F^{\mathrm{A}}_{\mu\nu}$ is given by,

$$F^{\mathrm{A}}_{\mu\nu} = \partial_{\mu}\mathrm{A}^{\mathrm{A}}_{\nu} - \partial_{\nu}\mathrm{A}^{\mathrm{A}}_{\mu} - g_{\mathrm{s}}f_{\mathrm{ABC}}\mathcal{A}^{\mathrm{B}}_{\mu}\mathcal{A}^{\mathrm{C}}_{\nu}, \tag{1.2}$$

where the SU(3) structure constant, f_{ABC}, is obtained as

$$[t^{\mathrm{A}}, t^{\mathrm{B}}] = if_{\mathrm{ABC}} \cdot t_{\mathrm{C}}. \tag{1.3}$$

The casimir factors C_{F} and C_{A}, are defined via the color algebra relations,

$$\begin{aligned} t^{\mathrm{A}}_{\mathrm{ab}} \cdot t^{\mathrm{A}}_{\mathrm{bc}} &= \delta_{\mathrm{ac}}C_{\mathrm{F}} \quad (C_{\mathrm{F}} \equiv \frac{N_{\mathrm{c}}^2 - 1}{2N_{\mathrm{c}}} = \frac{4}{3}), \\ f_{\mathrm{ACD}} \cdot f_{\mathrm{BCD}} &= \delta_{\mathrm{AB}}C_{\mathrm{A}} \quad (C_{\mathrm{A}} \equiv N_{\mathrm{c}} = 3). \end{aligned} \tag{1.4}$$

C_{F} and C_{A} are two useful constant factors associated with the gluon emission from a quark and from a gluon, respectively.

Two particularities of QCD are: the **confinement/asymptotic freedom** and the **chiral symmetry restoration/breaking**.

Confinement and asymptotic freedom

The intensity of the electromagnetic force is predicted by Quantum ElectroDynamics (QED) to be $\alpha_{\mathrm{em}} \simeq 1/137$. As a consequence of vacuum polarization, in QED the coupling constant varies with the momentum that is transferred in the interaction (Q^2) as

$$\alpha_{\mathrm{QED}}(Q^2) = \frac{\alpha_{\mathrm{em}}}{1 - \frac{\alpha_{\mathrm{em}}}{3\pi}\ln(\frac{Q^2}{m^2})}. \tag{1.5}$$

Similarly, QCD describes the strong interaction as governed by the strong coupling constant, α_{QCD}, which also depends on the momentum transferred in the interaction,

$$\alpha_{\mathrm{QCD}}(Q^2) = \alpha_{\mathrm{s}}(Q^2) = \frac{4\pi}{(11 - \frac{2}{3}n_{\mathrm{f}})\ln(\frac{Q^2}{\Lambda^2_{\mathrm{QCD}}})} \tag{1.6}$$

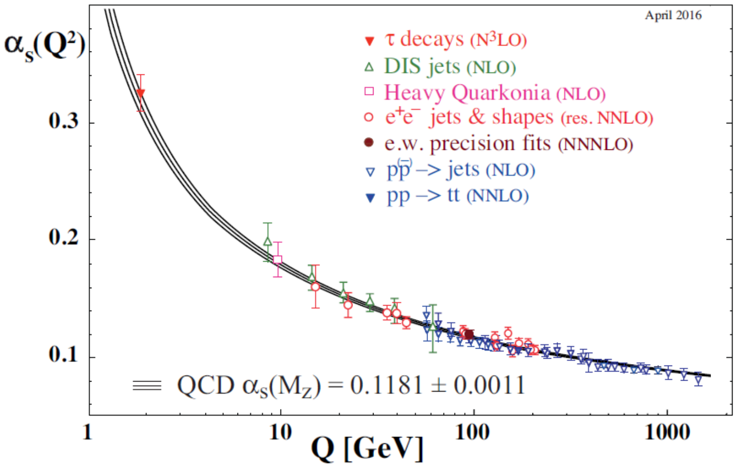

Figure 1.4: Summary of measurements of α_s as a function of the energy scale Q. The respective degree of perturbation QCD theory used in the extraction of α_s is indicated in brackets (NLO: next-to-leading order; NNLO: next-to-next-to leading order; NNLO: NNLO matched with resummed next-to-leading logs; NNNLO: next-to-NNLO). Figure taken from Ref. [8].

where, n_f is the number of light flavours, Q^2 is related to the momentum transfer in a given process, Λ_QCD is the non-perturbative QCD scale corresponding to a α_s value.

When the value of energy scale Q is small, the intensity of the coupling increases, which explains the fact that quarks are confined in the neutral color states, for example the baryons and mesons. This is known as color confinement. On the contrary, when the value of energy scale Q is large and α_QCD becomes small, quarks and gluons behave as free particles in the QCD vacuum, which is known as asymptotic freedom [9, 10], as observed in Fig. 1.4.

Chiral symmetry restoration/breaking

In absence of quark masses ($m_\mathrm{q} \approx 0$), the QCD Lagrangian can split into two independent sectors and they are symmetric under helicity transformations of the quarks. This is called chiral symmetry. The chiral symmetry refers to the symmetry of the right-handed and left-handed parts of quarks. Therefore, there is no interaction between left-handed (ψ_L) and right-handed (ψ_R) parts of quarks with different helicities.

Due to the strong coupling between right-handed and left-handed parts of quarks, the quark mass is not null in the QCD vacuum, which is defined as chiral condensate [11],

$$<\bar{\psi}\psi>=<\bar{\psi}_\mathrm{L}\psi_\mathrm{R}+\bar{\psi}_\mathrm{R}\psi_\mathrm{L}> \tag{1.7}$$

$<\bar{\psi}\psi>\neq 0$ when the chiral symmetry breaks.

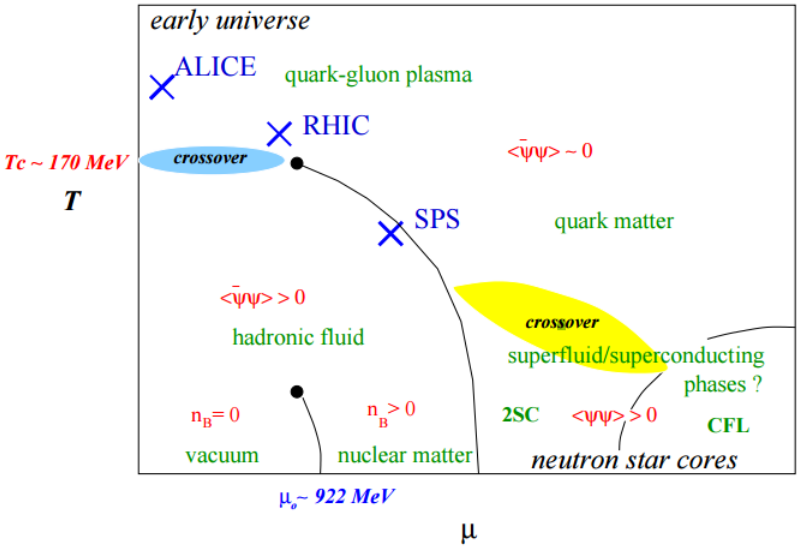

Figure 1.5: Phase diagram of QCD matter in the representation temperature T versus baryon chemical potential μ. Figure taken from Ref. [16].

On the contrary, at high energies one expects a restoration of the chiral symmetry. One can get $<\bar{\psi}\psi>= 0$, if the symmetry is conserved, so the quarks recover their almost-null mass of the QCD Lagrangian instead of their constituent mass. QCD explains the existence of the 8 Goldstone bosons (the 8 lightest mesons: $\pi^0, \pi^\pm, \mathrm{K}^0, \mathrm{K}^\pm, \bar{\mathrm{K}}^0, \eta$) [12], considering the chiral symmetry breaking.

1.2 Quark-Gluon Plasma and relativistic heavy-ion collisions

1.2.1 QCD phase diagram and Lattice QCD results

The QCD phase diagram in the representation temperature T versus baryon chemical potential μ [13, 16], is reported in Fig. 1.5. In the diagram, at low temperature and low density, quarks and gluons are confined into hadrons. The matter can be described as an hadronic gas. If the temperature is high enough the strength of the strong force becomes weak, and hence the quarks and gluons become deconfined. The deconfined state of matter is called Quark-Gluon Plasma (QGP).

Since the transition between quark confinement and deconfinement is a non-perturbative process, normal perturbative QCD (pQCD) approaches are no longer valid. The Lattice Quantum ChromoDynamics (LQCD) [17] deals with the challenge to characterize the transition from hadronic matter to QGP phase.

Figure 1.6 shows the pressure, energy density and entropy density of QCD matter from lattice QCD calculations. The Hadron Gas (HRG) thermodynamic potential provides an excellent approximation of the QCD equation of state in confined phase. The critical temperature is estimated to be $T_\mathrm{c} \sim 145 - 164$ MeV [18, 19, 20].

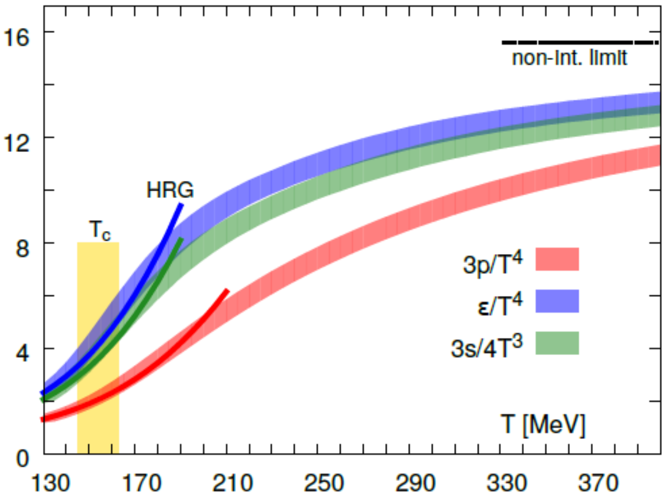

Figure 1.6: The pressure, energy density and entropy density of QCD matter as a function of temperature from lattice QCD calculations. Figure taken from Ref. [18].

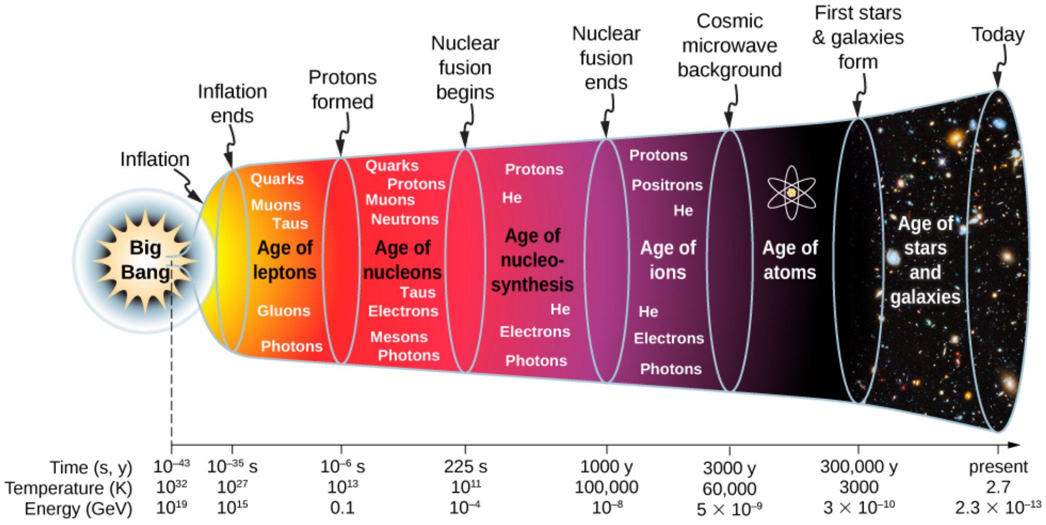

Figure 1.7: The evolution of the universe. Figure taken from Ref. [21].

In the Steffan-Boltzman statistics limit for an ideal gas and QGP, considering the energy density of an equilibrated ideal gas of particles with n_{dof} degrees of freedom, one gets

$$\varepsilon_\pi = n_{\text{dof}} \cdot \frac{\pi^2}{30}\mathrm{T}^4 = 3 \cdot \frac{\pi^2}{30}\mathrm{T}^4 \approx \mathrm{T}^4. \tag{1.8}$$

where n_{dof}=3 corresponds to the three possible pion charges.

For an ideal QGP energy density with two massless flavours (pion gas phase),

$$\varepsilon_{\text{QGP}} = n_{\text{dof}} \cdot \frac{\pi^2}{30}\text{T}^4 = [(2_{\text{f}} \cdot 2_{\text{s}} \cdot 2_{\text{q}} \cdot 3_{\text{c}})\frac{7}{8} + (2_{\text{s}} \cdot 8_{\text{c}})]\frac{\pi^2}{30}\text{T}^4 \approx 12.2\text{T}^4. \tag{1.9}$$

where n_{dof}=37 corresponds to the various possibilities of flavour, spin, quark number and color for pions in the deconfined phase.

Near the critical temperature, the dramatic increase of ε/T^4 seen in Fig. 1.6 can be interpreted as due to the change of n_{dof} from 3 for the pion gas phase to 37 (with 2 flavours) in the deconfined phase, where the additional color and quark flavour degrees of freedom are available.

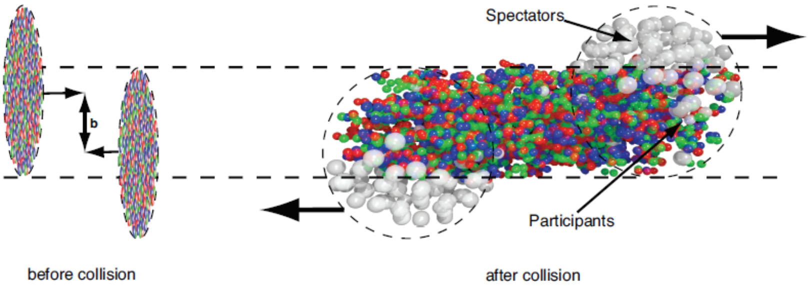

Figure 1.8: Schematic view of two colliding nuclei in the geometrical participant-spectator model. The distance in the transverse plane of the collisions between the centers of the two Lorentz contracted nuclei is the impact parameter (b). Figure taken from Ref. [24].

The QGP is expected to have constituted the universe a few micro-seconds after the Big-Bang [22, 31]. Shortly after the Big-Bang, the early universe was a high-temperature and high-density environment, the temperature of early universe was about 10^{12}K, see Fig. 1.7. On the other hand, deconfinement at large baryon chemical potential is expected to exist in the core of neutron stars [14]. The deconfinement at large baryon chemical potential is also considered to exist in the color superconductor [15]. In order to produce and study the deconfinement in the laboratory, a little bang was created by colliding heavy ions at the Super Proton Synchrotron (SPS) [29] at European Organization for Nuclear Research (CERN), Relativistic Heavy Ion Collider (RHIC) [39] at Brookhaven National Laboratory (BNL) and subsequently at the Large Hadron Collider (LHC) [134] at European Organization for Nuclear Research (CERN).

In the following section we focus on how the QGP can be studied in the laboratory.

1.2.2 Ultra-relativistic heavy-ion collisions

Geometry of heavy-ion collisions

In ultra-relativistic heavy-ion collisions, with velocities nearly equal to the velocity of light, the two highly Lorentz contracted nuclei approach each other. Then, nucleon-nucleon collisions happen in the region of geometrical overlap. This region can be characterized with various quantities. The impact parameter (b) can be determined by the distance between the centers of the two colliding nuclei as shown in Fig. 1.8. In a given centrality class, $< N_{\text{part}} >$ is defined as the mean number of participating nucleons, and $< N_{\text{coll}} >$ is used to express the mean number of binary nucleon-nucleon collisions. Both $< N_{\text{part}} >$ and $< N_{\text{coll}} >$ can be calculated by the Glauber model [26]. $< N_{\text{part}} >$ and $< N_{\text{coll}} >$ are two important quantities to characterize a collision.

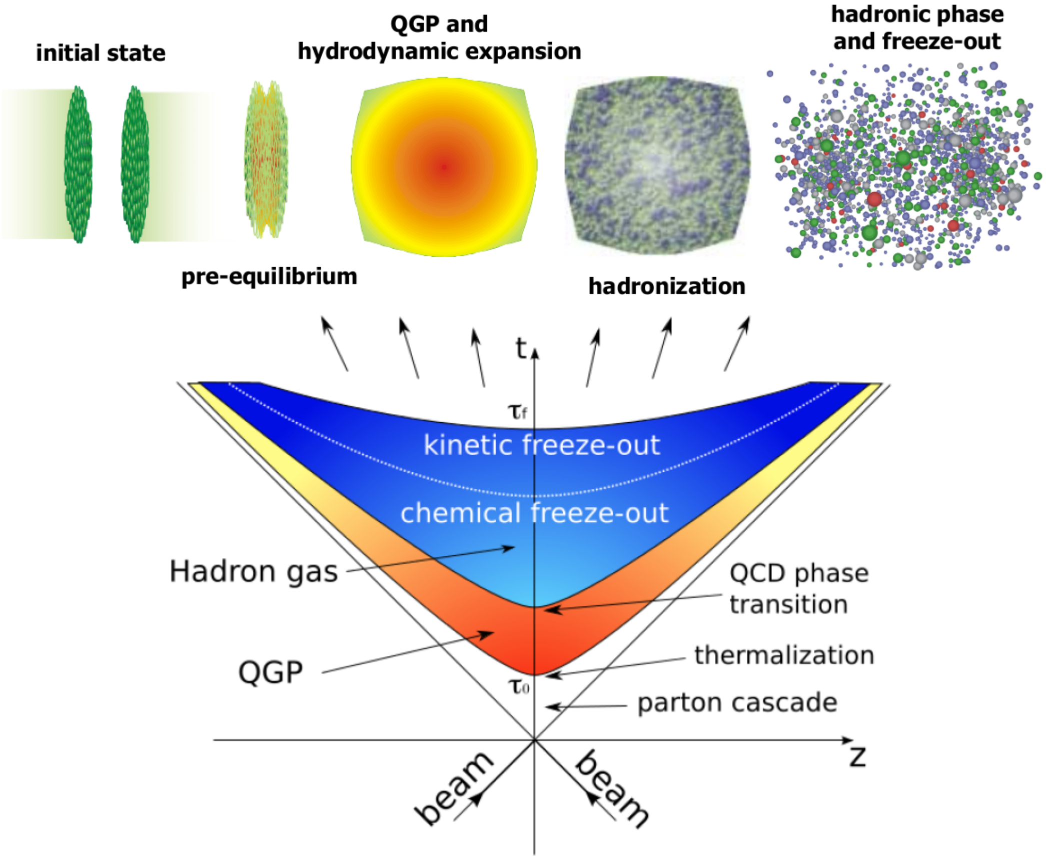

Figure 1.9: Top: schematic representation of the various stages in a ultra-relativistic nuclear collision. Bottom: space-time evolution of a heavy-ion collision. Figure taken from Ref. [27, 28].

Time evolution of heavy-ion collisions

A simple view of an ultra-relativistic heavy-ion collision is presented in Fig. 1.9.

Initial stage: The colliding nuclei are affected by Lorentz contraction and become as disks in the center-of-mass frame.

Pre-equilibrium: When nuclei collide, the initial collisions are hard collisions between nucleons in which many partons are liberated. A pre-equilibrium phase is created by the multiple interactions among the partons. The nuclei crossing time is thought to be much smaller than the characteristic time of the strong interaction ($\tau_{\text{cross}} << \tau_{\text{strong}} \approx 1/\Lambda_{\text{QCD}} \sim 1$ fm$/c$) [105].

QGP phase: After the hard interactions, nuclei pass through leaving behind the created partons. Those partons can re-scatter redistributing part of the energy deposited in the center-of-mass to thermalize and create a 'fireball'. If the attained energy density exceeds a critical energy density, the QGP might be formed.

Hadronization and freeze-out: Then the system tends to expand and cools down towards a hadronic phase. When the energy density is too low to allow inelastic collisions to produce particles, the chemical freeze-out is attained, the number of particles gets set. The system continues to expand and get colder, then the elastic collisions are no longer possible and the system reaches the kinetic freeze-out, the hadron kinetic properties get set. The hadrons stream then freely towards the detectors.

machine	SPS	RHIC	LHC
system	Pb–Pb	Au–Au	Pb–Pb
$\sqrt{s_{\text{NN}}}$ (GeV)	17	200	5500
$\text{d}N_{\text{ch}}/\text{d}y\|_{y=0}$	400	750	2000 – 4000
τ^0_{QGP} (fm$/c$)	1	0.2	0.1
$T_{\text{QGP}}/T_{\text{c}}$	1.1	1.9	3.0 – 4.2
ε (GeV/fm^3)	3	5	15 – 60
τ_{QGP} (fm$/c$)	≤ 2	2 – 4	≥ 10
τ_{f} (fm$/c$)	~ 10	20 – 30	30 – 40
V_{f} (fm^3)	$\sim 10^3$	$\sim 10^4$	$\sim 10^5$
μ_{B} (MeV)	250	20	1
process	soft	semi-hard	hard

Table 1.1: The relevant parameters and predictions for CERN-SPS, RHIC and CERN-LHC experiments. Adapted from Ref. [72].

Various heavy-ion experiments are operated at the Super Proton Synchrotron (SPS) at European Organization for Nuclear Research (CERN), Relativistic Heavy Ion Collider (RHIC) at BNL (Brookhaven National Laboratory, USA) and Large Hadron Collider (LHC) at CERN. Some relevant parameters and predictions for these heavy-ion experiments are listed in Tab. 1.1, which is adapted from Ref. [72]. This Table shows (from top to bottom) the available energy per nucleon pair in the center of mass for Pb-Pb or Au-Au collisions ($\sqrt{s_{\text{NN}}}$), charged-particle density at mid-rapidity ($\text{d}N_{\text{ch}}/\text{d}y|_{y=0}$), formation time of QGP (τ^0_{QGP} (fm$/c$)), ratio of QGP temperature to critical temperature ($T_{\text{QGP}}/T_{\text{c}}$), energy density ($\varepsilon$ (GeV/fm^3)), QGP life-time (τ_{QGP} (fm$/c$)), life-time (τ_{f} (fm$/c$)) and volume of the system at freeze-out (V_{f} (fm^3)), and baryonic chemical potential (μ_{B} (MeV)).

In the following we introduce the first QGP signals from SPS, first QGP properties from RHIC. Thanks to the higher beam energy, about 30 times higher than that at RHIC (see Tab. 1.1), as it will discussed in the following, the LHC provides precision measurements for the QGP characterization.

1.3 Probing the QGP in heavy-ion collisions

1.3.1 Selected highlights from the CERN-SPS heavy-ion program

The CERN-SPS [29] heavy-ion program has been carried from 1986 to 2003 with fixed-target experiments located in the North area (NA44, NA45, NA47, NA49, NA50, NA52, NA60) and West Area (WA97, WA98). These experiments have collected pp, p-A, and A-B collisions (A being nuclei such as O, S, In, Pb, and B also being nuclei such as Be, Au, Pb or U targets) from 40 AGeV until 158 AGeV. The measured results concerned the energy density [33], particle production [34], strangeness production [36, 37], direct photons [38] and charmonium production [32, 33, 35].

Energy density

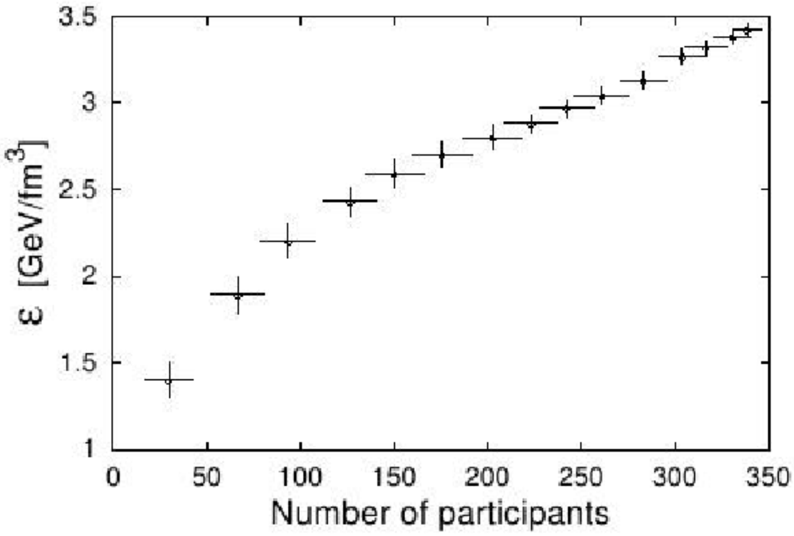

Figure 1.10: The initial energy density measured by SPS experiments as a function of the collision centrality determined by means of the number of participants. Figure taken from Ref. [33].

The initial energy density of the produced medium at the thermalization time is estimated within the Bjorken scenario [31],

$$\varepsilon = (\frac{\mathrm{d}N_\mathrm{h}}{\mathrm{d}y})_{y=0} \times \frac{\omega_\mathrm{h}}{\pi R_\mathrm{A}^2 \tau_0}, \tag{1.10}$$

where $(\frac{\mathrm{d}N_\mathrm{h}}{\mathrm{d}y})_{y=0}$ specifies the number of hadrons emitted per unit of rapidity at mid-rapidity, ω_h is the average energy of the hadrons in the beam direction, R_A is the nuclear radius, and τ_0 is the formation time of the thermal medium and is ≈ 1 fm/c (at the SPS). The initial energy density measured by SPS experiments is shown as a function of the centrality determined by means of the number of participants in Fig. 1.10 [33]. It increases with the centrality of the collision from about 1.4 GeV/fm^3 up to 3.5 GeV/fm^3. The values reached are well above the value of the deconfinement (0.18 - 0.5 GeV/fm^3 [18]) predicted by Lattice QCD calculations (see Sec. 1.2.1).

Chemical freeze-out temperature

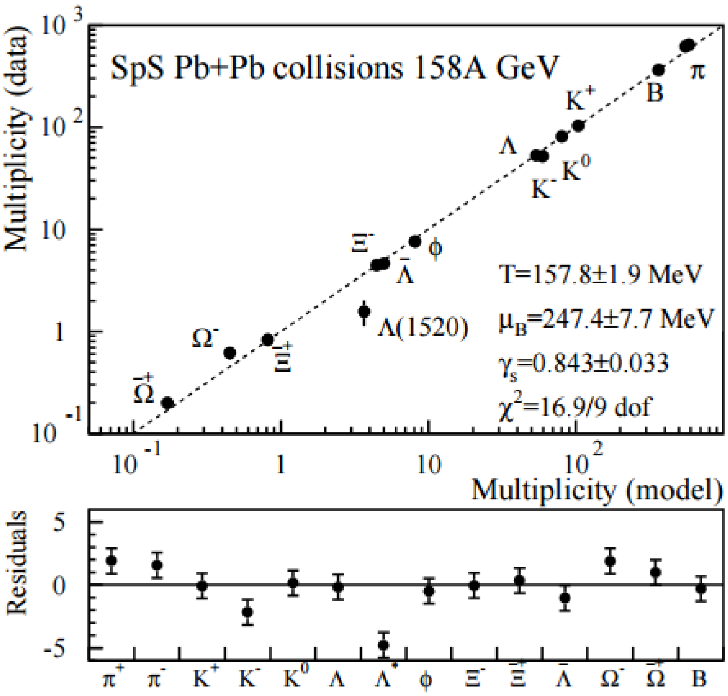

Figure 1.11: Hadron multiplicities in Pb-Pb collisions at 158 AGeV measured at SPS vs. prediction of the Statistical Hadronization Model. Figure taken from Ref. [34].

Figure 1.11 presents the multiplicity of various particles as a function of the event multiplicity in central Pb-Pb collisions at 158 AGeV obtained by NA49 and the adjustment with a Statistical Hadronization Model (SHM) [34]. The extracted temperature of T = 158 ± 2 MeV is similar to the temperature of deconfinement predicted by Lattice QCD (see Sec. 1.2.1). This is an indication that probably the medium has been created in the partonic region of the phase diagram.

Since the measured energy density is larger than the energy density for the deconfinement phase transition from LQCD predictions and the chemical freeze-out temperature is close to the critical temperature T_c predicted by Lattice QCD, there are good chances that the deconfined medium was formed at SPS energies. A selected highlight related to charmonium (J/Ψ) production is discussed in the following.

J/Ψ anamalous suppression

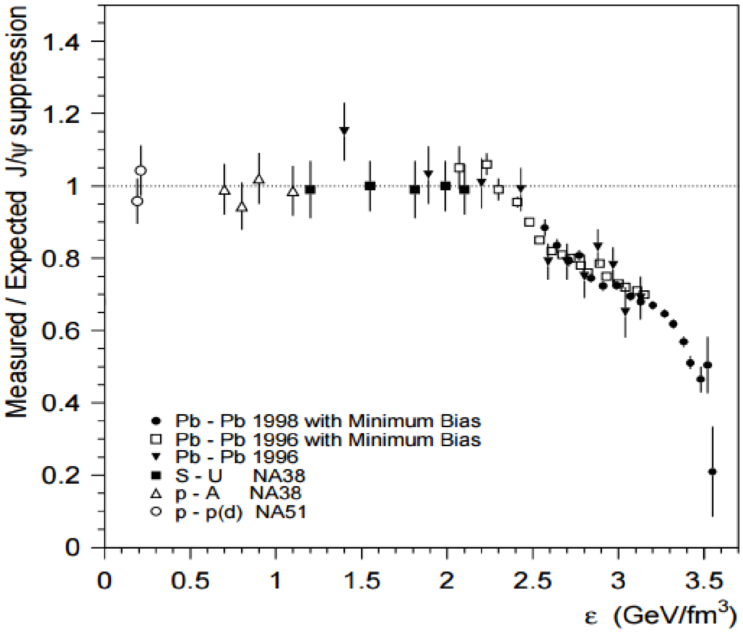

Figure 1.12: The measured J/Ψ yield to the expected yield in various collision systems mentioned in the figure. Figure taken from Ref. [33].

The J/Ψ (bound state of charm and anti-charm quarks) production has been intensively studied at SPS. A suppression of the J/Ψ yield by colour screening was proposed as a probe of the Quark-Gluon Plasma [33, 35]. T. Matsui and H. Satz argued that in presence of a QGP the confining potential of the charm- anti-charm pair is screened due to interactions with quarks and gluons and that prevents the binding of the charm and anti-charm pairs.

Figure 1.12 shows the ratio of the measured J/Ψ yield to the expected yield assuming that the only source of suppression is the normal nuclear absorption, as function of the energy density in various collision systems reported in the figure. The first drop in Fig. 1.12 is seen for energy densities larger than 2.3 GeV/fm^3 and an other drop appears when an energy density of 3.1 GeV/fm^3 is reached. At the SPS, 30-40% of the produced J/Ψ come from higher resonance decays. The first anomalous step could indicate a suppression of the higher resonances while the second drop could be due to the fact that the energy density is high enough to suppress the J/Ψ resonance [33].

Summary

A complete review of heavy-ion results from the CERN-SPS heavy-ion program can be found in Ref. [29]. From the various results obtained with NA44, NA45, NA49, NA50, NA52, NA47/WQ97 and WA98, the CERN announced officially on

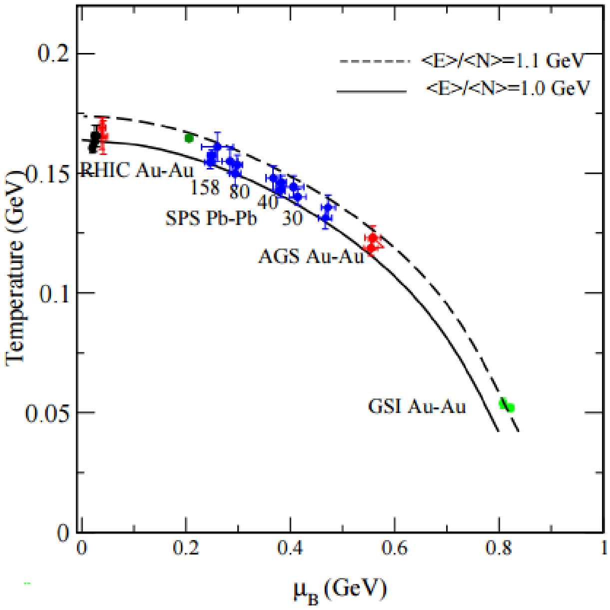

Figure 1.13: The chemical freeze-out temperature as a function of μ_B for different energies, as obtained from fits to data from RHIC, SPS, AGS, and SIS. The curves correspond to the freeze-out conditions (a constant energy density over particle density) $<E>/<N> = 1$ GeV and 1.1 GeV [42]. Figure taken from Ref. [43].

February 10, 2000 that there was "evidence of a new state of matter where quarks and gluons are not confined" [30].

1.3.2 Selected highlights from the RHIC experiments

The RHIC facility [39] includes two main experiments: the Pioneering High Energy Nuclear Interaction eXperiment (PHENIX) and Solenoidal Tracker At RHIC (S-TAR). The RHIC also includes two small experiments: the PHOBOS and BRAHMS. They collected a large variety of systems such as pp, p-Au, Cu-Cu, Cu-Au, Au-Au, U-U at energies per pair of nucleons in the centre-of-mass from about 7.7 GeV up to 200 GeV. The measurements concerned the energy density [41], chemical freeze-out temperature [42, 43], elliptic flow [44, 45], jet quenching [46, 47], direct photon [48], open heavy flavours [49] and quarkonia [49] .

Energy density and chemical freeze-out temperature

The energy density estimated in the 2% Au-Au most central collisions at $\sqrt{s_{\rm NN}} =$ 130 GeV is 4.6 GeV/fm^3 [41]. This corresponds to a 60% increase with respect to the value measured for Pb-Pb at $\sqrt{s_{\rm NN}} = 17.2$ GeV at the SPS (see Sec. 1.3.1). The chemical freeze-out temperature at RHIC is about 164 MeV, and is slightly larger than the chemical freeze-out temperature at SPS (see Fig. 1.13). This indicates that the deconfined medium was also formed at RHIC energies.

In the following, I will focus on two selected highlights: elliptic flow and jet quenching.

Elliptic flow

The elliptic flow (v_2) is caused directly by the initial spatial anisotropy of the collision geometry in the transverse plane, which is converted into an anisotropy in momentum space if enough scattering. On the other hand, as the anisotropy starts at the very beginning of the evolution, elliptic flow could reveal information on the thermodynamics properties of the medium in the early stage of heavy-ion collisions and fundamental thermalization time scale.

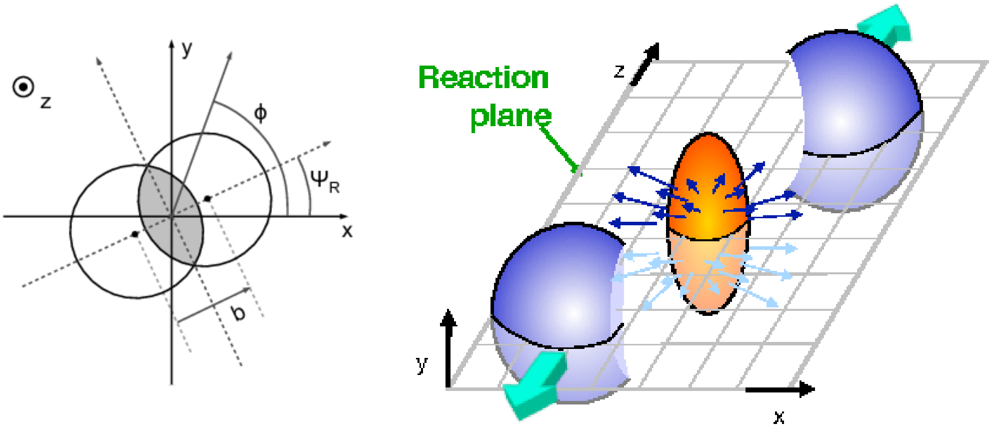

Figure 1.14: Geometry of the collision in a two-dimensional (left panel) and three-dimensional plane (right panel). Figures taken from Ref. [23, 25].

The azimuthal distribution of particles with respect to the reaction plane (see Fig. 1.14) is an observable used to quantify the flow effects and is expressed in the form of the Fourier expansion:

$$E\frac{\mathrm{d}^3N}{\mathrm{d}^3p} = \frac{1}{2\pi}\frac{\mathrm{d}^2N}{p_\mathrm{T}\mathrm{d}p_\mathrm{T}\mathrm{d}y}\left(1 + 2\sum_{n=1}^{\infty} v_\mathrm{n}(p_\mathrm{T}, y)\cos\left[n\left(\phi - \Phi_\mathrm{R}\right)\right]\right) \tag{1.11}$$

where ϕ is the particle azimuthal angle and Φ_R is the reaction plane angle. The reaction plane is defined by the beam direction (z direction) and the impact parameter direction. The coefficient v_n can be calculated by $v_\mathrm{n}(p_\mathrm{T}, y) =< \cos[n(\phi - \Phi_\mathrm{R})] >$. With an isotropic emission, each coefficient in the expansion should be equal to zero, leaving only the *radial flow*. The first coefficient v_1 is called *directed flow*. The second coefficient v_2, which characterizes the ellipticity of azimuthal distributions of the produced particles, is called *elliptic flow*.

At the early stage of evolution, hadrons have not formed and it has been proposed that the constituent quarks flow, so that the flow should be proportional to the number of constituent quarks n_q. The left panel of Fig. 1.15 shows v_2/n_q as

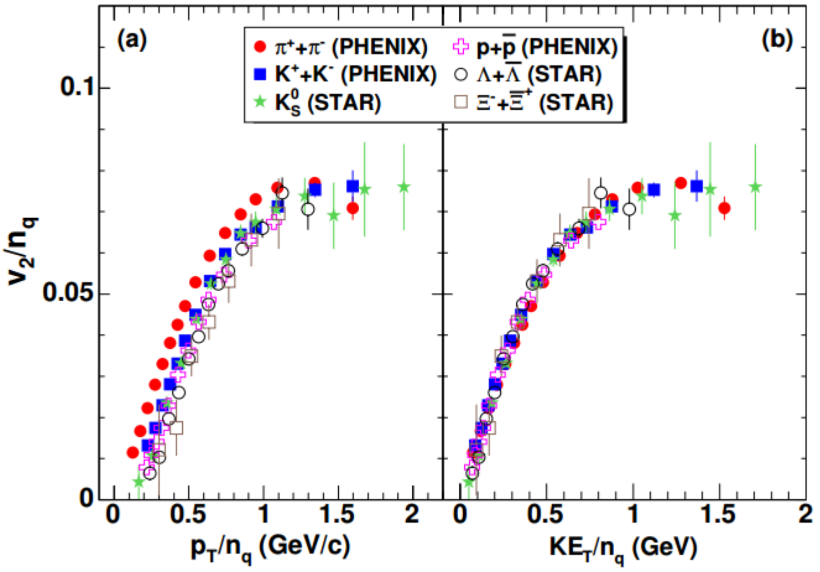

Figure 1.15: Measurements of elliptic flow (v_2) for identified hadrons plotted as v_2 divided by the number of constituent quarks n_q in the hadron as a function of $p_\mathrm{T}/n_\mathrm{q}$ (left) and $KE_\mathrm{T}/n_\mathrm{q}$ (right), with $KE_\mathrm{T} = m_\mathrm{T}$-$m_0$. Figure taken from Ref. [44].

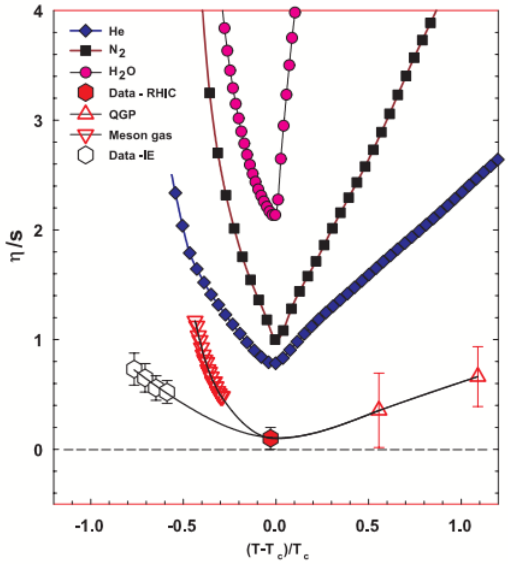

Figure 1.16: Compilation of the ratio of shear viscosity to entropy density for various substances: atomic He, molecular N_2 and H_2O (upper 3 symbols), QGP (upward triangles above T_c), pion gas (downward triangles below T_c) and empirical estimates from heavy-ion data. Figure taken from Ref. [45].

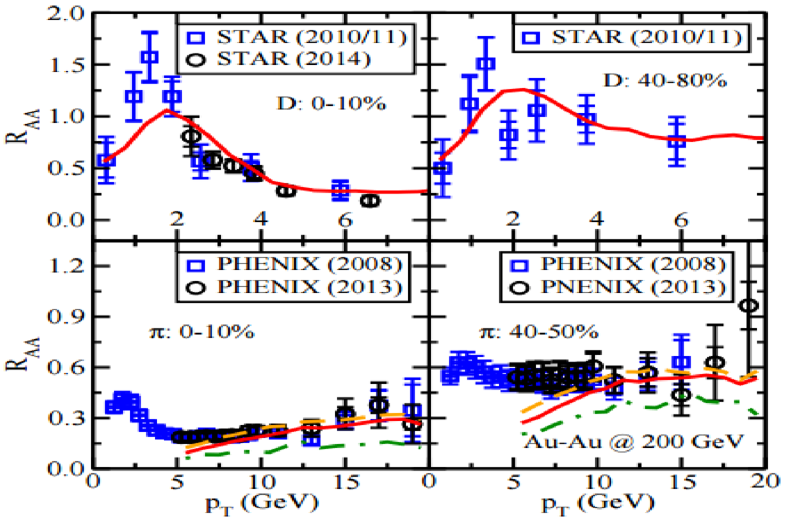

Figure 1.17: Nuclear modification factor R_{AA} for D (top left: 0-10%, top right: 40-80%) and π (bottom left: 0-10%, bottom right: 40-50%) mesons in Au-Au collisions at $\sqrt{s_{\mathrm{NN}}} = 200$ GeV by the PHENIX and STAR experiments at RHIC. Figure taken from Ref. [46].

a function of $p_{\mathrm{T}}/n_{\mathrm{q}}$. This would represent the constituent quark flow as a function of constituent quark transverse momentum. In relativistic hydrodynamics, at mid-rapidity, the transverse kinetic energy KE_{T} ($KE_{\mathrm{T}} = m_{\mathrm{T}}$-$m_0$, where $m_{\mathrm{T}} = \sqrt{p_{\mathrm{T}}^2 + m_0^2}$ and m_0 is the mass of the particle), rather than p_{T} is the relevant variable, and in fact v_2/n_{q} as a function of $KE_{\mathrm{T}}/n_{\mathrm{q}}$ seems to exhibit nearly perfect scaling [44] as shown in right panel of Fig. 1.15. So, the flow developed in the early stage of the collision prior the hadronization.

The new state of matter produced at RHIC reveals a strongly coupled Quark-Gluon Plasma (sQGP) with an extremely small shear viscosity to entropy density ratio of η/s. From the relativistic viscous hydrodynamic calculations [45], very low values of η/s are required to reproduce the RHIC elliptic flow data.

Figure 1.16 shows η/s as a function of (T-T_{c})/T_{c} ,where T is the temperature and $\mathrm{T_c}$ is the critical temperature. In the figure 1.16, the point labelled Data-RHIC was obtained by matching the elliptic flow data at RHIC with the results of viscous hydrodynamic calculations [45]. The value of η/s at RHIC is close to the lower limit of $1/4\pi$ (from theoretical calculations [45]), so the QGP behaves as a perfect fluid at RHIC.

Jet quenching

High-energy heavy-ion collisions can produce jets of elementary particles that emerge from these collisions. And then these jets interact strongly with the medium, leading to a reduction of their energy. This energy reduction is called "Jet quenching".

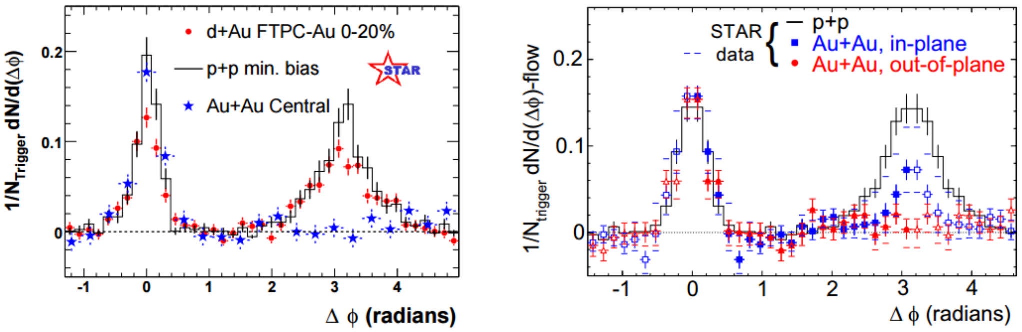

Figure 1.18: Di-hadron azimuthal correlations for pp, central d-Au and central Au-Au collisions from STAR (left panel), di-hadron correlations for different orientations of the trigger hadron relative to the Au-Au reaction plane from STAR (right panel). Figure taken from Ref. [47].

High-p_{T} particle suppression As a consequence of jet quenching, the high-p_{T} particle yield should be decreased while the yield of the low p_{T} hadrons should be enhanced. This effect can be evidenced from the nuclear modification factor R_{AA}, which compares the particle yields in nucleus-nucleus (AA) collisions with the yield in pp collisions, scaled by the number of binary nucleon-nucleon collisions N_{coll}, as illustrated with following equation:

$$R_{\mathrm{AA}}(p_{\mathrm{T}}) = \frac{\mathrm{d}^2 N_{\mathrm{AA}}/\mathrm{d}p_{\mathrm{T}}\mathrm{d}y}{< N_{\mathrm{coll}} >_{\mathrm{AA}} \ \mathrm{d}^2 N_{\mathrm{pp}}/\mathrm{d}p_{\mathrm{T}}\mathrm{d}y} \tag{1.12}$$

If AA collisions are a simple superposition of pp collisions (in the absence of nuclear effects), the nuclear modification factor should be unity ($R_{\mathrm{AA}} = 1$). R_{AA} differs from unity, when effects of the hot and dense medium produced in the collision breakup binary scaling.

Figure 1.17 shows the nuclear modification factor R_{AA} for D and π mesons in $\sqrt{s_{\mathrm{NN}}} = 200$ AGeV Au-Au collisions at the RHIC. The R_{AA} values of D and π mesons are smaller than one. These results indicate that the hot and dense medium was formed in heavy-ion collisions and the hard probes are quenched inside it. Moreover, in the semi-central and peripheral collisions the suppression is smaller than that in central collisions.

Di-hadron azimuthal correlations During the jet quenching processes, hard partons are always produced in back-to-back pairs. Since hard parton fragments into multiple particles within a restricted angular region (so-called jet), one would expect to observe angular correlations between the hadrons in jets. In the following, we discuss the disappearance of the back-to-back correlations.

In the left panel of Fig. 1.18 [47], the away-side ($\Delta\phi \approx \pi$) correlation peak is absent in central Au-Au collisions. On the contrary, peripheral Au-Au, d-Au and pp collisions exhibit the same shape of the near-side ($\Delta\phi \approx 0$) correlation peak. This phenomenon is explained because hard trigger hadrons are produced in hard parton scattering occurring on the surface of the collision region, but partons lose part of their energy when crossing the dense matter and the away-side peak is not formed. Another confirmation of the parton energy loss mechanism is shown in the right panel of Fig. 1.18. The suppression of the away-side peak depends strongly on the relative angle between trigger hadron and reaction plane (in-plane). For an out-of-plane (orthogonal to in-plane) trigger hadron, the correlated opposite jet must cross a longer path than in the reaction plane, leading to a larger energy loss.

Summary

A complete review of the results from RHIC experiments obtained until 2005 was published in Ref. [39]. These results allowed to make an announcement at a press conference to claim that [39, 40]: " RHIC has created a new state of hot, dense matter out of the quarks and gluons that are the basic particles of atomic nuclei, but it is a state quite different and even more remarkable than had been predicted. Instead of behaving like a gas of free quarks and gluons, as was expected, the matter created in RHIC's heavy ion collisions is more like a liquid [45]."

1.3.3 LHC: detailed QGP properties

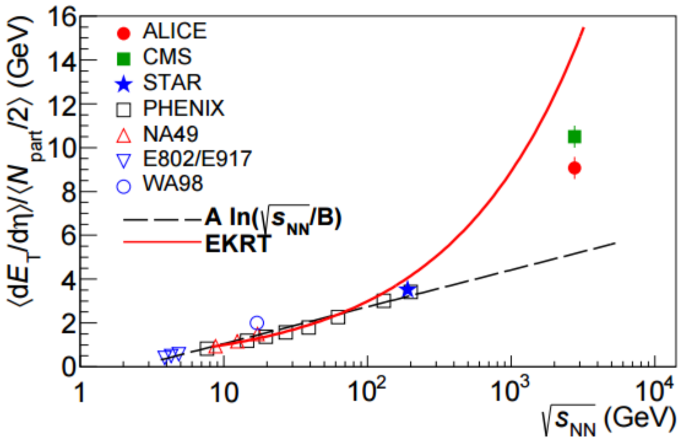

Figure 1.19: Transverse energy pseudorapidity density per participant pair for central AA collisions (0–7% centrality for NA49 and 0–5% for all other experiments) at mid-rapidity as a function of the collision energy. Figure taken from Ref. [50].

The experimental results from the LHC [134] (Large Hadron Collider) heavy-ion program confirmed the RHIC observations and provided additional evidence of the existence of new state of matter in this new energy regime. In the following, selected highlights are discussed.

Energy density, chemical freeze-out and initial temperature

Figure 1.19 shows the transverse energy pseudorapidity density measurement with ALICE [138] (A Large Ion Collider Experiment) and the one from CMS [136]

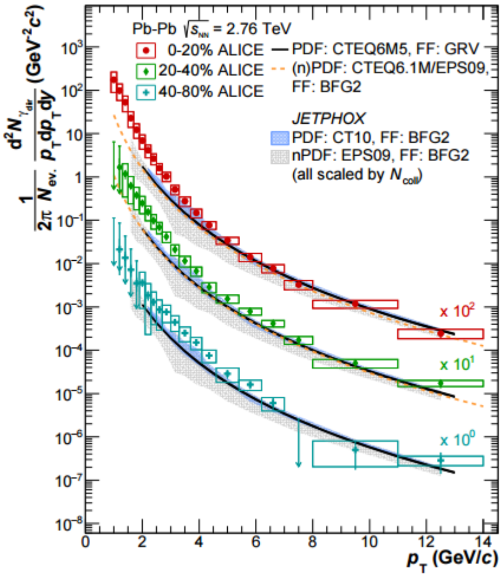

Figure 1.20: Direct photon p_T spectrum for Pb-Pb collisions at $\sqrt{s_{NN}} = 2.76$ TeV, compared to NLO pQCD calculations. Figure taken from Ref. [52].

(Compact Muon Solenoid) for the 0–5% centrality range. The energy density in the 0–5% central Pb-Pb collisions at $\sqrt{s_{NN}} = 2.76$ TeV with ALICE is about $\varepsilon = 12.3 \pm 1$ GeV/fm^3, and with the CMS measurement is about $\varepsilon = 14$ GeV/fm^3. Therefore, at the initial stage of central heavy-ion collisions, the energy density at the LHC is roughly 2-3 times higher than that reported at RHIC (see Sec. 1.3.2).

The chemical freeze-out temperature for the 10% most Pb-Pb central collisions at $\sqrt{s_{NN}} = 5.02$ TeV with ALICE is about 156 MeV [51], and it is slightly smaller than that measured at RHIC (see Sec. 1.3.2). This deviation is due to several possible explanations suggested in Ref. [73], including the effect of possible large baryon-antibaryon annihilation in the hadronic phase at the LHC.

The initial temperature of an equilibrated QGP state can be estimated by studying electromagnetic probes, which do not interact strongly with the medium and therefore carry information from the early stages of the collision. The measurement of direct photons at $\sqrt{s_{NN}} = 2.76$ TeV Pb–Pb collisions is presented in Fig. 1.20. The direct-photon spectrum is compared to NLO pQCD calculations for pp collisions scaled by the number of binary collisions, which describe well the photon spectrum for $p_T > 5$ GeV/c. However, the excess below 2 GeV/c, not described by these calculations, could be attributed to thermal photons. At the LHC, the inverse slope parameter extracted from an exponential fit in the low-p_T range $0.8 < p_T < 2.2$ GeV/c, corresponds to an initial temperature is T $=297 \pm 12(\text{stat}) \pm 41(\text{syst})$ MeV.

RHIC data can be described with initial temperatures between 170 and 235 MeV [38]. Therefore, the initial temperature value measured at the LHC is well above the temperature expected for the phase transition (145-164 MeV, see Sec. 1.2.1) and about 40% higher than the one reported at the RHIC [38].

In conclusion, the nuclear medium formed at the LHC is denser and hotter than at RHIC, which indicates that the QGP properties at LHC energies can be investigated in more detail.

1.3.3.1 Detailed QGP properties with soft probes (selected measurements)

The soft probes are used in heavy-ion physics studies to characterize the bulk matter properties and dynamical evolution of the system created in the collisions. In the following we focus on selected results concerning charged-particle multiplicity, angular correlations and fluctuations.

Charged-particle multiplicity

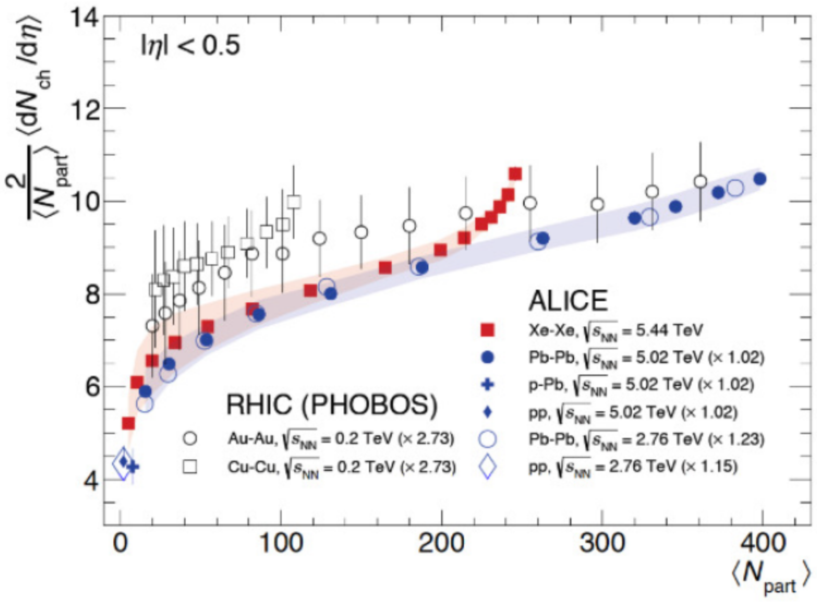

Figure 1.21: The mid-rapidity charged-particle multiplicity as a function of the number of participants measured in PHOBOS (RHIC) and ALICE experiments. Figure is taken from Ref. [56].

The particle multiplicity can provide information about relative contributions to particle production from hard scatterings, soft processes and energy density achieved in different systems collisions. The mid-rapidity charged-particle multiplicity normalised by the number of nucleon pairs participating in the collision as a function of the number of participants is presented in Fig. 1.21. The Xe-Xe results are higher than Pb-Pb results at a similar number of participants for the more central collisions. The same behavior was observed also at RHIC, where Cu-Cu multiplicities are larger than in Au-Au ones for the most central collisions. At a same centrality class, the charged-particle multiplicity measured at the LHC with ALICE is higher than that measured at RHIC.

Angular correlations and fluctuations

.

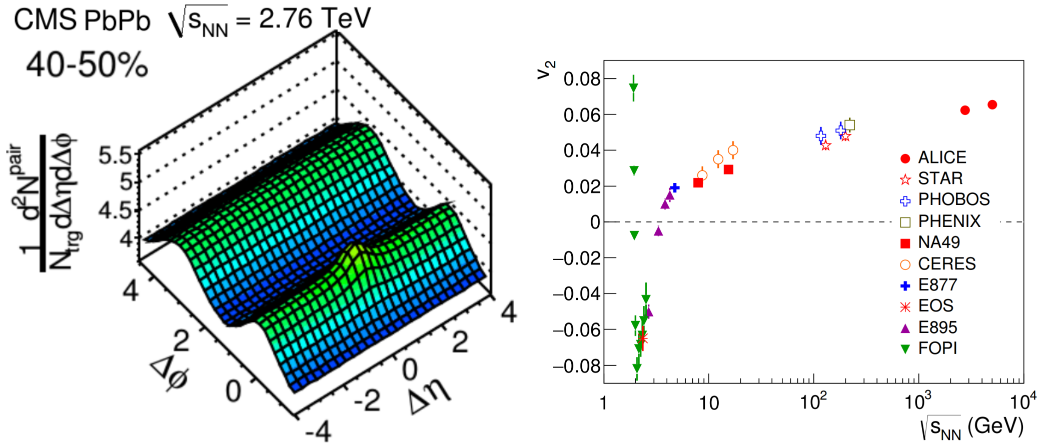

Figure 1.22: Two-dimensional $\Delta\eta\Delta\varphi$ per-trigger-particle associated yield of charged hadrons for Pb-Pb collisions at $\sqrt{s_{\rm NN}} = 2.76$ TeV. Figure taken from Ref. [53] (left). Integrated elliptic flow v_2 as a function of the collision energy [55, 54]. Figure taken from Ref. [54] (right).

From the $(\Delta\eta, \Delta\varphi)$ distributions measured in Au–Au collisions at RHIC [57, 58], we can observe a peak around $(\Delta\eta, \Delta\varphi) = (0, 0)$, originating primarily from jets and prominent long-range correlations, extended over several units of rapidity and centered in azimuth around $\Delta\varphi = 0$ (near-side) and $\Delta\varphi = \pi$ (away-side). The near-side ridge becomes stronger with increasing centrality and has mostly been associated with collective phenomena. Similar structures were observed in Pb-Pb collisions at the LHC [59, 60], as shown in Fig. 1.22.

The elliptic flow v_2 was measured in many experiments from low to high energies, up to $\sqrt{s_{\rm NN}} = 5.02$ TeV. The integrated v_2, shown in Fig. 1.22, increases with collision energy, mainly due to a larger mean $p_{\rm T}$ [61]. The v_2 increases by about 30% [61], in the transition from the highest RHIC to LHC energies, in agreement with hydrodynamic models [62, 63].

1.3.3.2 Detailed QGP properties with hard probes (selected measurements)

The **heavy favours** as probes of the QGP are introduced in Sec. 1.4. The heavy-favour results at the LHC are shown in Sec. 1.4.5. In the following we focus on selected measurements concerning high-$p_{\rm T}$ particles.

High $p_{\rm T}$ particles

The nuclear modification factor measured at SPS, RHIC and LHC is shown in Fig. 1.23 [64, 65]. Note that SPS result is shown for neutral pions, while RHIC results are shown for both neutral pions and charged particles (the most abundant charged-particle species are π, K and p), ALICE and CMS results are shown for charged particles. The LHC measurements show a slightly stronger suppression than those from RHIC [70, 71]. The largest measured suppression, in the $p_{\rm T}$ interval 6-8 GeV/c, is a factor of about seven at the LHC, while at RHIC a factor of five was observed. A completely new observation at the LHC is that with increasing $p_{\rm T}$, the suppression becomes smaller.

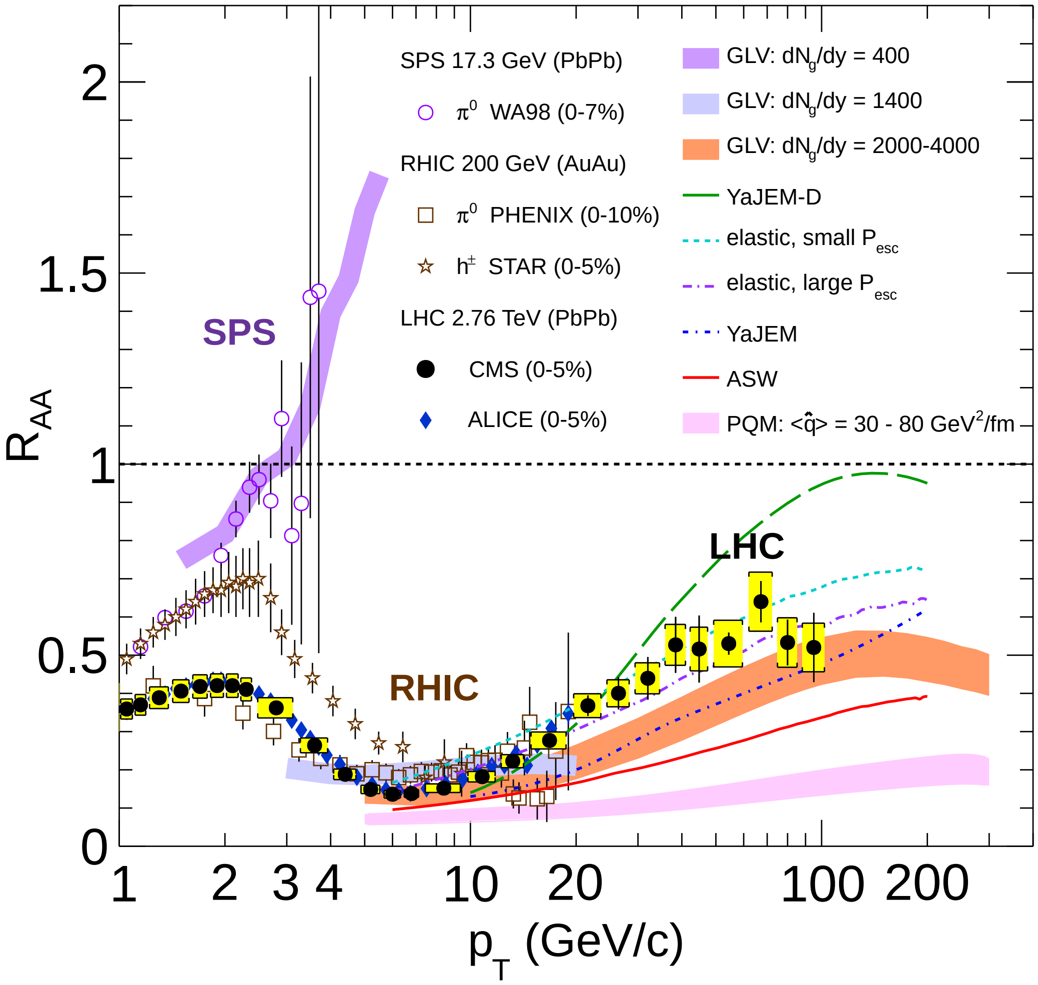

Figure 1.23: Nuclear modification factor $R_{\rm AA}$ in central heavy-ion collisions at three different $\sqrt{s_{\rm NN}}$, as a function of $p_{\rm T}$, for neutral pions (π^0), and charged particles [64, 65], compared to several theoretical predictions [66, 67, 68, 69]. The error bars on the points are the statistical uncertainties, and the yellow boxes around the CMS points are the systematic uncertainties. The bands for several of the theoretical calculations represent their uncertainties. Figure taken from Ref. [64].

A review of the results from LHC experiments obtained until 2017 has been published in Ref. [73, 74].

1.4 Heavy flavours as probes of the QGP

In particle physics, flavour refers to the species of elementary particles. The six flavours of quarks and six flavours of leptons are counted in SM [1, 2] (see Fig. 1.1). The quarks can be classified into two groups: light quarks, i.e. u,d and s quarks, and heavy quarks, i.e. c and b quarks (mean lifetime of the t quark is about $c\tau < 5 \times 10^{-25}$s [1] before it can hadronize).

In heavy-ion collisions:

1. Heavy quarks are produced through initial hard-scattering processes at time scales $\sim 1/2m_{\mathrm{c,b}}$ (of the order of 0.07 fm/c for charm and 0.02 fm/c for beauty), shorter than the QGP formation time ($\tau_0 \sim 0.1$–1 fm/c) [105], and therefore heavy quarks experience the whole medium evolution.
2. According to asymptotic freedom, the QCD running coupling α_{s} is small in heavy-flavour production and allows us to use perturbative QCD (pQCD) predictions.

Therefore, heavy-flavour (open heavy flavours and quarkonia) measurements are important tools to study the hot and dense partonic medium formed in ultra-relativistic heavy-ion collisions. Note that both initial and final-state effects are expected to enter in the production and propagation of heavy quarks.

1.4.1 Heavy-flavour hadron production in nucleon-nucleon collisions

Factorization theorem

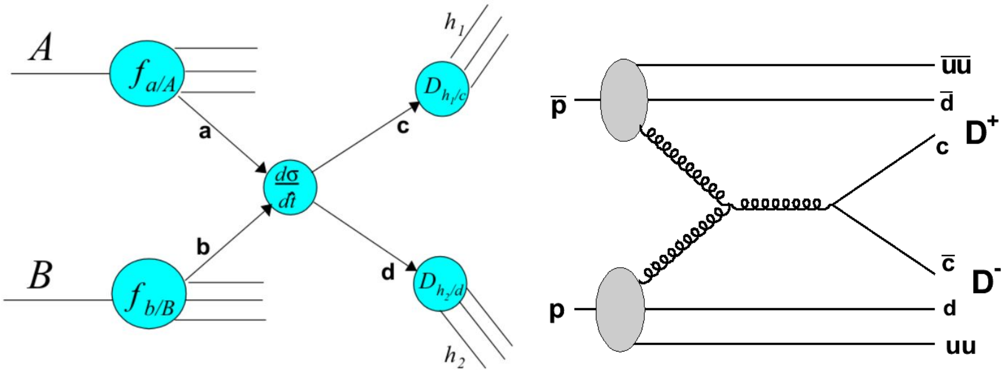

Figure 1.24: Examples of factorization diagrams (left panel) and D^+D^- production in $p\bar{p}$ collisions via $gg \to c\bar{c}$ (right panel).

In experiments, heavy flavours are measured in the hadronic channel ($\mathrm{H_Q}$) as illustrated in Fig. 1.24 or via their decay leptons in the final state (from B- and D-meson decays). Heavy-quark hadronic production can be calculated in nucleon-nucleon collisions with the pQCD framework according to the factorization theorem [75],

$$\begin{aligned}\frac{\mathrm{d}\sigma^{NN\to H_{\mathrm{Q}}X}}{\mathrm{d}p_{\mathrm{T}}}(\sqrt{s_{\mathrm{NN}}}, m_{\mathrm{Q}}, \mu_{\mathrm{F}}^2, \mu_{\mathrm{R}}^2) = \sum_{i,j=\mathrm{q},\bar{\mathrm{q}},\mathrm{g}} f_i(x_1, \mu_{\mathrm{F}}^2) \otimes f_j(x_2, \mu_{\mathrm{F}}^2) \otimes \\ \frac{\mathrm{d}\hat{\sigma}^{ij\to \mathrm{Q}(\overline{\mathrm{Q}})\{n\}}}{\mathrm{d}\hat{p}_{\mathrm{T}}}(\alpha_{\mathrm{s}}(\mu_{\mathrm{R}}^2), \mu_{\mathrm{R}}^2, \mu_{\mathrm{F}}^2, m_{\mathrm{Q}}, x_1 x_2 s_{\mathrm{NN}}) \otimes D_{\mathrm{Q}}^{\mathrm{H_Q}}(z).\end{aligned} \tag{1.13}$$

All subprocesses for open heavy-flavour hadron production are shown in Eq. 1.13. In the initial stage of nucleon-nucleon collisions, two partons (i and j) are extracted from each nucleon with momentum fractions $x_{i/j}$ according to the probabilities given by the parton distribution functions (PDF) $f_{i/j}(x_{i/j}, \mu_{\mathrm{F}}^2)$, where i/j reflects the species of partons (q, $\overline{\mathrm{q}}$ or g) and μ_{F} is the factorization scale.

Then, heavy flavours are produced during hard scatterings between the two extracted partons with virtuality $Q\sim x_1 x_2 s_{\mathrm{NN}}$ (Q related to the momentum transfer in a given process). The factor μ_{R}[1] is the renormalization scale.

After a heavy quark is formed, it will interact with other partons and fragment into an open heavy-flavour hadron. $D_{\mathrm{Q}}^{\mathrm{H_Q}}(z)$ is the heavy-quark fragmentation function, $z = p^{\mathrm{H_Q}}/p^{\mathrm{Q}}$ is the momentum fraction.

Parton Distribution Functions in the low Bjorken-x region

The distribution of Bjorken-x [31] for a given parton (gluon, valence quark, sea quark) is called the Parton Distribution Function (PDF), and it gives the probability to pick up a parton with momentum fraction from a nucleon. The LHC allows us to probe the parton distribution function of nucleon in the region of low values of Bjorken-x, as shown in Fig. 1.25.

We can consider the case of the production of a heavy-quark pair, $\mathrm{Q\bar{Q}}$, through the leading order gluon-gluon fusion process gg $\to \mathrm{Q\bar{Q}}$ in the collision of two ions with proton number Z_1, Z_2 and atomic number A_1, A_2. If the parton intrinsic transverse momentum in the nucleon can be neglected, the four-momentum of the two incoming gluons are $(x_1,\ 0,\ 0,\ x_1) \cdot (Z_1/A_1)\sqrt{s_{\mathrm{NN}}}/2)$ and $(x_2,\ 0,\ 0,\ x_2) \cdot (Z_2/A_2)\sqrt{s_{\mathrm{NN}}}/2)$. Then the invariant mass of the $\mathrm{Q\bar{Q}}$ pair is given by,

$$M^2_{\mathrm{Q\bar{Q}}} = \hat{s} = x_1 x_2 s_{\mathrm{NN}} = x_1 \frac{Z_1}{A_1} x_2 \frac{Z_2}{A_2} s_{\mathrm{pp}}, \tag{1.14}$$

and the rapidity in the laboratory is,

$$y_{\mathrm{Q\bar{Q}}} = \frac{1}{2}\ln[\frac{E+p_{\mathrm{z}}}{E-p_{\mathrm{z}}}] = \frac{1}{2}\ln[\frac{x_1}{x_2}\cdot\frac{Z_1 A_2}{Z_2 A_1}]. \tag{1.15}$$

---

[1] central value $\mu_{R,F} = \mu_0 = \sqrt{p_{\mathrm{T}}^2 + m^2}$

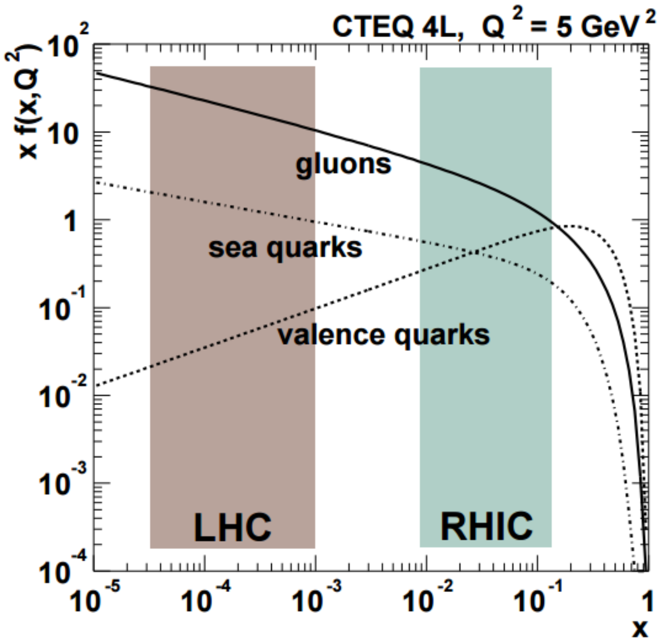

Figure 1.25: Parton distribution function (PDF) via the Bjorken-x [31] in the proton with $Q^2 = 5$ GeV^2 (CTEQ 4L PDF set used). Figure taken from Ref. [76].

For a symmetric colliding system ($A_1 = A_2,\ Z_1 = Z_2$),

$$x_1 = \frac{M_{\mathrm{Q\bar{Q}}}}{\sqrt{s_{\mathrm{NN}}}} \exp(+y_{\mathrm{Q\bar{Q}}}), \qquad x_2 = \frac{M_{\mathrm{Q\bar{Q}}}}{\sqrt{s_{\mathrm{NN}}}} \exp(-y_{\mathrm{Q\bar{Q}}}). \tag{1.16}$$

Figure 1.25 shows an example of the parton distribution function $xf(x,\ Q^2)$ from CTEQ 4L parameterization [76], and the value of virtuality, $Q^2 = 5$ GeV^2, corresponding to c$\bar{\text{c}}$ production threshold at leading order ($Q^2 = M^2_{\mathrm{Q\bar{Q}}} = sx_1x_2$). The LHC and RHIC Bjorken-x regions are indicated by the shaded areas and show that at the LHC heavy quarks allow one to investigate lower Bjorken-x values than at RHIC. Moreover, in particular at forward rapidity ($2.5 < y < 4$), the values of Bjorken-x down to about 10^{-5} can be accessed.

Partonic cross section

The partonic cross section is calculable as perturbative series of the strong coupling α_{s}. Hard scattering cross section is expanded in a perturbative series of powers of the α_{s} up to Leading Order or Next to Leading Order.

At **Leading Order** (**LO**) in α_{s}, there are only two sub-processes which contribute: q-$\bar{q}$ annihilation, $q + \bar{q} \to \bar{Q} + Q$, and gluon fusion, $g + g \to \bar{Q} + Q$. At **Next-to-Leading Order** (**NLO**), the virtual one-loop corrections to these 2→2 processes have to be included in addition to the following 2→3 processes: (i) higher order terms in pair creation, $q + \bar{q} \to \bar{Q} + Q + g$, (ii) flavour excitation, $g + g \to \bar{Q} + Q + g$, (iii) gluon splitting, $g + \bar{q} \to \bar{Q} + Q + \bar{q}$ and $g + q \to \bar{Q} + Q + q$.

At any order, the partonic cross section can be expressed in terms of the dimensionless scaling functions $f^{ij}_{nk}(\xi)$ [77]:

$$\hat{\sigma}^{ij\to \mathrm{Q}(\overline{\mathrm{Q}})}(\alpha_{\mathrm{s}}(\mu^2_{\mathrm{F}}),\mu^2_{\mathrm{R}},m_{\mathrm{Q}},\hat{\mathrm{s}}) = \frac{\alpha_{\mathrm{s}}(\mu^2_{\mathrm{F}})}{m^2_{\mathrm{Q}}}\sum_{n=0}^{\infty}(4\pi\alpha_{\mathrm{s}}(\mu^2_{\mathrm{F}}))^n \sum_{k=0}^{n} f^{ij}_{nk}(\xi)\ln^k\frac{\mu^2_{\mathrm{R}}}{m^2_{\mathrm{Q}}} \tag{1.17}$$

where $\xi = \hat{s}/4m^2_{\mathrm{Q}} - 1$, $\hat{s} = x_{\mathrm{i}}x_{\mathrm{j}}s_{\mathrm{NN}}$ is related to two partons i and j carrying momentum fractions multiplied by the partonic centre-of-mass energy, m_{Q} is the heavy quark mass, and μ_{F} and μ_{R} are the factorization and renormalization scales, respectively.

In Eq. (1.17), $n = 0$ gives the Leading Order cross section and $n = 1$ corresponds to the Next-to-Leading Order cross section.

In the **FONLL**[2] framework, the Fixed-Order (FO) plus Next-to-Leading Logarithms (NLL) calculation are matched together [78],

$$\mathrm{FONLL} = \mathrm{FO} + (\mathrm{RS} - \mathrm{FOM0}) \times \mathrm{G}(m_{\mathrm{Q}}, p_{\mathrm{T}}), \tag{1.18}$$

where, **FO** is the already existing computation of the cross section (fixed-order approach) and **RS** is the resummed cross section in the massless limit (resummed approach). In order to subtract from the RS result, the fixed-order terms already present in the FO calculation, we must provide an approximation to the latter where only logarithmic mass terms are retained. We will call this "massless limit" **FOM0** of FO calculations.

The cross section condition $\mathrm{d}\sigma_{\mathrm{FONLL}}/\mathrm{d}p_{\mathrm{T}} \to \mathrm{d}\sigma_{\mathrm{RS}}/\mathrm{d}p_{\mathrm{T}}$ for $p_{\mathrm{T}} \gg m_{\mathrm{Q}}$ implies that the matching function $\mathbf{G}(m_{\mathrm{Q}}, p_{\mathrm{T}})$ has to approach unity in this limit. Furthermore, in the limit of small transverse momenta, $\mathrm{d}\sigma_{\mathrm{FONLL}}/\mathrm{d}p_{\mathrm{T}}$ has to approach the fixed-order calculation $\mathrm{d}\sigma_{\mathrm{FO}}/\mathrm{d}p_{\mathrm{T}}$. This can be achieved by requiring that $\mathrm{G}(m_{\mathrm{Q}}, p_{\mathrm{T}}) \to 0$ for $p_{\mathrm{T}} \to 0$ [78].

Fragmentation function

The fragmentation function (FF) $D^{H_{\mathrm{Q}}}_{\mathrm{Q}}(z)$ gives the probability that a quark Q produces an hadron H_{Q} carrying a fraction z of the quark momentum. The fragmentation function which treats the desintegration of quarks and gluons into hadrons, is a non-perturbative process in QCD.

For light quarks, the QCD factorization theorem [79, 80] allows to factorize these non-perturbative effects into universal fragmentation functions together with the partonic cross section,

$$\int \frac{\mathrm{d}z}{z}\frac{\mathrm{d}\hat{\sigma}^{ij\to k}}{\mathrm{d}p^{\mathrm{h}}_{\mathrm{t}}}(\frac{p^{\mathrm{h}}_{\mathrm{T}}}{z},\mu)D^{\mathrm{h}}_{k}(z,\mu), \tag{1.19}$$

---

[2] FONLL is a unified framework which is valid in the entire kinematic range ($p_{\mathrm{T}} \ll m_{\mathrm{Q}}$, $p_{\mathrm{T}} \simeq m_{\mathrm{Q}}$, $p_{\mathrm{T}} \gg m_{\mathrm{Q}}$. In FONLL, the interpolating function is chosen to be $G(m_{\mathrm{Q}}, p_{\mathrm{T}}) = p^2_{\mathrm{T}}/(p^2_{\mathrm{T}}+a^2m^2_{\mathrm{Q}})$, where the constant is set to $a = 5$ [105].

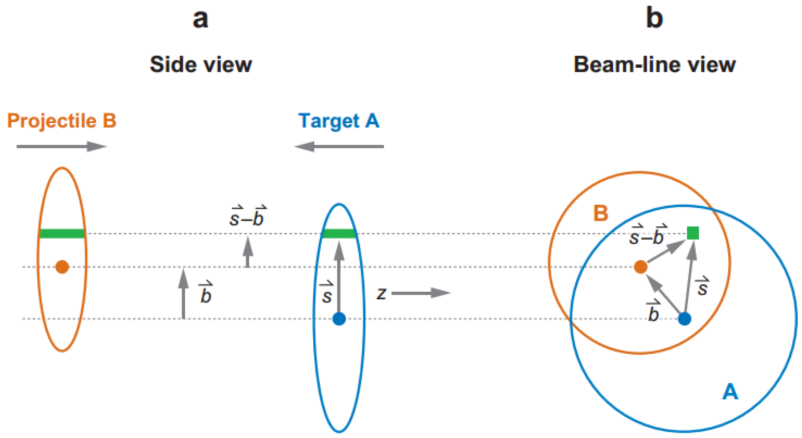

Figure 1.26: Schematic representation of the optical Glauber model geometry, with transverse (a) and longitudinal (b) views. Figure taken from Ref. [83].

where, i, j and k are the light partons, $p_{\mathrm{T}}^{\mathrm{h}}$ is the transverse momentum of light hadrons h, the factorization scale μ is a non-physical quantity of both partonic cross sections and fragmentation functions.

The process of fragmentation is different for heavy quarks. Due to their large masses that act as a cutoff for the collinear singularities which appear in higher orders in perturbative calculations, the perturbative calculations of heavy quark-production and non-perturbative fragmentation functions are separated, as shown in Eq. 1.13.

In Eq. 1.13 the average value of the fragmentation fraction z of heavy-quark is estimated as [81, 82]: $< z > \approx 1 - \frac{\Lambda_{\mathrm{H}}}{m_{\mathrm{Q}}}$. The Λ_{H} is the hadronic scale, the heavy-quark mass m_{Q} is much larger than Λ_{H}.

1.4.2 Binary scaling of heavy-flavour production in AB collisions

The geometry of heavy-ion collisions can be described via the Glauber model [26] as a simple superposition of independent nucleon-nucleon collisions, without taking into account any medium modification. The nucleons are distributed with a known density distribution function $\rho(s, z)$, as a function of their radius, usually measured experimentally. The nuclear density function $\rho(s, z)$ can be described by the **Woods-Saxon** distribution function [84, 85],

$$\rho(s, z) = \rho_0 \frac{1 + \omega \cdot (s/R)^2}{1 + \exp[(s - R)/z]}, \tag{1.20}$$

where ρ_0 is a normalization factor, R is the nuclear radius, z is the surface thickness, and ω allows for central non-regularity with a given nuclei. For a Pb nucleus case, the Woods-Saxon parameters in Eq. (1.20) are: $R = 6.624$ fm, $\rho_0 = 0.16$ fm^{-3} and $\omega = 0$ [86].

The collision geometry is shown in Fig. 1.26, where two heavy ions, A target and B projectile, are colliding at relativistic speed with impact parameter b. The impact parameter b and flux tube of nucleon at distance s are relative to nucleus centre. During the collision these tubes overlap. With a given nucleon, the probability per unit transverse area being located in the target flux tube is:

$$T_i(s) = \int \mathrm{d}z_i \cdot \rho(s_i, z_i). \tag{1.21}$$

where $T_{\mathrm{i}}(s)$ is the thickness function of a nucleus i ($i =$ A,B), $\rho(s_i, z_i)$ is the probability per unit volume, normalized to unity, for finding the nucleon at location (s_i, z_i).

The product of T_{A}, T_{B} can be used to define the nuclear "thickness function" or nuclear overlap function, and is given by:

$$T_{\mathrm{AB}} \doteq \int \mathrm{d}\vec{s} \cdot T_{\mathrm{A}}(\vec{s}) T_{\mathrm{B}}(\vec{s} - \vec{b}), \tag{1.22}$$

The relation between number of inelastic nucleon-nucleon collisions N_{coll} and the nuclear overlap function T_{AA} for a given centrality class within the Glauber Model [26] is,

$$T_{\mathrm{AA}} =< N_{\mathrm{coll}} > / \sigma_{\mathrm{NN}} \tag{1.23}$$

where σ_{NN} is the inelastic cross section in nucleus-nucleus collisions.

The nuclear modification factor of heavy-flavour production in AB collisions can be obtained using the number of inelastic nucleon-nucleon collisions $< N_{\mathrm{coll}} >_{\mathrm{AB}}$ or the nuclear overlap function $< T_{\mathrm{AB}} >$,

$$\begin{aligned} R_{\mathrm{AB}}(p_{\mathrm{T}}) &= \frac{\mathrm{d}^2 N_{\mathrm{AB}}/\mathrm{d}p_{\mathrm{T}}\mathrm{d}y}{< N_{\mathrm{coll}} >_{\mathrm{AB}}\ \mathrm{d}^2 N_{\mathrm{pp}}/\mathrm{d}p_{\mathrm{T}}\mathrm{d}y} \\ R_{\mathrm{AB}}(p_{\mathrm{T}}) &= \frac{\mathrm{d}^2 N_{\mathrm{AB}}/\mathrm{d}p_{\mathrm{T}}\mathrm{d}y}{< T_{\mathrm{AB}} > \mathrm{d}^2 \sigma_{\mathrm{pp}}/\mathrm{d}p_{\mathrm{T}}\mathrm{d}y} \end{aligned} \tag{1.24}$$

where $\mathrm{d}^2 N_{\mathrm{AB}}/\mathrm{d}p_{\mathrm{T}}\mathrm{d}y$ is the p_{T}- and y-differential yields in nucleus-nucleus collisions, $\mathrm{d}^2 N_{\mathrm{pp}}/\mathrm{d}p_{\mathrm{T}}\mathrm{d}y$ is the p_{T}- and y-differential yields in pp collisions, and $\mathrm{d}^2\sigma_{\mathrm{pp}}/\mathrm{d}p_{\mathrm{T}}\mathrm{d}y$ is the p_{T}- and y-differential cross section in pp collisions.

1.4.3 Heavy-flavour production in pA collisions: cold nuclear effects

Characterizing the hot and dense medium produced in heavy-ion (AA) collisions requires a quantitative understanding of the effects induced by the presence of nuclei in the initial-state, so-called Cold Nuclear Matter (CNM) effects. The CNM effects can be studied in proton-nucleus (pA) or deuteron-nucleus (dA) collisions. The heavy-flavour production in pA collisions can be used as control experiment for AA collisions and to investigate cold nuclear matter effects: such as the **nuclear shadowing** [94], **parton intrinsic transverse momentum (k_{T}) broadening (or Cronin effect)** [99] and **initial-state energy loss** [95].

In the following, I will focus on the following effects: nuclear shadowing and Cronin effect.

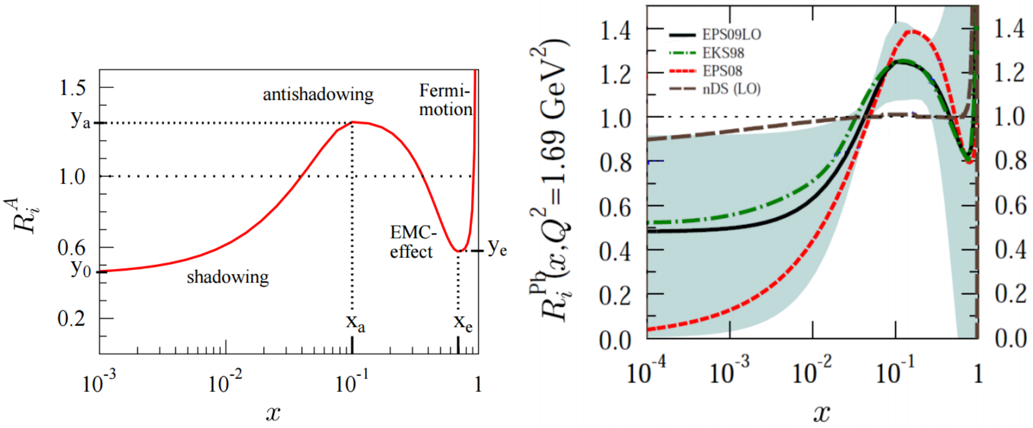

Figure 1.27: Left: ratios of nuclear parton distribution functions (nPDFs) $f_i^{\mathrm{A}}(x,Q^2)$ with respect to the parton distribution functions (PDFs) of free nucleons $f_i^{\mathrm{N}}(x,Q^2)$ as a function of Bjorken-x. Right: comparison of the gluon shadowing parametrisations EKS98 [90], EPS08 [91], nDS [92] at LO and EPS09 [93] at LO in a lead nucleus at $Q^2 = 1.69$ GeV^2. Figure taken from Ref. [93].

Nuclear shadowing

The fact that nuclear structure functions in nuclei are different from the superposition of those of their constituents nucleons is a well known phenomenon [87]. Bound nucleons (protons, and neutrons) in nucleus have different properties from the free ones due to the interactions and correlations inside the nucleus. In particular, in heavy-ion collisions, final-state observables are affected by the initial-state nuclear effects (the so-called cold nuclear effects).

It is believed that, different mechanisms will drive different cold nuclear effects in different Bjorken-x regions, and they are often grouped into the ratios of the nuclear parton distribution functions (nPDFs) $f_i^{\mathrm{A}}(x,Q^2)$ with respect to the parton distribution functions (PDFs) of free nucleons $f_i^{\mathrm{N}}(x,Q^2)$:

$$R_i^{\mathrm{A}}(x,Q^2) = \frac{f_i^{\mathrm{A}}(x,Q^2)}{f_i^{\mathrm{N}}(x,Q^2)}, \tag{1.25}$$

where i is the parton specie index (valence quark, sea quark or gluon). Bjorken-x is equal to $\frac{m_{\mathrm{T}}}{\sqrt{s_{\mathrm{NN}}}}\exp(\pm y)$ with the transverse mass $m_{\mathrm{T}} = \sqrt{m_0^2 + p_{\mathrm{T}}}$.

Figure 1.27 (left) shows a typical shape of $R_i^{\mathrm{A}}(x,Q^2)$ as a function of Bjorken-x. The behaviour of $R_i^{\mathrm{A}}(x,Q^2)$ as a function of Bjorken-x for a given fixed Q^2 can be divided into four regions:

- an excess towards $x \to 1$ and beyond, **Fermi motion** [88];
- $0.3 \lesssim x \lesssim 0.7$, a depletion in $R_i^{\mathrm{A}}(x,Q^2)$, **EMC** (EMC stands for European Muon Collaboration) effect [89];
- $0.1 \lesssim x \lesssim 0.3$, $R_i^{\mathrm{A}}(x,Q^2) > 1$, **anti-shadowing**;

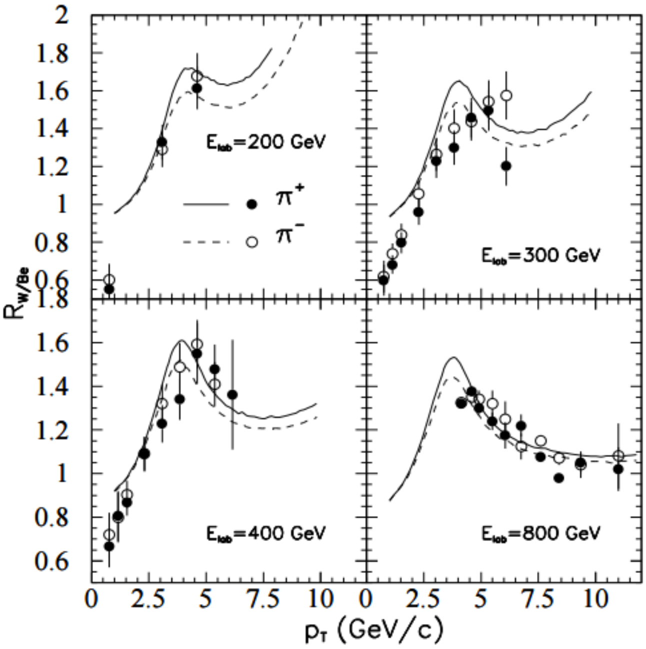

Figure 1.28: Ratios of charged pions spectra in p-W collisions over that in p-Be collisions as a function p_{T}. The results are normalized by the atomic number of the target nucleus. The curves are the parton model calculation with k_{T} broadening due to multiple parton scatterings. Figure taken from Ref. [97].

- $x \lesssim 0.1$, $R_i^{\mathrm{A}}(x, Q^2) < 1$, **shadowing**.

Four kinds of gluon shadowing parametrisations are compared: EKS98 [90], EPS08 [91], nDS [92] at LO and EPS09 [93]. As illustrated by Fig. 1.27 (right), this is investigated for a gluon nPDF.

The nuclear modification factor can be suppressed due to the shadowing (small Bjorken-x) contribution, while it can be enhanced for anti-shadowing (intermediate Bjorken-x). At small Bjorken-x, in the case of heavy-quark production at forward rapidity, one could expect $R_{\mathrm{AA}} < 1$ at low p_{T}, due to shadowing [105].

Parton intrinsic transverse momentum (k_{T}) broadening (known as the Cronin effect)

In proton-nuclear collisions the multiple scattering of partons in the nucleus before hard scatterings leads to transverse momentum broadening (known as the Cronin effect). One can study this effect in a model of multiple-parton scatterings [96].

Due to the multiple-parton scatterings prior to the hard processes, we consider the initial transverse momentum k_{T} of the beam partons is broadened. In Fig. 1.28, the ratios of charged pion spectra (dot-dashed lines for π^- and solid lines for π^+) in p-W collisions over that in p-Be collisions is presented as function of p_{T}.

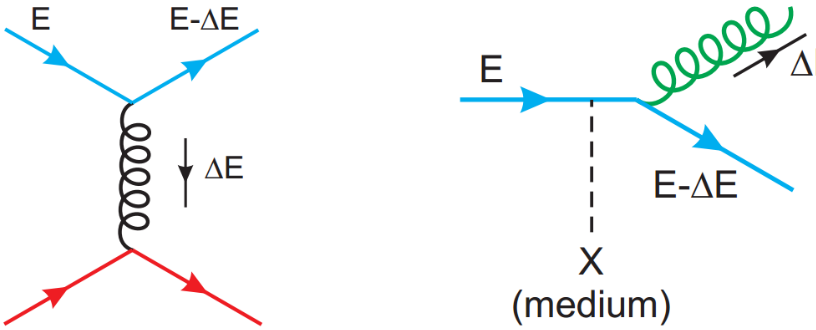

Figure 1.29: Left: diagram for collisional energy loss of a quark of energy E traversing a quark-gluon medium. Right: radiative energy loss of a quark of energy E traversing a quark-gluon medium. Figure taken from Ref. [98].

If there was no nuclear dependence due to multiple scatterings, the ratios would have a flat value of one. Since the transverse momentum broadening due to multiple parton scatterings is finite, its effect will eventually become smaller and disappear. Therefore, the p_{T} location of the maximum enhancement can give us the scale of average transverse momentum broadening. The cronin effect plays a role at intermediate p_{T} interval (e.g. p_{T} in 2-4 GeV/c), as displayed in Fig. 1.28.

1.4.4 Heavy-flavour production in AA collisions: hot nuclear effects

The partons created in the early stage of nucleus-nucleus collisions via hard scatterings go through the hot and dense medium formed, and partons lose a large fraction of their energy due to the interactions between partons inside the medium. In a general way, the total energy loss of a parton going through the QCD medium is the sum of collisional and radiative term, written as:

$$\Delta E = \Delta E_{\mathrm{rad}} + \Delta E_{\mathrm{coll}} \tag{1.26}$$

where ΔE_{rad} is the gluon bremsstrahlung energy loss contribution via medium-induced multiple gluon emission (**radiative energy loss**), and ΔE_{coll} is the collision energy loss with the medium constituents (**collisional energy loss**). Their different processes can be indicated briefly with the diagrams presented in Fig. 1.29.

Radiative energy loss

The gluon radiation expected to be the main mechanism of energy loss, the amount of energy lost is sensitive to:

- the medium properties (density);
- the path-length (L) that the parton travels inside the medium;

- the properties of the parton probing the medium: color charge (Casimir factor) and quark mass (dead core).

Several models are available for the study of the radiative energy loss, e.g. the Baier-Dokshitzer-Mueller-Peigne-Schiff and Zakharov (BDMPS-Z) [99] model expresses the energy loss as:

$$< \mathrm{E} > \propto \alpha_{\mathrm{s}} C_{\mathrm{R}} \hat{q} L^2 \tag{1.27}$$

where, the $\hat{q}$ is the transport coefficient related to the medium characteristics and to the gluon density $\mathrm{d}N_{\mathrm{g}}/\mathrm{d}y$; the α_{s} denotes the running coupling; the C_{R} is the Casimir factor, which is 4/3(3) for quark-gluon (gluon-gluon) coupling. The energy loss is proportional to L^2, taking into account the probability to emit a breemstrahlung gluon and the fact that radiated colored gluons can interact themselves with the medium.

Dead Cone Effect Due to the mass effect, the radiative energy loss of heavy quarks is different from that of light quarks in the nuclear medium. One of the differences is the suppression due to gluon bremsstrahlung from massive quarks at small angle [100],

$$\theta_0 = m_{\mathrm{Q}}/E, \tag{1.28}$$

where m_{Q} and E are the mass and initial energy of heavy quarks. This is the so-called dead cone effect. Since the dead cone effect reduced the medium induced gluon radiation, the suppression of leading open heavy-flavour hadron production rates is reduced and gluon radiating spectrum by massive quarks $\mathrm{d}P_{\mathrm{HQ}}$. The $\mathrm{d}P_{\mathrm{HQ}}$ can be obtained by using the radiative spectrum of massless quarks $\mathrm{d}P_{\mathrm{LQ}}$ times a suppression factor $F(k_{\mathrm{t}}, m_{\mathrm{Q}}, \mathrm{E})$, related to the transverse momentum of gluon (k_{t}), mass and energy of heavy quarks. This factor is named dead cone factor [101],

$$\mathrm{d}P_{\mathrm{HQ}} = \mathrm{d}P_{\mathrm{LQ}} \cdot F(k_{\mathrm{t}}, m_{\mathrm{Q}}, \mathrm{E}) = \mathrm{d}P_{\mathrm{LQ}} \cdot (1 + \frac{\theta_0^2}{\theta^2})^{-2} = \mathrm{d}P_{\mathrm{LQ}} \cdot (\frac{k_{\mathrm{t}}^2}{k_{\mathrm{t}}^2 + x^2 m_{\mathrm{Q}}^2}). \tag{1.29}$$

where $\theta = k_{\mathrm{t}}/\omega$ is the radiative angle of the gluon relative to the motion direction of the heavy quark and $x = \omega/\mathrm{E}$ is the energy fraction taken by the radiated gluon, ω is the energy of the radiated gluon.

With the dead cone effect (mass dependence), see Eq. 1.28 and 1.29 , the radiative energy loss of light quarks is expected to be smaller with respect to that for heavy quarks. On the other hand, according to QCD [7], radiative energy loss of quarks is expected to be smaller with respect to that of gluons due to: the Casimir factor (color charge dependence), which is 4/3(3) for quark-gluon (gluon-gluon) coupling. Therefore, the averaged energy loss of different particles can written as:

$$\Delta E_{\mathrm{g}}^{\mathrm{M=0},C_R=3} > \Delta E_{\mathrm{q}}^{\mathrm{M=0},C_R=4/3} > \Delta E_{\mathrm{c}}^{\mathrm{M\sim1.5\ GeV},C_R=4/3} > \Delta E_{\mathrm{b}}^{\mathrm{M\sim5\ GeV},C_R=4/3} \tag{1.30}$$

where g, q, c and b represent the gluon, light quark, charm quark and beauty quark, respectively.

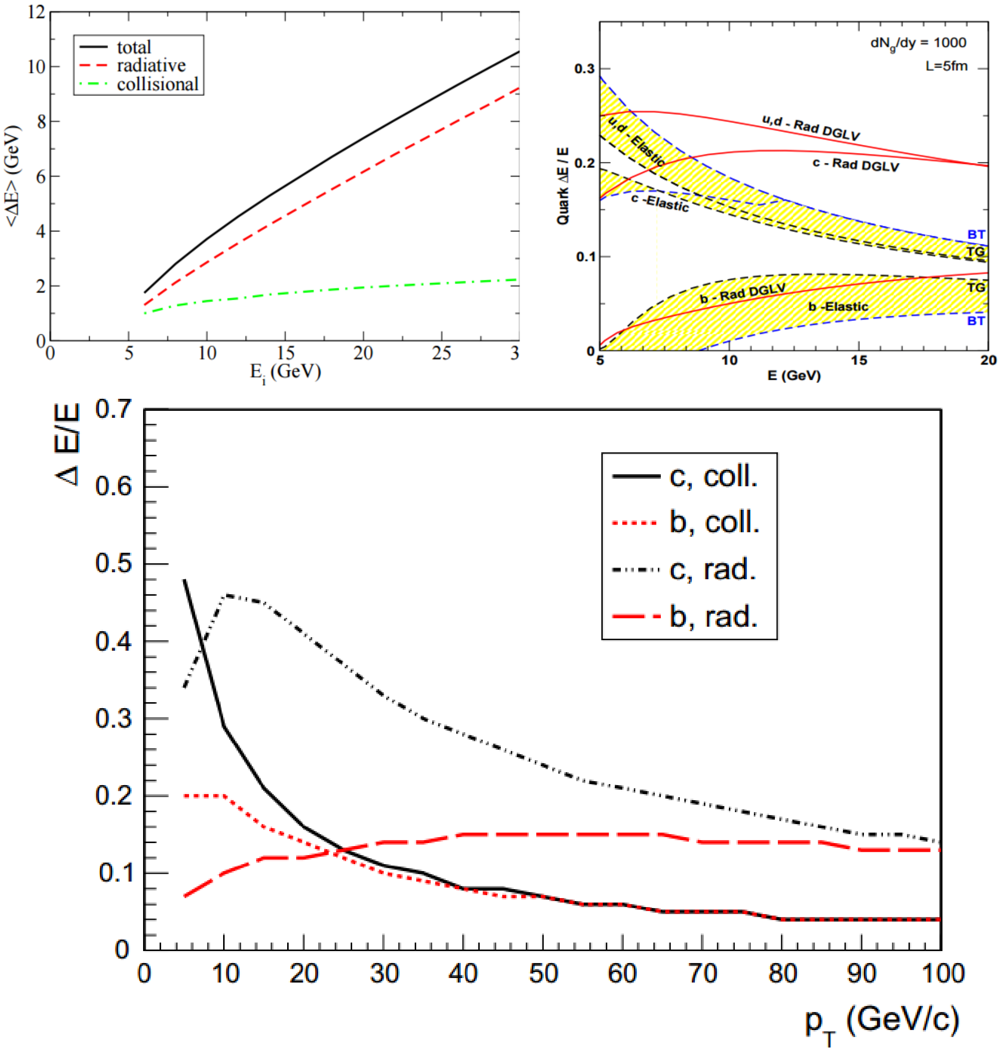

Figure 1.30: Upper: comparison of the average radiative and elastic energy loss of light-quarks (left) and light- and heavy-quarks (right) passing through the medium produced in central Au-Au collisions at RHIC energies as obtained by the AMY [102] and DGLV [103] models. Bottom: fractional energy loss evaluated for collisional and radiative processes and for charm and beauty quarks, at T = 304 MeV, with Djordjevic model [104]. Figure taken from Ref. [98, 105]

Collisional energy loss

Collisional energy loss through elastic scatterings with the medium constituents (Fig. 1.29, left) dominates at low particle momentum. The average energy loss in one scattering of a parton of energy E in a QGP medium of temperature T, is:

$$< \Delta E_{\mathrm{coll}} > \approx \frac{1}{\sigma \mathrm{T}} \int_{m_{\mathrm{D}}^2}^{t_{\max}} t \frac{\mathrm{d}\sigma}{\mathrm{d}t} \mathrm{d}t, \tag{1.31}$$

where $t = Q^2$ is the momentum transfer squared, $m_{\mathrm{D}}^2 \approx 4\pi\alpha_s T^2(1 + N_{\mathrm{f}}/6)$ is the Debye screening mass squared, $t_{\max}$ is the parton of energy E multiplied with a QGP medium of temperature T. The cross section is expressed as:

$$\frac{\mathrm{d}\sigma}{\mathrm{d}t} \approx C_{\mathrm{i}} \frac{4\pi\alpha_s^2(t)}{t^2}, \tag{1.32}$$

where $\alpha_s(t)$ is the coupling constant introduced in Eq. 1.6; $C_i = 9/4, 1, 4/9$ are the colour factors for gg, gq and qq scatterings, respectively.

As seen in upper plots of Fig. 1.30, $\Delta_{E_{\mathrm{coll}}}$ is in general a small correction compared to $\Delta_{E_{\mathrm{rad}}}$ for light quarks and gluons but it can be an important contribution for slower heavy quarks. The bottom plot of Fig. 1.30 presents the fractional energy loss corresponding to an effective temperature T = 304 MeV and a path length L = 5 fm. For charm quarks, the radiative energy loss starts to dominate at $p_{\mathrm{T}} > 10$ GeV/c, while this transition happens at $p_{\mathrm{T}} > 25$ GeV/c for beauty quarks.

1.4.5 Selected heavy-flavour physics results at the LHC

The heavy-flavour (open heavy flavour and quarkonia) measurements are important tools to study the hot and dense partonic medium formed in ultra-relativistic heavy-ion collisions (see Sec. 1.4).

In this section, we show some selected results obtained at the LHC that are relevant to the study of heavy flavours. The highlight results which will be presented in the following concern quarkonium results, D and B measurements, hierarchy of charged pion, non-strange D meson and non-prompt J/Ψ suppression, and heavy-flavour elliptic flow.

Quarkonium results

Figure 1.31 shows the J/Ψ R_{AA} as a function of $< N_{\mathrm{part}} >$ at $\sqrt{s_{\mathrm{NN}}} = 5.44$ (5.02) TeV in Xe-Xe(Pb-Pb) collisions at forward rapidity ($2.5 < y < 4$) with ALICE. The J/Ψ R_{AA} as a function of $< N_{\mathrm{part}} >$ presents a flat behaviour for $< N_{\mathrm{part}} >$ larger than 50. For $< N_{\mathrm{part}} >$ smaller than 50, the suppression is smaller. One can notice the results for both collision systems agree with each other for similar $< N_{\mathrm{part}} >$ within uncertainties. A comparison of the measurements at forward rapidity with a transport model [106, 107] is also shown in Fig. 1.31. The model is based on the thermal rate equation and contains continuous J/Ψ dissociation and regeneration in the QGP and the hadronic phase. The data for both systems and model agree

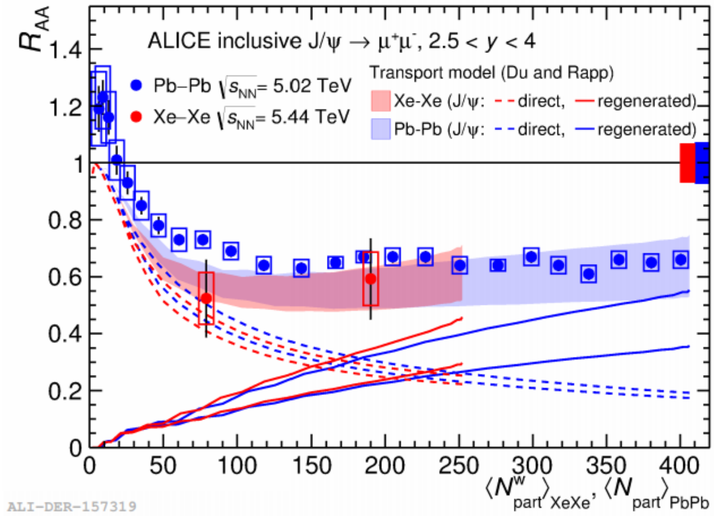

Figure 1.31: Inclusive J/Ψ R_{AA} as a function of $< N_{\mathrm{part}} >$ at $\sqrt{s_{\mathrm{NN}}} = 5.44$ (5.02) TeV in Xe-Xe and Pb-Pb collisions. Model calculations [106, 107] are presented with dashed lines for direct J/Ψ and with straight lines for regenerated J/Ψ. The bands are the predictions for inclusive J/Ψ. Figure taken from Ref. [111].

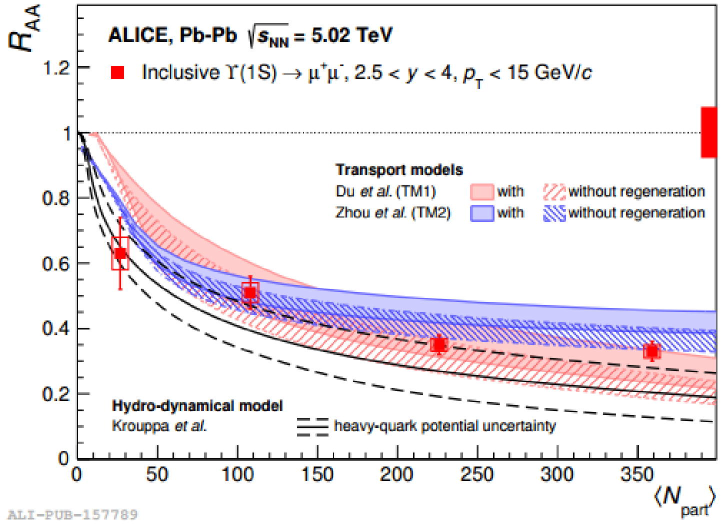

Figure 1.32: ϒ R_{AA} as a function of $< N_{\mathrm{part}} >$ in $\sqrt{s_{\mathrm{NN}}} = 5.02$ TeV Pb-Pb collisions, compared to transport [108, 109] and hydrodynamical [110] model calculations.. Figure taken from Ref. [111].

well, which indicates that similar $\sqrt{s_{\rm NN}}$ and $< N_{\rm part} >$ lead to similar relative contributions of suppression and (re)generation.

The Υ(1S) production has been also measured at forward rapidity in Pb-Pb collisions at $\sqrt{s_{\rm NN}} = 5.02$ TeV. An increase of the Υ(1S) suppression towards more central events is shown in Fig. 1.32. The measurement is compared with three model calculations (two transport models and one hydro-dynamical model calculations) [108, 109, 110] which all agree with the data within the uncertainties. The two transport models are shown with and without a regeneration component. Both versions agree with the data, which indicates that a regeneration component for bottomonium production should be negligible at LHC energies.

D measurements

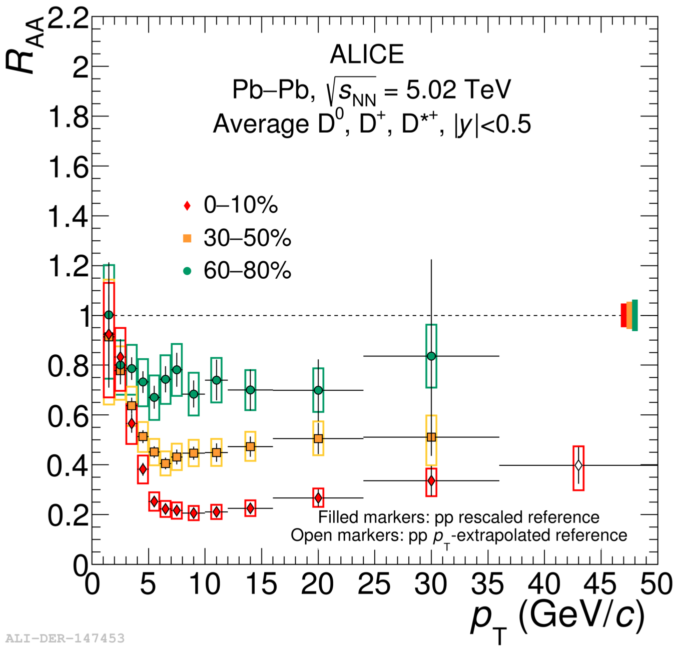

Figure 1.33: Non-strange D meson $R_{\rm AA}$ (average of D^0 , D$^+$ and D^{*+} $R_{\rm AA}$) as a function of $p_{\rm T}$ in Pb-Pb collisions at $\sqrt{s_{\rm NN}} = 5.02$ TeV . Figure taken from Ref. [116].

Open charm mesons have been measured by ALICE at mid-rapidity via the hadronic decay channels [112]. Figure 1.33 shows an example of the results concerning $p_{\rm T}$ dependence of the average $R_{\rm AA}$ of non-strange D mesons (D^0, D$^+$, and D^{*+}) in Pb-Pb collisions $\sqrt{s_{\rm NN}} = 5.02$ TeV [116] in various centrality classes. Due to the $R_{\rm AA}$ of D^0, D$^+$, and D^{*+} are compatible [112], they are often averaged in heavy-ion collisions. One can notice that in the 10% most central Pb-Pb collisions at $\sqrt{s_{\rm NN}} = 5.02$ TeV, the $R_{\rm AA}$ is measured up to $p_{\rm T} = 50$ GeV/c, the $p_{\rm T}$ reach is higher than that in Pb-Pb collisions at $\sqrt{s_{\rm NN}} = 2.76$ TeV [113, 114]. An increase of the suppression with increasing centrality is clearly observed. Moreover, at $p_{\rm T}$ of about 10 GeV/c, the D-meson yield is strongly suppressed for the most 10% central collisions by a factor of about five. This is due to final-state effects related to parton energy loss since in p-Pb collisions the R_{AA} of non-strange D mesons is consistent with unit within uncertainty [115] at high p_{T}.

B measurements

At LHC energies, in addition to charm, beauty production has been measured via non-prompt J/Ψ (originating from B-meson decays) in Pb-Pb collisions. The measurements of the inclusive B decays to J/Ψ + X, was performed by the ALICE and CMS collaborations [117, 118].

Hierarchy of suppression

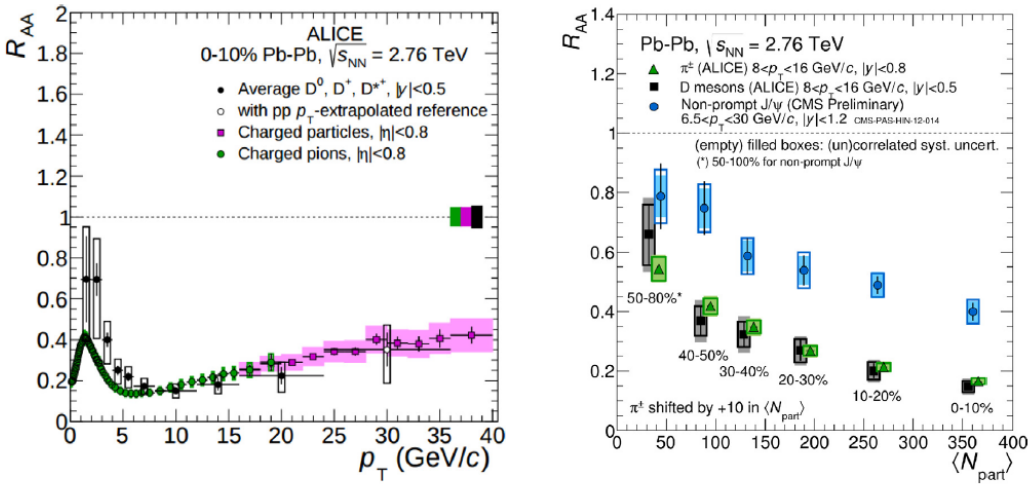

Figure 1.34: Left: non-strange D-meson R_{AA} (average of D^0, D$^+$ and D^{*+} R_{AA}) [113] compared to the π [119] and charged-particles R_{AA} as a function of p_{T} for the 10 % most central Pb-Pb collisions at $\sqrt{s_{\mathrm{NN}}}$ = 2.76 TeV. Figure taken from Ref.[113]. Right: charged-particle (black squares), D mesons (green triangles) and non-prompt J/Ψ (blue circles) R_{AA} as function of centrality ($< N_{\mathrm{part}} >$) for Pb-Pb collisions at $\sqrt{s_{\mathrm{NN}}}$ = 2.76 TeV. Figure taken from Ref. [120, 121].

As can be seen in the left panel of Fig. 1.34, a compatible result is shown for non-strange D-meson R_{AA} compared to the π and charged-particle R_{AA} as a function of p_{T} in the 10% most central Pb-Pb collisions. The right panel of Fig. 1.34 shows the R_{AA} of charged pions [120], D mesons [120] and non-prompt J/Ψ [121] as a function of centrality (average number of participating nucleons $< N_{\mathrm{part}} >$). The results show that the R_{AA} of D mesons and charged pions measured in the range $8 < p_{\mathrm{T}} <$ 16 GeV/c are consistent, within uncertainties $R_{\mathrm{AA}}(\mathrm{D}) \approx R_{\mathrm{AA}}(\pi)$ for all presented collision centralities [120]. Such trend is reproduced by models that include different fragmentation functions and shapes of the initial p_{T} distributions of the different parton types, in addition to the expected energy-loss effects (see Sec. 1.4.1).

The results presented in the right panel of Fig. 1.34 also show that the R_{AA} of non-prompt J/Ψ is larger than the R_{AA} of D mesons ($< p_{\mathrm{T}} >$ of B and D mesons ~ 10 GeV/c, but slightly different rapidity ranges), indicating $R_{\mathrm{AA}}(\mathrm{B}) > R_{\mathrm{AA}}(\mathrm{D})$, which is in agreement with the expectation of larger energy loss for charm than for beauty (see Sec. 1.4.1).

Elliptic flow

With the medium which is dominated by light quarks and gluons, the large energy loss suffered by heavy quarks in the QGP is an indication of their "strong coupling". If heavy quarks interact strongly with the medium, heavy-flavoured hadrons could inherit the medium azimuthal anisotropy, quantified by the elliptic flow v_2.

The ALICE collaboration measured the elliptic flow of D mesons. The averaged v_2 of D^0, D^+, and D^{*+} as a function of p_{T} is presented in upper panel of Fig. 1.35 for the centrality range 30–50%, where the elliptic flow signal is large. A non-zero v_2 of a heavy-flavoured particles is measured at intermediate p_{T}. The averaged non-strange D-meson R_{AA} as a function of p_{T} for the 10% most central Pb-Pb collisions at $\sqrt{s_{\mathrm{NN}}} = 5.02$ TeV is presented in the bottom panel of Fig. 1.35.

The simultaneous measurements of R_{AA} in central collisions and v_2 in semi-central collisions provide a powerful tool to disentangle the interplay of various energy loss mechanisms and impose important constraints on theoretical models. The comparison of the D-meson R_{AA} and v_2 with various models indicates that it is a challenging task to describe simultaneously the R_{AA} and v_2 of heavy-flavoured particles over the full p_{T} range.

1.4.6 Thesis objective: study of open heavy flavours via the semi-muonic decay channel

Open heavy-flavour production is measured with ALICE over a wide rapidity range: at mid-rapidity ($|y| < 0.9$) via the full reconstruction of hadronic decay channels of non-strange D mesons (D^0, D^+ and D^{*+}), $\mathrm{D}_{\mathrm{s}}^+$ mesons, and charmed baryons (Λ_{c}^+, Ξ_{c}), and via the identification of electrons from charm and beauty semi-leptonic decays. At forward rapidity ($2.5 < y < 4$), open heavy flavours are studied via the semi-muonic decay channel, this is the topic of my PHD thesis. Tt is worth pointing out that, the measurement of open heavy flavours at forward rapidity in the semi-muonic decay channel is facilitated by an experimentally triggerable observable and relatively large decay branching ratios (about 10%), thus resulting in relatively large statistics allowing for differential measurements over a wide p_{T} interval. Furthermore, the forward rapidity accessible by ALICE ($2.5 < y < 4$) allows us to test pQCD predictions in a region of small Bjorken-x (x values can be accessed down to about 10^{-5}).

Figure 1.36 shows the p_{T} dstribution of final-state muons after all selection cuts were applied, the distributions were obtained from a PYTHIA6 simulation of pp collisions at $\sqrt{s} = 2.76$ TeV [133].

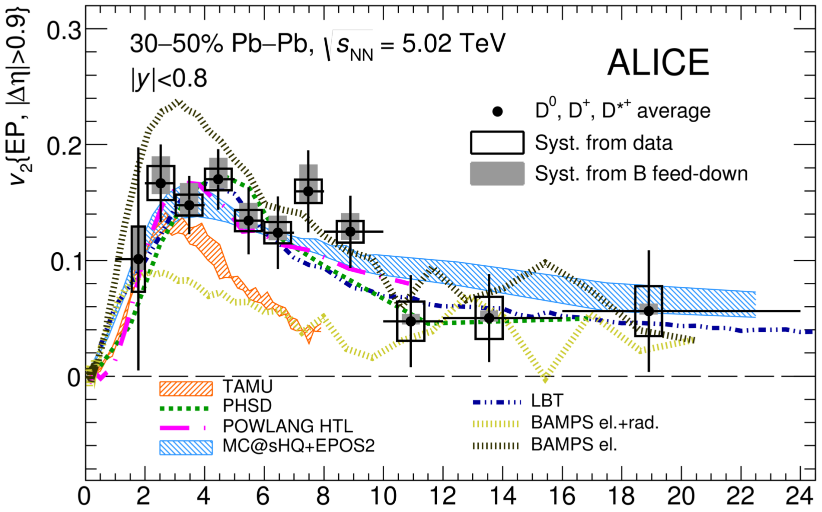

ALI-PUB-132101

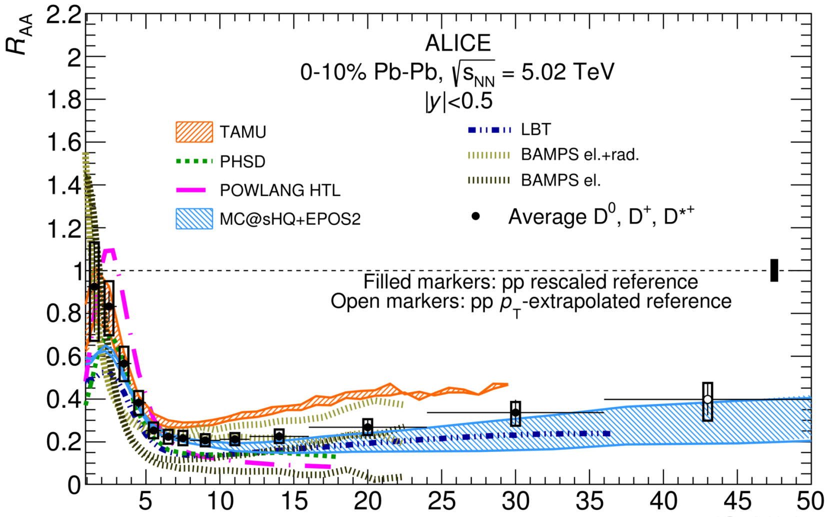

ALI-PUB-145280

Figure 1.35: Upper: averaged non-strange D-meson v_2 as a function of p_{T} for Pb-Pb collisions at $\sqrt{s_{\mathrm{NN}}} = 5.02$ TeV and the centrality range 30–50%. Bottom: averaged non-strange D meson R_{AA} as a function of p_{T} for Pb-Pb collisions at $\sqrt{s_{\mathrm{NN}}} = 5.02$ TeV and the centrality range 0–10%. Both results are compared with theoretical models [124, 125, 126, 127, 128, 129, 130]. Figures taken from Ref. [122, 123].

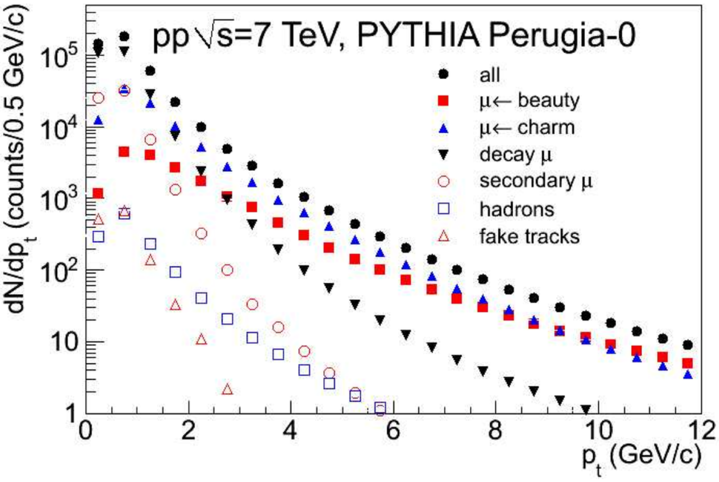

Figure 1.36: Transverse momentum distribution of reconstructed tracks in the ALICE muon spectrometer after all selection cuts were applied. The distributions were obtained from a PYTHIA simulation of pp collisions at $\sqrt{s} = 7$ TeV. Figure taken from Ref. [132].

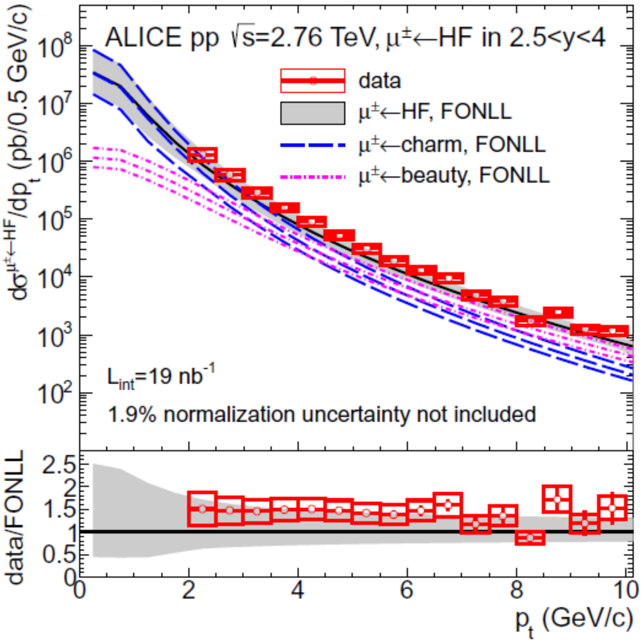

Figure 1.37: The p_{T}-differential cross-section of muons from heavy-flavour decays, measured in pp collisions at $\sqrt{s} = 2.76$ TeV. Figure taken from Ref. [133].

In order to get the heavy-flavour hadron decay muons, the following background contributions must be subtracted and/or rejected:

- muons from the decay of primary light hadrons including pions and kaons (the main contribution at low/intermediate p_{T}), muons from J/Ψ decays (maximium at $p_{\mathrm{T}} \sim 5$ GeV/c), muons from W and Z/γ^* decays (the main contribution at high p_{T});
- secondary muons: muons from secondary light-hadron decays produced inside the front absorber;
- punch-through hadrons and secondary hadrons escaping the front absorber and crossing the tracking chambers.

The simulation results indicate that the punch-through hadron and the contribution of fake tracks (tracks which are not associated to one single particle crossing the whole spectrometer) are negligible after all selection cuts were applied.

In the following, the main published results in pp and Pb-Pb collisions are summarized. They were obtained with Run-1 data.

The p_{T}-differential cross section of muons from heavy-flavour decays, measured in pp collisions at $\sqrt{s} = 2.76$ TeV with an integrated luminosity of 19 nb^{-1}, is shown in Fig. 1.37. The vertical bars are the statistical uncertainties. The boxes are the uncorrelated systematic uncertainties, accounting for detection efficiencies, alignment and background subtraction. The results are compared to FONLL calculations (see Sec. 1.4.1) and show a good agreement with the data within uncertainties. Similar results were also obtained for pp collisions at $\sqrt{s} = 7$ TeV [132].

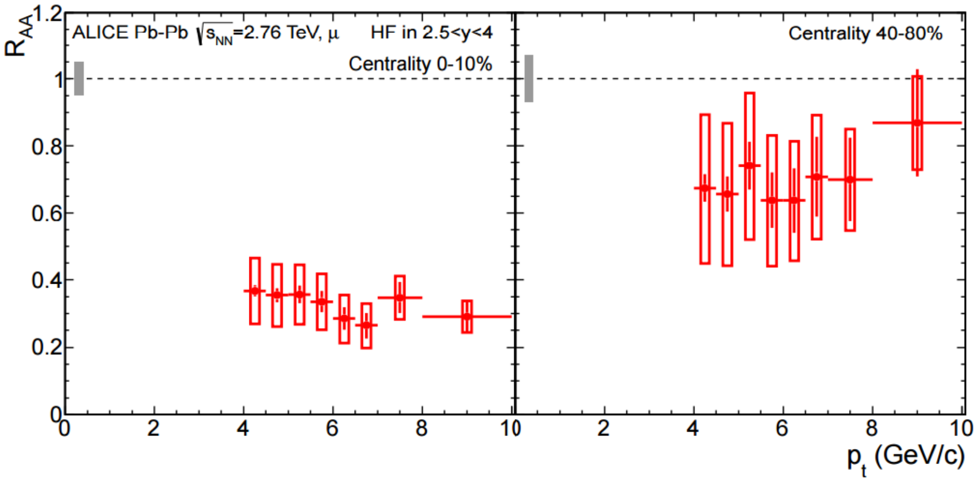

Figure 1.38: Nuclear modification factor as a function of transverse momentum for muons from heavy-flavour decay in the 0-10% central (left) and 40-80% peripheral (right) collisions. Figure taken from Ref. [133]

Figure 1.38 shows the nuclear modification factor as a function of the transverse momentum for muons from heavy-flavour hadron decays in the 0-10% central (left) and 40-80% peripheral (right) collisions. The vertical bars (boxes) are the statistical (uncorrelated systematic) uncertainties corresponding to data. The correlated uncertainties on the cross-section normalization of the pp reference and on nuclear overlap function $\langle T_{\mathrm{AA}} \rangle$ are shown as a filled box at $R_{\mathrm{AA}} = 1$. The nuclear modification factor is independent of p_{T} within uncertainties, and exhibits a factor 3-4 in the most central collisions. It is known that the in-medium energy loss is not the only mechanism that could lead to a reduction of the R_{AA}. In particular, the nuclear modification of the parton distributions in nuclei could lead to a variation of the initial hard-scattering probability, and a consequent variation of the heavy-flavour yield. R_{pPb} was found compatible with unity which indicated that cold nuclear effects are small [167]. This shows that the measured suppression is due to final-state effects.

In the following, we propose to perform more precise measurements and in an extended p_{T} interval of the production of muons from heavy-flavour hadron decays in pp and Pb-Pb collisions using the data samples collected in 2011 and 2015 [3]. Moreover, a new collisions system size, Xe-Xe collisions at $\sqrt{s_{\mathrm{NN}}} = 5.44$ TeV is also investigated using the data sample collected in 2017 during a short pilot run.

---

[3] In this thesis, the cross section of muons from heavy-flavour hadron decays measured in pp collisions at $\sqrt{s} = 5.02$ TeV uses the LHC15n data sample collected in 2015. The analysis and results of heavy-flavour suppression in Pb-Pb collisions at $\sqrt{s_{\mathrm{NN}}} = 5.02$ TeV uses the LHC15o data sample collected in 2015. For comparison at lower collision energy, in a extended p_{T} range with respect to published results [133], the Pb-Pb data sample at $\sqrt{s_{\mathrm{NN}}} = 2.76$ TeV collected in 2011 has been analyzed as well.

CHAPTER 2

The ALICE Experiment at the LHC

This chapter focuses on the description of A Large Ion Collider Experiment (ALICE), which is one of the four main experiments at the Large Hadron Collider (LHC) located at CERN and designed as a dedicated heavy-ion detector to mainly explore the properties of strongly-interacting matter created at extremely high energy densities and temperatures in ultra-relativistic heavy-ion collisions. It enables to measure hadrons, electrons, photons and muons produced in heavy-ion collisions up to the high particle multiplicity environment of the LHC. The introduction of the LHC experiments will be shown in Sec. 2.1. The ALICE layout, its different sub-systems and the detector upgrade project will be presented in Sec. 2.2, with particular emphasis on the detectors of the central barrel and forward muon arm, which are employed for the measurement of hadronic observables and semi-muonic observables (or dimuons). Then an overview of ALICE online system and ALICE offline framework will be introduced in Sec. 2.3 and Sec. 2.4, respectively.

2.1 The Large Hadron Collider (LHC)

The Large Hadron Collider (LHC) is the world's largest and most powerful particle collider, the most complex experimental facility ever built, and the largest single machine in the world [134]. It was built by the European Organization for Nuclear Research (CERN) between 1998 and 2008 in collaboration with scientists and engineers from over 100 countries, as well as hundreds of universities and laboratories. Recently (2018), the ALICE collaboration consists of about 1800 physicists from 178 institutes in 41 countries. It lies in a tunnel of 27 kilometres in circumference, at a depth ranging from 50 to 175 metres underground, at the France-Switzerland border near Geneva. It started to be operated from end of 2009 to early 2013 at an energy with the range of 0.9 to 8 TeV, about 4 times the previous world record for a collider. After two-years shutdown. The LHC was restarted in early 2015 for its second research run at $\sqrt{s} = 13$ TeV for pp collisions and at $\sqrt{s_{\mathrm{NN}}} = 5.02$ TeV for Pb-Pb collisions.

The aim of the LHC is to allow physicists to test the predictions of different theories of particle physics, including the measurements of the properties of the Higgs boson and the search for the large family of new particles predicted by supersymmetric theories, as well as other unsolved questions of physics.

The collider has four crossing points, around which are positioned seven detectors, each designed for certain kind of research. The LHC primarily collides proton

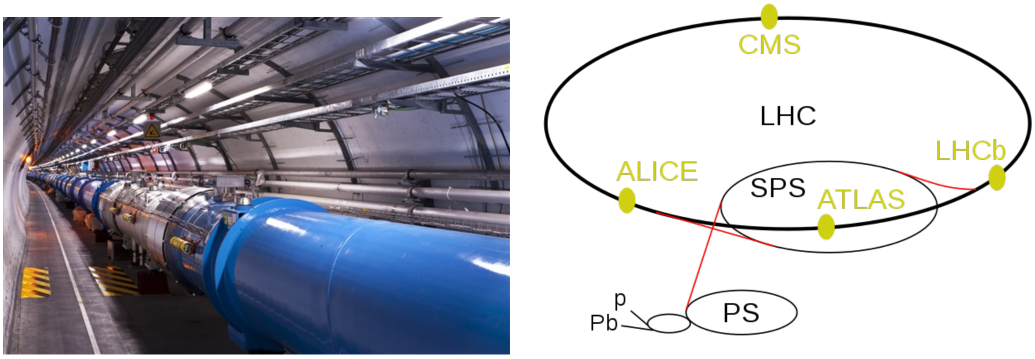

Figure 2.1: Left: a section of the LHC. Right: the LHC experiments and the preaccelerators. The path of the protons (and ions) begins at linear accelerators (marked p and Pb, respectively). They continue their way in the booster (the small unmarked circle), in the Proton Synchrotron (PS), in the Super Proton Synchrotron (SPS) and finally they get into the 27-km-long LHC tunnel. In the LHC there are 4 large experiments marked with yellow dots. Figures taken from Ref. [134].

beams, but it can also deliver beams of heavy ions. Proton-lead collisions were performed for short periods in 2013 and 2016, lead-lead collisions took place in 2010, 2011, 2015, and 2018, and a short pilot run of xenon-xenon collisions took place in 2017.

2.1.1 The LHC experiments

The LHC collider tunnel contains two adjacent parallel beamlines (or beam pipes) each containing a beam, which travel in opposite directions around the ring. The beams intersect at four points, see Fig. 2.1, around the ring, which is where the particle collisions take place.

1. A Toroidal LHC Apparatus (ATLAS) [135], one of two general-purpose detectors. ATLAS studies a wide range of physics, from the search for the Higgs boson [1] to extra dimensions and particles that could make up dark matter;

2. Compact Muon Solenoid (CMS) [136], the other general-purpose detector, like ATLAS, studies the Higgs boson and look for clues of new physics. Although it has the same scientific goals as the ATLAS experiment, it uses different technical solutions and a different magnet-system design;

3. LHC-beauty (LHCb) [137], LHCb investigates the slight differences between matter and antimatter [2] by studying a type of particle called the "beauty quark";

---

[1] The Higgs boson (H), which leads to the generation of the $W^{\pm}$ and Z^0 masses. The Higgs boson was discovered by ATLAS and CMS on 14 March, 2013.

[2] equal amounts of matter and antimatter were created in the Big Bang.

4. A Large Ion Collider Experiment (ALICE) [138], ALICE is designed to study the Quark-Gluon Plasma that is believed to have existed shortly after the Big Bang.

On the other hand, the other three of seven detectors have been constructed at the LHC, TOTal Elastic and diffractive cross section Measurement (TOTEM) [139], Monopole and Exotics Detector At the LHC (MoEDAL) [140] and Large Hadron Collider forward (LHCf) [141], are very much smaller and are for very specialized research. TOTEM and LHCf are installed close to the CMS interaction point and near the ATLAS, respectively. MoEDAL is installed in the same cavern of LHCb.

Before being injected into the main accelerator, the particles are prepared by a series of systems that successively increase their energy. The first system is the linear particle accelerator LINAC 2 generating 50 MeV protons, which feeds the Proton Synchrotron Booster (PSB). There the protons are accelerated to 1.4 GeV and injected into the Proton Synchrotron (PS), where they are accelerated to 26 GeV. Finally the Super Proton Synchrotron (SPS), see Fig. 2.1, is used to increase their energy further to 450 GeV before they are at last injected (over a period of several minutes) into the main ring.

2.2 ALICE detector overview

The ALICE Collaboration has built a dedicated detector to exploit the unique physics potential of nucleus-nucleus collisions at LHC energies. The main aim is to study the physics of strongly-interacting matter at the highest energy densities reached so far in the laboratory. In such conditions, an extreme phase of matter called the Quark-Gluon Plasma (QGP) is formed. Our universe is thought to have been in such a primordial state for the first few millionths of a second after the Big Bang. The properties of such a phase are key issues for Quantum Chromo Dynamics (QCD), the understanding of confinement-deconfinement and chiral phase transitions. For this purpose, we are carrying out a comprehensive study of hadrons, electrons, muons and photons produced in the collisions of heavy nuclei. ALICE is also studying proton-proton and proton-nucleus collisions both intrinsic purposes and as a comparison with nucleus-nucleus collisions.

2.2.1 Detector Layout

The layout of ALICE detector is shown in Fig. 2.2. The central barrel covers a pseudo-rapidity range of $|\eta| < 0.9$ (where hadrons, electrons and photons are measured), and is embedded in a large solenoidal magnet (L3) with a weak field (B $\leq$ 0.5 T), parallel to z [3]. From the vertex region to the outer part it is composed by the Inner Track System (ITS) [142] with six layers of silicon detectors, the cylindrical Time Projection Chamber (TPC) [143] which is the main tracking detector, the Transition Radiation Detector (TRD) [144] for electron identification and the

---

[3] The ALICE global reference frame is: z axis parallel to the beam direction and pointing towards the muon arm, x and y axes in the transverse plane perpendicular to the beam direction.

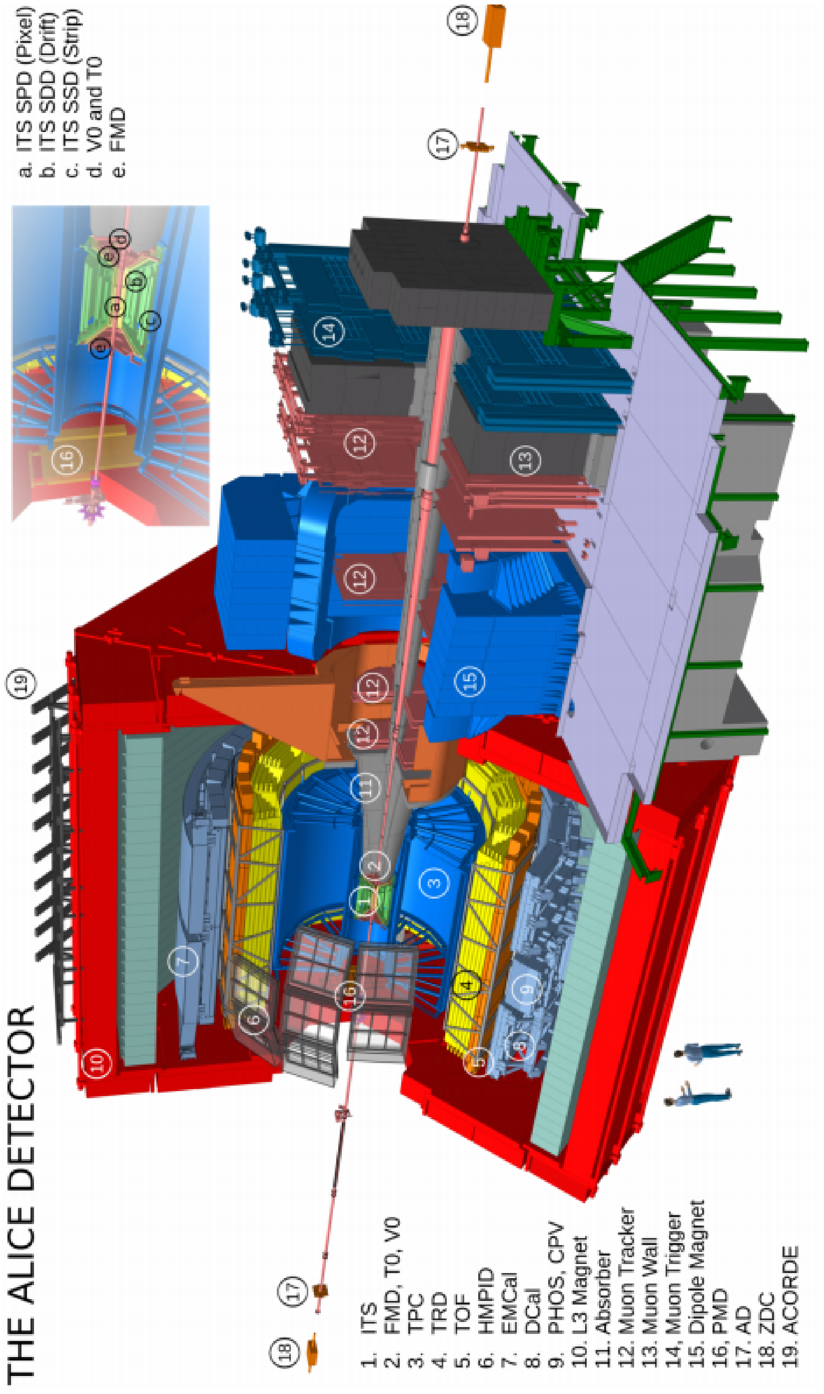

Figure 2.2: 3-D view of the ALICE detector with its different sub-detectors in the LHC Run2. The insert shows the different sub-detectors surrounding the interaction point. The length of the ALICE detector is about 24 m. The two ZDC are located at more than 100 m from the interaction point. Figure taken from Ref. [151].

Detector	Acceptance (η, ϕ)	Position (m)	Dimension (m^2)	Channels
ITS layer 1,2 (SPD)	±2, ±1.4	0.039, 0.076	0.21	9.8 M
ITS layer 3,4 (SDD)	±0.9, ±0.9	0.150, 0.239	1.31	133 000
ITS layer 5,6 (SSD)	±0.97, ±0.97	0.380, 0.430	5.0	2.6 M
TPC	± 0.9 at $r = 2.8$ m ± 1.5 at $r = 1.4$ m	0.848, 2.466	readout 32.5 m^2 Vol. 90 m^3	557 568
TRD	±0.84	2.90, 3.68	716	1.2 M
TOF	±0.9	3.78	141	157 248
HMPID	± 0.9, $1.2^\circ < \phi < 58.8^\circ$	5.0	11	161 280
PHOS	± 0.12, $220^\circ < \phi < 320^\circ$	4.6	8.6	17 920
EMCal	± 0.7, $80^\circ < \phi < 187^\circ$	4.36	44	12 672
ACORDE	± 1.3, $-60^\circ < \phi < 60^\circ$	8.5	43	120
Muon spectrometer				
Tracking station 1	$-2.5 < \eta < -4$	−5.36	4.7	1.08 M
Tracking station 2		−6.86	7.9	
Tracking station 3		−9.83	14.4	
Tracking station 4		−12.92	26.5	
Tracking station 5		−14.22	41.8	
Trigger station 1		−16.12	64.6	21 000
Trigger station 2		−17.12	73.1	
ZDC:ZN	$\lvert\eta\rvert < 8.8$	±116	2 × 0.0049	10
ZDC:ZP	$6.5 < \lvert\eta\rvert < 7.5$	±116	2 × 0.027	10
ZDC:ZEM	$4.8 < \eta < 5.7$ $-16^\circ < \phi < 16^\circ$ and $164^\circ < \phi < 169^\circ$	7.25	2 × 0.027	10
PMD	$2.3 < \eta < 3.7$	3.64	2.59	2 221 184
FMD disc 1	$3.62 < \eta < 5.03$	inner: 3.2	0.266	51 200
FMD disc 2	$1.7 < \eta < 3.68$	inner: 3.2 outer: 0.752		
FMD disc 3	$-3.4 < \eta < -1.7$	inner: −0.628 outer: −0.752		
V0A	$2.8 < \eta < 5.1$	3.4	0.548	32
V0C	$-1.7 < \eta < -3.7$	−0.897	0.315	32
T0A	$4.61 < \eta < 4.92$	3.75	0.0038	12
T0C	$-3.28 < \eta < -2.97$	0.727	0.0038	12

Table 2.1: Summary of the ALICE detector subsystems. Extracted from [151].

Time Of Flight (TOF) [145] for the identification of protons, kaons and pions, all of them with full azimuth acceptance. Two other detectors with smaller acceptance complement the central barrel, the High-Momentum Particle Identification Detector (HMPID) [146] consisting of an array of ring-imaging Cherenkov counters and the Photon Spectromenter (PHOS) [147] which is an electromagnetic calorimeter. The Electromagnetic Calorimeter (EMCAL) [148] and Di-Jet Calorimeter (DCal) [149] , which are dedicated to the physics of high-p_{T} photon and jets. An array of plastic scintillators, ALICE COsmic Ray DEtector (ACORDE) [150], placed above the solenoid magnet, is built to trigger on cosmic rays events for calibration and alignment.

The forward muon spectrometer covers a pseudorapidity range of $-4 < \eta < -2.5$. Tt is designed to investigate the quarkonia (J/ψ and Υ families), open heavy flavour via single muons, electro-weak probes (W and Z bosons) and low mass mesons (ρ, ω, ϕ). For this purpose it consists, from the interaction vertex, of a front absorber, a beam shield, five tracking stations, a muon filter and two trigger stations [151, 153, 152].

In addition, the ALICE global detectors are the Forward Multiplicity Detector (FMD) [154] made of silicon trips; the Photon Multiplicity Detector (PMD) [155] made of layers of lead converter; in order to take care of event characterization and beam luminosity measurement, the V0 [154] (made of two arrays of scintillators) and the T0 [154] (two arrays of Cherenkov counters), located on each side of the interaction point are used; the Zero Degree Calorimeter (ZDC) [156] consisting of two hadronic calorimeters, one for protons and one for neutrons, is used for event centrality evalution and to reject eletromagnetic interactions.

The main characteristics of the ALICE detector subsystems are shown in Tab. 2.1. The acceptance in η is calculated from the nominal interaction point. The position is the approximate distance from the interaction point to the front of the detector. The dimension corresponds to the total area covered by active detector elements. The quantity "channels" is the total number of independent electronic readout channels. In case a detector is subdivided, the numbers refer to the individual components (e.g. pixel layers 1 and 2, muon tracking stations 1-5).

2.2.2 Global detectors

Forward Multiplicity Detector (FMD)

The Forward Multiplicity Detector (FMD) [154] has a special role in ALICE. It is designed to measure the charged particles produced in the collisions and emitted at small angles relative to the beam direction. The FMD also provides an independent measurement of the orientation of the collisions in the vertical plane, which can be used with measurements from the barrel detector to investigate flow, jets, etc.

It is the primary detector to measure the multiplicity distribution of charged particles over a wide kinematical range (rapidity coverage in the interval $1.7 < \eta < 5.0$ and $-3.4 < \eta < -1.7$ corresponding to an angular interval of about 0.75 degrees to 21 degrees with respect to the beam direction, see Fig. 2.3).

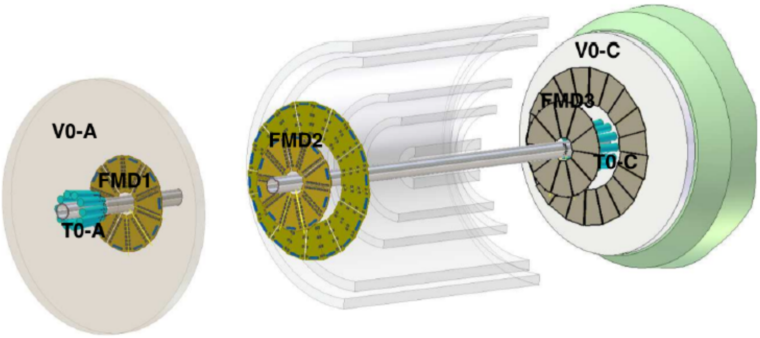

Figure 2.3: Schematic representation of the forward detectors. The FMD rings (FMD1, FMD2 and FMD3) can be observed. The two V0 (A and C side) as well as the two T0 detectors are shown. Figure taken from Ref. [154].

The FMD rapidity coverage is complementary to the ITS, so the combination of the information of the two detectors provide charged-particle multiplicity distributions in a wide rapidity range -3.4 $< \eta <$ 5.0.

V0 detector

The V0 [154] detector is a small angle detector consisting of two arrays of 32 scintillating counters, called V0A and V0C, which are installed on either side of the ALICE interaction point of the two LHC beams. This detector has several functions. It provides Minimum Bias triggers and Centrality Triggers for the central barrel detectors in pp and AA collisions. It measures the charge (energy deposited) of the particles and the time of their arrival in each of the 64 channels. The V0A is located 330 cm away from the vertex on the side opposite to the muon spectrometer. The V0C is fixed at the front face of the hadronic absorber, 90 cm from the vertex. They cover the pseudo-rapidity ranges 2.8 $< \eta <$ 5.1 (V0A) and -3.7$< \eta <$ -1.7 (V0C) for collision vertex at the central position, see Fig. 2.3. They are segmented into counters distributed in four rings.

The V0 system can reject events arising from interaction of the beam particles with the residual particles in the beam pipe vacuum (beam-gas interaction) by measuring the difference of the time-of-flight between the two counters. The V0 provides the online L0 (see Sec. 2.3.1) Minimum-Bias (MB) trigger. It is also used to determine the centrality of the collision.

The V0 detector is the default collision centrality estimator in ALICE. The centrality is obtained by summing up the energy deposited in the two disks of VZERO. This observable scales directly with the number of primary particles generated in the collision and therefore with the centrality. Figure 2.4 shows the distribution of the sum of amplitudes in the V0 scintillators in Pb-Pb collisions at $\sqrt{s_{\rm NN}}$ =5.02 TeV. The distribution is adjusted with the NBD-Glauber fit shown as a line. The V0 detector is also used for luminosity measurements.

T0 detector

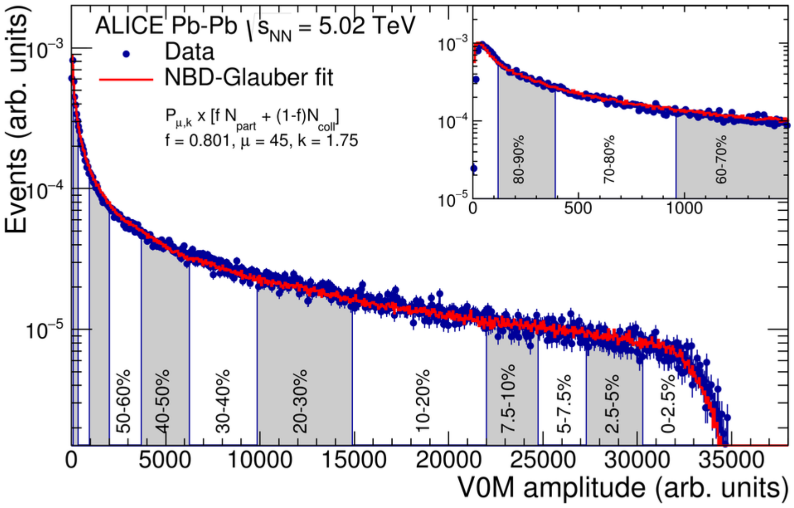

Figure 2.4: Distribution of the sum of amplitudes in the V0 scintillators in Pb-Pb collisions at 5.02 TeV. The distribution is fitted with the NBD-Glauber fit shown as a line. Figure taken from Ref. [157].

The T0 [154] detector consists of two arrays (T0-A and T0-C) of Cherenkov counters with the IP in-between. The distance from the IP to T0-C is 70 cm while on the opposite side the distance from T0-A to the IP is about 3.6 m. T0-C covers the pseudorapidity range -3.3 $< \eta <$ -2.9 and T0-A of 4.6 $< \eta <$ 5.0, see Fig. 2.3.

The T0 detector is required to fulfil the following functions:

1. To supply main signals to the ALICE L0 trigger;
2. To deliver an early (prior to L0 trigger) wake-up to TRD;
3. To give a precise start signal for time-of-flight (TOF) particle identification.

T0 is the fast timing and trigger detector of ALICE. It gives the key trigger and timing signals, measures on-line vertex position and gives a rough centrality estimation. Data from T0 are crucial not only for extraction of the precise interaction time but also for the normalisation in proton-proton and heavy-ion runs.

Zero Degree Calorimeter (ZDC)

In ALICE two sets of hadronic ZDCs [156] are located at 116 m on either side of the Interaction Point (IP). Each ZDC set is made by two distinct detectors: one for spectator neutrons (ZN), covering the pseudorapidty ranges $|\eta| < 8.8$, and one for spectator protons (ZP), covering the pseudorapidty ranges $6.5 < \eta < 7.5$. They are able to count spectator nucleons (nucleons not taking part in the collision) by measuring the deposited energy. They are therefore used for centrality estimation as well as reaction plane determination.

In addition, two small electromagnetic calorimeters (ZEM) are placed at about 7 m from the IP, on both sides of the LHC beam pipe, opposite to the muon arm covering, the pseudorapidty ranges $4.8 < \eta < 5.7$. They are used to measure the energy carried by the photons in the forward direction. This provides further information on the event centrality.

The centrality information provided by the ZDC is also used for triggering at Level 1 (L1, see Sec. 2.3.1).

Photon Multiplicity Detector (PMD)

The PMD [155] has high granularity and full azimuthal coverage in the pseudorapidity region $2.3 < \eta < 3.5$. It is located at 3.67 m from the interaction point on the opposite side of the Muon Spectrometer.

The detector has two planes, one for charged-particle veto and the other for preshower detection. Both planes have a honeycomb proportional chamber design. The detector measures the multiplicity and spatial distributions of photons on an event-by-event basis. The PMD is able to study event shapes and fluctuations as well as providing estimations of the transverse electromagnetic energy.

2.2.3 Central barrel detectors

Inner Tracking System (ITS)

The ITS [142] is the innermost detector of ALICE and its main purpose is to participate in tracking and to provide vertexing measurements to the experiment. Figure 2.5 displays the general view of ITS. It includes six cylindrical layers. From the inside to the outside, we can find two layers of Silicon Pixel Detectors (SPD); two layers of Silicon Drift Detectors (SDD); two layers of Silicon Strip Detectors (SSD). The main parameters of each of the three detector types are reported in Tab. 2.1.

Basically, the ITS is used for:

1. Primary vertices reconstruction with a high resolution (much better than 100 μm);
2. Reconstruction of secondary vertices from decays of hyperons and D and B mesons;
3. Tracking and identification of low p_{T} particles which are strongly bent by the magnetic field and will not enter the TPC.

Time Projection Chamber (TPC)

The ALICE TPC [143] is the main tracking detector in ALICE, providing track finding, momentum measurement and particle identification via $\mathrm{d}E/\mathrm{d}x$. It is in charge of tracking and charged-particle momentum determination with a good two-track separation, to enable particle identification and event vertex position evaluation. It is able to identify charged-particle p_{T} up to ~ 100 GeV/c in $|\eta| < 0.9$.

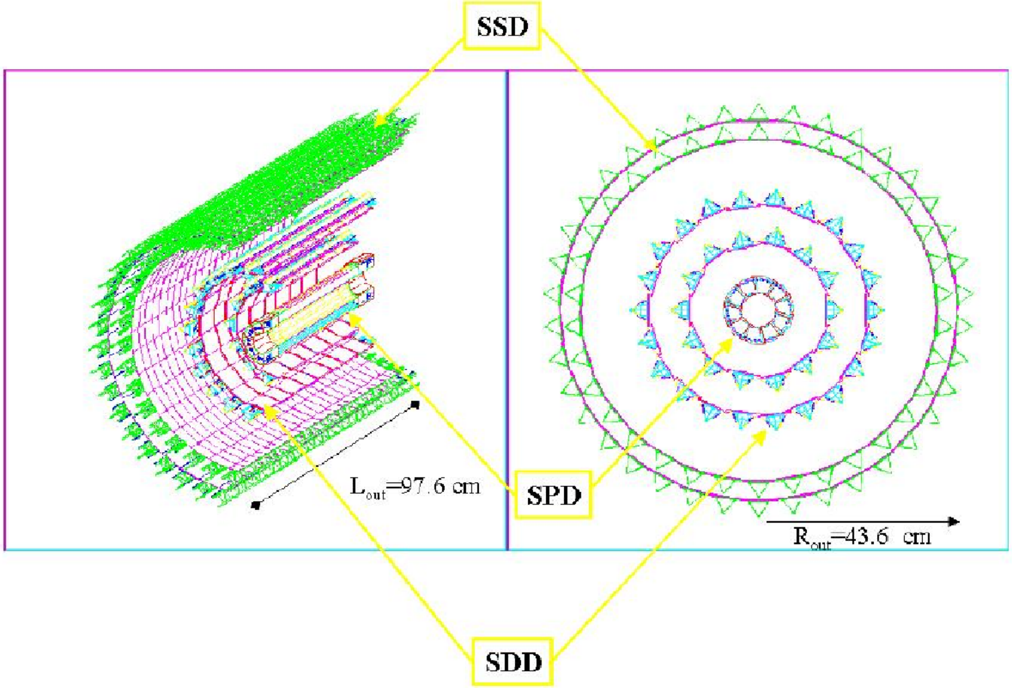

Figure 2.5: Layout of ITS. Figure taken from Ref. [142]

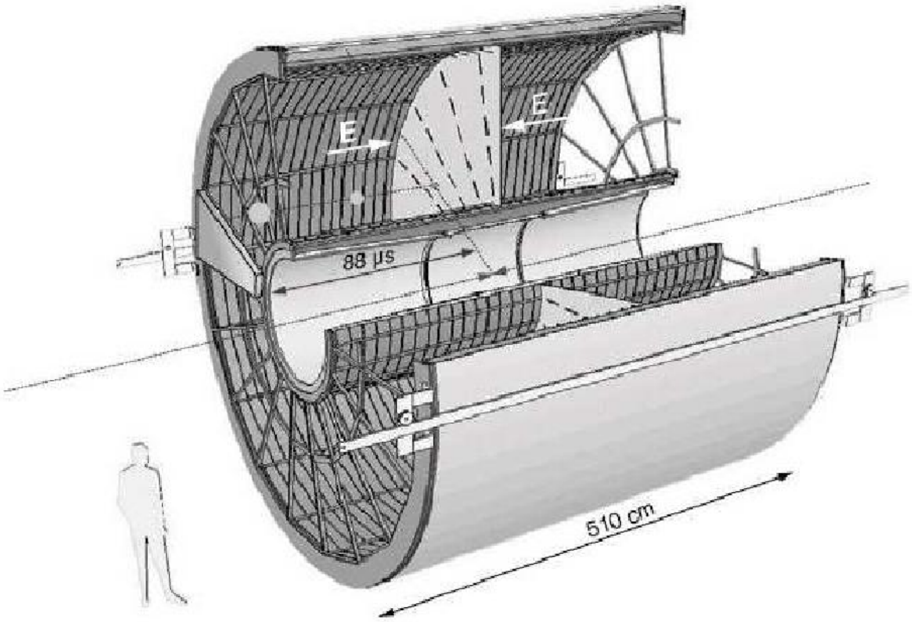

Figure 2.6: Layout of TPC. Figure taken from Ref. [143]

A view of TPC is reported in Fig. 2.6. It has an inner radius of 80 cm, given by the maximum acceptable hit density (0.1 cm^{-2}), and an outer radius of 250 cm, given by the length required for a $\mathrm{d}E/\mathrm{d}x$ resolution better than 10%, necessary for particle identification. The gas mixture $\mathrm{Ne/CO_2}$ (90%/10%) is optimized for drift velocity, low electron diffusion and low radiation length.

Charged particles crossing the gas of the TPC ionize the gas atoms along their path, liberating electrons that drift towards the end plates of the detector. The characteristics of the ionization process caused by fast charged particles passing through a medium can be used for particle identification. The velocity dependence of the ionization strength is connected to the well-known Bethe-Bloch formula, which describes the average energy loss of charged particles through inelastic Coulomb collisions with the atomic electrons of the medium. More details about TPC are given in the TPC Technical Design Report [143].

Transition Radiation Detector (TRD) and Time Of Flight (TOF)

The TRD [144] covers $|\eta| < 0.9$ and is situated between the TPC and the TOF detectors. It is composed by 18 sectors, and each sector is made of 6 layers and 5-fold segmentations along the beam axis. Electrons and positrons can be discriminated from other charged particles using the emission of transition radiation, X-rays emitted when the particles cross many layers of thin materials. The identification of electrons and positrons is achieved using a TRD.

The TOF [145] detector is positioned outside the TRD and has an internal radius of 370 cm and an external one of 390 cm for an overall logitudinal length of 7.45 m. It covers the central pseudorapidity region ($|\eta| < 0.9$) and plays an important role in the identification of charged particles (pions, kaons and protons) from low momentum up to momenta of a few GeV/c. TOF measurements yield the velocity of a charged particle by measuring the flight time over a given distance along the track trajectory.

High-Momentum Particle Identification Detector (HMPID) and PHOton Spectrometer (PHOS)

The HMPID [146] is a Ring Imaging Cherenkov Counter (RICH) detector to determine the speed of particles beyond the momentum range available through energy loss and through time-of-flight measurements. The detector covers the pseudorapidity $|\eta| < 0.6$ and 57.6^0 in azimuth (about 5% of the central barrel phase space). ALICE HMPID's momentum range is up to 3 GeV for pion and kaon discrimination and up to 5 GeV for kaon and proton discrimination.

PHOS [147] is a high-resolution electromagnetic calorimeter which measures the photons coming out of the extremely hot plasma created in the lead-lead collisions at the LHC. It is positioned on the bottom of the ALICE set-up, and covers a pseudorapidity range $|\eta| < 0.12$ and azimuthal angle of 100^0. PHOS is optimized for measuring photons and neutral mesons up to momenta about 10 GeV/c, through their decay into two photons.

ElectroMagnetic CALorimeter (EMCal), Di-Jet Calorimeter (DCal) and ALICE COsmic Ray DEtector (ACORDE)

The EMCal [148] is a lead-scintillator sampling calorimeter with large acceptance (110 degrees azimuthal, from -0.7 to 0.7 on pseudorapidity). The EMCAL enhances ALICE capabilities for jet quenching measurements. It enables the possibility for an unbiased L0 trigger (see Sec. 2.3.1) for high energy jets and improves jet energy resolution. It is an apparatus able to measure the energy of the particles, in particular of photons and electrons. During the Long Shutdown after Run 1 the DCal with same material as EMCal was installed, it is placed in opposition to EMCal. Recently it has extended the physics capabilities of the EMCal by enabling back-to-back jet correlation measurements.

The ACORDE [150] is made up of 60 scintillator modules distributed on the three upper faces of the ALICE magnet yoke. Each module is made of two 0.2 x 2 m^2 scintillating planes put in coincidence to minimize noise. It provides a cosmic ray trigger, which is used for calibration and alignment of the TPC, TRD and ITS. Together with these detectors, ACORDE allows us to study high-energy cosmic rays through the detection of atmospheric muons.

2.2.4 Forward muon spectrometer

Muon detection is performed in the pseudorapidity range $-4 < \eta < -2.5$, by the ALICE muon spectrometer [158]. It is used to measure the production of single muons from decays of heavy-flavor hadrons (D and B mesons) and the $W^{\pm}$ and Z^0 bosons. It is also designed to measure the production of quarkonia (J/Ψ, $\psi(2S)$, Υ, Υ', Υ'', with a mass resolution good enough to separate the bottomonium states), and low mass vector mesons (ρ, ω, ϕ) via their di-muon ($\mu^+\mu^-$) decay channel. The layout of the muon spectrometer is represented in Fig. 2.7.

It is composed of following sub-detectors:

Front absorber, Beam shield and Muon filter

The muon spectrometer consists of a 10 interaction length passive front absorber (4 m of length), located as close as possible from the interaction point, at 90 cm, in order to reduce the background of muons from π and K decays in the tracking chambers.

The beam shield is made of tungsten, lead and stainless steel. It shields the muon chambers from high rapidity particles and from secondary particles.

The muon filter is an iron wall of 1.2 m thick (7.2 interaction length passive) situated between the tracking and the trigger chambers, at 15 m from the interaction point. It reduces further the hadronic background on the trigger chambers.

The dipole magnet

The magnetic field is a key element of the muon spectrometer. Charged particles passing through a magnetic field are deflected. Then, the measurement of their

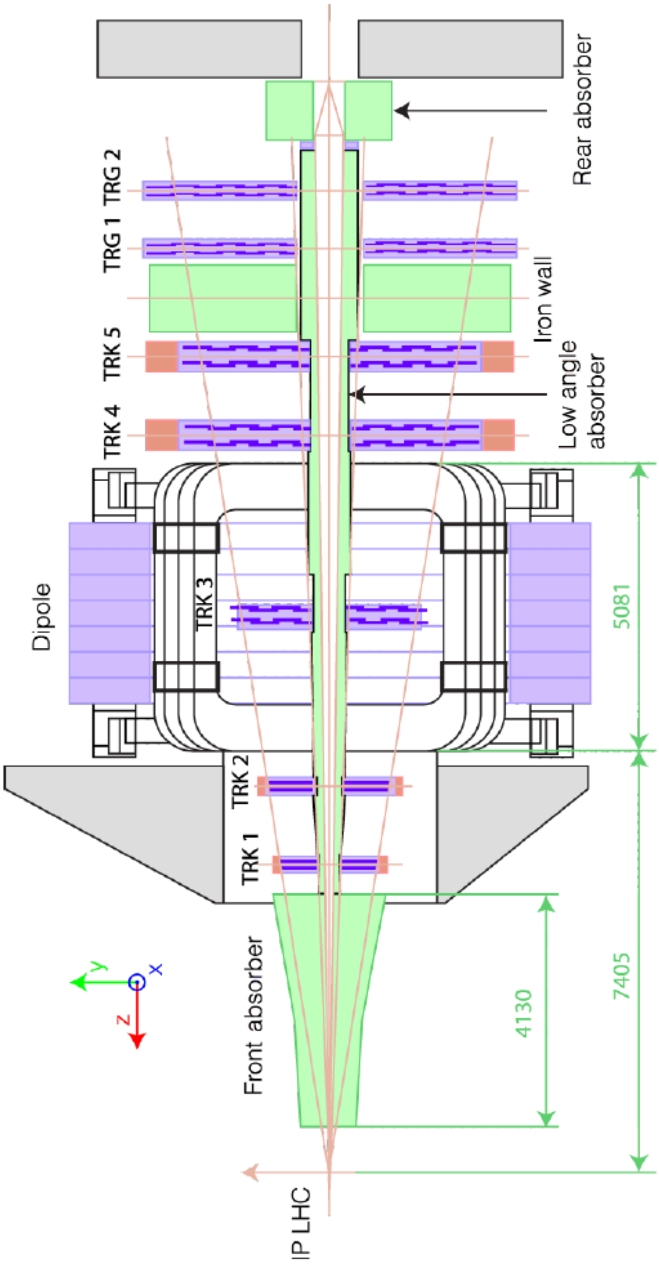

Figure 2.7: Layout of the ALICE muon spectrometer. Figure taken from Ref. [158].

Muon Detection	
polar, azimuthal angle coverage	$171^{\circ} < \theta < 178^{\circ}$, 360°
minimum muon momentum	4 GeV/c
pseudo-rapidity coverage	$-4 < \eta < -2.5$
Front Absorber	
longitudinal position (from IP)	$-5030 < z - 900$ mm
total thickness (materials)	$\sim 10\lambda_{\mathrm{int}}$, $\sim 60X_0$ (carbon-concrete-steel)
Dipole Magnet	
nominal magnetic field, field integral	0.67 T, 3 Tm
free gap between poles	$2.972 - 3.956$ m
overall magnet length	4.97 m
longitudinal position (from IP)	$-z = 9.94$ m (centre of the dipole coils)
Tracking Chambers	
no. of stations, no. of planes of station	5, 2
longitudinal position of stations	$-z = 5357, 6860, 9830, 12920, 14221$ mm
anode-cathode gap (equal to wire pitch)	2.1 mm for st. 1, 2.5 mm for st. $2 - 5$
gas mixture	80%Ar/20%CO_2
pad size st. 1 (bending plane)	4.2×6.3, 4.2×12.6, 4.2×25.2 mm^2
pad size st. 2 (bending plane)	5×7.5, 5×15, 5×30 mm^2
pad size st. 3, 4 and 5 (bending plane)	5×25, 5×50, 5×100 mm^2
max. hit dens. st. $1 - 5$ (central Pb–Pb×2)	$5.0, 2.1, 0.7, 0.5, 0.6 \cdot 10^{-2}$hits/cm^2
spatial resolution (bending plane)	$\simeq 70$ μm
Tracking Electronics	
total no. of FEE channels	1.08×10^6
shaping amplifier peaking time	1.2 μs
Trigger Chambers	
no. of stations, no. of planes of station	2, 2
longitudinal position of stations	$-z = 16120, 17120$ mm
total no. of RPCs, total active surface	72, ~ 140 m^2
gas gap	single, 2 mm
electrode material and resistivity	Bakelite$^{\mathrm{TM}}$, $\rho = 2 - 8 \times 10^9$ Ωcm
gas mixture	Ar/$C_2H_2F_4$/i-buthane/SF_6 (50.5/41.3/7.2/1)
pitch of readout strips (bending plane)	$10.6, 21.2, 42.5$ mm (for trigger st. 1)
max. strip occupancy bend. (non bend.) plane	3% (10%) in central Pb–Pb
max. hit rate on RPCs	3 (40) Hz/cm^2 in Pb–Pb (Ar–Ar)
Trigger Electronics	
total no. of FEE channels	2.1×10^4
no. of local trigger cards	$234 + 8$

Table 2.2: Summary of the main characteristics of the muon spectrometer. Extracted from Ref. [151].

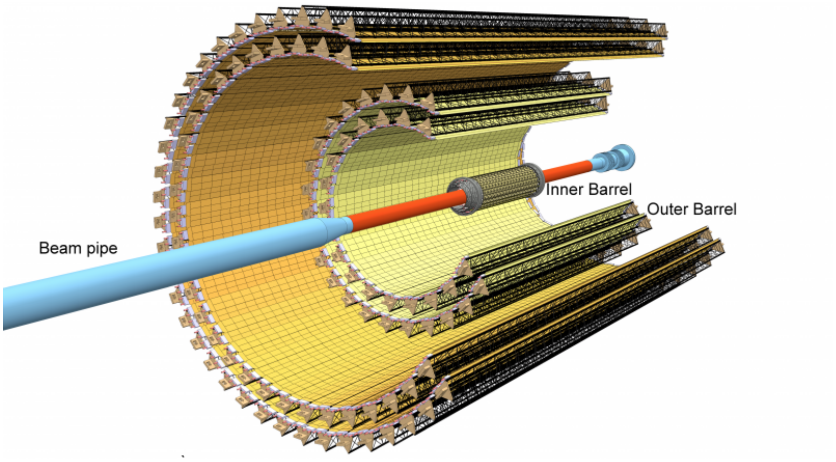

Figure 2.8: The general layout of the upgraded ITS detector with respect to Fig. 2.5. Figure taken from Ref. [159].

curvature allows the determination of the particle momenta and charge. It is at 7 m from the interaction vertex, has about 5 m of longitude, an aperture of 3.9 m and a weight of 900 tons. It provides an axial magnetic field $B \leq 0.7$ T, and the field integral from the interaction point to the muon filter is 3 Tm.

The tracking system

The tracking system consists of five stations of two planes of Cathode Pad Chambers (CPC) each, that corresponds to a total of ten detection planes. Two tracking stations are placed upstream the dipole magnet, one inside, and two downstream. When a charged particle crosses the detector, it ionizes the gas, and the created electrons travel to the anode wires driven by the electric field. Close to the anode wires, and due to the higher electric field in this region, the electrons are able to ionize the gas in its turn. The two cathode plane readout capability of the detector with high granularity allows about 40 μm position resolution.

The trigger system

The trigger system is composed by two stations of two planes each of single gap Resistive Plate Chambers (RPC). They are placed behind the muon iron wall, at 16 m (station 1) and 17 m (station 2) from the interaction point.

The characteristics of the chambers response are: the signal rise time is about 2 ns, and the time resolution is of the order of 1-2 ns. This allows a fast signal treatment and a short dead time. The trigger system identifies muon candidates or dimuons above two thresholds which can be set offline, e.g. at about 1 (or 0.5) and 4 GeV$/c$. It also allows us to do a first evaluation of the particle charge, and identify positive and negative single muon tracks and like-sign and unlike-sign muon pairs. During data taking period, several trigger types are foreseen: low p_{T} like-sign and unlike-sign dimuons, and single muons with low and high p_{T} trigger cuts.

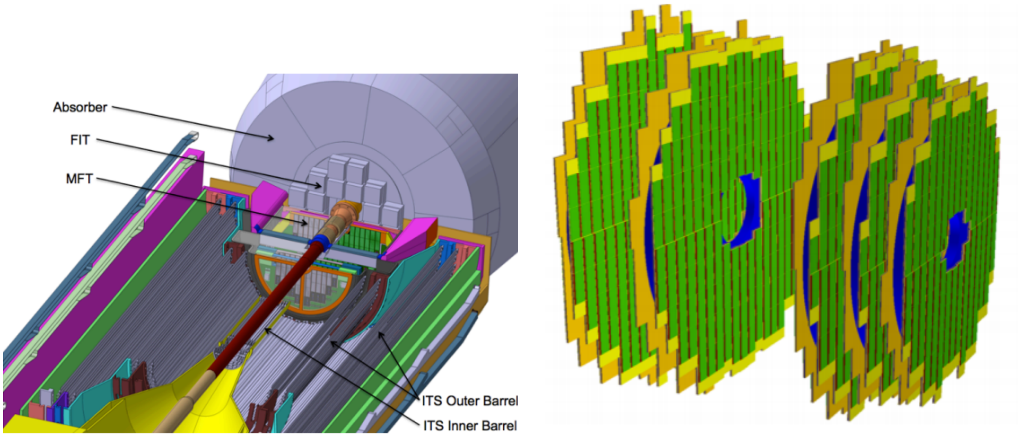

Figure 2.9: Layout of the MFT detector in ALICE (Left). Layout of the active area of the MFT detector (Right). Figures taken from Ref. [158].

2.2.5 ALICE detector upgrade project

ALICE is preparing a major upgrade which will be operated after the Long Shutdown foreseen to start in December 2018. The upgraded ALICE detector will have significantly enhanced read-out capabilities, and improved accuracy and efficiency in tracking particles and identifying the interaction vertex. The goal is to accumulate an integrated luminosity of 10 nb^{-1} MB Pb-Pb collisions.

Besides the partial redesign of the readout electronics to cope with the increased readout rate which may reach 50 kHz (presently this is about 8 kHz), the upgrade includes a new beam pipe with a smaller diameter, a new Inner Tracking System (ITS, Fig. 2.8), a vertex tracker for forward muons, the Muon Forward Tracker (MFT), the upgrade of the Time Projection Chamber based on Gas Electron Multiplier (GEM), the new Fast Integration Trigger detector (FIT) and the upgrade of the online and offline system (O^2 system).

The upgraded ITS will improve the track position resolution at the primary vertex by a factor of 3 or even larger with respect to the present detector. It features a standalone tracking efficiency comparable to what can be presently achieved by combining the information of the ITS and the TPC.

The Muon Forward Tracker (Fig. 2.9) is a Si-tracking detector which will add vertexing capabilities to the muon spectrometer. Therefore, new measurements not possible with the muon spectrometer alone will become accessible and the MFT will also increase the sensitive of several other measurements.

The massive amount of data arriving from the detector and the need for compression and partial reconstruction requires a very powerful data processing system, called O^2, that combines functionalities that are presently split into "Online", "Offline" and the High Level Trigger. This system will then compress and partially reconstruct the events in order to allow efficient storage of all the events.

ALICE muon spectrometer upgrade

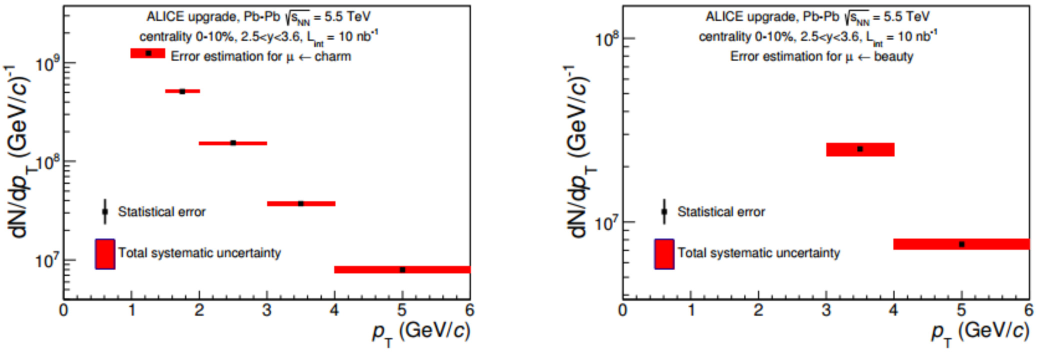

Figure 2.10: Expected transverse momentum distributions of single muons from charm (left) and beauty (right) decays with their respective statistical and systematic uncertainties. Figure taken from Ref. [158].

An upgrade of the muon spectrometer is foreseen due to the increase of luminosity and an interaction rate from 8 kHz (maximum) in Run 1 to 50 kHz (Pb-Pb collisions) after the second long shutdown (2019-2020). The upgrade is summarized in the following:

1. Upgrade of Front End Electronics of trigger chambers to run in genuine avalanche mode (slow down chamber aging);

2. Upgrade of electronics of tracking and trigger systems for readout at minimum bias rate (muon trigger becomes muon identifier);

3. Addition of a new detector, the Muon Forward Tracker (MFT), which will improve the physics capabilities of the muon spectrameter by providing vertexing in the forward rapidity region.

The Muon Forward Tracker consists of two half-MFT cones (Fig. 2.9, Right). Each half-MFT cone consists of 5 half-disks positioned along the beam axis, in the direction of the MUON spectrometer. The MFT covers the pseudo-rapidity acceptance $-3.6 < \eta < -2.45$. The MFT will contribute significantly to the study of heavy-flavour production both in the single muon and the dimuon channels, thanks to the possibility to discriminate muons from charm and beauty decays down to low $p_{\rm T}$ even in central Pb-Pb collisions. It should be noticed that performing these measurements at the lowest $p_{\rm T}$ is crucial in order to extract the total charm and beauty cross sections with the smallest possible dependence on models. The performance of the MFT (and muon spectrometer) for the measurement of muons from charm and beauty decays, separately, is presented in Fig. 2.10. We can observe that it will be possible to measure the open charm yield in the semi-muonic decay channel down to $p_{\rm T} = 1$ GeV/c, with total uncertainties within 10%. For the open beauty yield, in the single muon channel, robust enough measurements will be possible for $p_{\rm T} >$ 3 GeV/c.

2.2.6 ALICE data taking periods during LHC Run-1 and Run-2

ALICE collected Pb-Pb, pp and p-Pb collisions during LHC Run-1 and Run-2 which are reported in Tab. 2.3. One can notice the significant increase in integrated luminosity in pp, p-Pb, and Pb-Pb collisions from Run-1 to Run-2, which allows more precise investigations in Run-2. Moreover in Run-2, Xe-Xe collisions have been collected at $\sqrt{s_{\mathrm{NN}}} = 5.44$ TeV during a pilot run of about 6 hours.

Year(s)	System	$\sqrt{s_{\mathrm{NN}}}$ (TeV)	Integrated Luminosity (nb^{-1})
Run-1			
2009-2010	pp	0.9	~0.15
2011	pp	2.76	~1.1
2010-2011	pp	7	~4800
2012	pp	8	~9700
2013	p-Pb	5.02	~30
2010-2012	Pb-Pb	2.76	~0.1
Run-2			
2015	pp	5.02	~100
2015-2016	pp	13	~14000
2016	p-Pb	5.02	~3
2016	p-Pb	8.16	~20
2015	Pb-Pb	5.02	~0.4
2017	Xe-Xe (B = 0.2 T)	5.44	~300
2018	Pb-Pb	5.02	~1

Table 2.3: ALICE data taking periods, The nominal magnetic field was B = 0.5 T except for Xe-Xe system. Table taken from Ref. [236].

2.3 The ALICE online system

2.3.1 Trigger system

Using the information of the detector signals and the LHC bunch filling scheme, the ALICE Central Trigger Processor (CTP) generates the trigger decision [160]. It selects events with different features at rates which can be scaled down to suit physics requirements and the restrictions imposed by the bandwidth of the Data Acquisition (DAQ) system. Every machine clock cycle (about 25 ns or one bunch crossing) the CTP evaluates the trigger inputs from the detectors. Due to the different event processing speed of the detectors, the ALICE trigger is a 3-level system, level 0 (L0), level 1 (L1) and level 2 (L2).

The trigger classes define how the CTP handles the trigger inputs (a trigger class is made of the logical AND and OR of different trigger inputs and CTP vetoes (see later). The read-out detectors can be grouped in trigger clusters, so more than one detector can measure the event. The CTP can send independent trigger signals to each cluster. In this way, while a slow detector is processing an event, another fast detector can process other events.

The basic scheme of the decision levels can be summarised as:

1. The L0 trigger inputs (also called L0b, b for "before the CTP") are the first one which arrive to the CTP. They are sent by detectors such as V0, T0, SPD, EMCAL (photon trigger signal), PHOS and MTR. The CTP can select an event by checking if the trigger inputs fulfil the logical conditions of a certain trigger class. The CTP sends a L0 trigger signal (also called L0a, a for "after the CTP") to the corresponding read-out detectors in the trigger cluster(s). The L0 level has a latency of 1.2 μs (from the interaction to the arrival of the L0 trigger signal to the read-out detectors);

2. The L1 trigger inputs are sent to the CTP by detectors such as the TRD, ZDC and EMCAL (neutral-jet trigger) after the online calculation of some characteristics of the event. The CTP makes a decision and sends a L1 trigger signal, which arrives to the read-out detectors with a latency of $\sim$6.5 μs. This latency is caused by the computation time in the TRD and EMCAL and the propagation time to the ZDC. The L0 and L1 trigger signals trigger the buffering of the event data in the detector FEE. If the L1 trigger signal does not arrive in time to the read-out detectors they ignore the event;

3. The L2 decision is taken after $\sim$100 μs (corresponding to the drift time of the TPC). The High Level Trigger system (HLT) is able to take more refined trigger decisions by means of an online pre-analysis of the data. It is also in charge of compressing the TPC data without loss of physical information. During Run 1, all events with L1 were accepted by L2.

There is a number of reasons why the CTP does not generate the L0 signal (CTP vetoes). Some examples are: there is at least one detector in a cluster which is busy; the L0 trigger input does not match with a bunch crossing (this is used to suppress the background); the past-future protection (if a collision happens within the TPC drift time, the event is not taken to avoid pile up) or the downscaling of a certain trigger class to allow more DAQ bandwidth for rare events.

2.3.2 Data acquisition system

The goal of the ALICE DAQ system is to carry out the dataflow from the detector up to the data storage. The DAQ dataflow starts at the detector FEE. The data are then transferred to a farm of computers, the Local Data Concentrator (LDC), where the different data fragments corresponding to the information of one event are checked for data integrity, processed and assembled into sub-events. The sub-events information is sent to the Global Data Collector computers (GDC), which build the events combining the information of several LDCs. The Global Data Storage Servers (GDS) store the data. Finally the data are migrated to the CERN computing centre, and duplicated to some Tier 1s computing centres, where they become available for the offline reconstruction.

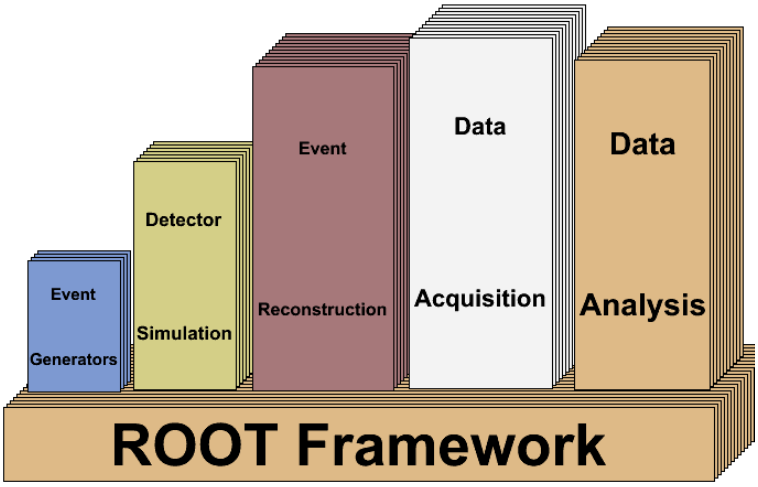

Figure 2.11: ROOT framework and its application to high-energy physics experiments. Figure taken from Ref. [165].

2.3.3 Reconstruction

Once the raw data are written by the DAQ into a disk buffer at the CERN computing center, the data are copied to permanent tapes and, in parallel, a first pass processing is performed. During the first pass reconstruction, high-precision alignment and calibration data are produced. The detector alignment and calibration data are stored in the Offline Condition Data Base (OCDB). With the data reconstruction information, a first set of Event Summary Data (ESD) is produced. Moreover, a filtering of the data in the ESDs for specific analyses can be done to produce the first Analysis Object Data (AOD). The feedback derived from the first pass, including analysis, is used to tune the code for the second pass processing.

2.4 The ALICE offline framework

This section focuses on the description of the software which is used and developed to perform simulation, recontruction and analysis with the ALICE experiment.

2.4.1 Software Platform

The ALICE off-line framework, AliRoot based on the Object Oriented / C++ environment of ROOT [161], allows to reconstruct and analyze physics data coming from simulations and real interactions.

The structure of ROOT is very well suited to deal with amounts of data which are collected from the high-energy physics (HEP) experiments. It provides the packages for event generation, detector simulation, event reconstruction, data acquisition and data analysis, as shown in Fig. 2.11. It also includes the interfaces for different computing facilities (such as ALICE Computing Grid and PROOF).

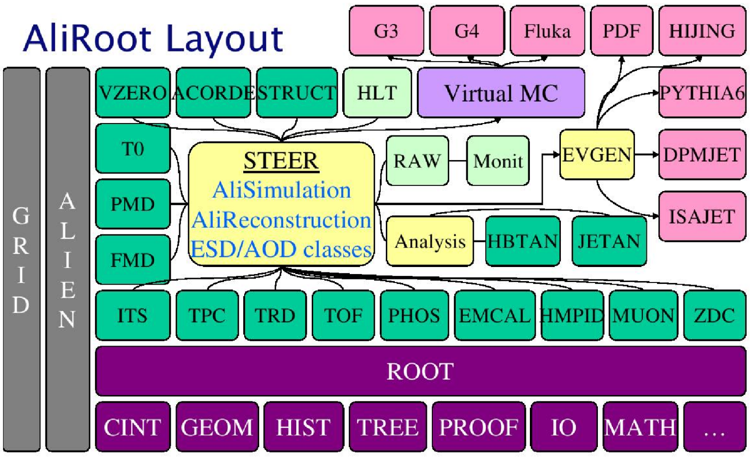

Figure 2.12: The AliRoot framework. Figure taken from Ref. [165].

AliRoot was developed as an extension of ROOT to include the geometry of detectors in ALICE, and the response to the passage of particles.

The AliRoot framework is schematically shown in Fig. 2.12. The central module of it is called STEER, which provides an interface to detector specific codes, to event generators, to Monte Carlo simulations and to steer classes for the reconstruction. Many Monte-Carlo generators (such as PYTHIA6 written in FORTRAN language and HIJING written in C++ language) are used for event simulations. AliRoot allows the use of three different Monte Carlo transport packages, GEANT3 [162], GEANT4 [163], and FLUKA [164]. GEANT3 and FLUKA are written in FORTRAN, and GEANT4 is written with C++. With specific codes, the sub-detectors provide independent modules for simulation and local reconstruction. The output of the global reconstruction is detector independent and is stored in the ESD (Event Summary Data) or AOD (Analysis Object Data) files.

During Run 2, the AliRoot has been divided in two parts:

- AliRoot which contains all common tools for the geometry of detectors, simulations and reconstruction;
- AliPhysics consists of task codes for our analysis, the directory in AliPhysics is created for each working group. Finally, AliPhysics is totally depend of AliRoot. All sources of AliRoot and AliPhysics can accessible from GitHub.

2.4.2 Event simulation and reconstruction

Figure 2.13 presents, in the left part of parabola, the simulation and the right part is the reconstruction procedure which also will be used for the real data.

The different steps of the simulation and reconstruction processes are reported as follows,

Event generation generating the particles produced in a given type of collisions;

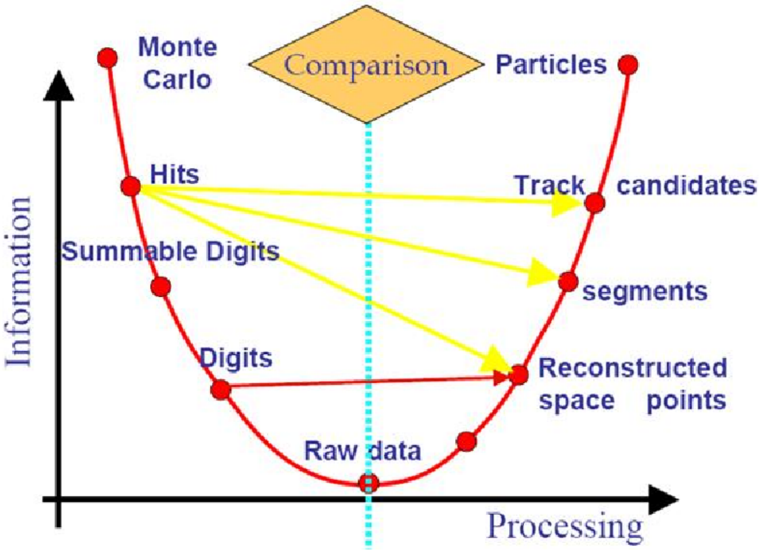

Figure 2.13: The event simulation and reconstruction chain. Figure taken from Ref. [165].

Particle transport the final-state particles are transported through the virtual detectors, and take into account all the processes occuring to the particles in the detector system;

Digitization hits are transformed into digits, which represent the real detector response and take into account apparatus effects, such as noise due to the front-end electronics. Raw-data format, digits are subsequently transformed into the 'raw' format, identical to the one that will directly come from the data acquisition system during data taking. During cluster reconstruction: the reconstruction of the signal starts, several digits are grouped together (clusterization procedure) in order to find a cluster which represents the signal given by a particle in the detector;

Event reconstruction the first step is the local reconstruction, where the reconstructed points are found, by calculating the center of the clusters. The reconstructed points are an estimation of the position where a particle crossed the sensitive area of the detector. The second step is the global reconstruction where the reconstructed points are associated into tracks, which contain information on the kinematic variables, the identity and the energy loss of the particles.

2.4.3 Analysis framework

The layout of the ALICE analysis framework is displayed in Fig. 2.14. The AnalysisManager is the basic class of this framework used to organize the tasks and the input/output data of these tasks. The principle of the analysis framework is that the input data are storaged in the input data container managed by the input handler firstly, then the task managers decide the input for each task and connect

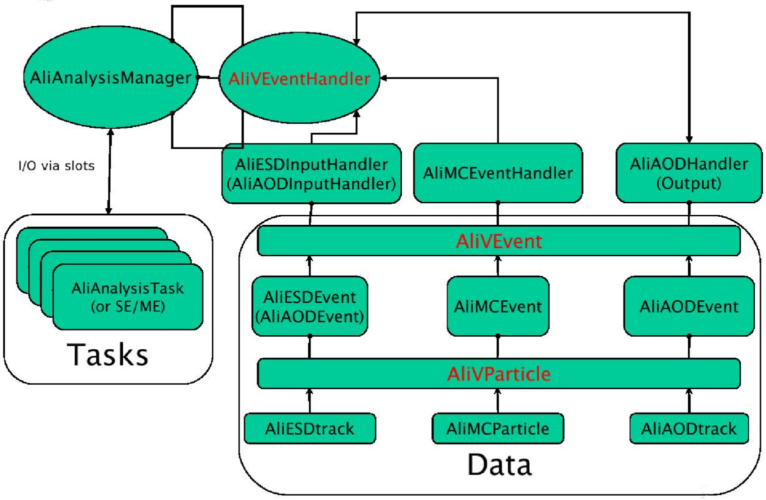

Figure 2.14: The analysis framework. Figure taken from Ref. [165].

the input data to the corresponding task via special containers. After getting the input data, each task can run its analysis procedure in parallel. Finally, the analysis results will be stored in the designated output container via the output handler.

2.4.4 Muon analysis framework

The single muon analyses are discussed within the Physics Analysis Group concerning heavy flavour hadron decay muons (PAG-HFM) which is part of the Physics Working Group on open heavy flavours (PWG-HF). Within AliPhysics, the muon analysis framework is composed of the six main class modules shown in Fig. 2.15:

- AliAnalysisTaskSEMuonsHF: inherits from AliAnalysisTaskSE for single event analysis, and is the main task to implement the ALICE analysis framework;

- AliMuonInfoStoreRD: extracts and stores the muon track information from data, and implement the single muon track selection cuts;

- AliDimuInfoStoreRD: combines the single muon information stored in AliMuonInfoStoreRD into dimuon pairs. To avoid the reusing of the storage ressources, it just saves the hyperlinks to the corresponding two single muons. Then it calculates the dimuon pair kinematics and implements the dimuon pair selection cuts;

- AliMuonInfoStoreMC: inherits from AliMuonInfoStoreRD, and deals with simulated inputs. The reconstructed information saved in AliMuonInfoStoreRD has the same form as that from reconstructed (or real) data. The additional MC truth information is extracted and stored in this module. It includes a method to disentangle muons originating from different sources.

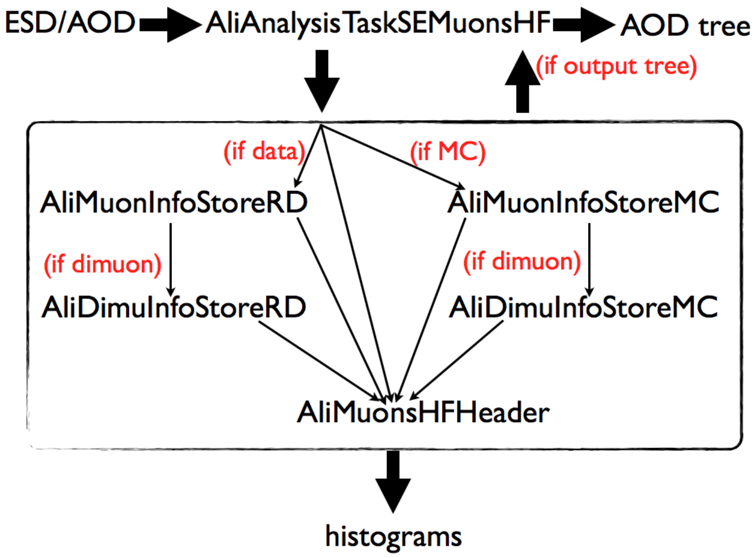

Figure 2.15: The analysis framework of heavy-flavour decay muons. Figure taken from Ref. [166].

- AliDimuInfoStoreMC: inherits from AliDimuInfoStoreRD, deals with simulated inputs. It saves the two hyperlinks to the AliMuonInfoStoreMC objects. The methods for identifying different dimuon sources are implemented here;
- AliMuonsHFHeader: extracts and stores the event level information, like the event trigger mask, vertex position, collision centrality and so on.

CHAPTER 3

Measurements of the production of muons from open heavy-flavour hadron decays in pp collisions

This chapter aims at describing the measurements of the p_{T}-differential production cross section of muons from heavy-flavour hadron decays in pp collisions at $\sqrt{s} = 5.02$ TeV in the rapidity range $(2.5 < y < 4)$[1] and in various sub-rapidity intervals, as well as the p_{T}-integrated production cross section as a function of rapidity (Sec. 3.1). As it will be discussed, the results are in agreement with FONLL calculations within uncertainties, although the data lie in the upper limit of the model predictions. The results with improved statistical and systematic precision compared with the Run 1 measurements for pp collisions at $\sqrt{s} = 2.76$ and 7 TeV will provide an important reference for the computation of the nuclear modification factor of muons from heavy-flavour hadron decays in Pb–Pb collisions at $\sqrt{s_{\mathrm{NN}}} = 5.02$ TeV, and in Xe-Xe collisions at $\sqrt{s_{\mathrm{NN}}} = 5.44$ TeV via an energy scaling based on FONLL predictions. The p_T-differential production cross section ratios between different centre-of-mass energies and rapidity intervals are also measured and described within experimental and theoretical uncertainties by predictions based on perturbative QCD. Moreover, the publication proposal of the measurements of the production of muons from open heavy-flavour hadron decays in pp collisions is approved by ALICE, the draft is being reviewed by the ALICE collaboration.

The various steps of the analysis are first described. That concerns:(i)the event and track selections, (ii) normalization of the muon samples to the equivalent number of minimum-bias events, (iii) muon background estimation (muons from J/ψ decays, muons from light-hadron decays (muons from charged π and K decays), muons from W and Z/γ^* decays and secondary light-hadron decays), (iv) corrections, and (v) estimation of systematic uncertainties.

In this chapter, we also discuss the pp reference at $\sqrt{s} = 5.44$ TeV (Sec. 3.2) using an energy scaling method and the pp reference at $\sqrt{s} = 2.76$ TeV (Sec. 3.3) with the p_{T}-extrapolation method of the published results which were limited to the p_T interval at $2 < p_{\mathrm{T}} < 10$ GeV/c.

---

[1] The muon spectrometer covers a negative pseudo-rapidity range in the ALICE reference frame. η and y variables are identical for muons in the acceptance of the muon spectrometer, and in pp collisions the physics results are symmetric with respect to $\eta(y) = 0$. They will be presented as a function of y, with positive values.

3.1 Measurements in pp collisions at $\sqrt{s} = 5.02$ TeV

3.1.1 Data samples and muon selections

The pp data have been collected in the 2015 LHC15n period, just before the Pb–Pb run. The analysis is based on AODs of the muon pass2 reconstruction (AOD174) and is performed with the AliRoot version vAN-20160120. The sub-detectors used for this analysis are the muon spectrometer, the SPD, the V0 and the T0 (chapter 2). The SPD is used for the primary vertex reconstruction. Both V0 and T0 are used for the luminosity determination. They are also used for trigger. The data used in the analysis have been collected with the minimum-bias (MB) trigger (for normalization purposes) and muon triggers with Muon Single Low (MSL) and Muon Single High (MSH) [2]. The following runs have been selected after the Quality Assurance (QA) checks. The run list is:

- LHC15n, muon_calo_pass2, AOD174, 25 runs:
  244340 244343 244351 244355 244359 244364 244377 244411 244416 244418 244421 244453 244480 244481 244482 244483 244484 244531 244540 244542 244617 244619 244626 244627 244628

The event and track selections are the standard ones used in previous single muon analyses. An offline event selection (Physics Selection) is applied and a reconstructed vertex is required. Various kinematic cuts are applied for track selection. Tracks are required to be reconstructed within the acceptance of the muon spectrometer ($-4 < \eta < -2.5$) and to have a polar angle at the end of the absorber (θ_{abs}) from 170 to 178 degrees. One also requires that the track candidate in the tracking system matches the track reconstructed in the trigger system. Finally, a selection on the Distance of Closest Approach (DCA) to the primary vertex of each track weighted with its momentum (p) is also applied. The maximum value is set to $6\sigma_{p\times\mathrm{DCA}}$, where $\sigma_{p\times\mathrm{DCA}}$ is the resolution on this quantity [167]. This latter further reduces the contribution from fake tracks coming from the association of uncorrelated clusters in the tracking chambers and beam-induced background tracks.

The effect of the cuts on the measured p_{T} distributions of inclusive muons is shown in Fig. 3.1 for MB, MSL and MSH trigger events, and Tab. 3.1 and 3.2 give the number of events and tracks after the various cuts previously discussed are applied. The final p_{T} spectra and corresponding statistical uncertainties for MSL and MSH triggered events are displayed in Fig. 3.2 in left and right panel, respectively. One can notice that by combining MSL and MSH data samples, one can perform the measurements of inclusive muons up to $p_{\mathrm{T}} = 20$ GeV/c with a good statistical precision (the relative statistical uncertainty is about 16% in $18 < p_{\mathrm{T}} < 20$ GeV/c

---

[2] The data sample consists of muon-triggered events requiring the coincidence of the minimum-bias (MB) trigger condition and at least one candidate track with a p_{T} above a threshold value in the muon trigger system. The MB trigger is formed by a coincidence between signals in the two V0 arrays. Data were collected using two different muon trigger p_{T} thresholds, of about 0.5 GeV/c and 4.2 GeV/c, defined as the p_{T} value for which the muon trigger probability is 50%. In the following, the low- and high-p_{T} trigger threshold samples are referred to as MSL and MSH, respectively.

and $2.5 < y < 4$ with MSH). Both MSL and MSH triggers are used, and we will shift from MSL to MSH at $p_{\mathrm{T}} = 7$ GeV/c, hence well above the MSH p_{T} threshold. Moreover, this will allow us to measure the R_{AA} in Pb-Pb collisions without no need of p_{T} extrapolation for the pp reference [168].

Finally, the production cross section of muons from heavy-flavur hadron decays will be measured in the region $p_{\mathrm{T}} > 2$ GeV/c where the contamination of muons from secondary light-hadron decays is small [182], also see Fig. 1.36. Simulations with PYTHIA 6 event generator and GEANT 3 show that this contribution is about 3.5% at $p_{\mathrm{T}} = 2$ GeV/c and it decreases drastically with increasing p_{T} to become smaller than 1% above $p_{\mathrm{T}} = 3$ GeV/c. Similar results were also found with other event generators and transport codes in previous Run 1 studies.

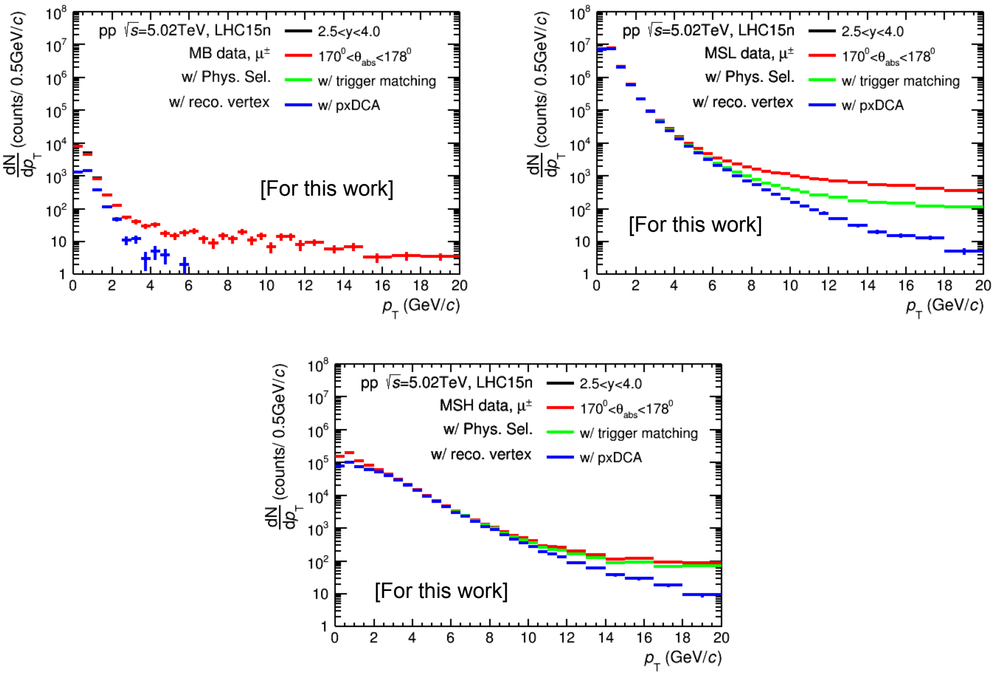

Figure 3.1: Transverse momentum distributions of inclusive muons with different selection cuts at event and track level in pp collisions at $\sqrt{s} = 5.02$ TeV for MB (up, left), MSL (up, right) and MSH (bottom) triggered events.

		N_{evt}(After Phys. Sel.)	+ Rec. Vertex
LHC15n	MB	$5.552 \cdot 10^5$	2.93%
	MSL	$3.448 \cdot 10^7$	1.13%
	MSH	$1.665 \cdot 10^6$	1.23%

Table 3.1: Number of events after the event selection conditions are applied.

The full rapidity interval has been also divided into five sub-rapidity intervals of width 0.3. As shown in Fig. 3.3, the present statistics also allows us to perform the

		n_{trk}(+evt level cut)	$+\ \eta$	$+\ \Theta_{\mathrm{abs}}$	+ TrM	+ p×DCA
LHC15n	MB	17178	13.50%	2.98%	77.43%	0.12%
	MSL	$2.0310 \cdot 10^{7}$	8.37%	0.53%	5.95%	0.39%
	MSH	$8.4033 \cdot 10^{5}$	9.52%	0.38%	32.70%	2.15%

Table 3.2: Number of tracks after event selection conditions and with the various analysis cuts.

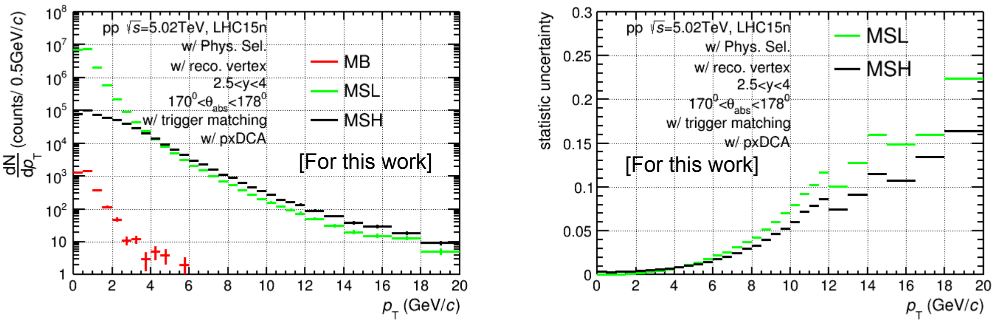

Figure 3.2: Transverse momentum distributions of inclusive muons after all selection cuts are applied in pp collisions at $\sqrt{s} = 5.02$ TeV for MSL and MSH triggered events (left) and corresponding statistical uncertainties (right).

measurements up to $p_{\mathrm{T}} = 20$ GeV/c for all y intervals by using large p_{T} intervals in the high p_{T} region, in particular for the most forward rapidity bin. The statistical uncertainty in the most forward rapidity bin ($3.7 < y < 4$) is about 21% for $13 < p_{\mathrm{T}} < 20$ GeV/c.

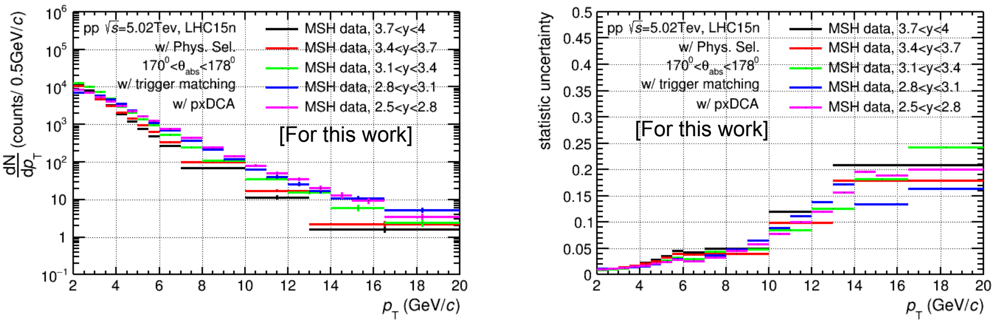

Figure 3.3: Left: transverse momentum distributions of inclusive muons after all selection cuts are applied in pp collisions at $\sqrt{s} = 5.02$ TeV for MSH triggered events. The distributions are shown for five sub-rapidity intervals mentioned in the figure. Right: corresponding statistical uncertainties.

3.1.2 Normalization procedure

In order to get the equivalent number of minimum-bias (MB) events and the corresponding integrated luminosity for MSL and MSH triggered data samples, one needs to determine the normalization factor ($F_{\rm norm}^{\rm MSL/MSH}$) for these data samples. The strategy is the same as the one used in the J/ψ analysis for the same system and centre-of-mass energy [169]. It has been also discussed in detail for the single muon analysis in Pb–Pb collisions at $\sqrt{s_{\rm NN}} = 5.02$ TeV [168]. Both offline and scaler methods have been implemented. As described hereafter, in the offline method one applies the muon trigger condition on MB events, while in the online method one uses the trigger rates e.g. the L0b trigger scalers stored in the Offline Conditions Database (OCDB). Once the normalization factor is determined, the equivalent number of events for a given process is calculated as $N_{\rm MB}^{\rm eq} = F_{\rm norm}^{\rm MSL/MSH} \times N_{\rm MSL(MSH)}$.

Pile-up correction

A correction for pile-up is needed for both online and offline methods. The pile-up correction is calculated run by run as:

$$F_{\rm pile-up}^{\rm i} = \mu^{\rm i}/(1-e^{-\mu^{\rm i}}) \tag{3.1}$$

with

$$\mu^{\rm i} = -\ln\left(1 - {\rm purity}_{\rm MB}^{\rm i} \times \frac{{\rm L0bRate^i}_{\rm MB}}{N_{\rm colliding}^{\rm i} \times f_{\rm LHC}}\right). \tag{3.2}$$

$\mu^{\rm i}$ is the mean value of the Poisson distribution which describes the probability to have n collisions when the beams cross each other. The variable ${\rm purity}_{\rm MB}^{\rm i}$ is the purity factor (CINT7) associated to MB trigger and is computed as the ratio of physics selected events to the total number of events. ${\rm L0bRate}_{\rm MB}^{\rm i}$ and $N_{\rm colliding}$ are the rates of number of MB events recorded by the L0b counters and the number of interacting bunches, respectively. $f_{\rm LHC} = 11245$ Hz is the collision frequency of the LHC. Note that recently the $\mu^{\rm i}$ values for MB trigger can be found also in the Run Condition Table (RCT). We checked that the values calculated with Eq. 3.2 are the same as the one available in the RCT.

The pile-up correction has been also evaluated for MB event trigger with T0 (C0TVX trigger) instead of MB event trigger with V0 (CINT7 trigger) using the same procedure since, as it will be discussed later, the C0VTX needs to be used with the online method. In this case, the ${\rm purity}_{\rm MB}^{\rm i}$ factor is 100% [169]. The T0 trigger rates can be affected by pile-up of two events hitting T0A and T0B, separately. This correction was evaluated following the strategy described in [170] and was found negligible (smaller than 0.02%) [171].

The variables ${\rm L0bRate}_{\rm MB}^{\rm i}$, run duration, $N_{\rm colliding}$ and ${\rm purity}_{\rm MB}^{\rm i}$ (CINT7) are displayed as a function of run number in Fig. 3.4. The resulting pile-up correction factor for CINT7 and C0TVX MB triggers is shown in Fig. 3.5. The pile-up correction is smaller than 3% (about 1%) in the first half of the LHC15n period for CINT7 (C0VTX) MB triggers, and is negligible for the rest of the period for both triggers.

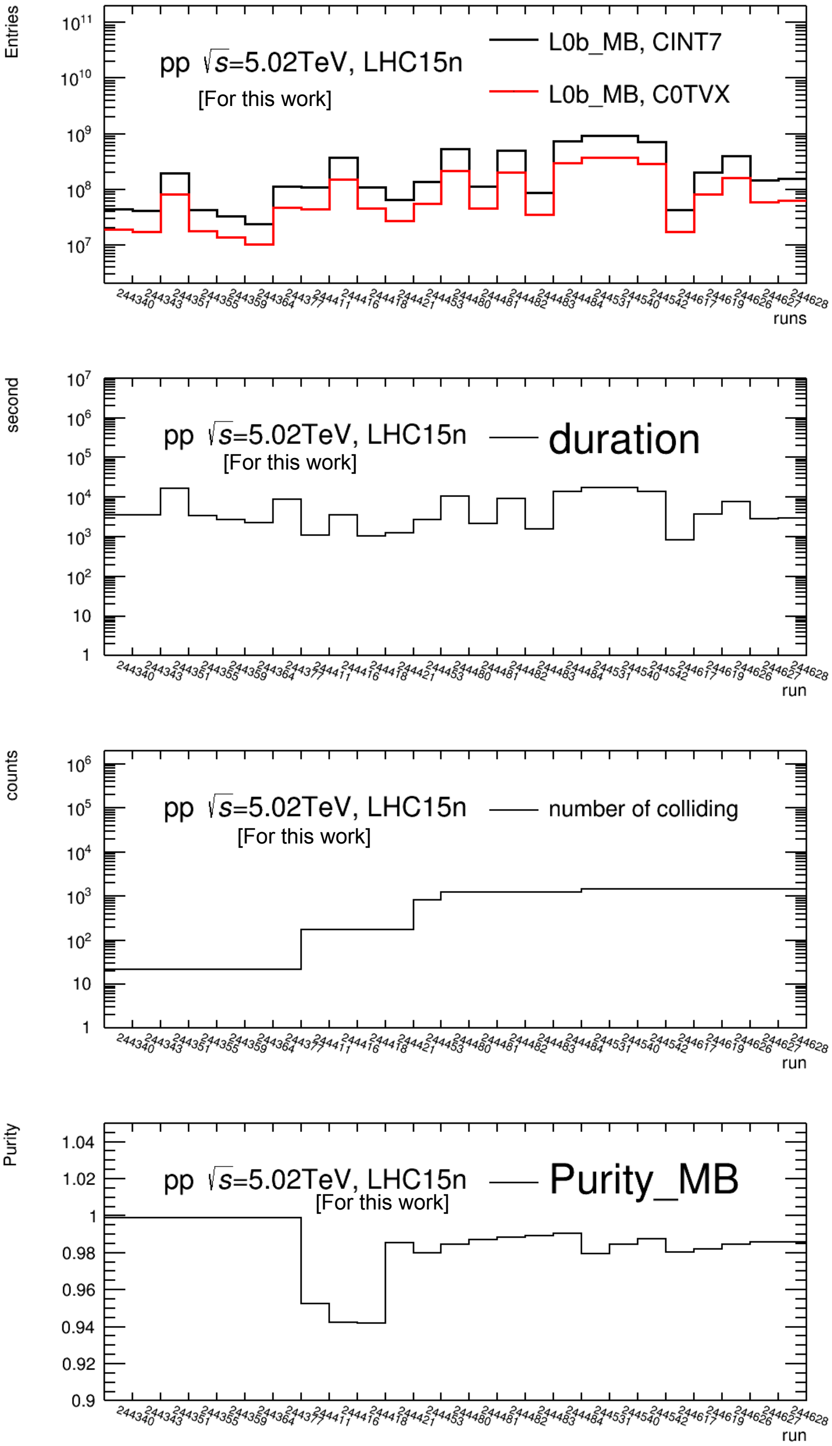

Figure 3.4: L0b rates, run duration, number of interaction bunches and purity of minimum-bias trigger CINT7 as a function of run number.

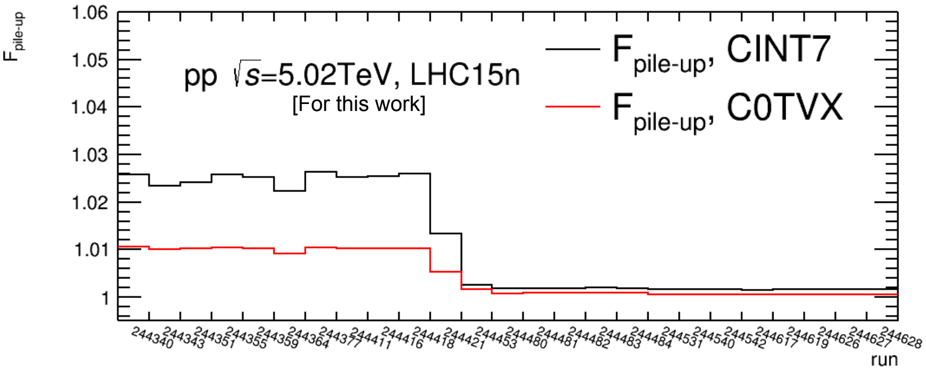

Figure 3.5: Pile-up correction for CINT7 and COVTX minimum-bias triggers as a function of run number.

Offline method

The normalization factors for MSL ($F^{\rm MSL}_{\rm norm}$) and MSH ($F^{\rm MSH}_{\rm norm}$) triggers are calculated on a run by run basis according to:

$$F^{\rm i}_{\rm norm}({\rm MSL}) = \frac{N^{\rm i}_{\rm MB} \times F^{\rm i}_{\rm pile-up}}{N^{\rm i}_{\rm (MB\&\&0MSL)}} \tag{3.3}$$

$$F^{\rm i}_{\rm norm}({\rm MSH}) = F^{\rm i}_{\rm pile-up} \times \frac{N^{\rm i}_{\rm MB}}{N^{\rm i}_{\rm (MB\&\&0MSL)}} \times \frac{N^{\rm i}_{\rm MSL}}{N^{\rm i}_{\rm (MSL\&\&0MSH)}} \tag{3.4}$$

$N^{\rm i}_{\rm MB}$ and $N^{\rm i}_{\rm MSL}$ are the number of MB and MSL triggers after the offline selection. $N^{\rm i}_{\rm (MB\&\&0MSL)}$ and $N^{\rm i}_{\rm (MSL\&\&0MSH)}$ are the sample of MB events containing a 0MSL input and the sample of MSL events containing a 0MSH input, respectively. 0MSL ($=18$) and 0MSH ($=19$) are the ID of the Central Trigger Processor (CTP) trigger inputs for MSL and MSH triggers. $F_{\rm pile-up}$ is the pile-up correction factor associated with MB (CINT7) trigger.

The final value is the weighted average, i.e. using the number of MSL or MSH events as a weight:

$$F^{\rm MSL/MSH}_{\rm norm} = \frac{\sum_i F^{\rm MSL/MSH}_{\rm norm}/(\sigma^2)^{\rm MSL/MSH}_{\rm stat}}{\sum_i 1/(\sigma^2)^{\rm MSL/MSH}_{\rm stat}} \tag{3.5}$$

The statistical uncertainty is calculated as:

$$[\Delta F^{\rm MSL/MSH}_{\rm norm}]_{\rm stat} = \sqrt{\frac{1}{\sum_i 1/(\sigma^2)^{\rm MSL/MSH}_{\rm stat}}} \tag{3.6}$$

Scaler method

This method relies on the L0b trigger inputs (scalers) taken from the Offline Conditions Database (OCDB). However, due to a contamination of $\mathrm{L0b_{MB}}$ scalers by V0 after pulses, the C0TVX trigger is used instead of CINT7 (MB) trigger. The normalization factor is computed run by run as:

$$F^{\mathrm{i}}_{\mathrm{norm-onl}}(\mathrm{MSL(MSH)}) = \frac{\mathrm{L0b^{i}_{C0VTX}} \times \mathrm{purity^{i}_{C0VTX}} \times F^{\mathrm{i}}_{\mathrm{pile-up}}}{\mathrm{L0b^{i}_{MSL(MSH)}} \times \mathrm{purity^{i}_{MSL(MSH)}}} \tag{3.7}$$

where $\mathrm{L0b^{i}_{C0VTX}}$, $\mathrm{L0b^{i}_{MSL}}$ and $\mathrm{L0b^{i}_{MSH}}$ are the scaler (trigger rate) values recorded at L0b level for C0VTX, MSL and MSH triggers, respectively. The quantity $\mathrm{purity_{C0VTX}}$ is the ratio of events, after the offline event selection, to the total number of events and is equal to unity. The variable $\mathrm{purity_{MSL(MSH)}}$ is the fraction of accepted MSL (MSH) triggered events that pass the offline event selection. The final value is calculated as in the offline method. Note that this method does not suffer from lack of statistics as it is the case for the offline method.

Normalization factor results

The run by run normalization factor from the online (black symbols) and offline (green symbols) methods are displayed in Fig. 3.6 for MSL (upper) and MSH (bottom) triggers.

The final normalization factor values from offline and online (scalers) methods are summarized in table 3.3. As expected, the statistical uncertainties are negligible with the online method.

	Offline	Online
MSL	82.80 ± 1.01	34.3 ± 0.05
MSH	3307.2 ± 43.1	1370.9 ± 2.2

Table 3.3: Normalization factor for muon-triggered events. The quoted uncertainties are the statistical ones.

In order to compare the results based on CINT7 (offline method) and C0VTX (online method) triggers, one needs to calculate the MSL and MSH cross sections as:

$$\sigma_{\mathrm{MSL/MSH}} = \frac{\sigma_{\mathrm{VdM}}}{F^{\mathrm{MSL/MSH}}_{\mathrm{norm}}}. \tag{3.8}$$

σ_{VdM} is the visible cross section measured in van der Meer scans for T0 and V0 [172]. The corresponding values are $\sigma^{\mathrm{V0}}_{\mathrm{VdM}} = (51.2 \pm 1.2)$ mb and $\sigma^{\mathrm{T0}}_{\mathrm{VdM}} = (21.6 \pm 0.4)$ mb, and the uncertainties are the systematic ones. The run by run comparison is shown in Fig. 3.7 for MSL (upper) and MSH (bottom) triggers. One observes that both offline and online methods give compatible results within uncertainties.

Table 3.4 summarizes also the MSL and MSH cross sections determined using the normalization factors given in Tab. 3.3.

Finally, the normalization factor that will be used to compute the cross section of muons from heavy-flavour hadron decays is obtained with the online method based on the C0VTX trigger.

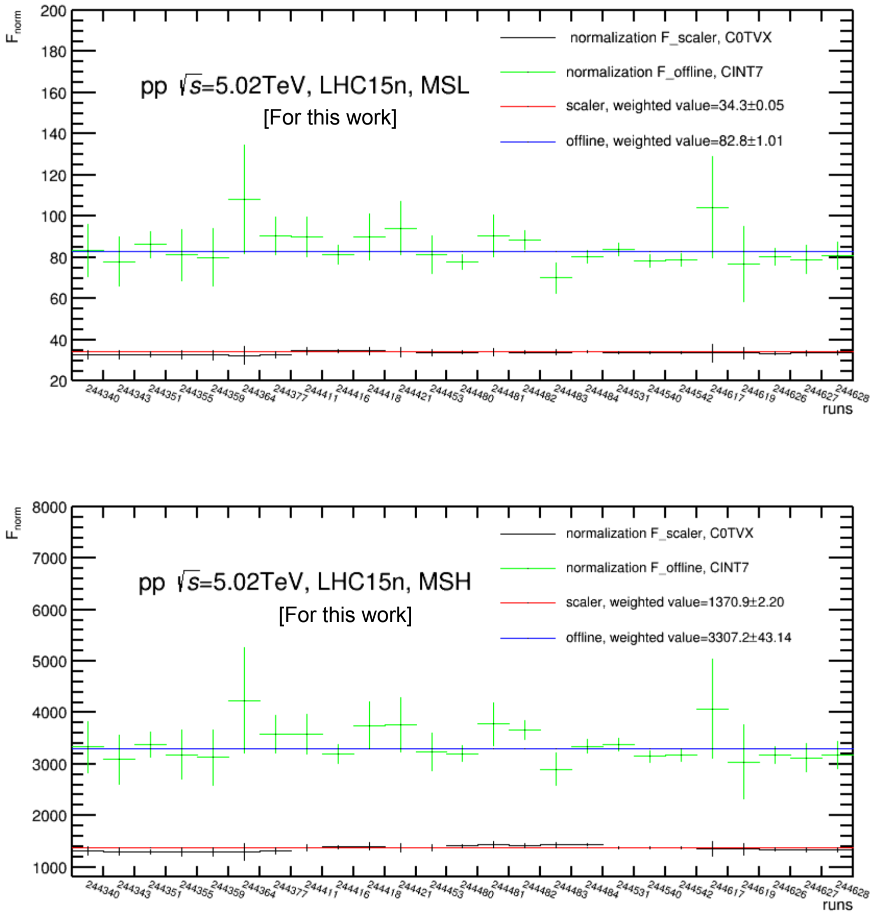

Figure 3.6: Normalization factors for MSL (upper) and MSH (bottom) triggers as function of run number. Green (black) symbols refer to offline (online) methods.

	Offline	Online
MSL	0.6184 ± 2.63% mb	0.6347 ± 1.86% mb
MSH	0.0155 ± 2.68% mb	0.0158 ± 1.86% mb

Table 3.4: MSL and MSH cross sections. The quoted uncertainties include the statistical uncertainty on normalization factor and the systematic uncertainty on $\sigma_{\rm VdM}$ that are added in quadrature.

The resulting normalization factors are: $F_{\rm norm}^{\rm MSL} = 34.3$ and $F_{\rm norm}^{\rm MSH} = 1370.9$. The corresponding integrated luminosity is given by

$$L_{\rm int} = \frac{N_{\rm MSL(MSH)} \times F_{\rm norm}^{\rm MSL(MSH)}}{\sigma_{\rm VdM}^{\rm T0}}, \tag{3.9}$$

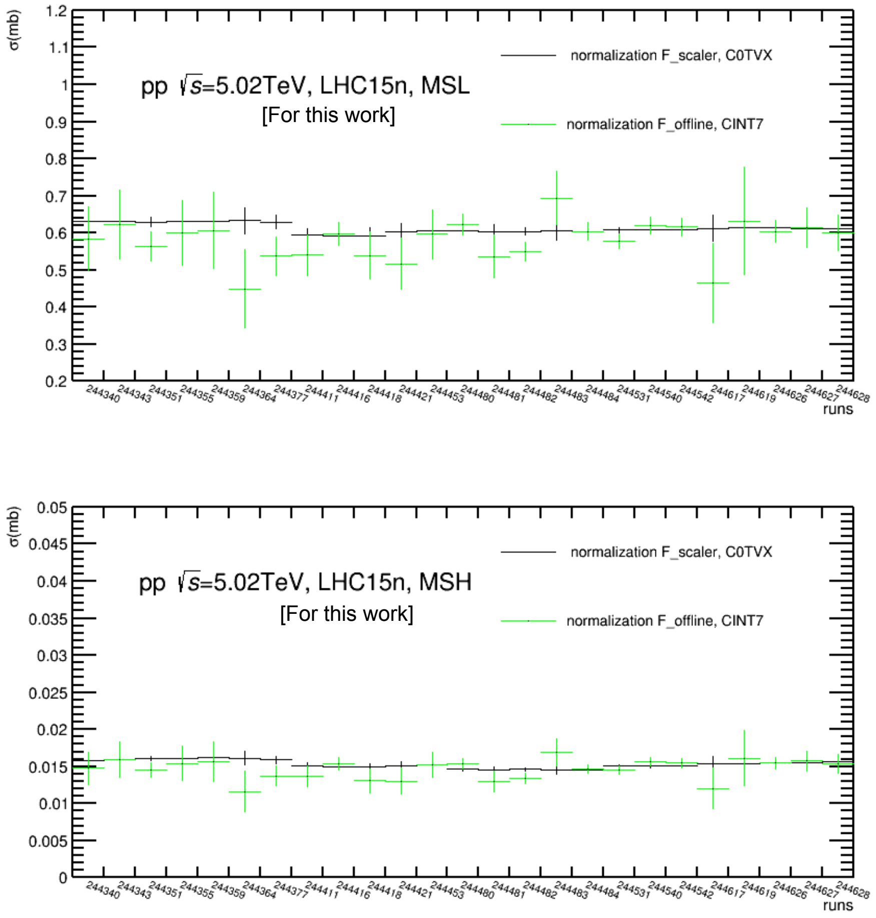

Figure 3.7: MSL (upper) and MSH (bottom) cross sections as function of run number. Green (back) symbols refer to offline (online) methods.

where $\sigma^{\mathrm{T0}}_{\mathrm{VdM}} = (21.6 \pm 0.4)$ mb. The total systematic uncertainty on σ_{T0} of 2.1% contains contributions from the measurement of the T0 trigger cross section using the Van der Meer scan technique (2.05%) and the stability of the T0 trigger during data taking (0.4%) [172]. The systematic uncertainty on L_{int} reflects the systematic uncertainty on $\sigma^{\mathrm{T0}}_{\mathrm{VdM}}$. This leads to $L_{\mathrm{int}} = 53.7 \pm 1.1\ \mathrm{nb}^{-1}$ and $L_{\mathrm{int}} = 104.4 \pm 2.2\ \mathrm{nb}^{-1}$ for MSL and MSH triggers, respectively.

3.1.3 Acceptance times efficiency correction

Strategy and results

The p_{T}-differential acceptance times tracking and trigger efficiency ($A \times \varepsilon$) is estimated from a procedure based on a full simulation using as inputs a parameterization of the p_{T} and y distributions of muons from heavy-flavour hadron decays predicted by FONLL calculations using CTEQ6.6 as Parton Distribution Functions. The detector description and its response are modeled using the GEANT3 transport package. The evolution of the detector over time is also taken into account by doing a run-by-run simulation, the simulated statistics being proportional to the number of muon triggers. The functions that are used to parameterize the FONLL p_{T} and y distributions of muons from charm and beauty decays are: $p_1\cdot(e^{\mathrm{p}_2(1-\mathrm{e}^{\mathrm{x}\cdot\mathrm{p}_3})}+p_4)\cdot\dfrac{1}{x^{p_5}}\cdot(p_6+x\cdot p_7+x^2\cdot p_8)$ and $x^8\cdot p_1+x^6\cdot p_2+x^4\cdot p_3+x^2\cdot p_4+x\cdot p_5+p_6$, respectively. The fit parameters are p_1, p_2, p_3, p_4, p_5, p_6, p_7 and p_8. Note that these functions have been already used in other analyses for pp collisions at different beam energies and p–Pb collisions at $\sqrt{s_{\mathrm{NN}}}$ = 5.02 TeV. Figure 3.8 presents the predicted p_{T} and y distributions of muons from heavy-flavour hadron decays by FONLL and the corresponding fit functions just mentioned.

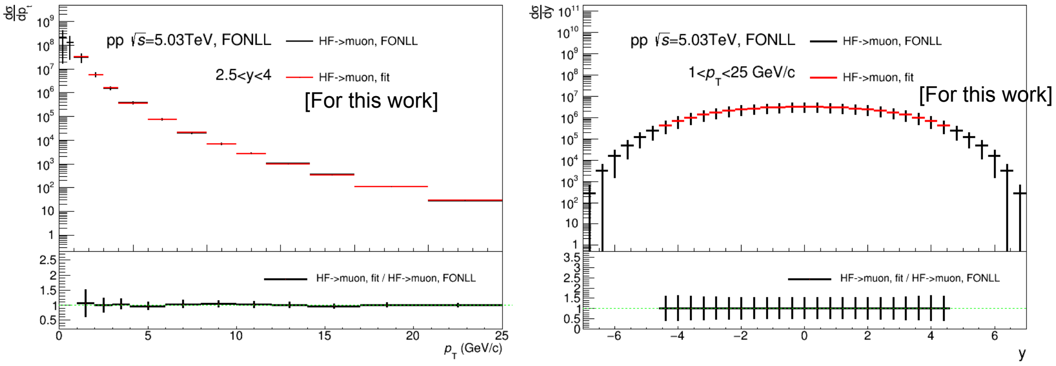

Figure 3.8: Predicted FONLL p_{T} and y distributions (back) for pp collisions at $\sqrt{s}$ = 5.02 TeV. The fit functions are also shown (red).

The $A\times\varepsilon$ as a function of reconstructed and generated p_{T} is shown in Fig. 3.9, left and right panels, for MSL and MSH triggers. For reconstructed $p_{\mathrm{T}} > 3-4$ GeV/c, the $A\times\varepsilon$ tends to saturate at a value close to 90% in MSL with a very slight increase at high p_{T}. For MSH trigger, the efficiency plateau is reached about $p_{\mathrm{T}} = 15$ GeV/c. It is interesting to observe that the $A\times\varepsilon$ versus generated p_{T} becomes completely flat at high p_{T}, hence confirming that the slight increase is a alignment effect. Note that in the following a two-dimensional correction $A\times\varepsilon$ correction is applied.

The $A\times\varepsilon$ as a function p_{T} has been also studied in five sub-rapidity intervals. The two-dimensional $A\times\varepsilon$ matrices are displayed for MSL and MSH triggers, in left and right panels of Fig. 3.10. The $A\times\varepsilon$ as a function of reconstructed (generated) p_{T} is also presented in three rapidity bins in Fig. 3.11 in upper and (lower) panels. One can notice that the $A\times\varepsilon$ plateau for MSH tends to be reached at higher p_{T} for the local boards at the boarder of the trigger chambers e.g. $2.5 < y < 2.8$. Similar trends as in the full rapidity interval are evidenced for $A\times\varepsilon$ as a function of generated p_{T} in various sub-rapidity intervals ($2.5 < y < 2.8$ and $3.7 < y < 4$ bins chosen as examples).

Comparison of p_{T} distributions for MSL and MSH triggered events

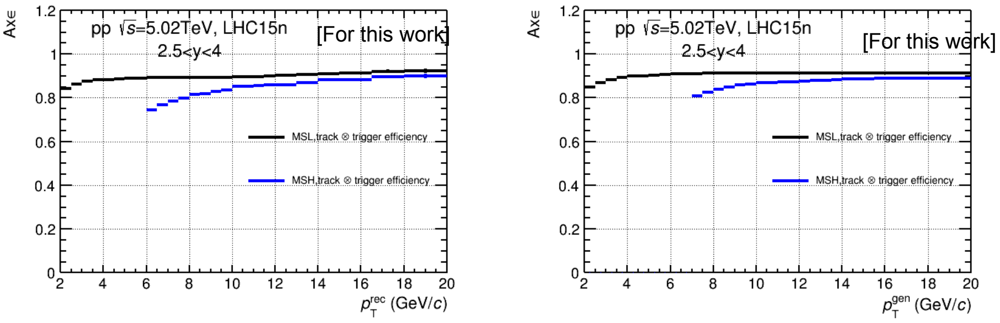

Figure 3.9: $A \times \varepsilon$ as a function of reconstructed (left) and generated (right) p_{T} from a simulation using as input a parameterization of p_{T} and y distributions from FONLL.

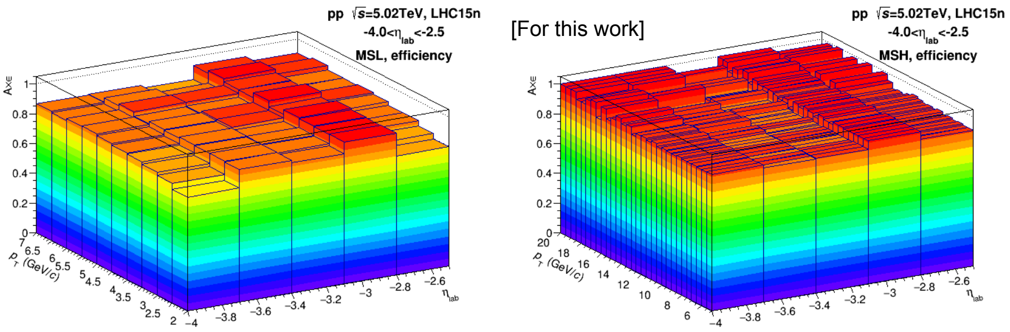

Figure 3.10: $A \times \varepsilon$ as a function of p_{T} and rapidity for MSL (left) and MSH (right) data samples.

The ratio of the p_{T} distribution of inclusive muons corrected for $A \times \varepsilon$ and normalized to the equivalent number of minimum-bias events in MSL triggered events to that in MSH triggered events is reported in Fig. 3.12 for the full rapidity range (left), and in the two sub-rapidity intervals $-4 < \eta < -3.4$ and $-3.4 < \eta < -2.5$ [3] (right). The ratio is consistent with unity within statistical uncertainties. The deviation between MSL and MSH amounts to 3% in the full rapidity range. As a function of rapidy, the deviation remains stable within about 1.5–3.5%.

3.1.4 Estimation of the muon background contributions

The p_{T} distribution of muons from heavy-flavour hadron decays at forward rapidity is obtained after the subtraction of the muon background to the corrected inclusive muon yield and is expressed as:

---

[3] The statistics is not sufficient to draw this ratio in all sub-rapidity intervals of 0.3 width and up to $p_{\mathrm{T}} = 20$ GeV/c.

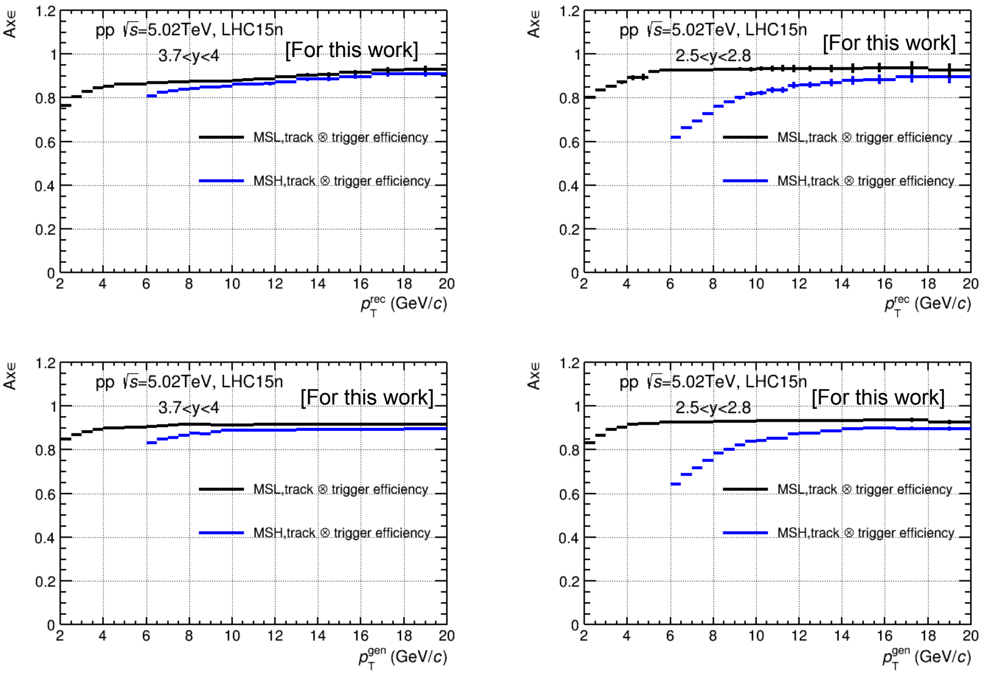

Figure 3.11: $A \times \varepsilon$ as a function of p_{T} in various y intervals mentioned on the figures for MSL and MSH triggers. Upper (lower) plots show the $A \times \varepsilon$ as a function of reconstructed (generated) p_{T}.

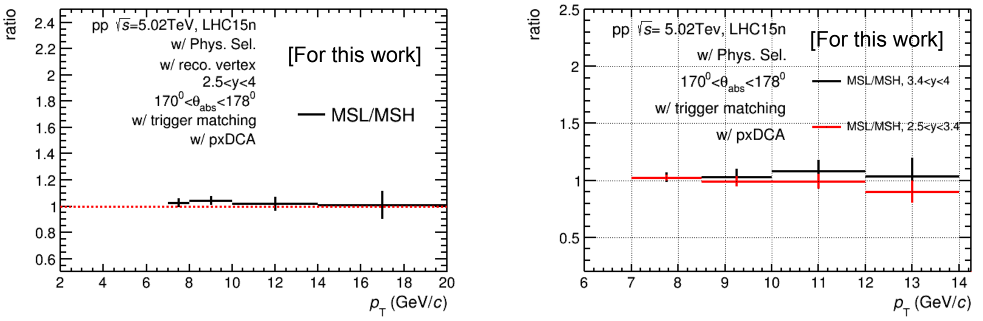

Figure 3.12: Ratio of the p_{T} distributions with MSL and MSH triggers after normalization to the equivalent number of minimum-bias events and after applying the $A \times \varepsilon$ correction for the full rapidity range (left) and in various sub-rapidity intervals (right).

$$\frac{dN_{\mathrm{pp}}^{\mu\leftarrow HF}}{dp_{\mathrm{T}}} = \frac{dN_{\mathrm{pp}}^{incl.\ \mu}}{dp_{\mathrm{T}}} - \frac{dN_{\mathrm{pp}}^{\mu\leftarrow K,\pi}}{dp_{\mathrm{T}}} - \frac{dN_{\mathrm{pp}}^{\mu\leftarrow sec.K,\pi}}{dp_{\mathrm{T}}} - \frac{dN_{\mathrm{pp}}^{\mu\leftarrow W/Z,\gamma^*}}{dp_{\mathrm{T}}} - \frac{dN_{\mathrm{pp}}^{\mu\leftarrow J/\psi}}{dp_{\mathrm{T}}}. \tag{3.10}$$

The main background contribution at low/intermediate p_{T} is the component of muons from primary charged pion and kaon decays, while at high p_{T} ($p_{\mathrm{T}} >\sim$ 14–15 GeV/c) the main source of background is the component of W/Z,γ^*-decay muons. Other background sources will also be discussed in the following. The relative contribution of muons from secondary charged pion and kaon decays with respect to inclusive muons decreases strongly with p_{T}, from about 4% at $p_{\mathrm{T}} = 2$ GeV/c to become smaller than 1% at $p_{\mathrm{T}} = 5$ GeV/c. The contribution of J/ψ decay muons to the single muon p_{T} distribution is small over the whole p_{T} range compared to the other background contributions, the fraction of J/ψ decay muons relative to inclusive muons being 1–4%. The Υ contribution can be ignored according to the production cross sections, compared to J/ψ ones, and will be not discussed in the following.

Muons from primary pion and kaon decays

The procedure implemented for the estimation of the contribution of muons from primary charged pion and kaon decays to the single muon p_{T} distribution uses as inputs, the published ALICE mid-rapidity charged π and K pp reference employed for the corresponding R_{pPb} measurement at $\sqrt{s_{\mathrm{NN}}} = 5.02$ TeV [173]. The reference π and K spectra at $\sqrt{s} = 5.02$ TeV, shown in Fig. 3.13, were obtained by interpolating data measured at $\sqrt{s} = 2.76$ and 7 TeV.

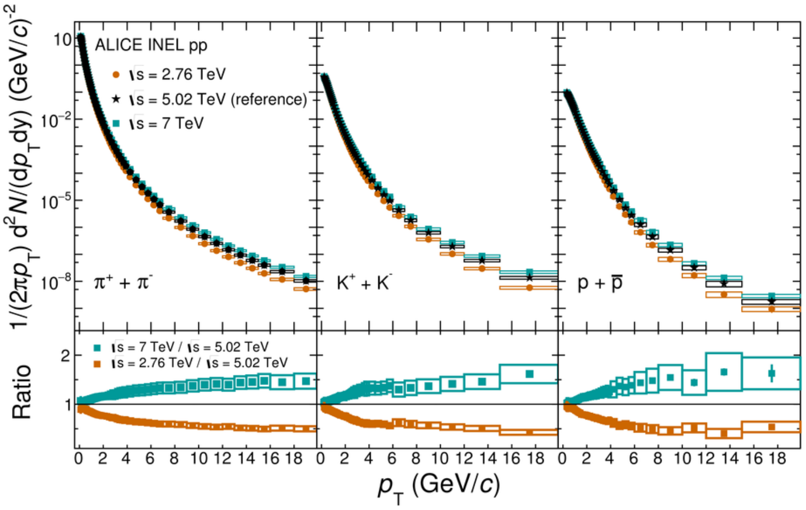

Figure 3.13: Mid-rapidity pp reference at $\sqrt{s} = 5.02$ TeV for charged pions and kaons [173].

The three main steps that will be discussed in the following are:

- Transverse momentum extrapolation of mid-rapidity charged pion and kaon spectra at higher p_{T};
- Extrapolation towards forward rapidity of the p_{T}-extrapolated mid-rapidity charged pion and kaon spectra;

- Production of decay muons via fast detector simulations of decay kinematics and absorber effect.

a. p_{T} extrapolation of charged pion and kaon spectra

In order to estimate the p_{T} distribution of muons from heavy-flavour hadron decays up to $p_{\mathrm{T}} = 20$ GeV/c, one needs to extrapolate the input π and K distributions to higher p_{T}, up to about $p_{\mathrm{T}} = 40$ GeV/c [174]. This is done according to following steps. The π and K distributions are fitted 1000 times with a power-law function after the statistical and systematic uncertainties are added in quadrature and results with $\chi^2/\mathrm{ndf} > 1.5$ are discarded. The fit range is $7 < p_{\mathrm{T}} < 20$ GeV/c. It was checked that varying slightly the lower limit of the fit range has a negligible effect on the final π and K distributions[4]. Finally the central value (μ) and systematic uncertainty (σ) are the ones from the Gaussian distribution at a given $p_{\mathrm{T}}^{\mathrm{extrap}}$ interval.

The extrapolated p_{T} distributions of mid-rapidity charged pions and kaons are shown in Fig. 3.14. The resulting systematic uncertainties are displayed in Fig. 3.15. The latter amount to about 10% in the measured p_{T} region ($p_{\mathrm{T}} < 20$ GeV/c), and varies within about 10–40% in the extrapolated p_{T} region depending on the particle species.

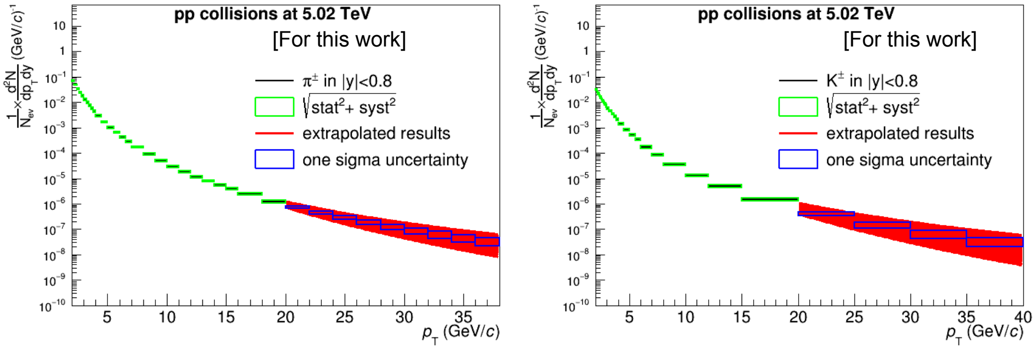

Figure 3.14: Mid-rapidity extrapolated charged π and K p_{T} distributions.

The rapidity extrapolation of charged pions and kaons is performed as:

$$\frac{\mathrm{d}^2 N^{\pi^{\pm}(K^{\pm})}}{\mathrm{d}p_{\mathrm{T}}\mathrm{d}y} = F_{\mathrm{extrap}}(p_{\mathrm{T}}, y) \cdot \left[\frac{\mathrm{d}^2 N^{\pi^{\pm}(K^{\pm})}}{\mathrm{d}p_{\mathrm{T}}\mathrm{d}y}\right]_{\mathrm{mid}-y}, \tag{3.11}$$

where $F_{\mathrm{extrap}}(p_{\mathrm{T}}, y)$ is the p_{T}-dependent rapidity extrapolation factor.

The rapidity extrapolation is obtained with Monte Carlo simulations based on PYTHIA 6.4.25 (Perugia-2011), and PHOJET event generators[5]. The systematic uncertainty is given by the difference between PYTHIA 6 and PHOJET simulations. The rapidity distributions of charged pions and kaons with $p_{\mathrm{T}} > 2$ GeV/c from

---

[4] Fits were performed by varying the lower p_{T} limit between 6 GeV/c and 8 GeV/c.

[5] It was checked that PYTHIA 8 predictives give comparable results as PYTHIA 6 and PHOJET simulations

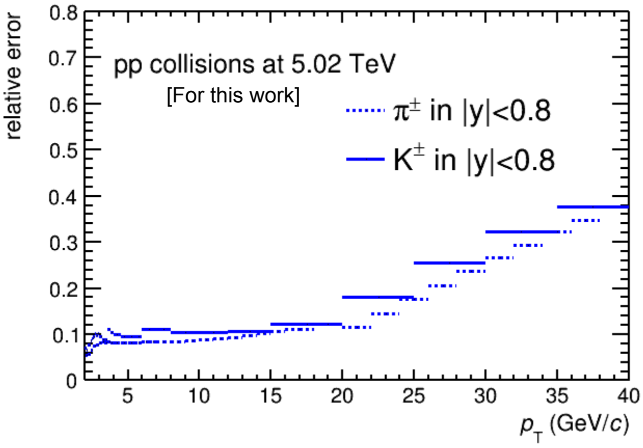

Figure 3.15: Systematic uncertainties of the extrapolated mid-rapidity charged π and K distributions.

PYTHIA 6 and PHOJET are fitted with the polynomial function $x^8 \cdot p_1 + x^6 \cdot p_2 + x^4 \cdot p_3 + x^2 \cdot p_4 + x \cdot p_5 + p_6$, as shown in Fig. 3.16. The corresponding ratio between the simulated rapidity distribution for charged π (K) from PYTHIA and PHOJET and the polynomial function is compatible with unity, as presented in Fig. 3.17.

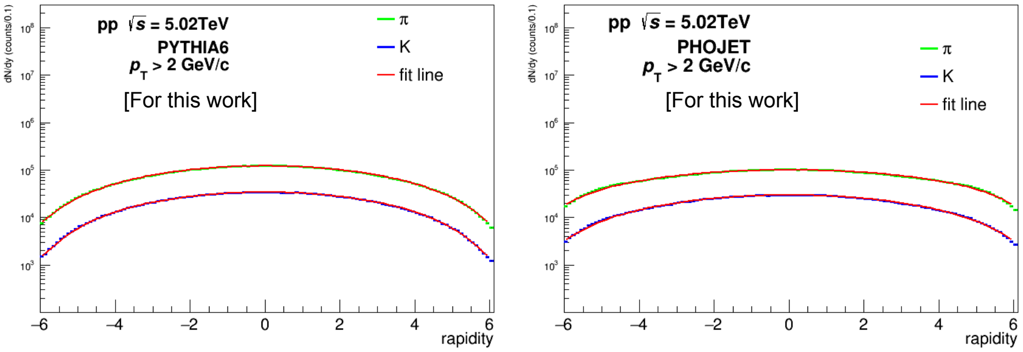

Figure 3.16: Rapidity distribution charged π and K with $p_T > 2$ GeV/c from PYTHIA (left) and PHOJET (right) and corresponding polynomial fit.

Moreover, a p_T-dependent extrapolation is introduced by applying a p_T-dependent correction to the polynomial fit of the rapidity distributions shown in Fig. 3.17. In that purpose, high statistics PYTHIA 8 simulations were performed in order to get the generated p_T distributions of charged π and K up to $p_T = 40$ GeV/c. The simulations were performed for various Colour Reconnection settings CR = 0 (MPI), 1 (new QCD), 2 (no colour reconnection) in order to estimate the systematic uncertainty on the p_T-dependent correction factors. The ratio of the p_T distribution of charged π and K in various y intervals relative to that at mid-rapidity

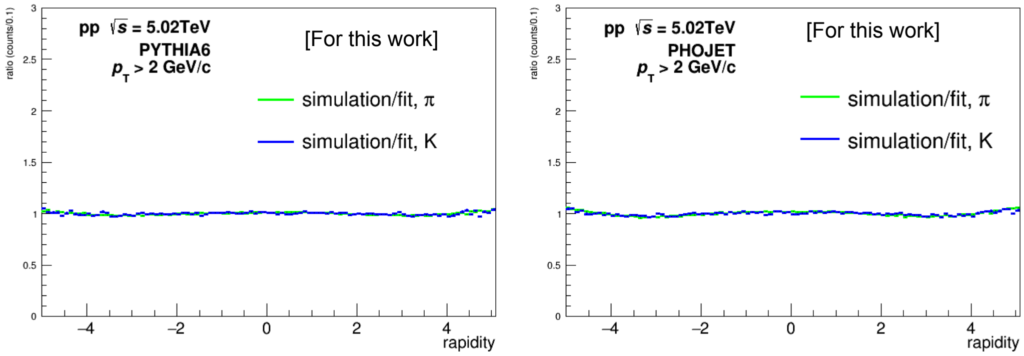

Figure 3.17: Ratio of the charged π and K rapidity distributions for $p_{\mathrm{T}} > 2$ GeV/c from PYTHIA (left) and PHOJET (right) to that obtained with the polynomial function.

($|y| < 0.8$), rescaled to the first p_{T} bin is displayed in Fig. 3.18. The p_{T} dependence of the ratio in the high p_{T} region, in particular, is confirmed and the effect is more pronounced for charged K than for charged π and increases with increasing rapidity.

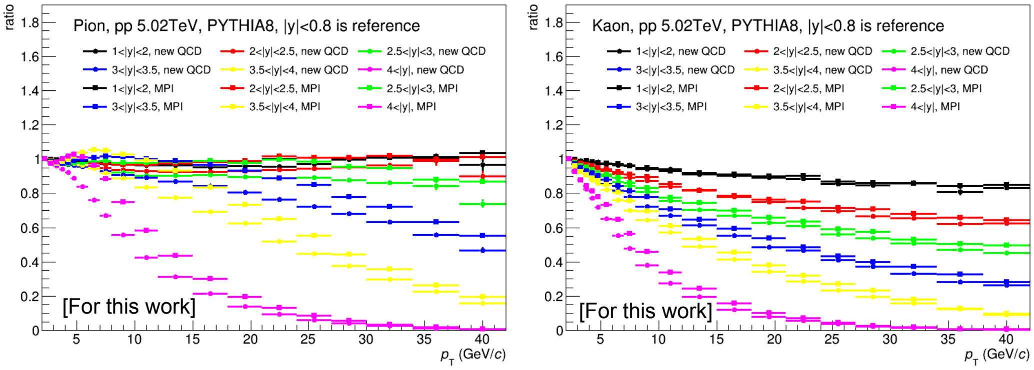

Figure 3.18: Rescaled ratio of the generated p_{T} distribution of charged π (left) and charged K (right) in different intervals relative to that within $|y| < 0.8$ from PYTHIA 8 simulations with various colour reconnection options.

However, it worth to mention that the evolution of the ratio with p_{T} could depend on model ingredients. Indeed, one can notice that, in $1 < |y| < 4$, the differences between colour reconnection options amount at most to about 10% and 20% for charged π and K, respectively (Fig. 3.19). The implementation of p_{T} extrapolation of charged pion and kaon spectra is also discussed in [179, 180].

c. Generation of muons from charged pion and kaon decays

As in all single muon analyses, in the last step, muons from charged pion and kaon decays are produced according to a fast simulation of decay kinematics and absorber effect. The needed inputs are the p_{T}- and y-extrapolated charged π and K distributions. The fast simulation procedure includes following steps: i) generate

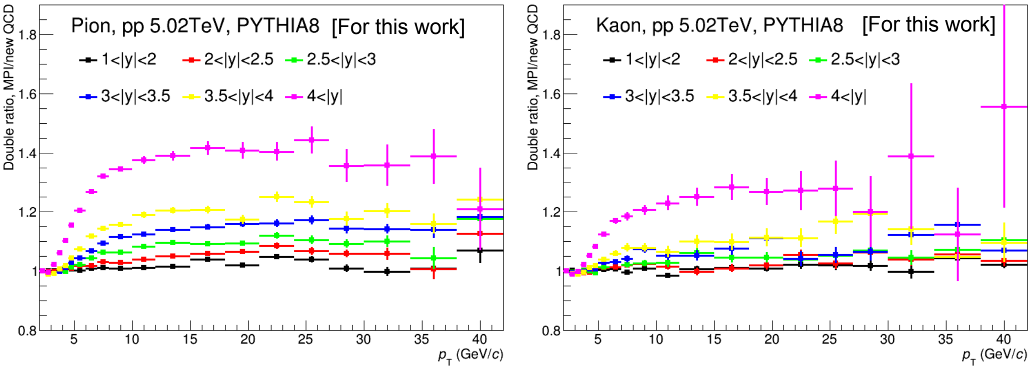

Figure 3.19: Double ratio of the ratio of the generated p_{T} distributio in a given rapidity interval to that in $|y| < 0.8$ for CR $= 0$ to the same ratio for CR $=1$ for charged π (left) and K (right).

charged π and K according to uniform p_{T} and y distributions to save CPU time, ii) force charged π and K to decay into muons using PYTHIA decayer, iii) consider the absorber effect and iv) weight the decay muon p_{T} and y distributions according to the p_{T}- and y-extrapolated charged π and K distributions. In previous analyses, the absorber effect was taken into account by considering only charged π and K which decay before reaching a distance corresponding to one interaction length in the absorber i.e. with a muon production point $z_{\mathrm{v}} < 130$ cm and a systematic uncertainty of 15%. For the present analysis, the description of the absorber effect in the fast simulations has been improved and will be used to extract the production cross sections of muons from heavy-flavour hadron decays (see description hereafter). These recent improvements on the absorber effect description in the fast simulations have been intensively discussed in [176, 177, 178, 179, 180]. Full simulations have shown that the sharp cut on z_v at 130 cm tends to underestimate the decay muon production but the results are still within the current 15% systematic uncertainty on absorber effect (see later). Fast simulations indicate that the relative production probability of charged π and K with $p_{\mathrm{T}} > 2$ GeV/c is proportional to the position of the production point z_{v} (figure 3.20).

The relative production probability for muons from pion and kaon decays with p_{T} (hadron) > 2 GeV/c (normalized to the bin content $-50 < z_{\mathrm{v}} < -10$ cm) from full realistic simulations performed with PYTHIA 6 and PHOJET are presented in Fig. 3.21. Muons from positive and negative pions and kaons have a similar relative production probability (left panel) and both PHOJET and PYTHIA simulations give same results within uncertainties (right panel).

Moreover, the results presented in Fig. 3.21 indicates that the decay vertex of muons from pion and kaon is parameterized with one or two exponentials depending on z_{v} value (Fig. 3.22). The fit function is written as

$$f(z_{\mathrm{v}}) = \exp(z_{\mathrm{v}}) \times f_{\mathrm{abs}}(z_{\mathrm{v}}), \tag{3.12}$$

with $f_{\mathrm{abs}}(z_{\mathrm{v}}) = 1$ and $f_{\mathrm{abs}}(z_{\mathrm{v}}) = \exp(z_{\mathrm{v}})$ if $z_{\mathrm{v}} \geq$ -90 cm (before the absorber)

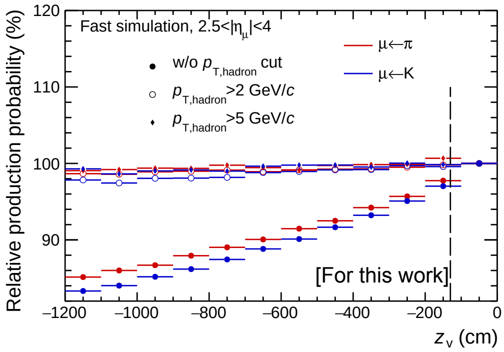

Figure 3.20: Relative production probability as a function of (z_{v}) in $2.5 < y < 4$ for charged decay π and K, and several p_{T} cuts mentioned in the figure.

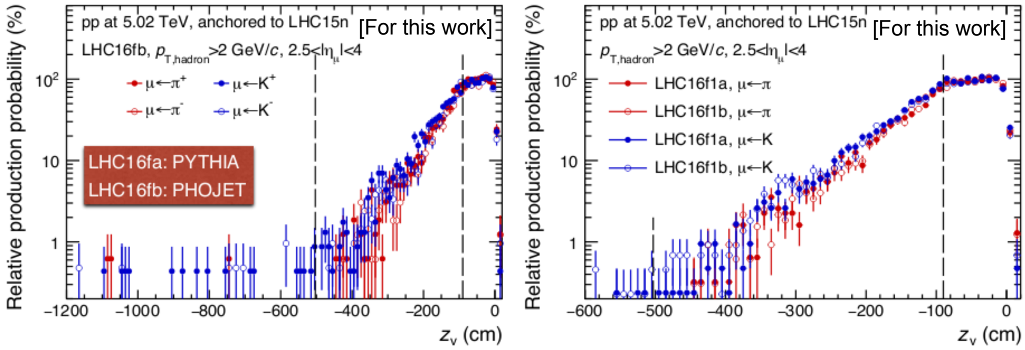

Figure 3.21: Relative production probability as a function of (z_{v}) in $2.5 < y < 4$ for muons from charged π and K with PHOJET (left) and comparisons between PYTHIA and PHOJET (right).

and $-503 < z_{\mathrm{v}} < 90$ cm (inside the front absorber), respectively. The first exponential represents the decay probability whereas the second corresponds to the hadron absorption probability. For smaller z_{v} values ($z_{\mathrm{v}} <$ -503 cm), the production probability is negligible (zero).

In order to validate this absorber parameterization, the p_{T} distributions of muons from charged π and K obtained with fast detector simulations have been compared with those from full simulations. The results were found in agreement within 1%–2% in $2.5 < y < 4$ and the deviations do not exceed 3% in various sub-rapidity intervals [179, 180]. Therefore, the updated systematic uncertainty on the absorber effect that will be considered amounts to about 4%. It is smaller than the one assigned with the strategy employed for run-1 analyses, the later being 15%.

Finally, we also compared in Fig. 3.23 the present strategy for the absorber effect description with the one where one considers only charged π and K that decay before reaching a distance corresponding to one interaction length in the absorber i.e. with a muon production point $z_{\mathrm{v}} < 130$ cm and a systematic uncertainty of

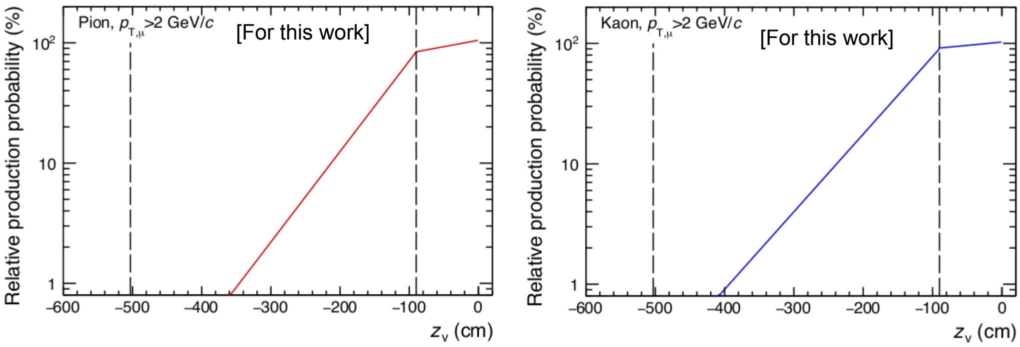

Figure 3.22: Parameterization of the relative production probability as a function of z_v in $2.5 < y < 4$ for charged π (left) and charged K (right) with $p_\mathrm{T} > 2$ GeV/c.

15%. Although the observed differences between the two methods are compatible within uncertainties, the production of muons from charged π (K) is enhanced by about 4% (15%) with the improved strategy.

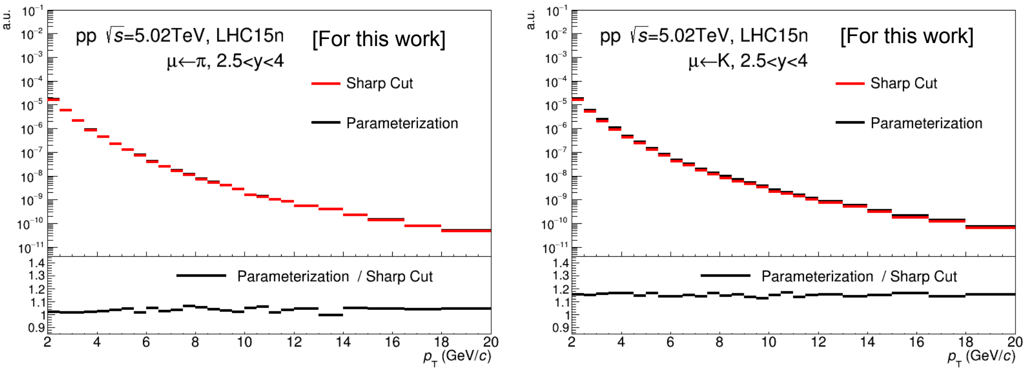

Figure 3.23: Comparison of the p_T distribution of muons from pion (left) and kaon (right) decays using a sharp cut on z_v and the parameterization for the description of the absorber effect in the fast simulations.

Figure 3.24 presents the effect of the rapidity extrapolation on the charged π and K p_T distribution with PYTHIA 6 and PHOJET. The uncertainty reaches about 9% and 6% for charged π and K, respectively. We also studied the effect of the p_T-dependent rapidity extrapolation. Figure 3.25 presents a comparison of the p_T distributions of muons from charged π and K decays in $2.5 < y < 4$, obtained using the two strategies for the rapidity extrapolation of the mid-rapidity p_T distributions towards forward rapidity e.g. without and with taking into account a p_T-dependent correction. As expected, the differences between the two methods increase with increasing p_T. The background contribution becomes smaller with the improved strategy for both the absorber effect description and the rapidity extrapolation, in particular at high p_T and for charged K. Indeed, the differences reach about 15% and

50% for charged π and K, respectively, in the high p_{T} region where this background source is small (few %, see background fraction results).

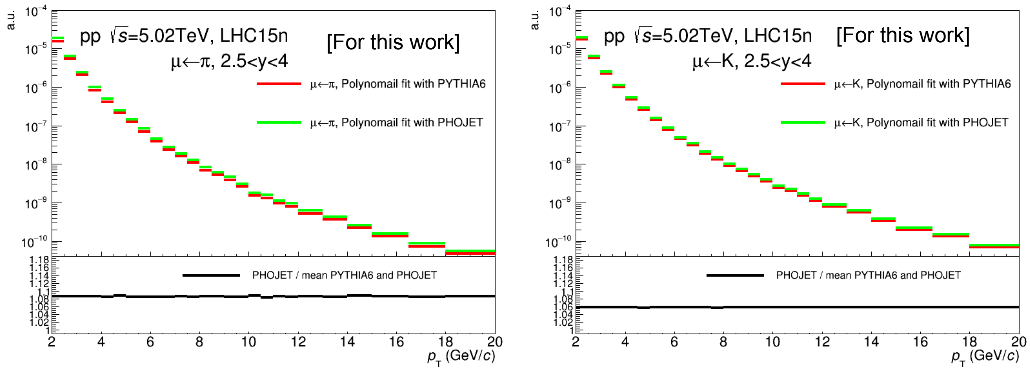

Figure 3.24: Comparison of the p_{T} distribution of muons from charged π (left) and charged K (right) obtained using the absorber effect parameterization and the polynomial function of the rapidity extrapolation.

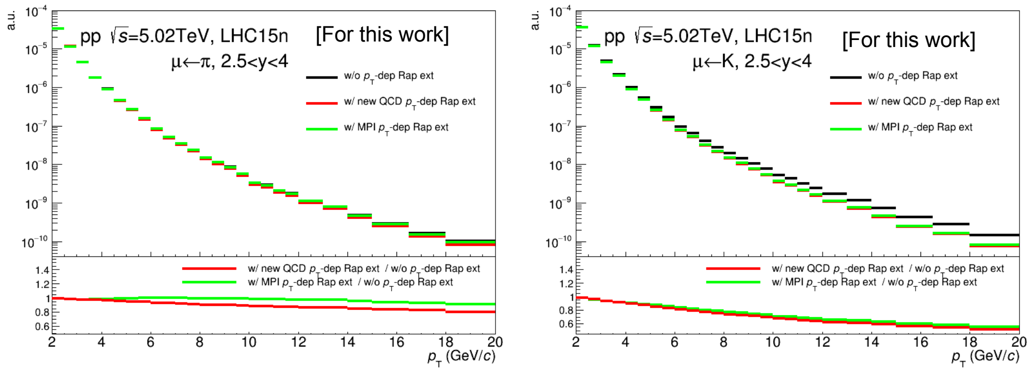

Figure 3.25: Comparison of the p_{T} distribution of muons from charged π (left) and charged K (right) obtained using the absorber effect parameterization and the two strategies for the rapidity extrapolation.

The final distributions of muons from charged π and K decays (Fig. 3.26) are obtained considering for the central value the mean between the results obtained with colour reconnection option CR = 0 and 1. The corresponding systematic uncertainty on models is derived from the difference with respect to the mean value (Fig. 3.26, bottom). This systematic uncertainty increases slightly with p_{T} and is in the range 0–5% (0–3%) for muons from charged π (K) decays.

Figure 3.27 shows the estimated p_{T} distribution for muons from charged pion decays (black) and muons from charged kaon decays (blue) in $2.5 < y < 4$ (left), as well the various systematic uncertainty sources (right). The systematic uncertainty sources affecting the produced muons from pion and kaon decays include

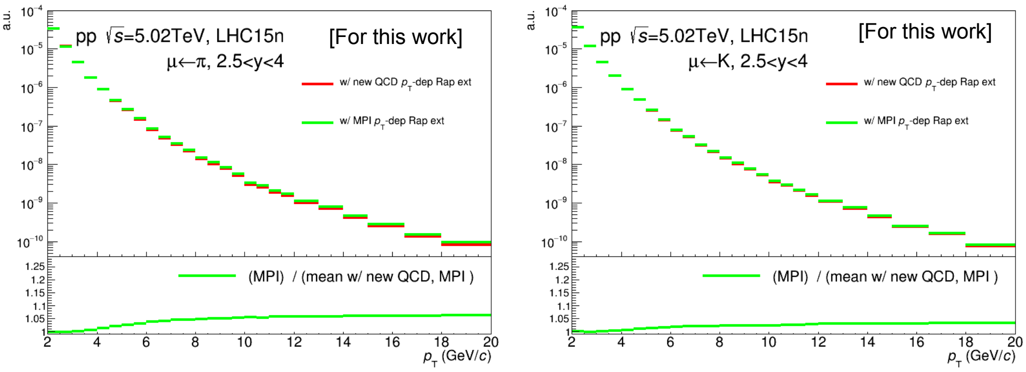

Figure 3.26: Comparison of the p_{T} distribution of muons from charged π (left) and K (right) using the new strategy for both absorber description and rapidity extrapolation and different model parameters.

contributions from i) the mid-rapidity charged π and K distributions and the p_{T} extrapolation to higher p_{T} (from about 7%–9% ($p_{\mathrm{T}} = 2$ GeV/c) to 21–22% ($p_{\mathrm{T}} = 20$ GeV/c), depending on the particle type, ii) the polynominal rapidity extrapolation (about 9% and 6% for muons from charged π and K decays) and the p_{T}-dependent correction (negligible for $p_{\mathrm{T}} < 4$ GeV/c and increasing uo to about 6% (3%) for muons from charged π (K) decays) and iii) the absorber effect (about 4%). The various sources are added in quadrature. This leads to systematic uncertainty in the range from about 11% ($p_{\mathrm{T}} = 2$ GeV/c) until 24% ($p_{\mathrm{T}} = 20$ GeV/c), before propagation to the final results e.g. the production cross section of muons from heavy-flavour hadron decays.

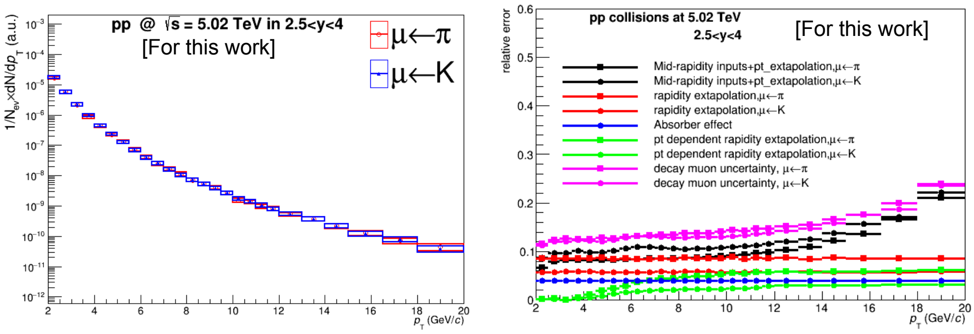

Figure 3.27: Estimated distributions of muons from charged pion and kaon decays (left) and associated systematic uncertainties (right) in $2.5 < y < 4$.

The fraction of muons from charged π decays and muons from charged K decays relative to inclusive muons as a function of p_{T} is shown in the bottom part of Fig. 3.28 (the upper part of the figure presents the various spectra). As expected, it decreases with increasing p_{T}. It varies from about 20% at $p_{\mathrm{T}} = 2$ GeV/c until 2–3%

at $p_{\rm T} = 20$ GeV/c. One can also notice that the fraction of muons from charged π decays and muons from charged K decays are similar.

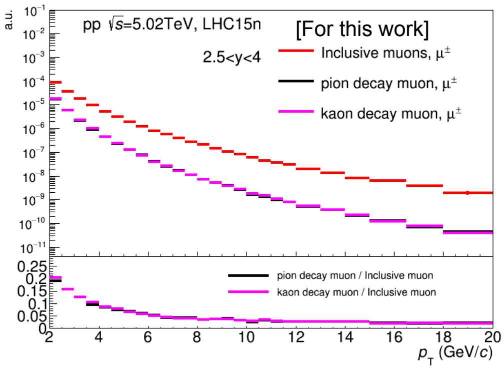

Figure 3.28: Estimated distributions of muons from charged pion and kaon decays and measured inclusive muon distributions (top), and associated fraction of muons from charged pion and kaon decays relative to inclusive muons (bottom) in $2.5 < y < 4$.

The contribution of muons from pion and kaon decays has been also estimated in the five sub-rapidity intervals in the range $2.5 < y < 4$ following the same procedure as in the full rapidity coverage. Figure 3.29 depicts the $p_{\rm T}$ distribution of muons from charged pion (kaon) decays and corresponding fraction with respect to inclusive muons in some of these rapidity bins e.g. $2.5 < y < 2.8$ (top, left), $3.1 < y < 3.4$ (top, right) and $3.7 < y < 4$ (bottom). The fraction of muons from charged π (K) decays exhibits a dependence on rapidity, in the low/intermediate $p_{\rm T}$ region, in particular. It is smaller for the most forward rapidity intervals. At $p_{\rm T} = 2$ GeV/c, it varies from about 24% for $2.5 < y < 2.8$ down to 12–13% for $3.7 < y < 4$ for both muons from charged π and K decays. At high $p_{\rm T}$, the fraction of muons from charged pion and kaon decays does not depend significantly on rapidity and amounts to about 2–3% at $p_{\rm T} = 20$ GeV/c.

Muons from secondary pion and kaon decays

The contribution of muons from secondary charged pion and kaon decays is estimated by means of simulations using PYTHIA 6.425 [183] and the GEANT3 transport code [184]. This contribution affects the low $p_{\rm T}$ region from $p_{\rm T} = 2$ GeV/c up to about $p_{\rm T} = 5$ GeV/c, only. The relative contribution with respect to inclusive muons decreases strongly with $p_{\rm T}$, from about 4% at $p_{\rm T} = 2$ GeV/c to become smaller than 1% at $p_{\rm T} = 5$ GeV/c. It also varies with rapidity, by decreasing down to about 2% in the interval $3.7 <$ y < 4.

Muons from W and Z/γ^* decays

The contribution of muons from W-boson and Z-boson/γ^* decays is estimated with simulations using the POWHEG NLO event paired with PYTHIA 6.425 for

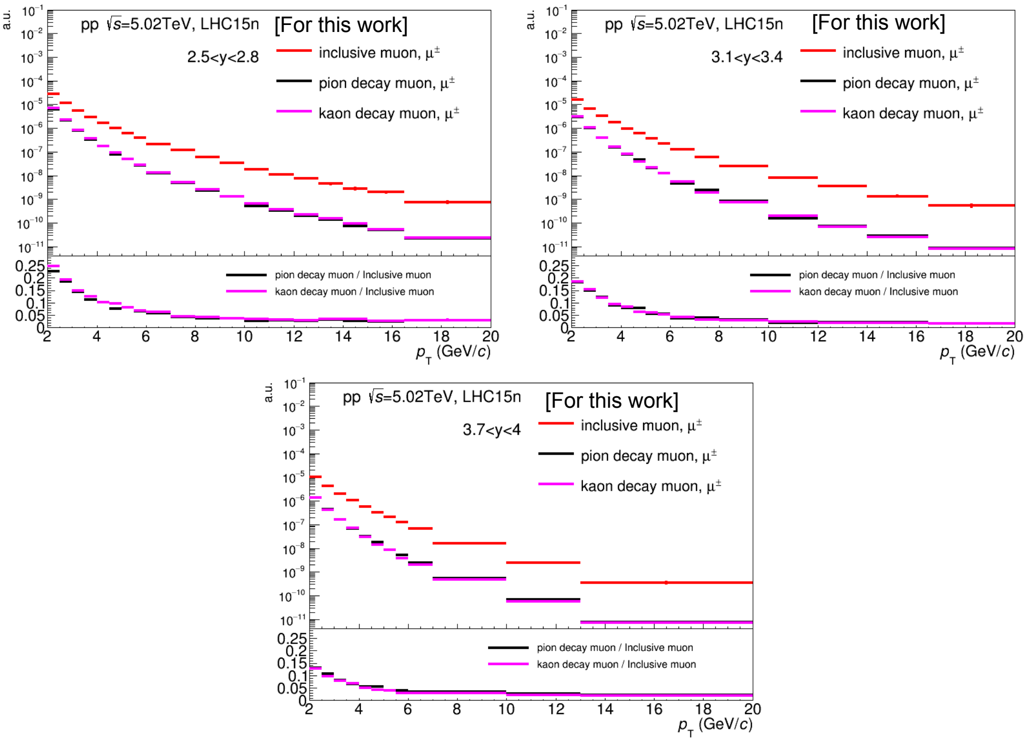

Figure 3.29: Estimated distributions of muons from charged pion and kaon decays and measured inclusive muon distributions, and associated fraction of muons from charged pion and kaon decays relative to inclusive muons for the rapidity intervals $2.5 < y < 2.8$ (top, left), $3.1 < y < 3.4$ (top, right) and $3.7 < y < 4$ (bottom).

parton shower. The calculations use the CT10 Parton Distribution Functions. The p_{T} and y distributions of $\mathrm{W}^{\pm}$ and Z/γ^{*} decay muons in the 4π acceptance and the corresponding p_{T} distribution in the muon spectrometer acceptance are displayed in Fig. 3.30, upper plots and bottom plot, respectively. One can notice that more muons from W^{+} decays than for W^{-} decays are produced in the mid-rapidity region, while an opposite trend is observed at forward rapidity. Also more muons from Z/γ^{*} decays than from $\mathrm{W}^{\pm}$ decays are produced at very large rapidities ($y > 4$). The contribution of Z/γ^{*} decay muons dominates in the low p_{T} region. At forward rapidity, in $2.5 < y < 4$, the yield of muons from W^{-} decays is larger than the one of muons from W^{+} decays, and Z/γ^{*} decay muons dominate over W-decay muons for $p_{\mathrm{T}} < 10$ GeV/c.

Figure 3.31 presents the fraction of W decay muons, Z/γ^{*} decay muons and $\mathrm{W}/\mathrm{Z}/\gamma^{*}$ decay muons with respect to muons from heavy-flavour hadron decays from FONLL (left) and of $\mathrm{W}/\mathrm{Z}/\gamma^{*}$ decay muons with respect to inclusive muons (right) as a function of p_{T} in $2.5 < y < 4$. The contribution of Z/γ^{*} decay muons is negligible over almost the whole p_{T} range and is smaller than 3% at $p_{\mathrm{T}} = 20$ GeV/c. The fraction of W-decay muons is negligible for $p_{\mathrm{T}} <$ 14–15 GeV/c and is about

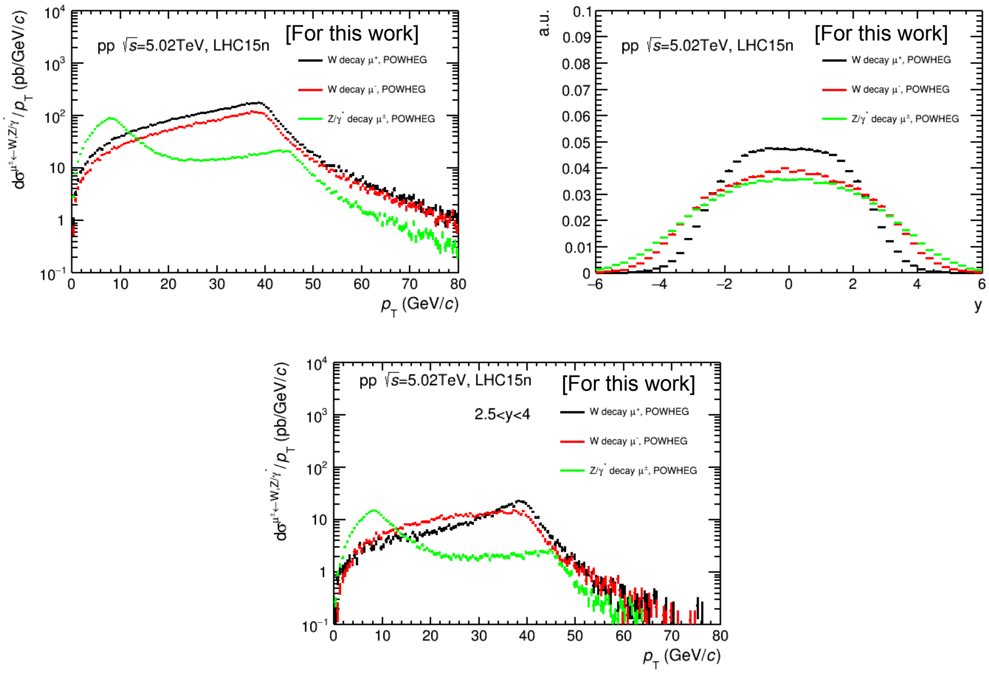

Figure 3.30: p_{T} (top, left) and y (top, right) distributions of $\mathrm{W}^{\pm}$ and Z/γ^{*} decay muons in the 4π acceptance and corresponding p_{T} distribution in $2.5 < y < 4$.

12% at $p_{\mathrm{T}} = 20$ GeV/c. The total contribution of $\mathrm{W}/\mathrm{Z}/\gamma^{*}$ decay muons relative to inclusive muons is negligible for $p_{\mathrm{T}} < 14$ GeV/c and amounts to about 12% in $18 < p_{\mathrm{T}} < 20$ GeV/c.

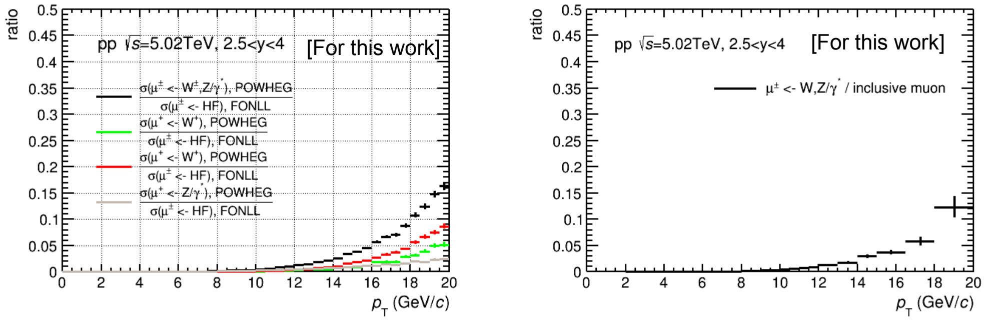

Figure 3.31: Fraction of muons from W and Z/γ^{*} decays as a function of p_{T} with respect to muons from heavy-flavour hadron decays from FONLL (left) and with respect to inclusive muons (right) in $2.5 < y < 4$.

The total contribution of $\mathrm{W}/\mathrm{Z}/\gamma^{*}$ decay muons with respect to inclusive muons has been also estimated in several sub-rapidity as shown in Fig. 3.32. The results indicate that this background fraction with respect to inclusive muons exhibits a dependence on rapidity when moving from $3.7 < y < 4$ towards $2.5 < y < 2.8$ (Fig. 3.32)[6]. In the interval $14 < p_{\rm T} < 20$ GeV/c aceessible in all sub-rapidity intervals, it varies within 3%–6%.

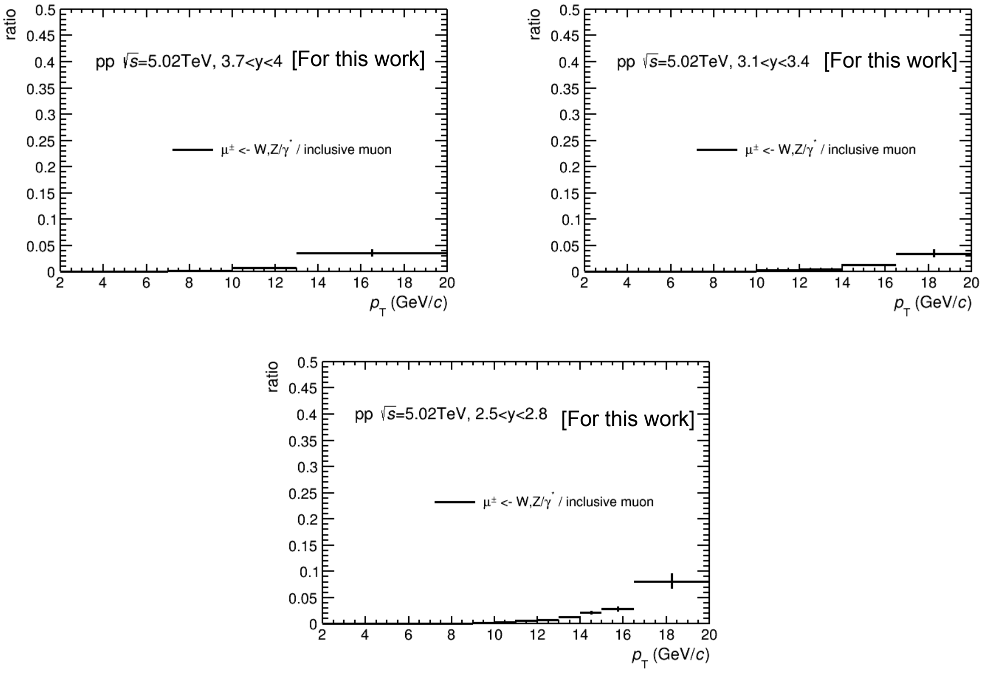

Figure 3.32: Fraction of muons from W/Z/γ^* decays as a function of $p_{\rm T}$ with respect to inclusive muons in three sub-rapidity intervals mentioned on the figures.

The $p_{\rm T}$-differential μ^-/μ^+ ratio before and after the subtraction of the W and Z/γ^* background contribution is displayed in Fig. 3.33. An asymmetry is clearly seen in the high $p_{\rm T}$ region before the subtraction of W/Z/γ^*-decay muons. After the subtraction of W/Z/γ^*-decay muons, the μ^-/μ^+ ratio is compatible with unity over the whole $p_{\rm T}$ region within uncertainties.

Since no measurement is yet available for pp collisions at $\sqrt{s} = 5.02$ TeV, the systematic uncertainty is estimated by including the CT10 PDF uncertainties. Also comparison with CTEQ6L PDF set were performed. This leads to a systematic uncertainty of about 8% (7%) for muons from W (Z/γ^*) decays. Note a similar systematic uncertainty was obtained when comparing the W production cross section from POWHEG with the existing measurement performed in the CMS Collaboration for pp collisions at $\sqrt{s} = 2.76$ TeV [206].

Muons from J/ψ decays

---

[6] Due to the limited statistics, for some rapidity intervals, the comparison is performed in $14 < p_{\rm T} < 20$ GeV/c, only.

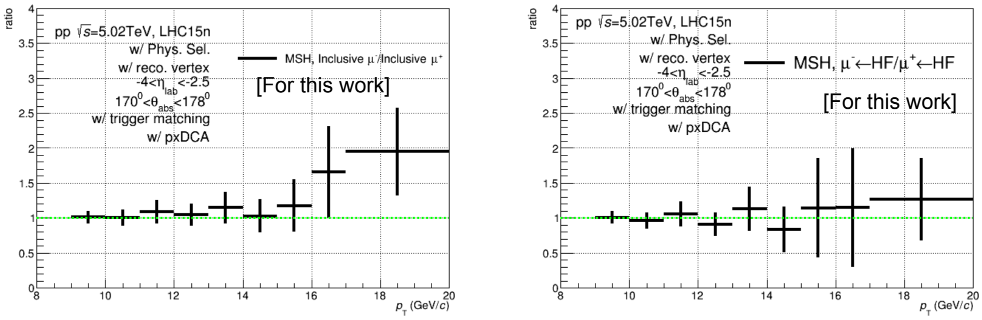

Figure 3.33: p_{T}-differential μ^{-}/μ^{+} ratio before (left) and after (right) the subtraction of muons from W and Z/γ^{*} decays in $2.5 < y < 4$.

The contribution of J/ψ decay muons to the inclusive muon p_{T} distribution is obtained using fast detector simulations. The needed inputs are the J/ψ p_{T} and y distributions measured at forward rapidity with ALICE [169] at $\sqrt{s} = 5.02$ TeV. An extrapolation of the rapidity distribution measured in $2.5 < y < 4$ to a wider acceptance is performed to avoid border effects. The used functions are a gaussian or $\mathrm{f}(y) = \mathrm{p}_0 \cdot (1 + \mathrm{p}_1 \cdot \mathrm{y}^2)$, p_0 and p_1 being the fit parameters. Moreover, the measured p_{T} distributions available until $p_{\mathrm{T}} = 12$ GeV/c are extrapolated to higher p_{T} using the function:

$$\mathrm{f}(p_{\mathrm{T}}) = C \frac{p_{\mathrm{T}}}{(1 + (p_{\mathrm{T}}/p_0)^2)^n}, \tag{3.13}$$

where p_0, C and n are free parameters. The extrapolation procedure is similar to that implemented for charged pions and kaons The uncertainty of the J/ψ p_{T} distribution ranges from about 5%-20% ($p_{\mathrm{T}} < 12$ GeV/c) until 30% ($p_{\mathrm{T}} < 20$ GeV/c). The uncertainty affecting the y distribution in $2.5 < y < 4$ varies within about 4.6%–8.6%, the largest value being considerd outside the muon spectrometer acceptance. The p_{T}- and y-extrapolated distributions shown in Fig. 3.34 are used to weight the output of fast detector simulations. Indeed, in these fast detector simulations, J/ψ are generated according to uniform p_{T} and y distributions, and are forced to decay in dimuons. Then the generated p_{T} and y distributions of muons from J/ψ decays are weighted according to the p_{T}- and y-extrapolated differential J/ψ cross sections and corrected for the branching ratio. The obtained p_{T} distribution of muons from J/ψ decays (green histogram) and corresponding systematic uncertainty are presented in upper left and right panels of Fig. 3.35, the derived fraction of muons from J/ψ decays with respect to inclusive muons being displayed in the bottom panel. The contribution of muons from J/ψ decays varies within about 1–4%, the maximum being at $p_{\mathrm{T}} \sim 4-6$ GeV/c. The systematic uncertainty on the estimation of muons from J/ψ decays ranges from about 10%–12% in $4 < p_{\mathrm{T}} < 6$ GeV/c and increases up to about 35% at $p_{\mathrm{T}} = 20$ GeV/c.

We also estimated the contribution of muons from J/ψ decays in different subrapidity intervals following the same strategy. The corresponding maximum fraction

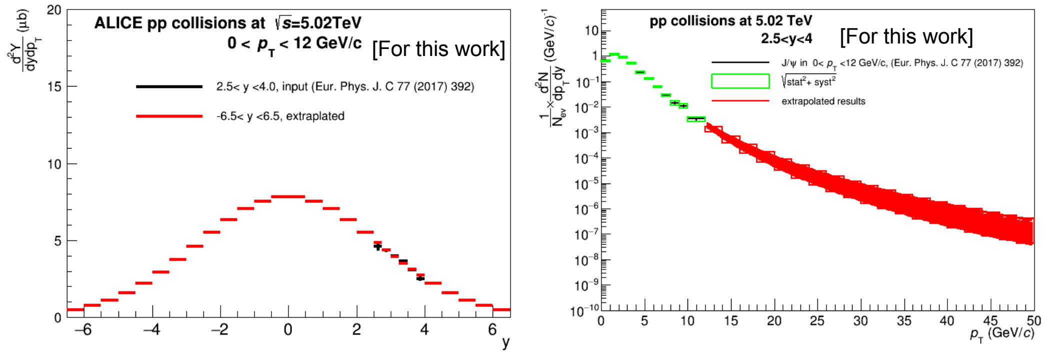

Figure 3.34: p_T- and y-differential production cross sections of J/ψ. The p_T and y distributions are measured by ALICE in $2.5 < y < 4$ and $p_T < 12$ GeV/c. Polynomial or Gaussian fits are used for the rapidity extrapolation.

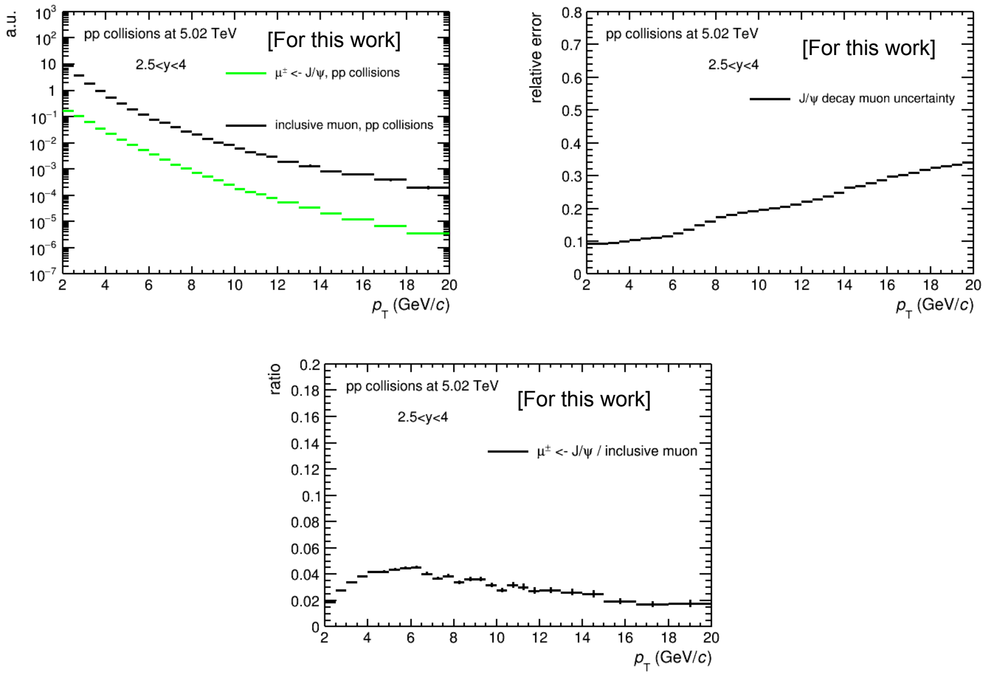

Figure 3.35: p_T distribution of muons from J/ψ decays (up, left) and corresponding systematic uncertainty (up, right), and fraction with respect to inclusive muons (bottom).

relative to inclusive muons at $p_T \simeq$ 4–6 GeV/c varies within about 4%–6%. Few examples of the J/ψ decay muon contamination are displayed in Fig. 3.36.

Figure 3.37 summarizes the estimated relative contribution of the various sources of background to the inclusive muon yield as a function of p_T for the rapidity interval $2.5 < \mathrm{y} < 4$. The vertical bars are the statistical uncertainties and the boxes are

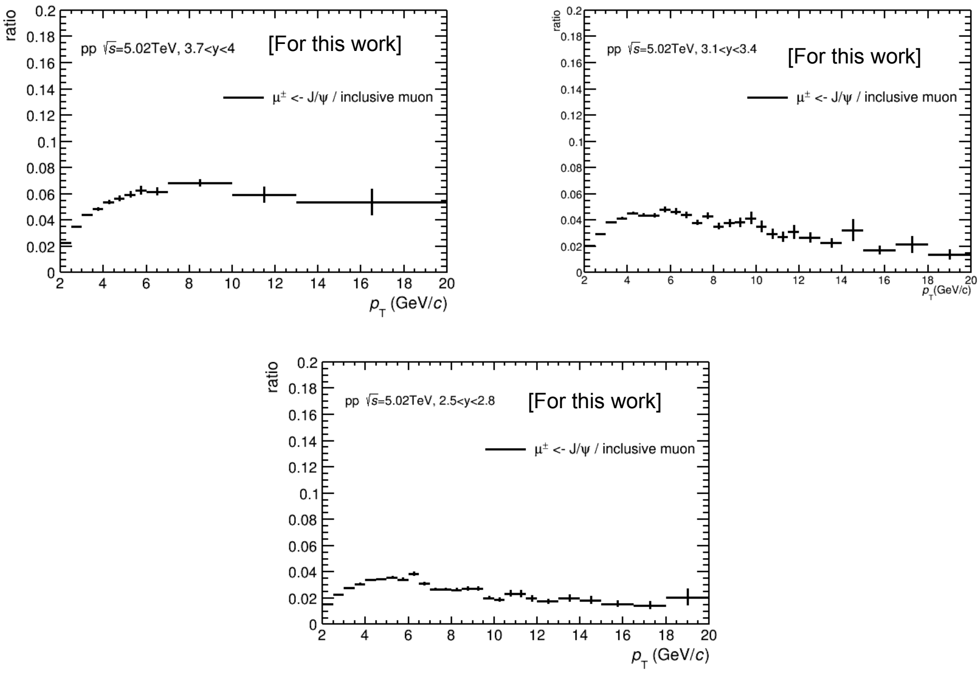

Figure 3.36: Fraction of muons from J/ψ decays with respect to inclusive muons as a function of p_{T} in various rapidity bins: $3.4 < y < 3.7$ (upper, left), $3.1 < y < 3.4$ (upper, right), $2.5 < y < 2.8$ (bottom).

the systematic uncertainties on inclusive muons and muon background sources.

3.1.5 Systematic uncertainty sources

Several sources of systematic uncertainty affecting the measurement of the p_{T}- and y-differential production cross section of muons from heavy-flavour hadron decays are evaluated. These are the systematic uncertainties on the inclusive muon yield, the estimated background sources (charged pion(kaon) decay muons, secondary charged pion(kaon) decay muons, W/Z/γ^* decay muons and J/ψ decay muons.) and the integrated luminosity.

Detector response

The systematic uncertainty on the inclusive muon yield contains the systematic uncertainty on the muon tracking efficiency and the systematic uncertainty associated with the muon trigger efficiency. A systematic uncertainty due to the efficiency of the matching between tracks reconstructed in the muon tracking chambers and trigger chambers needs also to be considered. A p_{T}-dependent systematic uncertainty is also assigned to take into account the track resolution and alignment.

The systematic uncertainty on muon tracking efficiency is estimated by comparing the single-muon tracking efficiency in data and simulation. The results discussed

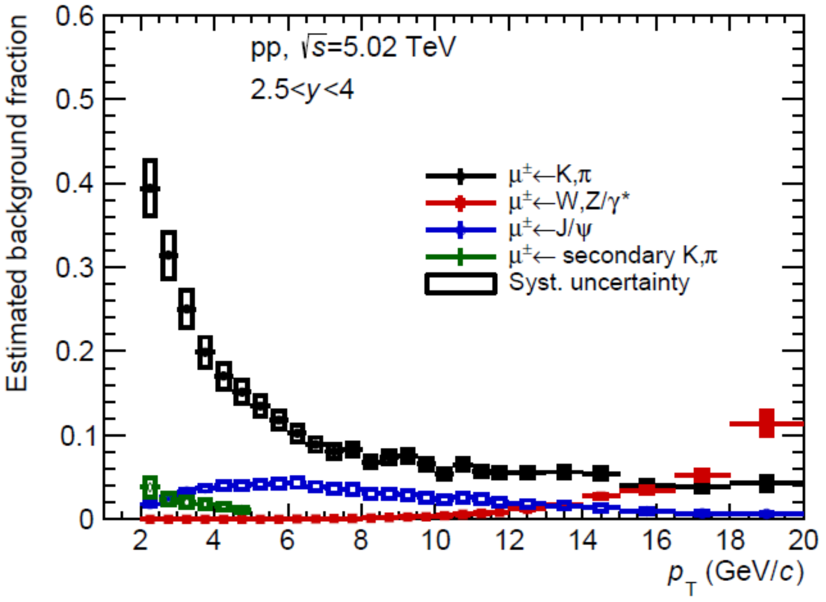

Figure 3.37: Estimated background fraction with respect to inclusive muons as a function of p_{T} for the interval $2.5 < y < 4$ in pp collisions at $\sqrt{s} = 5.02$ TeV. Statistical uncertainties (vertical bars) and systematic uncertainties (boxes) are shown.

in [169] and obtained for single muons, indicate that this systematic uncertainty amounts to 0.5% in average with variations depending on the kinematics, the maximum being always with 2–3σ. This systematic uncertainty is uncorrelated as a function of p_{T} and y. This systematic uncertainty is smaller than that obtained for the other periods [169]. This is due to the fact that the data taking period was short and consequently the detector conditions were more stable and easier to describe in the MC simulations.

The systematic uncertainty on muon trigger has two contributions: the trigger response and the intrinsic trigger chamber efficiency. The latter is determined by varying in simulation the efficiency of each local board by its uncertainty, and comparing the $A \times \varepsilon$ obtained with the default trigger efficiencies and modified ones for MSL and MSH. Full simulations using a parameterization of muons from heavy-flavour hadron decays from FONLL have been performed for this study. The extracted systematic uncertainty evaluated for both MSL and MSH is of the order of 1%, with almost no dependence on p_{T}. It is taken from the study done for Pb-Pb collisions, the differences in the efficiency maps being of same order of magnitude as the ones in Pb-Pb collisions.

In the standard procedure, the systematic uncertainty on the trigger response for MSL, with a p_{T}-trigger threshold of 1 GeV/c, is obtained from the ratio of the MSL single muon p_{T} distribution to the one obtained with the "All p_{T}" trigger cut e.g. with MB trigger, in data and in the simulation of pure signals. In the present analysis, the p_{T}-trigger threshold of MSL is about 0.5 GeV/c that is to say the same as the "All p_{T}" trigger cut. Therefore a new strategy has been implemented [169]. The MSL/All ratio where "All" corresponds to single muons selected without requiring matching with the trigger, is first evaluated with MC simulations. This ratio cannot be computed in the data due to hadronic contamination when the matching with the trigger is not required. Assuming that the trigger response per local board is independent of time and the relative difference between data and MC simulations is the same for a p_{T} trigger cut of 1 GeV/c and 0.5 GeV/c, the relative difference between MSL/"All p_{T}" in data and MC simulations is evaluated for Pb–Pb collisions where the low p_{T}-trigger threshold is 1 GeV/c. Then the trigger response for MSL in the pp data sample at $\sqrt{s} = 5.02$ TeV is:

$$\{\frac{\text{"All } p_{\mathrm{T}}\text{"}}{\text{All}}\}_{\text{pp−data}}(p_{\mathrm{T}}) = \{\frac{\text{"All } p_{\mathrm{T}}\text{"}}{\text{All}}\}_{\text{pp−MC}}(p_{\mathrm{T}}) \times \frac{\{\frac{\text{MSL}}{\text{"All } p_{\mathrm{T}}\text{"}}\}_{\text{PbPb−data}}(s \cdot p_{\mathrm{T}})}{\{\frac{\text{MSL}}{\text{"All } p_{\mathrm{T}}\text{"}}\}_{\text{PbPb−MC}}(s \cdot p_{\mathrm{T}})}, \tag{3.14}$$

the quantity s being given by

$$s = \frac{p_{\mathrm{T}}^{\text{cut}}]_{\text{PbPb−MC}}}{p_{\mathrm{T}}^{\text{cut}}]_{\text{pp−MC}}} \tag{3.15}$$

The $p_{\mathrm{T}}^{\text{cut}}$ is defined as the p_{T} value where the trigger response reaches half of the difference of its maximum and minimum. In the region $p_{\mathrm{T}} > 2$ GeV/c, this gives for MSL a systematic uncertainty close to 1%, with almost no dependence on p_{T} and y, in our region of interest.

For the systematic uncertainty on the MSH trigger response, the normalized and corrected (by $A \times \varepsilon$) p_{T} distributions obtained with MSL and MSH data samples have been compared. This leads to a systematic uncertainty close to 3% in the full rapidity range. The systematic uncertainty varies within 1.5%–3.5% as a function of y, the largest systematic uncertainty being for the region closer to mid-rapidity.

The systematic uncertainty on muon trigger-tracking is related to the choice of χ^2 cut used in defining the matching between the reconstructed tracks in the tracking chambers and the trigger tracklets [169]. This systematic uncertainty amounts to 0.5% for single muons and is considered as uncorrelated as a function of p_{T} and y.

The systematic uncertainty on tracking resolution and alignment was first evaluated by means of simulations using various mis-alignment files and comparing the p_{T}-differential distributions for μ^+, μ^- and $\mu^- + \mu^+$ with respect to the default realistic mis-alignment [7]. It was estimated for the Pb–Pb run which took place just after the pp run at $\sqrt{s} = 5.02$ TeV. Since there was no change in the alignment of the spectrometer between these two periods, the estimated systematic uncertainty of $0.5\% \times p_{\mathrm{T}}$ can be used (see [168]).

The evaluation of this systematic uncertainty has been recently improved by considering the track resolution and alignment. In that purpose, a data-driven method was developed, in which the simulation of the tracker response is based on a parameterisation of the measured resolution of the clusters associated to a track.

---

[7] alignment stored in "full" OCDB (Offline Conditions DataBase) at generation level and in "raw" OCDB in reconstruction level

The distribution of the difference between the cluster and the reconstructed track positions on each chamber is parameterised with an extended Crystal Ball function and used to simulate the smearing of the track parameters. The mis-alignment of the spectrometer leads to a shift of the reconstructed momentum going in opposite direction for μ^+ and μ^-. The effect of a global mis-alignment of the spectrometer is mimicked by shifting the distribution of the track deviation in the magnetic field in opposite directions for positive and negative tracks. The initial smearing parameters ($\sigma_{\text{shift}} = 0$) are tuned to reproduce the measured ratio of the μ^+ p_{T} distribution corrected for $A \times \varepsilon$ to that for μ^-. Figure 3.38 shows the result of the tuning of initial smearing parameters from the comparison of the measured μ^+/μ^- ratio corrected for $A \times \varepsilon$ to the same ratio with initial smearing parameters i.e. $\sigma_{\text{shift}} = 0$. The double ratio is compatible with unity within 1%, which indicates that the tuned smearing parameters reproduce the corrected measured μ^+/μ^- ratio.

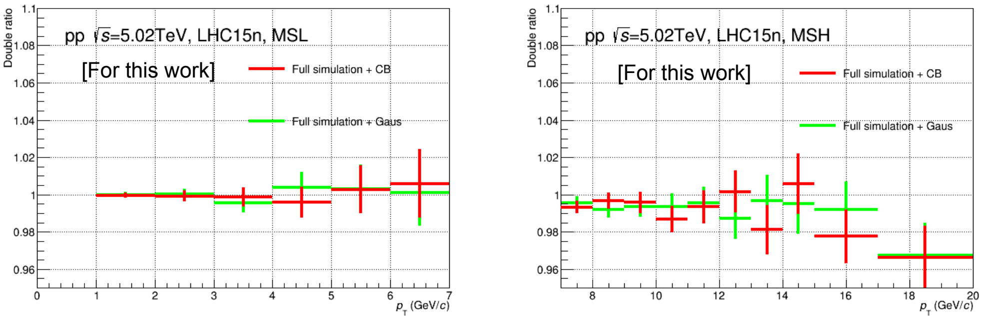

Figure 3.38: Corrected p_{T}-differential μ^+/μ^- ratio to the same ratio with $\sigma_{\text{shift}} = 0$ for MSL (left) and MSH (right) events.

Afterwards, the smearing parameter i.e. σ_{shift} was varied in order to recover the symmetry of the p_{T}-differential μ^+/μ^- ratio in the intermediate p_{T} region dominated by muons from heavy-flavour hadron decays as shown in 3.39. The results indicate that the optimized value corresponds to $\sigma_{\text{shift}} = 1.2$. Finally, the systematic uncertainty on track resolution and mis-alignment is obtained by comparing the corrected p_{T} distribution of muons from heavy-flavour hadron decays with $\sigma_{\text{shift}} = 0$ and $\sigma_{\text{shift}} = 1.2$. In the full acceptance, the corresponding systematic uncertainty is negligigle for $p_{\text{T}} < 7$ GeV/c and it increases with p_{T} to reach about 15% in the highest p_{T} bin (Fig. 3.40).

The systematic uncertainty on track resolution and mis-alignment has been studied also in different rapidity intervals (see figure 3.41). The variations observed in the highest p_{T} interval for the various rapidity intervals do not exceed 4% compared to the full acceptance ($2.5 < y < 4$). As a function of rapidity, from the most central interval ($2.5 < y < 2.8$) to the most forward one ($3.7 < y < 4$), one observes a small increase of the systematic uncertainty of about 8% in the highest p_{T} interval ($14 < p_{\text{T}} < 20$ GeV/c).

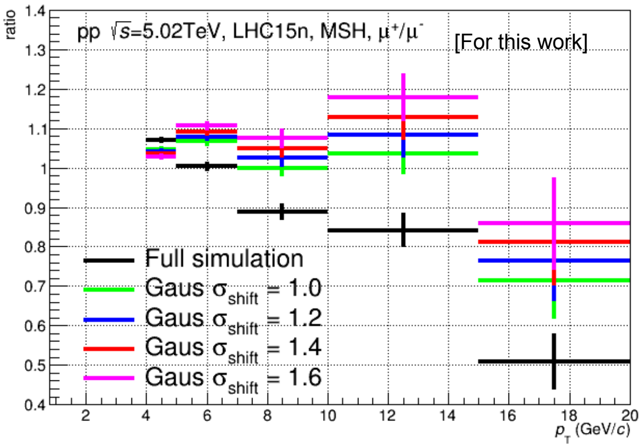

Figure 3.39: Ratio of the corrected p_{T}-differential μ^+/μ^- ratio with various σ_{shift} values.

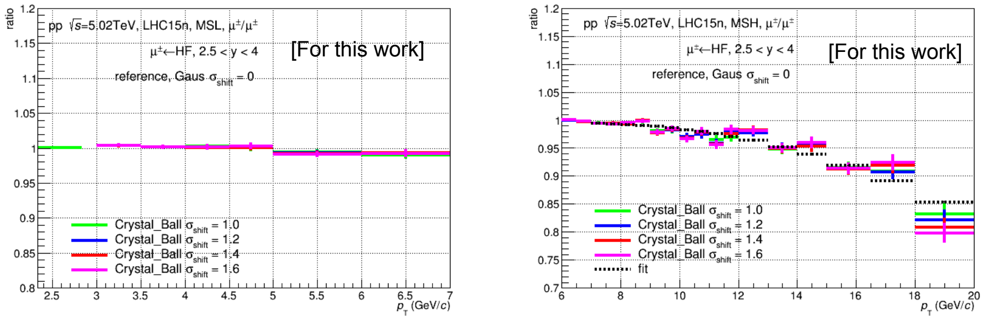

Figure 3.40: Ratio of the corrected p_{T}-differential distribution of muons from heavy-flavour hadron decays with $\sigma_{\mathrm{shift}} = 0$ to that with $\sigma_{\mathrm{shift}} = 1{,}2$ for MSL and MSH triggered events in left and right panel, respectively.

The normalization uncertainty discussed in Sec. 3.1.2 includes the systematic uncertainty on $\sigma_{\mathrm{VdM}}^{\mathrm{T0}}$ of 2.1%. This is a global systematic uncertainty that will be not be included in the systematic uncertainty boxes but mentioned in the legend of figures.

Table 3.5 summarizes the values of the various systematic uncertainty sources after propagation to the measurement of the production cross section of muons from heavy-flavour hadron decays in $2.5 < y < 4$. They are also displayed as a function of p_{T} in Fig. 3.42 for the full rapidity range.

The total systematic uncertainty in $2.5 < y < 4$ varies in the range 6-16% and is dominated by the systematic uncertainty on track resolution and alignment in the high-p_{T} region.

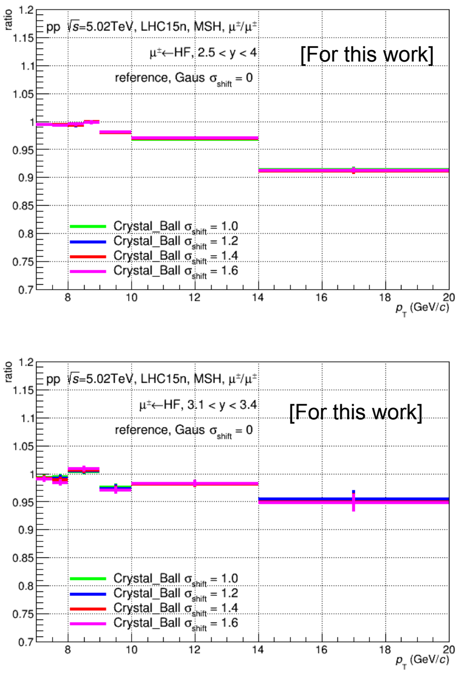

Figure 3.41: Ratio of the corrected p_{T}-differential distribution of muons from hevay-flavour hadron decays with $\sigma_{\mathrm{shift}} = 0$ to that with $\sigma_{\mathrm{shift}} = 1{,}2$ for MSH-triggered events in various rapidity intervals.

Sources	vs. p_{T}
Tracking efficiency	0.5%
Trigger efficiency	1.4% (MSL), 3.2% (MSH)
Matching efficiency	0.5%
Resolution and alignment	0–15% (negligible for $p_{\mathrm{T}} < 7$ GeV/c)
π (K) decay muons	1–4% (1–4%)
Secondary π, K decay muons	0–1.8%
W/Z/γ^* decay muons	0–1.1%
J/ψ decay muons	0–0.7%
$\sigma_{\mathrm{VdM}}^{\mathrm{T0}}$	2.1%

Table 3.5: Systematic uncertainties considered in the measurement of muons from heavy-flavour hadron decays in $2.5 < y < 4$

3.1.6 Results and model comparisons

In the following, we present the p_{T}- and y- differential production cross section of heavy-flavour hadron decay muons. The ratios of the production cross section between collision energies and rapidity regions are also discussed. All results are compared with the FONLL predictions. Moreover, in order to ensure that this comparison is done properly, the uncertainties on FONLL predictions should also

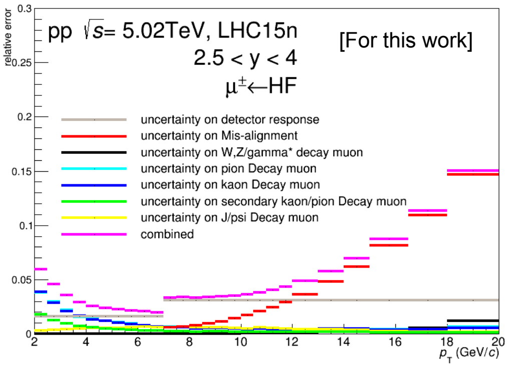

Figure 3.42: Systematic uncertainty sources as a function of p_{T} in the full range range ($2.5 < y < 4$).

be considered.

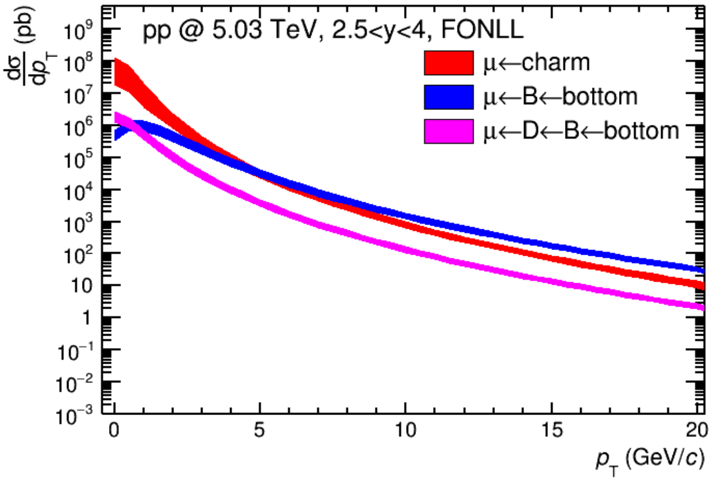

Figure 3.43: The production cross sections of muons from charm and beauty decays from FONLL predictions in $2.5 < y < 4$, in pp collisions at $\sqrt{s} = 5.03$ TeV.

Uncertainty propagation with FONLL predictions: uncertainty determination at muon level

By considering the fragmentation and semi-muonic decays with appropriate branching ratio, we get the p_{T}-differential production cross section at muon level for charm and beauty, as shown in Fig. 3.43.

There are three kinds of muon sources:

1. muons from charm quarks ($\mu \leftarrow D \leftarrow c$)
2. muons from beauty quarks ($\mu \leftarrow B \leftarrow b$)

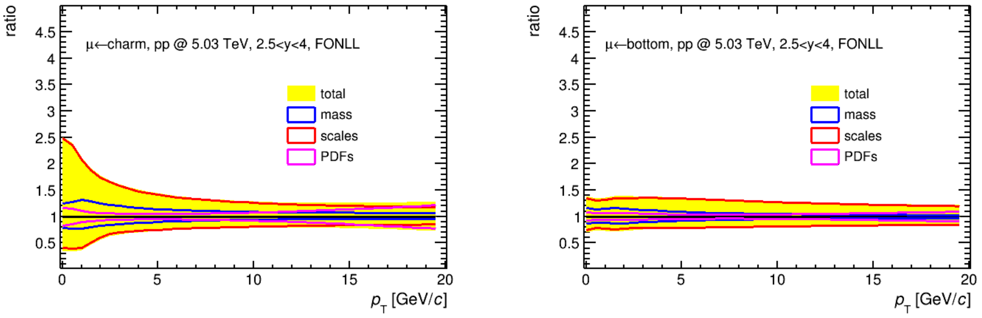

Figure 3.44: The rescaled ratios of production cross sections with respect to the central values for $\mu \leftarrow$ *charm* (left) and $\mu \leftarrow$ *bottom* (right) from FONLL predictions in $2.5 < y < 4$, in pp collisions at $\sqrt{s} = 5.03$ TeV.

3. muons from the indirect decay of beauty quarks ($\mu \leftarrow D \leftarrow B \leftarrow b$)

In order to simplify the description in this section, we named these three kinds of muons as charm μ, beauty μ and feed-down μ, respectively. The uncertainties at quark level should be propagated at the muon level and the additional uncertainty on the fragmentation process should also be included. Due to the hard fragmentation of heavy quarks, the uncertainty on the fragmentation with different kinds of fragmentation functions is very small, and by comparing with the other uncertainty sources it is negligible [186]. In this case, the results for different kinds of muons shown in Fig. 3.43 and Fig. 3.44 only include the same uncertainty sources at quark level.

For the comparison with data, we should add the production cross sections of these three kinds of muons together. The uncertainty on these three kinds of muon sources are not independent and cannot be propagated quadratically. The following steps are used [230] for the uncertainty propagation:

1. add the central values of the production cross section of these three kind of muons together to get the central value of the production cross section for muons from open heavy-flavour decays;

2. for both m_c and m_b one can choose three different values, this will give 9 kinds of combinations, the maximum and minimum differences between these 9 combinations and the central cross section value give the upper and lower uncertainties from the quark masses, $\sigma^{\max}_{\text{mass}}$ and $\sigma^{\min}_{\text{mass}}$;

3. one changes the QCD scales independently for muons from charm and those from beauty (the beauty μ and feed down μ) while keeping the other parameters unchanged, in order to estimate the upper and lower uncertainties from the QCD scales, $\sigma^{\max}_{\text{scales}}$ and $\sigma^{\min}_{\text{scales}}$. For each case, there are 7 combinations of μ_R and μ_F values which satisfy the conditions of $0.5\mu_0 < \mu_R, \mu_F < 2\mu_0, 0.5 <$

$\mu_{\rm R}/\mu_{\rm F} < 2$:

$$\begin{aligned}\mu_{\rm R} = \mu_0, &\quad \mu_{\rm F} = \mu_0,\\ \mu_{\rm R} = 0.5\mu_0, &\quad \mu_{\rm F} = 0.5\mu_0,\\ \mu_{\rm R} = 2\mu_0, &\quad \mu_{\rm F} = 2\mu_0,\\ \mu_{\rm R} = 2\mu_0, &\quad \mu_{\rm F} = \mu_0,\\ \mu_{\rm R} = \mu_0, &\quad \mu_{\rm F} = 2\mu_0,\\ \mu_{\rm R} = \mu_0, &\quad \mu_{\rm F} = 0.5\mu_0,\\ \mu_{\rm R} = 0.5\mu_0, &\quad \mu_{\rm F} = \mu_0.\end{aligned} \tag{3.16}$$

Finally by combining the charm and beauty together, we can get a total of 49 combinations for the QCD scales by mixing the QCD scales;

4. the upper and lower uncertainties from PDFs, $\sigma^{\rm max}_{\rm PDFs}$ and $\sigma^{\rm min}_{\rm PDFs}$, are propagated quadratically.

After all above steps, the upper and lower uncertainties on the production cross sections of muons from heavy-flavour decays are obtained by adding quadratically the corresponding uncertainties on quark masses, QCD scales and PDFs, as shown in Fig. 3.44.

Results and model comparisons

Figure 3.45 presents the $p_{\rm T}$-differential production cross section of muons from heavy-flavour hadron decays in the whole acceptance of the muon spectrometer ($2.5 < y < 4$). Vertical bars (smaller than the symbols) and open boxes are the statistical uncertainties and systematic uncertainties. The latter include all systematic uncertainty sources except the global systematic uncertainty on normalization. The $p_{\rm T}$-differential production cross sections of muons from heavy-flavour hadron decays is measured with high precision over a wide $p_{\rm T}$ interval, from $p_{\rm T}$ = 2 GeV/c up to $p_{\rm T}$ = 20 GeV/c. A higher precision both on statistical and systematic sides is reached, compared to similar analyses performed at $\sqrt{s}$ = 2.76 and 7 TeV with run-1 data [182, 175], the range of improvement factor is 2.2-3.5. These improvements have different sources: i) better understanding of the detector response (alignment and absorber effect, in particular) , ii) more data-driven strategy for the estimation of the contribution of muons from light-hadron decays, iii) refinements in the estimation of some uncertainty sources and iv) larger integrated luminosity and use of both MSL and MSH triggers. The results are compared with FONLL predictions [185] (black curve for the central values and shaded band for the systematic uncertainty. The theoretical uncertainties correspond to uncertainties on quark masses, QCD scales and PDFs. The uncertainty band is the envelope of the resulting cross sections. The ratio data/FONLL is shown in the bottom panel. The data are well described by FONLL calculations within uncertainties, although at the upper limit of model calculations, in particular at low and intermediate $p_{\rm T}$.

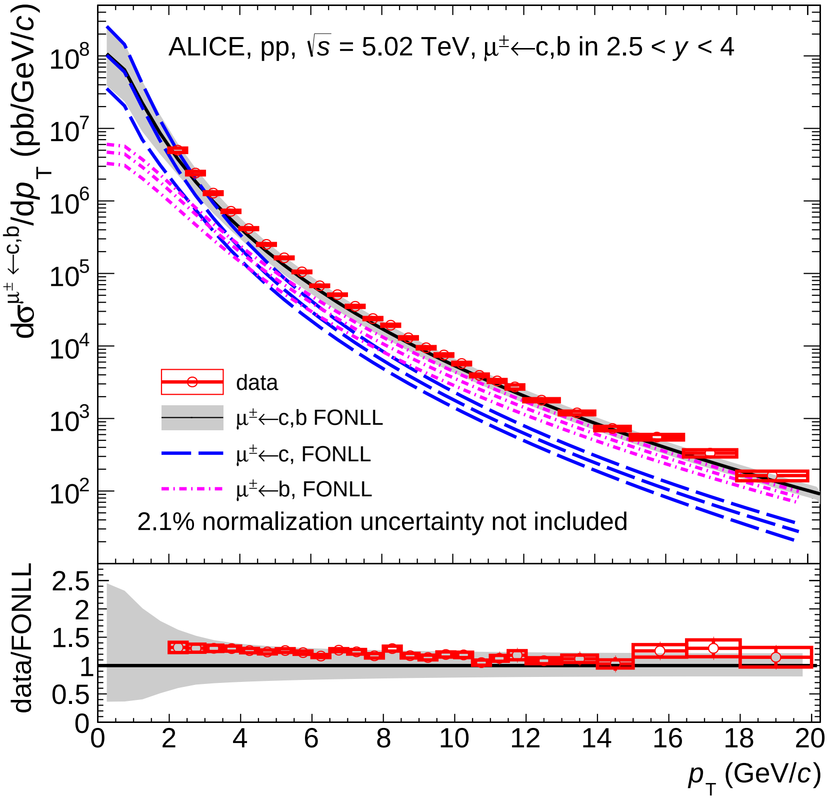

Figure 3.45: p_{T}-differential cross sections of muons from heavy-flavour hadron decays in $2.5 < y < 4$ compared with FONLL calculations.

The p_{T}-differential production cross section of muons from heavy-flavour hadron decays using the 2015 pp data sample at $\sqrt{s} = 5.02$ TeV has been compared with the one used for the computation of the R_{AA} results at $\sqrt{s_{\mathrm{NN}}} = 5.02$ TeV approved as preliminary by ALICE [168]. The latter was based on the measured p_{T}-differential production cross section of muons from heavy-flavour hadron decays in $2 < p_{\mathrm{T}} < 12$ GeV/c at $\sqrt{s} = 7$ TeV scaled to $\sqrt{s} = 5.02$ TeV according to FONLL predictions. At higher p_{T}, the FONLL predictions were scaled according to the ratio between FONLL and the pp reference in $p_{\mathrm{T}} < 12$ GeV/c. The comparison presented in Fig. 3.46 indicates the two pp references are compatible within uncertainties. However, the precision of the measurement obtained by using the run-2 data is improved (see also Fig. 3.42 and Fig. 3.47) and we use this reference for the computation of the final R_{AA} results in Pb-Pb and Xe-Xe collisions.

The p_{T}-integrated cross section of muons from heavy-flavour hadron decays has been studied as a function of y for two p_{T} intervals $2 < p_{\mathrm{T}} < 7$ GeV/c (Fig. 3.48, left) and $7 < p_{\mathrm{T}} < 20$ GeV/c (Fig. 3.48, right). The data are in agreement with FONLL predictions within uncertainties. However, in the high p_{T} region ($7 < p_{\mathrm{T}} < 20$ GeV/c) where the beauty contribution dominates over the charm

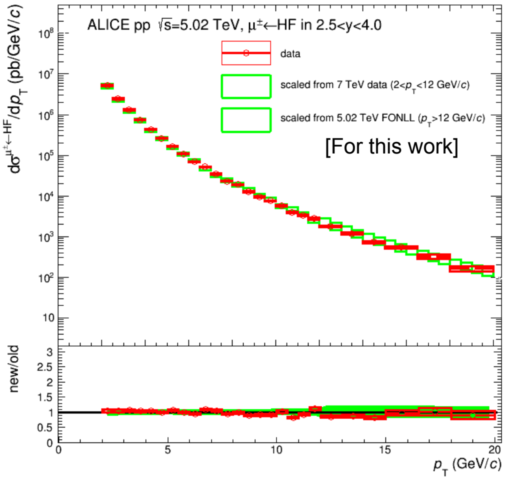

Figure 3.46: Comparison of the p_T-differential cross sections of muons from heavy-flavour hadron decays measured with the 2015 pp sample and using both pp data at $\sqrt{s}$ = 7 TeV and FONLL predictions.

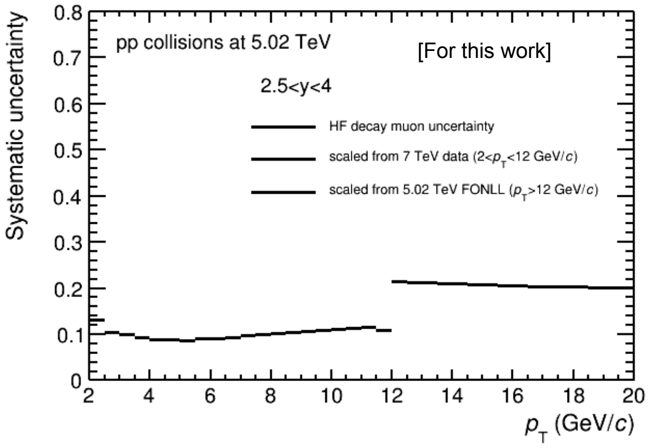

Figure 3.47: Systematic uncertainty on the p_T-differential cross section of muons from heavy-flavour hadron decays using both pp data at $\sqrt{s}$ = 7 TeV and FONLL predictions.

contribution[8], the agreement between data and FONLL is slightly better since the ratio data/FONLL varies between 1.1 and 1.3, depending on rapidity (the ratio is in the range 1.3–1.5 in the interval $2 < p_\mathrm{T} < 7$ GeV/c).

---

[8] According to FONLL predictions, in the high p_T region ($7 < p_\mathrm{T} < 20$ GeV/c), the beauty contribution represents about 70% of the muon yield of charm and beauty decays

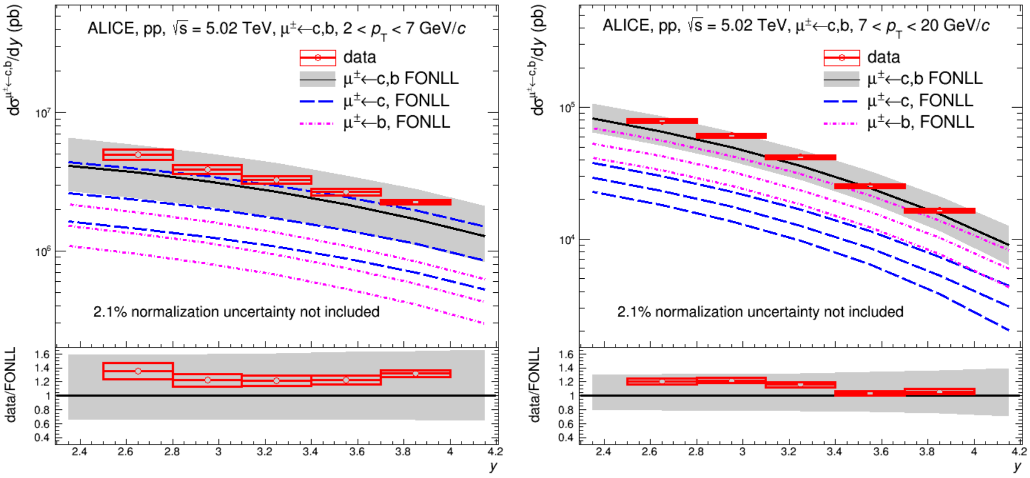

Figure 3.48: Production cross section of muons from heavy-flavour hadron decays as a function of rapidity for the p_{T} intervals $2 < p_{\mathrm{T}} < 7$ GeV/c (left) and $7 < p_{\mathrm{T}} < 20$ GeV/c (right), and comparisons with FONLL calculations. The plots in the bottom part of the figures show the data/FONLL ratio.

The p_{T}-differential production cross section of muons from heavy-flavour hadron decays is also measured in five sub-rapidity intervals in the range $2.5 < y < 4$ as shown in Fig. 3.49 and the ratio between data and FONLL is presented in Fig. 3.50. The FONLL calculations provide a overall good description of the data up to $p_{\mathrm{T}} = 20$ GeV/c, in all rapidity intervals within experimental and theoretical uncertainties. The values are systematically larger than the central values of the model calculations at low/intermediate p_{T} by a factor of about 1.5 with a decreasing trend as p_{T} increases.

Finally, similar agreement with FONLL calculations was also reported with the measurements of muons from heavy-flavour hadron decays performed in pp collisions at $\sqrt{s} = 2.76$ and 7 TeV [175, 182] and recently at $\sqrt{s} = 8$ TeV, as well as with D mesons and electrons from heavy-flavour hadron decays at mid-rapidity [187, 188, 189, 190, 191, 192].

The ratio of open heavy-flavour production cross sections between centre-of-mass energies and rapidity regions was presented as a powerful observable for sensitive tests of pQCD-based calculations and to constrain gluon PDF at forward rapidity [193]. While the absolute production cross sections as predicted by FONLL are associated with large systematic uncertainties, dominated by the scale uncertainties, the ratios of production cross sections at different centre-of-mass energies are predicted with a good accuracy [193]. Indeed, the predicted ratio is computed assuming the systematic uncertainties correlated between the two centre-of-mass energies. The ratio of the measured p_{T}-differential cross section of muons from heavy-flavour hadron decays for pp collisions at $\sqrt{s} = 7$ TeV to that at $\sqrt{s} = 5.02$ TeV in the rapidity interval $2.5 < y < 4$ is reported in Fig. 3.51. The systematic

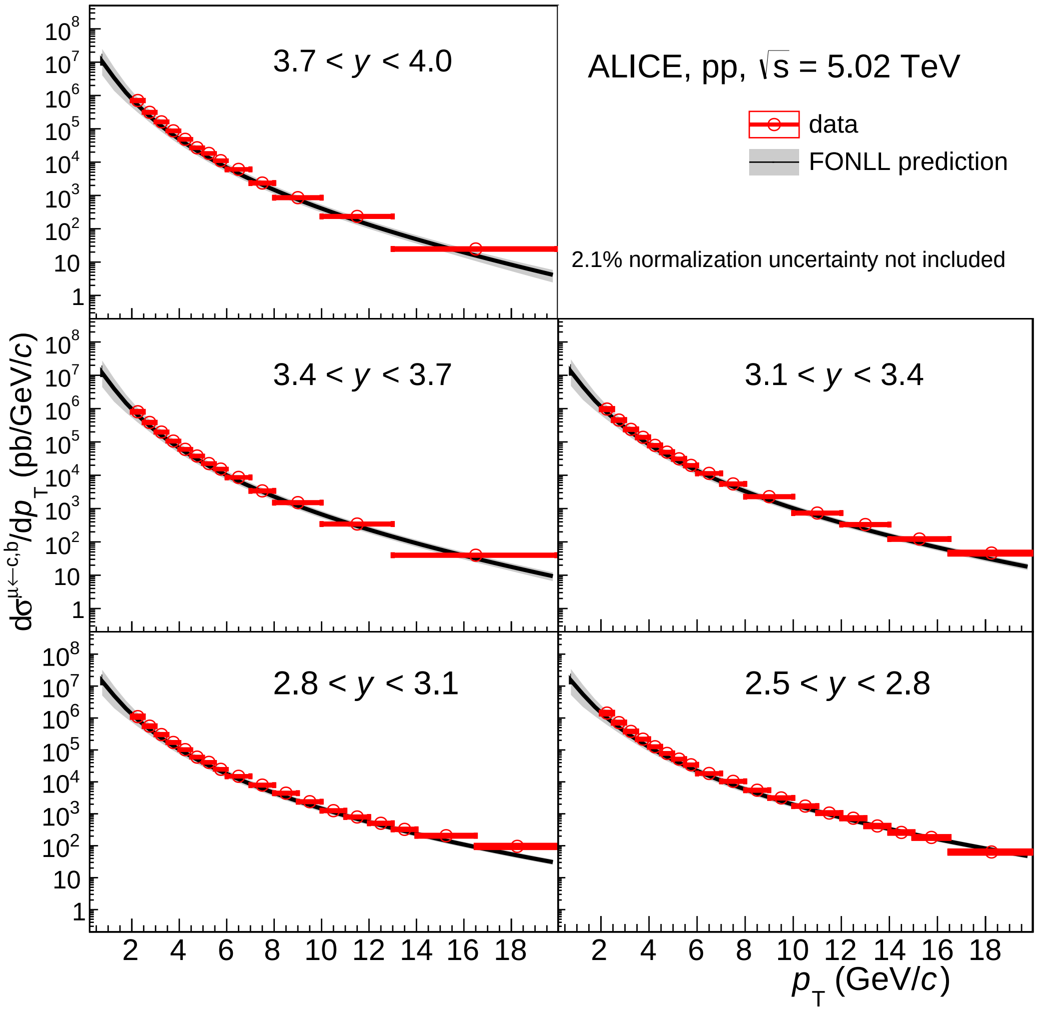

Figure 3.49: Production cross section of muons from heavy-flavour hadron decays as a function of p_{T} for five rapidity intervals within $2.5 < y < 4$ and comparisons with FONLL calculations.

uncertainties between the two measurements are considered as uncorrelated when forming the ratio and the main contribution comes from the measurement at $\sqrt{s}$ = 7 TeV. The ratio exhibits a smooth increase with increasing p_{T} from about 1.5 (p_{T} = 2 GeV/c) until 2 (p_{T} = 12 GeV/c). The measured ratio is well reproduced by FONLL calculations.

The ratio of the p_{T}-differential cross section of muons from heavy-flavour hadron decays between the two extreme rapidity intervals is presented in Fig. 3.52, which is also a powerful observable to test pQCD calculations [193]. When forming the ratio, the systematic uncertainties on tracking efficiency, trigger efficiency and tracking-trigger matching are considered as correlated, while the systematic uncertainty on track resolution and alignment is partially correlated. The other sources of system-

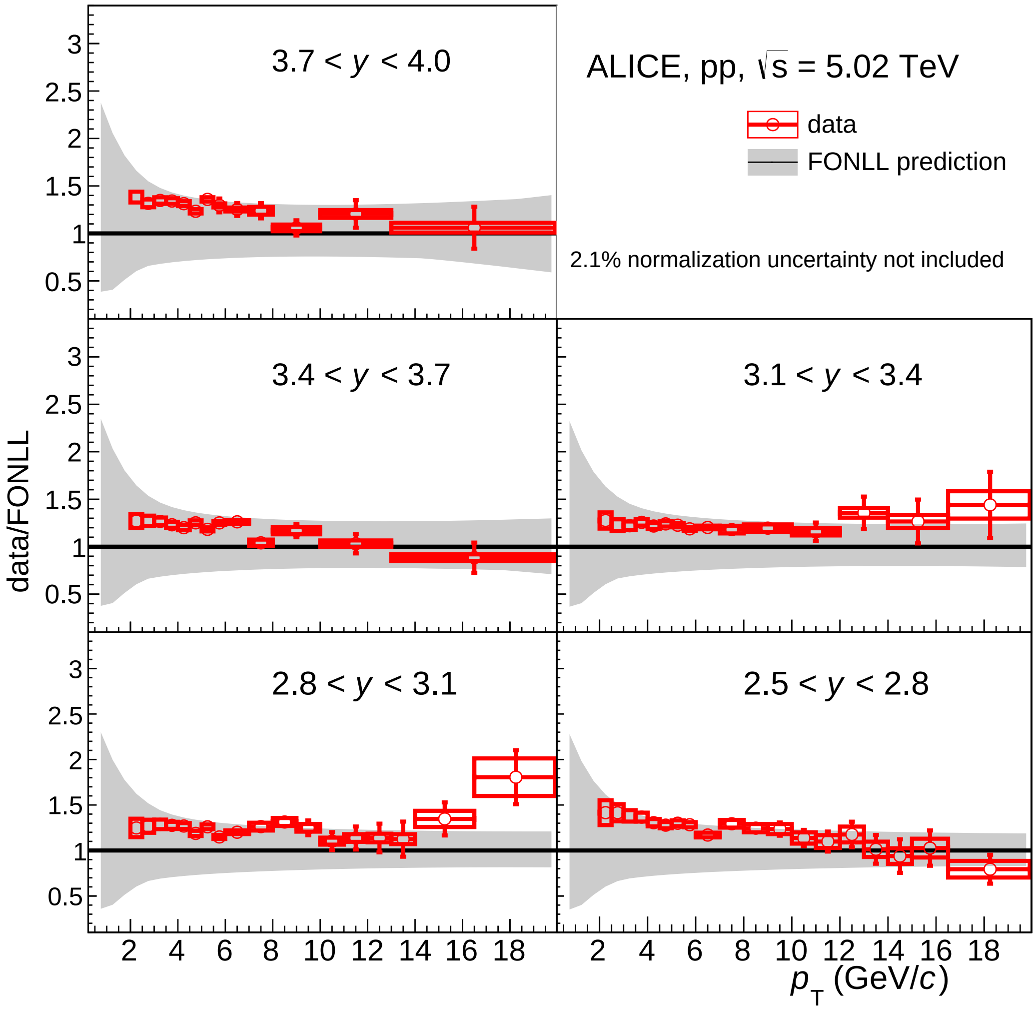

Figure 3.50: Data/FONLL ratios as a function of p_{T} for the five rapidity intervals within $2.5 < y < 4$.

atic uncertainties are treated as uncorrelated. The ratio decreases significantly with increasing p_{T} from about 0.49 down to 0.15. The measured ratio is compared with FONLL predictions which describe well the data within their uncertainties.

3.1.7 Conclusion

We have presented new measurements of the p_{T}- and y-differential production cross section of muons from heavy-flavour hadron decays at forward rapidity ($2.5 < y < 4$) in pp collisions at a centre-of-mass energy $\sqrt{s} = 5.02$ TeV over a significantly extended p_{T} range ($2 < p_{\mathrm{T}} < 20$ GeV/c) and with reduced uncertainties, compared to published results at $\sqrt{s} = 2.76$ and 7 TeV. The p_{T}- and y-differential production cross sections are described within uncertainties by the FONLL calculations. These

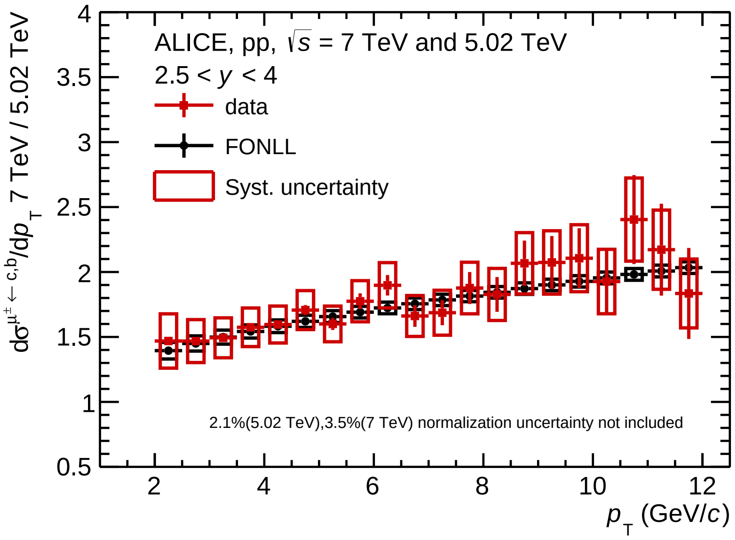

Figure 3.51: Ratio of the p_{T}-differential production cross section of muons from heavy-flavour hadron decays at forward rapidity in pp collisions at $\sqrt{s} = 7$ TeV to that at $\sqrt{s} = 5.02$ TeV. Statistical uncertainties (bars) and systematic uncertainties (boxes) are shown. The uncertainties on luminosity at the two centre-of mass energies are not included. The ratio is compared with FONLL predictions.

measurements will represent an essential reference for the study of effects induced by the hot strongly-interacting medium created in Pb-Pb collisions at $\sqrt{s_{\mathrm{NN}}} = 5.02$ TeV. Moreover, they bring new constraints on ingredients of pQCD-based calculations.

3.2 pp reference at $\sqrt{s} = 5.44$ TeV: energy scaling method

In order to calculate the nuclear modification factor of muons from heavy flavour decays in Xe-Xe collisions at $\sqrt{s_{\mathrm{NN}}} = 5.44$ TeV, one needs the pp reference at the same center-of -mass energy. As it will be discussed in the following, this is done by scaling with FONLL the measured p_{T}-differential cross section of muons from heavy flavour hadron decay in pp collisions at $\sqrt{s} = 5.02$ TeV.

3.2.1 Energy scaling factor

In order to obtain the reference cross section at $\sqrt{s} = 5.44$ TeV, the scaling factor that will be applied to the p_{T}-differential cross section of muons from heavy-flavour decays measured in pp collisions at $\sqrt{s} = 5.02$ TeV is calculated with FONLL predictions. Figure 3.53 shows the scaling factor obtained by combining different sets of c and b quark masses and assuming that quark masses are unchanged at

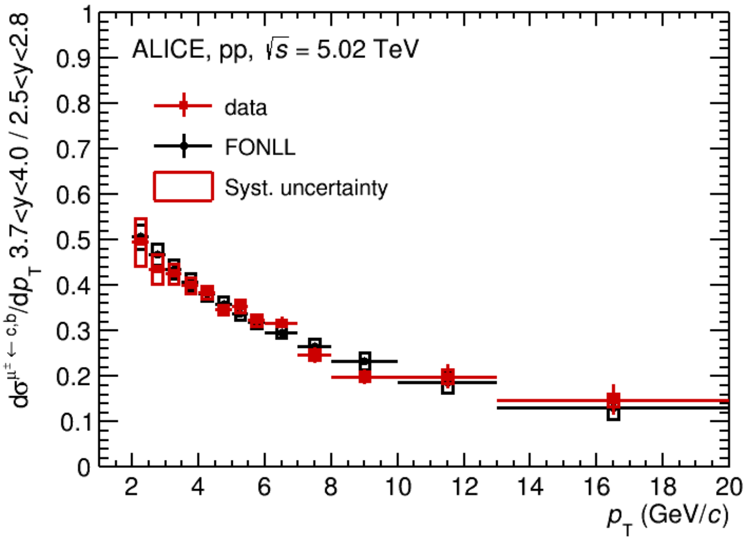

Figure 3.52: Ratio of the p_T-differential production cross section of muons from heavy-flavour hadron decays in pp collisions at $\sqrt{s} = 5.02$ TeV in $3.7 < y < 4$ to that in $2.5 < y < 2.8$. Statistical uncertainties (bars) and systematic uncertainties (boxes) are shown. The uncertainties on luminosity at the two centre-of mass energies are not included. The ratio is compared with FONLL predictions.

5.02 TeV and 5.44 TeV. The scaling factor depends on p_T, in particular in the low p_T range ($p_T < 2$ GeV/c). It decreases from about 0.94 to 0.83 in the p_T range 0–10 GeV/c (Fig. 3.53, left panel). The p_T range is limited to 8 GeV/c since the statistics collected in the short Xe-Xe run allows us to compute the nuclear modification factor up to 6-8 GeV/c depending on the collision centrality, only. The relative uncertainty is depicted in the right panel of Fig. 3.53. Changes in the quark masses introduce a systematic uncertainty smaller than 0.5% for $p_T < 2$ GeV/c, which can be neglected at higher p_T (range of interest for the measurement of the cross section of muons from heavy-flavour hadron decays).

As for electrons at central rapidity [230], the influence of the pQCD scale variations on the FONLL scaling factor was investigated in two cases: (1) same scales for charm and beauty (correlated scales, colour lines in Fig. 3.54); (2) different scales for charm and beauty (uncorrelated scales, black lines in Fig. 3.54). Very similar results are obtained with correlated or uncorrelated scales for charm and beauty. At low p_T ($p_T < 2$ GeV/c) the uncertainty on the scaling factor reaches about 3%, while in the interval $2 < p_T < 10$ GeV/c, it is smaller than 1%, independently of p_T.

In summary, the FONLL scaling factor as a function of p_T obtained for different sets of quark masses (blue boxes) and pQCD scales (red boxes), as just discussed, is shown in Fig. 3.55 (left panel). The relative scaling factor is also shown in the right

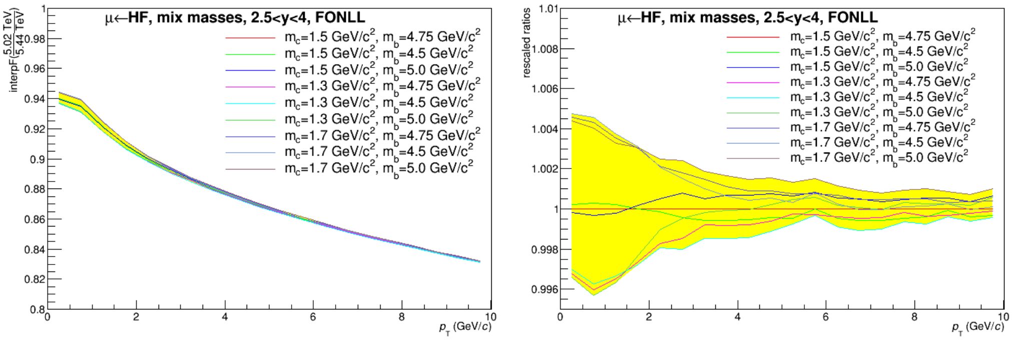

Figure 3.53: Left: FONLL scaling factor from 5.02 TeV to 5.44 TeV for the measurement of the p_{T}-differential cross section of muons from heavy-flavour hadron decays with different combinations of quark masses indicated on the figure; Right: corresponding relative systematic uncertainty.

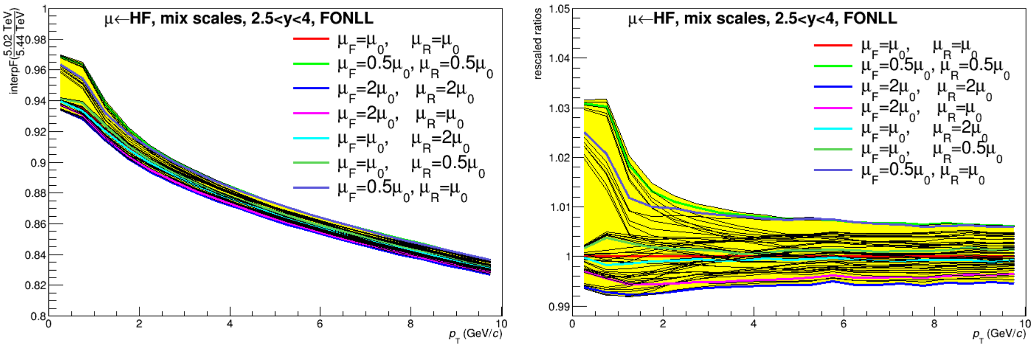

Figure 3.54: Left: FONLL scaling factor from 5.02 TeV to 5.44 TeV for the measurement of p_{T}-differential cross section of muons from heavy-flavour hadron decays with different combinations of QCD scales as indicated on the figure; Right: corresponding relative systematic uncertainty.

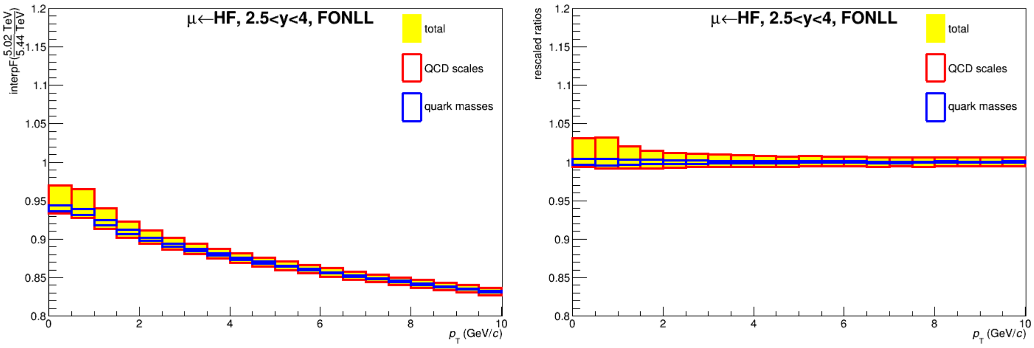

Figure 3.55: Left: FONLL scaling factor from 5.02 TeV to 5.44 TeV for the measurement of the p_{T}-differential cross section of muons from heavy-flavour hadron decays with different combinations of QCD scales (red boxes) and quark masses (blue boxes). The yellow band is the total systematic uncertainty. Right: corresponding relative systematic uncertainty.

panel of the figure. For the systematic uncertainty from energy scaling, we consider the spread of the ratio obtained with the different sets of parameters (yellow band).

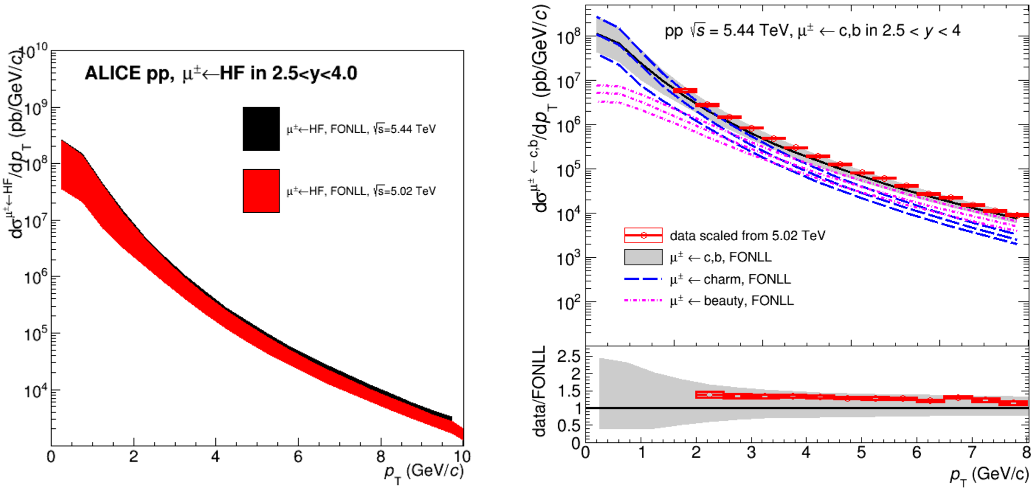

Figure 3.56: Left: p_{T}-differential cross section of muons from heavy-flavour hadron decays in pp collisions at $\sqrt{s} = 5.02$ TeV and 5.44 TeV from FONLL. Right: p_{T}-differential cross section of muons from heavy-flavour hadron decays in pp collisions at $\sqrt{s} = 5.44$ TeV.

Results and model comparisons

The p_{T}-differential cross section of muons from heavy-flavour hadron decays in pp collisions at $\sqrt{s} = 5.44$ TeV needed for the computation of the R_{AA} of muons from

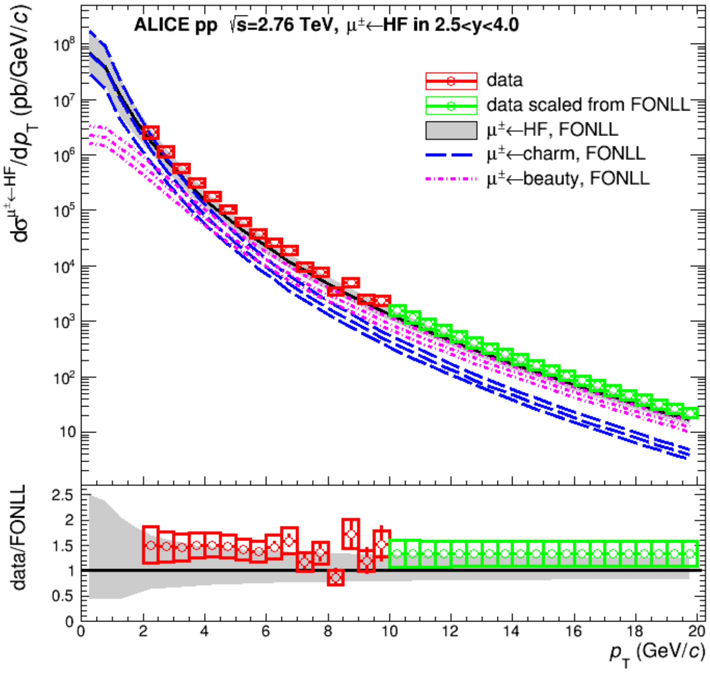

Figure 3.57: pp reference at 2.76 TeV in the forward rapidity region.

heavy-flavour hadron decays in Xe-Xe collisions at $\sqrt{s_{\rm NN}} = 5.44$ TeV is obtained by applying a pQCD-driven energy scaling to the $p_{\rm T}$-differential cross section of muons from heavy-flavour hadron decays measured in pp collisions at $\sqrt{s} = 5.02$ TeV in $2 < p_{\rm T} < 20$ GeV/c (see Sec. 3.1). The energy scaling factor, from 5.02 TeV to 5.44 TeV, and its related systematic uncertainty are obtained using FONLL calculations with different sets of factorization and renormalization scales and quark masses are discussed in Sec. 3.2 (see also Ref. [230]).

The left panel of Fig. 3.56 displays the production cross of muons from heavy-flavour decays in pp collisions at 5.02 TeV and 5.44 TeV from FONLL predictions. The $p_{\rm T}$-differential cross section of muons from heavy-flavour hadron decays at $\sqrt{s}$ = 5.44 TeV is shown on right panel of Fig. 3.56.

The results are in agreement with FONLL calculations within uncertainties, although the data lie at the upper limit of the model predictions, as already observed at other centre-of-mass energies.

3.3 pp reference at $\sqrt{s} = 2.76$ TeV: $p_{\rm T}$ extrapolation

In order to extend the published measurement of the $R_{\rm AA}$ of heavy-flavour hadron decay muons in Pb-Pb collisions at $\sqrt{s} = 2.76$ TeV up to 20 GeV/c, one needs to get the cross section of heavy-flavour decay muons in pp collisions at $\sqrt{s} = 2.76$ TeV up to 20 GeV/c. The $p_{\rm T}$-differential cross section of heavy-flavour decay muons in $2 < p_{\rm T} < 10$ GeV/c in pp collisions at $\sqrt{s} = 2.76$ TeV is published [175].

We use FONLL calculations to extrapolate the published measured p_{T}-differential cross section in a higher p_{T} region.

The scaling factor $K_{2.76\mathrm{TeV}}$ is obtained by using a constant to fit the ratio between data and FONLL in $2 < p_{\mathrm{T}} < 10$ GeV/c;

	2 – 10 GeV/c	3 – 10 GeV/c	4 – 10 GeV/c
$K_{2.76\mathrm{TeV}}$	1.33	1.32	1.31
uncertainty from fit	5.6%	5.8%	6.1%

Table 3.6: Scaling factor $K_{2.76\mathrm{TeV}}$ to extrapolate the measured pp reference to the high p_{T} region

Different fit ranges were used to extract the $K_{2.76\mathrm{TeV}}$ factor as reported in Tab. 3.6. The pp reference in $10 < p_{\mathrm{T}} < 20$ GeV/c is obtained using the average $K_{2.76\mathrm{TeV}}$ value (Tab. 3.6) which is 1.32. Then the pp reference in the p_{T} extrapolated region is:

$$\frac{\mathrm{d}\sigma^{\mu\leftarrow\mathrm{HF}}_{pp(2.76TeV)}}{\mathrm{d}p_{\mathrm{T}}} = K_{2.76TeV} \times \frac{\mathrm{d}\sigma^{FONLL}_{pp(2.76TeV)}}{\mathrm{d}p_{\mathrm{T}}} \tag{3.17}$$

Finally, the p_{T} differential cross section of muons from heavy-flavour hadron decays at forward rapidity ($2.5 < y < 4$) in pp collisions at $\sqrt{s} = 2.76$ TeV is shown in Fig. 3.57.

In the extrapolated region, $10 < p_{\mathrm{T}} < 20$ GeV/c, the systematic uncertainty on the pp reference includes: the uncertainty on the pp measurement and on FONLL calculations (quark masses, QCD scales and PDFs). The total uncertainty is within 15%-25% in the whole p_{T} range, $2 < p_{\mathrm{T}} < 20$ GeV/c, depending on p_{T}.

Chapter 4

Analysis strategy for the open heavy-flavour hadron decay muon measurement in Pb-Pb collisions at $\sqrt{s_{\mathrm{NN}}} = 5.02$ and 2.76 TeV

We focus on the measurement of the heavy-flavour hadron decay muon production at forward rapidity (production cross section, and nuclear modification factor R_{AA}) in Pb-Pb collisions at $\sqrt{s_{\mathrm{NN}}} = 5.02$ TeV and 2.76 TeV. The measurement of the pp reference needed for the computation of the R_{AA} at the two centre of mass energies are discussed in Chap. 3.

The analysis of Pb-Pb collisions at $\sqrt{s_{\mathrm{NN}}} = 5.02$ TeV and 2.76 TeV uses the LHC15o data sample collected in 2015 and LHC11h data sample collected in 2011, respectively. In order to identify muons from heavy-flavour hadron decays, many steps are needed such as data quality assurance, event and muon track selections (see Sec. 4.1), normalization (see Sec. 4.2), acceptance × efficiency corrections (Sec. 4.3), background subtraction (Sec. 4.4) and estimation of the systematic uncertainty sources (Sec. 4.5). All the steps are discussed in the following.

4.1 Data samples and muon selection

4.1.1 Data samples at 5.02 and 2.76 TeV

The Pb-Pb analysis at $\sqrt{s_{\mathrm{NN}}}$ = **5.02 TeV** is based on the AODs of the pass1 muon reconstruction (AOD175) and is performed with the AliRoot version vAN-20160512. Pb-Pb collisions are collected at $\sqrt{s_{\mathrm{NN}}} = 5.02$ TeV with minimum bias (MB) trigger (used for normalization purposes) and muon triggers corresponding to muon single low (MSL) and high (MSH) triggers with p_{T}-trigger thresholds of about 1 and 4.2 GeV/c, respectively. The following runs, after Quality Assurance (QA) checks for muon triggers [195] have been considered.

- LHC15o, muon_pass1, AOD175, 137 runs:
- Negative Polarity (–) 246994 246991 246989 246984 246982 246980 246949 246948 246945 246942 246937 246930 246871 246867 246865 246864 246859 246855 246851 246847 246846 246845 246844 246809 246808 246807 246806 246805 246804 246765 246763 246760 246759 246758 246757 246755 246751

246750 246676 246675 246495 246493 246488 246487 246434 246433 246431 246428 246424 246392 246391

- Positive Polarity (++) 246390 246276 246275 246272 246225 246222 246220 246217 246182 246181 246178 246153 246152 246151 246148 246115 246113 246089 246087 246053 246049 246048 246042 246037 246036 246012 246003 246001 245996 245963 245954 245952 245949 245833 245831 245829 245793 245785 245775 245766 245759 245752 245738 245731 245729 245705 245700 245692 245683 245554 245543 245542 245540 245535 245507 245505 245504 245501 245496 245450 245446 245410 245409 245407 245401 245353 245347 245346 245345 245343 245259 245253 245233 245232 245231 245152 245151 245146 245145 245068 245066 245064 244983 244982 244980 244918

Note that the following 17 runs (246671, 246648, 246639, 246583, 246575, 246568, 246567, 246553, 246543, 246271, 245453, 245452, 245439, 245411, 245396, 245349, 245148) have been rejected either because the ZDC is not present (all events rejected when applying Physics Selection) or because of Low Voltage trips in the muon tracking chambers.

The $\sqrt{s_{\rm NN}}$ = **2.76 TeV** Pb–Pb collisions have been collected with minimum-bias trigger and muon triggers corresponding to muon single low and high triggers with $p_{\rm T}$-trigger thresholds set at around 0.5 and 4.2 GeV/c, respectively.

The entire analysis is based on AODs from muon pass2 reconstruction, AliRoot version is vAN-20140926. The following runs, after Quality Assurance checks for muon single low and muon single high triggers [196] have been considered.

- LHC11h, muon_pass2, AOD119, 132 runs:
167706 167713 167806 167807 167808 167813 167814 167818 167915 167920 167921 167985 167986 167987 167988 168066 168069 168076 168107 168108 168115 168172 168173 168175 168181 168203 168205 168206 168207 168208 168212 168213 168310 168311 168318 168322 168325 168341 168342 168356 168361 168362 168458 168460 168461 168464 168467 168511 168512 168514 168777 168826 168992 169035 169040 169044 169045 169091 169094 169099 169138 169144 169145 169148 169156 169160 169167 169236 169238 169411 169415 169417 169418 169419 169420 169475 169498 169504 169506 169512 169515 169550 169553 169554 169555 169557 169586 169587 169588 169590 169835 169837 169838 169846 169855 169858 169859 169965 169969 170027 170036 170040 170081 170083 170084 170085 170088 170089 170091 170155 170159 170163 170193 170203 170204 170207 170228 170230 170268 170269 170270 170306 170308 170309 170311 170312 170313 170315 170387 170388 170572 170593

Note that runs 169683 and 170162 (pure minimum-bias runs, muon triggers not activated) and runs 170389 and 170390 (pure muon trigger runs, minimum-bias trigger not activated) are rejected from the analysis.

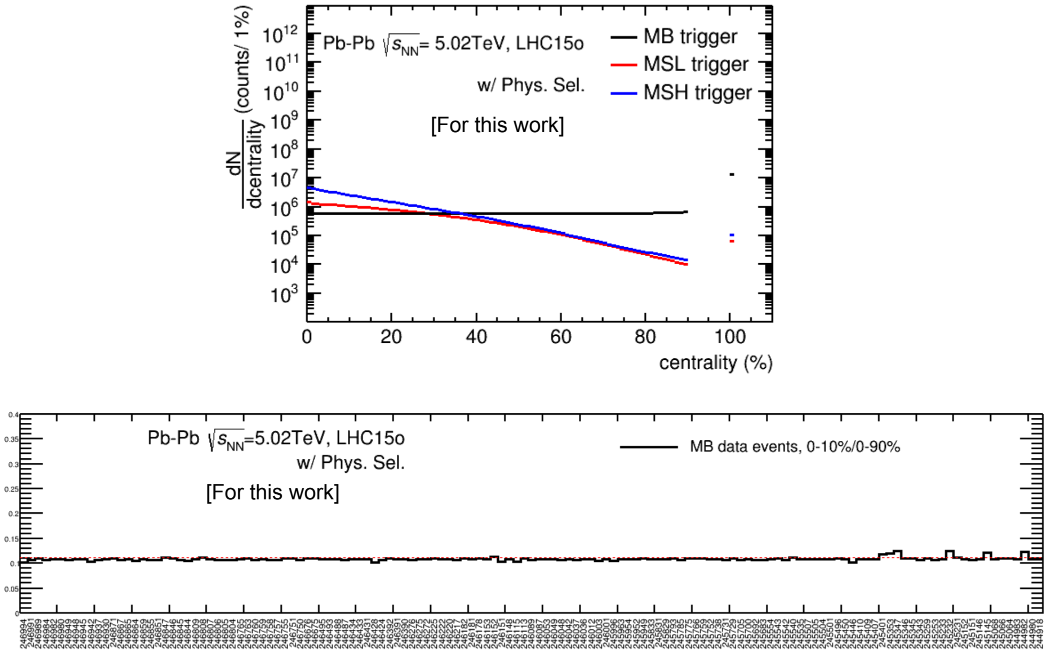

Figure 4.1: Upper: centrality distribution of MB, MSL and MSH triggers in Pb–Pb collisions at $\sqrt{s_{\mathrm{NN}}} = 5.02$ TeV. Bottom: ratio between 0–10% and 0–90% centrality classes in MB collisions as a function of the run number, starting from last run of the LHC15o period.

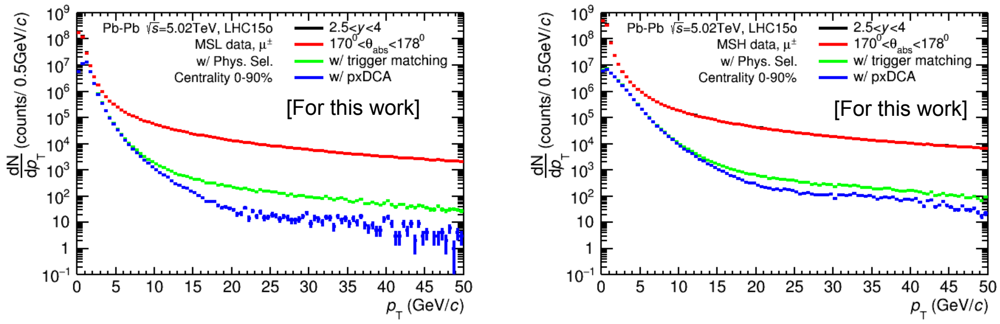

Figure 4.2: Transverse momentum distributions of inclusive muons with different selection cuts at event and track level in Pb–Pb collisions at $\sqrt{s_{\mathrm{NN}}} = 5.02$ TeV (centrality class: 0–90%) for MSL (left) and MSH (right) triggers.

4.1.2 Event and track selections at $\sqrt{s_{\mathrm{NN}}} = 5.02$ TeV

The event and track selections are the standard ones used in previous single muon analyses with Run-1 data and in pp collisions at $\sqrt{s} = 5.02$ TeV. An offline event selection (Physics Selection) is applied and a reconstructed vertex within ±10 cm along the beam axis is required and the number of contributors for reconstructed vertex is larger than 0. The 0–90% centrality interval is selected since the MB trigger is fully efficient for these events. The centrality distribution for the various triggers and the ratio between MB events in 0–10% and 0–90% for each run is shown in Fig. 4.1 in upper and bottom panel, respectively. The MB trigger exhibits a uniform behaviour which, as expected, is not the case of muon triggers. The ratio between MB events in 0–10% and 0–90% can be considered as stable over the whole LHC15o period.

Various kinematic cuts are applied for the track selection. Tracks are required to be reconstructed within the acceptance of the muon spectrometer ($-4 < \eta_{\mathrm{lab}} < -2.5$) and to have a polar angle at the end of the absorber (θ_{abs}) from 170 to 178 degrees. One also requires that the track candidate in the tracking system matches the track reconstructed in the trigger system. Finally, the $p \times$ DCA cut within 6σ (see chapter 3) was applied in order to remove beam-induced background and particles produced in the absorber. The effect of the cuts on the measured p_{T} distributions of inclusive muons is shown in Fig. 4.2 for MSL and MSH trigger events in the centrality interval 0–90%. One can notice that by combining MSL and MSH triggered events, one can perform the measurements up to very high p_{T} i.e. $\sim$ 40–50 GeV/c in the centrality class 0-90%. The observed shape at high p_{T} corresponds to the region where the W decay muon contribution sticks out [198].

Tables 4.1 and 4.2 give the number of events and tracks for the different triggers after the event and track selections.

		N_{evt} (After Phys.Sel)	+ Rec.Vertex	+ cent(0-90%)	N_{evt}
LHC15o	MB	$1.71 \cdot 10^8$	3.0 %	19.8%	$1.39 \cdot 10^8$
	MSL	$4.85 \cdot 10^7$	3.5%	0.1%	$4.68 \cdot 10^7$
	MSH	$1.14 \cdot 10^8$	8.1%	0.2%	$1.05 \cdot 10^8$

Table 4.1: Number of events in the centrality class 0–90% after the event selection conditions are applied (Physics selection and reconstructed vertex, percentages of rejected tracks by each cut) in Pb–Pb collisions at $\sqrt{s_{\mathrm{NN}}} = 5.02$ TeV.

		n_{trk}(+ event cuts)	+ η	+ θ_{abs}	+ TrM	+ p×DCA
LHC15o	MB	$6.51 \cdot 10^7$	32.7%	2.95%	70.96%	1.61%
	MSL	$5.24 \cdot 10^8$	34.2%	3.16%	88.23%	1.53%
	MSH	$1.49 \cdot 10^8$	36.5%	2.65%	96.78%	3.37%

Table 4.2: Number of tracks after event selection and with the various analysis cuts for the centrality interval 0–90% (percentages of rejected tracks by each cut) in Pb–Pb collisions at $\sqrt{s_{\mathrm{NN}}} = 5.02$ TeV.

From the p_{T} distribution of inclusive muons after selection cuts are applied (Fig. 4.3), one can conclude that by shifting from MSL to MSH triggered events at $p_{\mathrm{T}} = 7$ GeV/c, well above the MSH p_{T} threshold, the collected statistics allows us to investigate R_{CP} (R_{AA}) up to about 20 GeV/c in all centrality classes. The corresponding statistical uncertainty in $18 < p_{\mathrm{T}} < 20$ GeV/c is $\sim$ 5% and 18% for

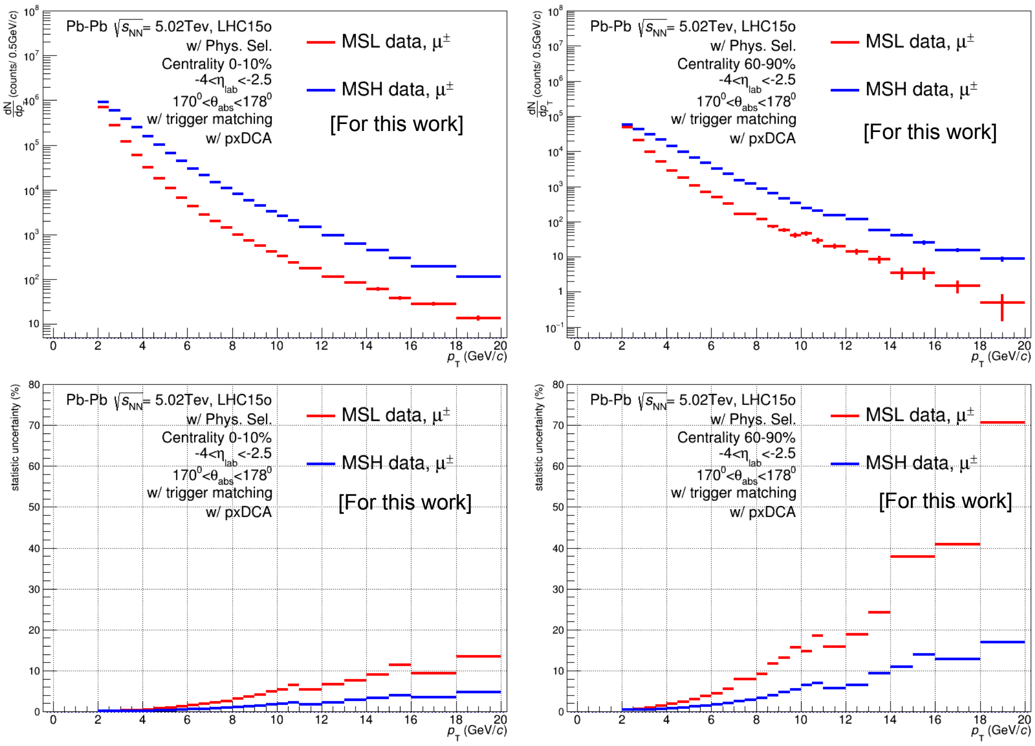

Figure 4.3: Inclusive muon p_T distribution after selection cuts (upper panels) and statistical uncertainty in each p_T bin (lower panels), in Pb-Pb collisions at $\sqrt{s_{NN}}$ = 5.02 TeV (left plots: 0–10% centrality class, right plots: 60–90% centrality class).

central and peripheral collisions, respectively. The choice of the upper p_T limit of 20 GeV/c in the present analysis is due to both the limited statistics in the peripheral centrality class and the pp reference (the reference is measured in pp collisions at $\sqrt{s} = 5$ TeV, see [197]) and, the W contribution which starts to increase significantly beyond this limit [198].

4.1.3 Event and track selections at $\sqrt{s_{NN}} = 2.76$ TeV

An offline event selection (Physics Selection) and a reconstructed vertex are required. Same kinematic cuts as in Pb–Pb collisions at $\sqrt{s_{NN}} = 5.02$ TeV are applied for track selection. The effect of the cuts on the measured p_T distributions of inclusive muons is shown in Fig. 4.4 for MSL and MSH trigger events. One can notice that by using MSL and MSH triggered events, one can perform the measurements up to 20 GeV/c (centrality class: 0-90%).

Tables 4.3 and 4.4 give the number of events and tracks for the different triggers after cuts in Pb–Pb collisions at $\sqrt{s_{NN}} = 2.76$ TeV

From the p_T distribution of inclusive muons shown after selection cuts are applied in Fig. 4.5, one can conclude that by combining MSL and MSH triggered events ($3 < p_T < 6.5$ GeV/c for MSL, $6.5 < p_T < 20$ GeV/c for MSH), the collected

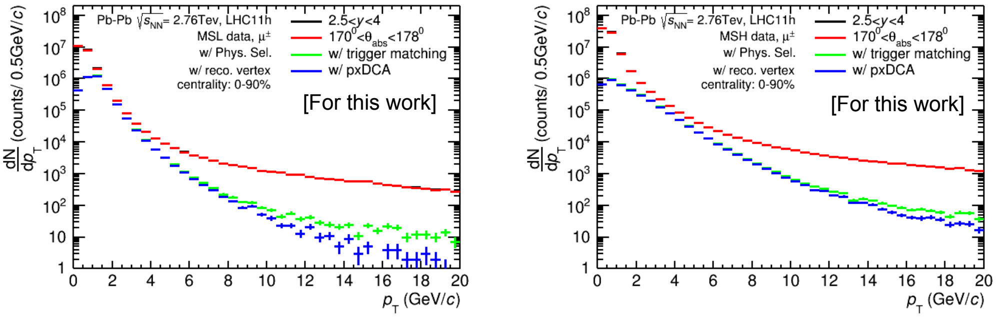

Figure 4.4: Transverse momentum distributions of inclusive muons with different selection cuts at event and track level in Pb–Pb collisions at $\sqrt{s_{\rm NN}} = 2.76$ TeV.

		n_{evt}(After Phys. Sel.)	+ Rec. Vertex	+ 0-90% Cent
LHC11h	MB	$4.55 \cdot 10^6$	2.37% (reject)	8.03%
	MSL	$6.13 \cdot 10^6$	8.98%	0.07%
	MSH	$2.03 \cdot 10^7$	13.61%	0.05%

Table 4.3: Number of events after Physics Selection and reconstructed vertex selection in Pb–Pb collisions at $\sqrt{s_{\rm NN}} = 2.76$ TeV.

		n_{trk}(+evt level cut)	+ η	+ $\Theta_{\rm abs}$	+ TrM	+ p×DCA
LHC11h	MB	$8.65 \cdot 10^6$	19.74%	2.84%	65.40%	0.466%
	MSL	$2.99 \cdot 10^7$	21.38%	2.61%	83.81%	0.590%
	MSH	$1.09 \cdot 10^8$	23.17%	2.72%	95.41%	1.523%

Table 4.4: Number of tracks after event selections and analysis cuts in Pb–Pb collisions at $\sqrt{s_{\rm NN}} = 2.76$ TeV.

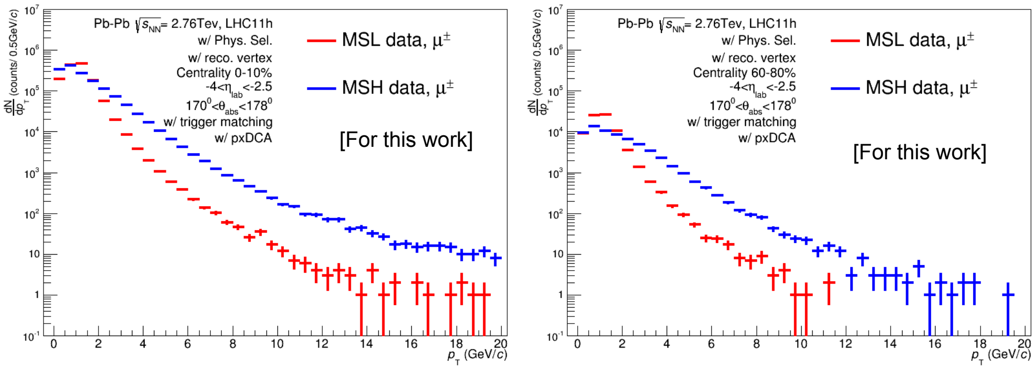

Figure 4.5: Inclusive muon $p_{\rm T}$ distribution after selection cuts in various centrality classes in Pb–Pb collisions at $\sqrt{s_{\rm NN}} = 2.76$ TeV. (left: 0-10%, right: 60-80%)

statistics allows us to investigate the R_{AA} in $3 < p_{\mathrm{T}} < 20$ GeV/c in central collisions (0–10% centrality class) and $3 < p_{\mathrm{T}} < 14$ GeV/c in peripheral collisions (centrality class 60–80%).

4.2 Normalization procedure

In order to get the equivalent number of minimum-bias events for MSL and MSH triggered data samples, one needs to determine the normalization factor ($F_{\mathrm{norm}}^{\mathrm{MSL/MSH}}$) for these data samples. Both offline and scaler methods have been implemented in Pb–Pb collisions at $\sqrt{s_{\mathrm{NN}}} = 5.02$ TeV. In Pb–Pb collisions at $\sqrt{s_{\mathrm{NN}}} = 2.76$ TeV, the offline method uses also the semi-central and central triggers in addition to MB trigger, allowing us to calculate the systematic uncertainty on the normalization factor. As described hereafter, in the offline method one applies the muon trigger condition on minimum-bias events, while in the online method one uses the trigger rates. Once this factor is determined, the equivalent number of minimum bias events ($N_{\mathrm{MB}}^{\mathrm{eq}}$) is calculated as $N_{\mathrm{MB}}^{\mathrm{eq}} = F_{\mathrm{norm}}^{\mathrm{MSL/MSH}} \times N_{\mathrm{MSL(MSH))}}$.

4.2.1 Normalization at $\sqrt{s_{\mathrm{NN}}} = 5.02$ TeV

Offline method The normalization factors for MSL ($F_{\mathrm{norm}}^{\mathrm{MSL}}$) and MSH ($F_{\mathrm{norm}}^{\mathrm{MSH}}$) triggers are calculated in the centrality class 0–90% on a run by run basis according to:

$$F_{\mathrm{norm}}^{\mathrm{i}}(\mathrm{MSL}) = \frac{N_{\mathrm{MB}}^{\mathrm{i}} \times F_{\mathrm{pile-up}}^{\mathrm{i}}}{N_{(\mathrm{MB\&\&0MSL})}^{\mathrm{i}}} \tag{4.1}$$

$$F_{\mathrm{norm}}^{\mathrm{i}}(\mathrm{MSH}) = F_{\mathrm{pile-up}}^{\mathrm{i}} \times \frac{N_{\mathrm{MB}}^{\mathrm{i}}}{N_{(\mathrm{MB\&\&0MSL})}^{\mathrm{i}}} \times \frac{N_{\mathrm{MSL}}^{\mathrm{i}}}{N_{(\mathrm{MSL\&\&0MSH})}^{\mathrm{i}}} \tag{4.2}$$

N_{MB} and N_{MSL} are the number of MB and MSL triggers after the offline selection. $N_{(\mathrm{MB\&\&0MSL})}$ and $N_{(\mathrm{MSL\&\&0MSH})}$ are the sample of MB events containing a 0MSL input and the sample of MSL events containing a 0MSH input, respectively. 0MSL (= 13) and 0MSH (= 14) are the ID of the Central Trigger Processor (CTP) trigger inputs for MSL and MSH triggers. The pile-up being negligible in the 2015 Pb–Pb run (less than 0.1%), no pile-up correction is needed ($F_{\mathrm{pile-up}} = 1$). The final value is the weighted average, using the relative statistical uncertainty, i.e. the number of events as a weight (Eq. 4.3).

$$F_{\mathrm{norm}}^{\mathrm{MSL/MSH}} = \frac{\sum_i F_{\mathrm{norm}}^{\mathrm{MSL/MSH}} / (\sigma^2)_{\mathrm{stat}}^{\mathrm{MSL/MSH}}}{\sum_i 1/(\sigma^2)_{\mathrm{stat}}^{\mathrm{MSL/MSH}}} \tag{4.3}$$

The statistical uncertainty is calculated as:

$$[\Delta F_{\mathrm{norm}}^{\mathrm{MSL/MSH}}]_{\mathrm{stat}} = \sqrt{\frac{1}{\sum 1/(\sigma^2)_{\mathrm{stat}}^{\mathrm{MSL/MSH}}}} \tag{4.4}$$

That gives $F^{\mathrm{MSL}}_{\mathrm{norm-off}} = 3.62 \pm 0.0025$ and $F^{\mathrm{MSH}}_{\mathrm{norm-off}} = 14.96 \pm 0.019$ (the quoted uncertainty are statistical uncertainty).

Figure 4.6 presents the normalization factor for MSL and MSH triggers as a function of the run number (green symbols for the offline method). One can notice that the run by run values are affected by quite large statistical uncertainties due the collected statistics in the MB sample. In order to avoid statistical fluctuations, the following online method has been also implemented.

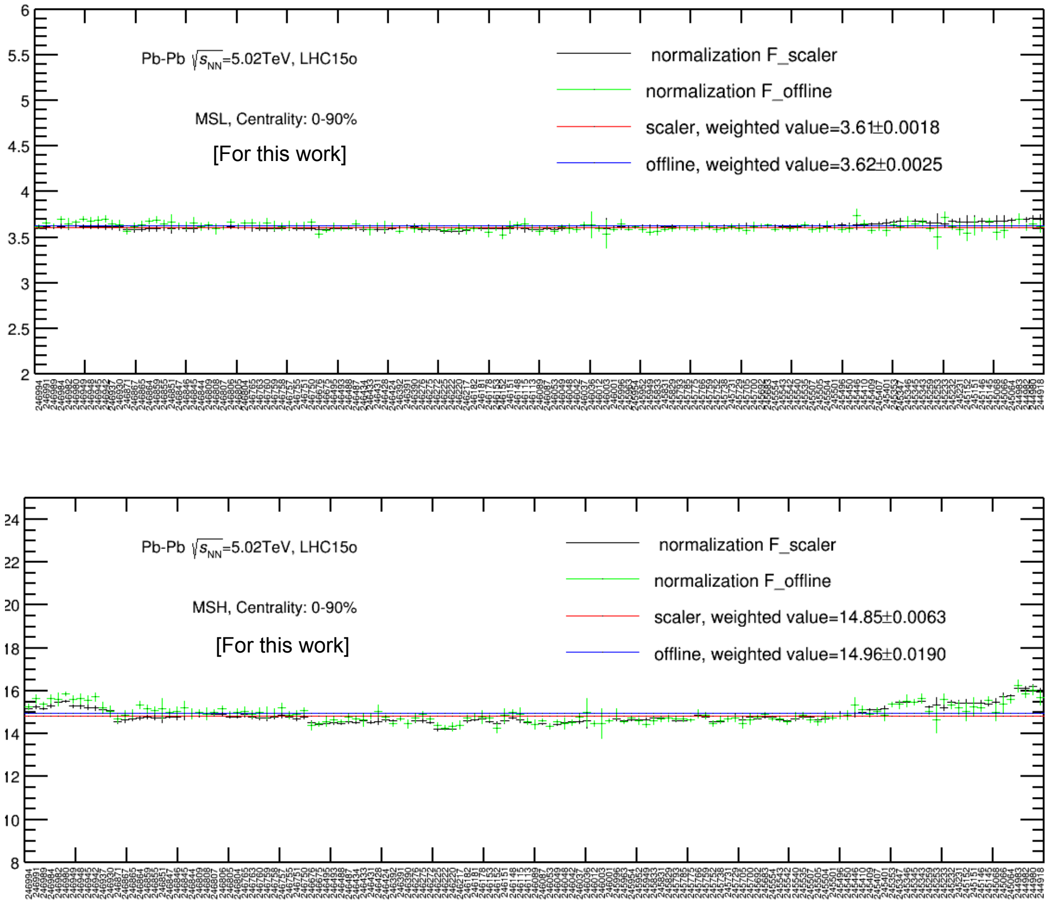

Figure 4.6: Normalization factor as a function of run number (starting from last run of the LHC15o period), to obtain the equivalent number of MB events in Pb–Pb collisions in Pb–Pb collisions at $\sqrt{s_{\mathrm{NN}}} = 5.02$ TeV for MSL (upper panel) and MSH (lower panel) triggers.

Online method This method relies on the L0b counting rates (scalers) taken from the Offline Conditions DataBase (OCDB). However, due to a contamination of $\mathrm{L0b_{MB}}$ scalers by V0 after pulses, the C0V0M semi-central trigger is used. This trigger covers the centrality interval 0–60%. The normalization factor is computed run by run as:

$$F^{\mathrm{i}}_{\mathrm{norm-onl}}(\mathrm{MSL(MSH)}) = \frac{L0b^{\mathrm{i}}_{\mathrm{C0V0M}} \times PS^{\mathrm{i}}_{\mathrm{C0V0M}} \times F_{\mathrm{pile-up}}}{L0b^{\mathrm{i}}_{\mathrm{MSL(MSH)}} \times PS^{\mathrm{i}}_{\mathrm{MSL(MSH)}}}, \tag{4.5}$$

where $L0b_{\mathrm{C0V0M}}$, $L0b_{\mathrm{MSL}}$ and $L0b_{\mathrm{MSH}}$ are the scaler values recorded for C0V0M, MSL and MSH triggers, respectively. The quantity PS_{C0V0M} is the ratio of events, after the offline event selection, to the total number of events. This quantity being consistent with unity except for one run [199], one uses $PS_{\mathrm{C0V0M}} = 1$[1]. The variable $PS_{\mathrm{MSL(MSH)}}$ is the fraction of accepted MB, MSL, MSH triggered events that pass the offline event selection and is shown in Fig. 4.7. $F_{\mathrm{pile-up}}$ is the pile-up correction factor for minimum-bias events that is neglected ($F_{\mathrm{pile-up}} = 1$).

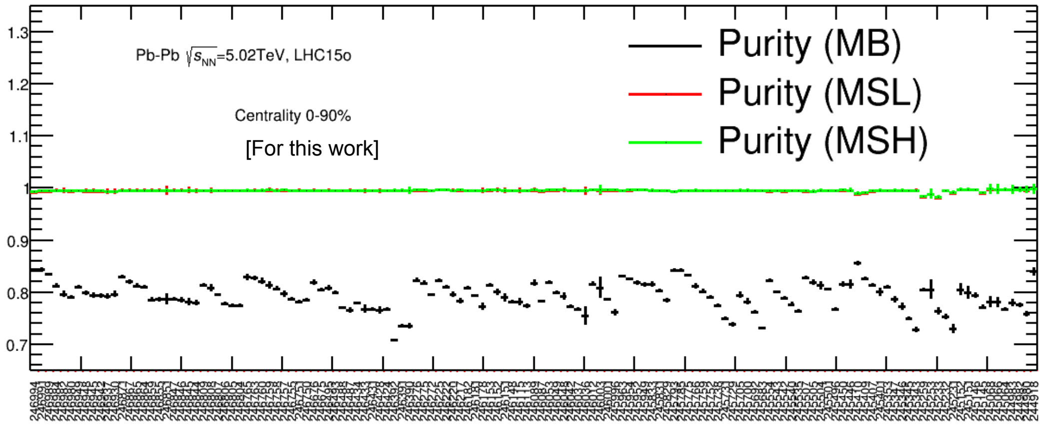

Figure 4.7: Purity of accepted MB, MSL, MSH trigger events that pass the offline event selection versus run number (starting from the last run in LHC15o period) in Pb–Pb collisions at $\sqrt{s_{\mathrm{NN}}} = 5.02$ TeV.

In addition, with C0V0M trigger a correction needs to be introduced since, as shown in Fig. 4.8, the cut at 60% in centrality is not sharp. Indeed, one observes that, due to the V0 ageing, the ratio of events in the 60–70% centrality class to those in the 0–70% centrality class ($R^{\mathrm{i}}_{\mathrm{corr}}$, Eq. 4.6) decreases with increasing run number. Finally, the corrected results are scaled to the same centrality as in the offline method (0–90%). Therefore, the final normalization factor obtained with the online method in the 0–90% centrality class is:

$$F^{\mathrm{i}}_{\mathrm{norm-onl}}(\mathrm{MSL(MSH)})|_{0-90\%} = F^{\mathrm{i}}_{\mathrm{norm-onl}}(\mathrm{MSL(MSH)}) \cdot \frac{9(1 - R^{\mathrm{i}}_{\mathrm{corr}})}{6}, \tag{4.6}$$

---

[1] The physics selection is not included in the partition. The physics selection relies on the events also triggered by another class, the CINT7 which is included in physics selection, see Fig. 4.7.

where $F^{\mathrm{i}}_{\mathrm{norm-onl}}(\mathrm{MSL(MSH)})$ and $R^{\mathrm{i}}_{\mathrm{corr}}$ are for a given run, the normalization factor in the 0–60% centrality class and the ratio of events in the 60–70% centrality class to that in the 0–70% centrality class, respectively.

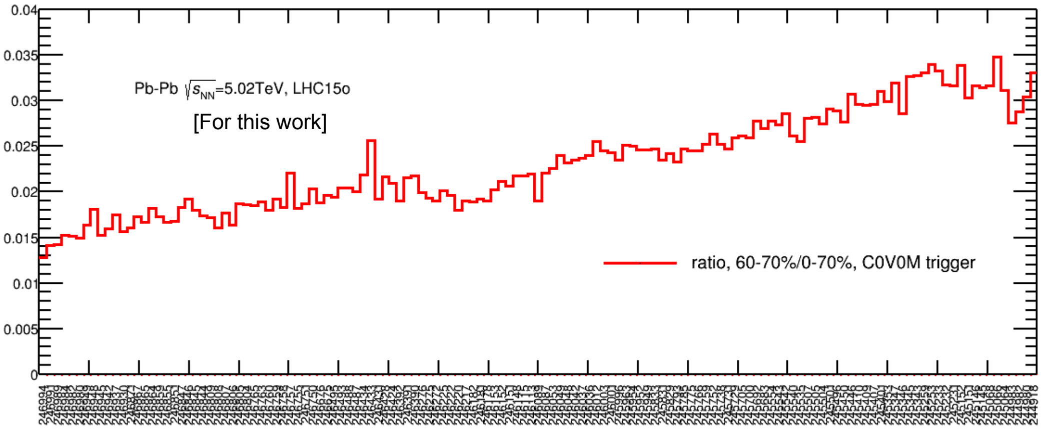

Figure 4.8: $R^{\mathrm{i}}_{\mathrm{corr}}$ ratio of events in the 60–70% centrality class to that in the 0–70% centrality class versus run number (starting from the last run in LHC15o period) in Pb-Pb collisions at $\sqrt{s_{\mathrm{NN}}} = 5.02$ TeV.

The run by run normalization factor from the online method (black symbols) is compared to that obtained with the offline method in Fig. 4.6. The results from the two methods are in good agreement and as expected the results from the online method are affected by smaller statistical uncertainties. The final value of the normalization factor with the online method is obtained using the same procedure as with the offline method (Eqs 4.3-4.4). This leads to: $F^{\mathrm{MSL}}_{\mathrm{norm-onl}} = 3.61 \pm 0.0018$ (stat.) and $F^{\mathrm{MSH}}_{\mathrm{norm-onl}} = 14.85 \pm 0.0063$ (stat.).

Final results Finally, the normalization factors used to get the equivalent number of minimum-bias events with MSL and MSH triggers in the 0–90% centrality class are:

$F_{\mathrm{norm}}(\mathrm{MSL}) = 3.61 \pm 0.0018(\mathrm{stat.}) \pm 0.01(\mathrm{syst.})$ and $F_{\mathrm{norm}}(\mathrm{MSH}) = 14.85 \pm 0.0063(\mathrm{stat.}) \pm 0.11(\mathrm{syst.})$. The final value and statistical uncertainty are obtained with the scaler method, and the systematic uncertainty is the difference between the offline and online methods and is smaller than 1% (0.3% for MSL and 0.7% for MSH).

Normalization factor and equivalent number of MB events in various centrality classes

As a function of centrality, the normalization factor in 0–90% is scaled with the fraction of the inelastic cross section of a given centrality class with respect to the 0–90% centrality class C^{c} (e.g. 10/90 for the 0–10% centrality class, 20/90 for the 20–40% centrality class). Therefore, the equivalent number of minimum-bias events in a given centrality class c is given by:

$$N^{\mathrm{c}}_{\mathrm{MB}} = F_{\mathrm{norm}}(0-90\%) \cdot C^{\mathrm{c}} \cdot N_{\mathrm{MSL(MSH)}}(0-90\%), \tag{4.7}$$

C^{c} being the scaling factor in a given centrality class c.

Alternatively, one can also determine the equivalent number of minimum-bias events in a given centrality class c as

$$N^{\mathrm{c}}_{\mathrm{MB}} = F^{\mathrm{c}}_{\mathrm{norm}} \cdot N^{\mathrm{c}}_{\mathrm{MSL(MSH)}}, \tag{4.8}$$

where $F^{\mathrm{c}}_{\mathrm{norm}}$ is the normalization factor in the c centrality class, determined according to Eqs. 4.1–4.2. Note that the normalization factor in a given centrality class ($F^{\mathrm{c}}_{\mathrm{norm}}$) can be compared to the one measured for the centrality class 0–90% by applying, in addition to the scaling factor, a correction to account for the non-uniformity of the centrality distribution of muon triggers. This procedure was already implemented in Pb–Pb collisions at $\sqrt{s_{\mathrm{NN}}} = 2.76$ TeV (2011 heavy-ion data) to get the normalization factor with central and semi-central triggers [200].

centrality	F_{norm}	N_{MSL}	N_{MB}	N_{MB} (from $F_{\mathrm{norm}}(0-90\%)$)
0–10%	1.26	$1.465 \cdot 10^7$	$1.846 \cdot 10^7$	$1.877 \cdot 10^7$
10–20%	1.63	$1.143 \cdot 10^7$	$1.863 \cdot 10^7$	$1.877 \cdot 10^7$
20–40%	2.72	$1.384 \cdot 10^7$	$3.765 \cdot 10^7$	$3.754 \cdot 10^7$
40–60%	6.98	$5.308 \cdot 10^6$	$3.704 \cdot 10^7$	$3.754 \cdot 10^7$
60–90%	36.1	$1.565 \cdot 10^6$	$5.65 \cdot 10^7$	$5.63 \cdot 10^7$

Table 4.5: Normalization factor, number of muon-triggered events, and equivalent number of MB events obtained from F_{norm} calculated in each centrality class (4th column) and from F_{norm} in 0–90% (5th column) in various centrality classes for MSL triggered events in Pb–Pb collisions at $\sqrt{s_{\mathrm{NN}}} = 5.02$ TeV.

centrality	F_{norm}	N_{MSH}	N_{MB}	N_{MB} (from $F_{\mathrm{norm}}(0-90\%)$)
0–10%	3.77	$4.614 \cdot 10^7$	$1.739 \cdot 10^8$	$1.731 \cdot 10^8$
10–20%	6.59	$2.623 \cdot 10^7$	$1.729 \cdot 10^8$	$1.731 \cdot 10^8$
20–40%	14.65	$2.362 \cdot 10^7$	$3.46 \cdot 10^8$	$3.462 \cdot 10^8$
40–60%	49.5	$7.05 \cdot 10^6$	$3.49 \cdot 10^8$	$3.462 \cdot 10^8$
60–90%	262.5	$1.946 \cdot 10^6$	$5.09 \cdot 10^8$	$5.193 \cdot 10^8$

Table 4.6: Normalization factor, number of muon triggered-events and, equivalent number of MB events obtained from F_{norm} calculated in each centrality class (4th column) and from F_{norm} in 0–90% (5th column) in various centrality classes for MSH triggered events in Pb–Pb collisions at $\sqrt{s_{\mathrm{NN}}} = 5.02$ TeV.

As just mentioned, the normalization factors as a function of centrality can also be calculated directly using the offline method. The equivalent numbers of MB events in various centrality classes obtained using the two procedures (Eqs. 4.7-4.8) are summarized in Tab. 4.5 and 4.6 for MSL and MSH data samples, respectively.

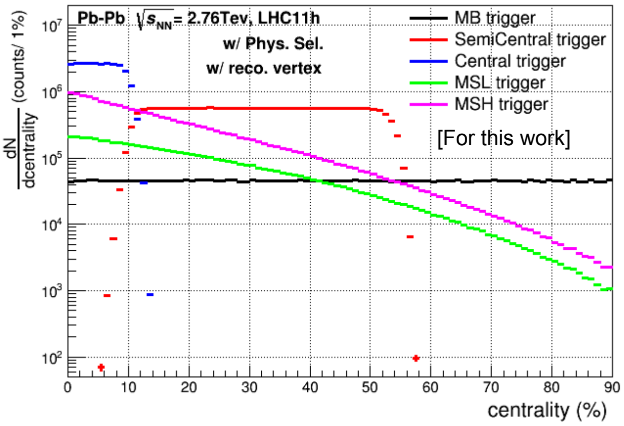

Figure 4.9: Number of events for MB. semi-central and central triggers in Pb–Pb collisions at $\sqrt{s_{\mathrm{NN}}} = 2.76$ TeV

One can notice the nice agreement within uncertainties with the results obtained in 0–90% after scaling. In the following, the equivalent number of MB events calculated with Eq. 4.7 will be used (smaller statistical uncertainties on normalization factor determined in 0–90%).

Table 4.7 summarizes the equivalent number of minimum-bias events in the 0–90% centrality class and corresponding analyzed integrated luminosity for MB, MSL and MSH triggered events. The latter are obtained using an inelastic Pb–Pb cross section in Pb–Pb collisions at $\sqrt{s_{\mathrm{NN}}} = 5.02$ TeV is $7.7 \pm 0.1^{+0.5}_{-0.6}$ b [225].

The corresponding integrated luminosity is given by

$$L_{\mathrm{int}} = \frac{N_{\mathrm{MSL(MSH)}} \times F^{\mathrm{MSL(MSH)}}_{\mathrm{norm}}}{\sigma^{Pb-Pb}_{\mathrm{V0}}}, \tag{4.9}$$

	N_{evt}	$L_{\mathrm{int}}(\mu\mathrm{b}^{-1})$
MB	$1.388 \cdot 10^8$	18.0
MSL	$4.679 \cdot 10^7$	21.9
MSH	$1.049 \cdot 10^8$	202.3

Table 4.7: Equivalent number of minimum-bias events and integrated luminosity for MB, MSL and MSH triggers in Pb–Pb collisions at $\sqrt{s_{\mathrm{NN}}} = 5.02$ TeV in the 0–90% centrality class.

4.2.2 Normalization at $\sqrt{s_{\mathrm{NN}}} = 2.76$ TeV

The strategy is different from the one discussed in Pb–Pb collisions at $\sqrt{s_{\mathrm{NN}}} = 5.02$ TeV. Here, in order to get the equivalent number of minimum-bias events for MSL and MSH triggers, one can determine the normalization factor for MSL and MSH data samples by means of minimum-bias (MB), semi-central (Semi-CENT) and central (CENT) triggered events. Note that a restricted centrality range is used for minimum-bias (0-90%), semi-central (15-50%) and central (0-8%) triggers as the distributions are not uniform over the whole centrality range (see Fig. 4.9).

Normalization strategy The normalization factor for MSL and MSH triggers are defined as:

$$F_{\mathrm{norm}}^{\mathrm{Trigger}}(MSL, 0-90\%) = \frac{N_{\mathrm{event}}^{\mathrm{Trigger}}}{N_{\mathrm{event}}^{(\mathrm{Trigger\&\&0MSL})}} \times \frac{N_{\mathrm{event}}^{\mathrm{MB}}(0-90\%)}{N_{\mathrm{event}}^{\mathrm{MB}}(x\%)} \times \frac{N_{\mathrm{event}}^{\mathrm{MSL}}(x\%)}{N_{\mathrm{event}}^{\mathrm{MSL}}(0-90\%)} \tag{4.10}$$

$$F_{\mathrm{norm}}^{\mathrm{Trigger}}(MSH, 0-90\%) = \frac{N_{\mathrm{event}}^{\mathrm{Trigger}}}{N_{\mathrm{event}}^{(\mathrm{Trigger\&\&0MSH})}} \times \frac{N_{\mathrm{event}}^{\mathrm{MB}}(0-90\%)}{N_{\mathrm{event}}^{\mathrm{MB}}(x\%)} \times \frac{N_{\mathrm{event}}^{\mathrm{MSH}}(x\%)}{N_{\mathrm{event}}^{\mathrm{MSH}}(0-90\%)}, \tag{4.11}$$

where the $N_{\mathrm{event}}^{\mathrm{Trigger}}$ is number of events for different triggers (MB, central and semi-central) in the restricted centrality range. OMSL=7 and OMSH=9 are the identifier of Central Trigger Processor (CPT) trigger inputs for MSL and MSH. Note that as the Pb-Pb collisions at $\sqrt{s_{\mathrm{NN}}} = 5.02$ TeV, the pile-up correction is also negligible due to the low rate in the 2011 heavy-ion Run.

Figure 4.10 presents the uncorrected normalization factor (first term, $\frac{N_{\mathrm{event}}^{\mathrm{Trigger}}}{N_{\mathrm{event}}^{(\mathrm{Trigger\&\&0MSL})}}$) for MSL-triggered events as a function of run number. Figure 4.11 presents the uncorrected normalization factor (first term, $\frac{N_{\mathrm{event}}^{\mathrm{Trigger}}}{N_{\mathrm{event}}^{(\mathrm{Trigger\&\&0MSH})}}$) for MSH triggered events as a function of run number.

Since the centrality range of each trigger is different, the normalization factor needs to be corrected by a factor 35/90 for semi-central triggered events and 8/90 for central triggered events (second term, $\frac{N_{\mathrm{event}}^{\mathrm{MB}}(0-90\%)}{N_{\mathrm{event}}^{\mathrm{MB}}(x\%)}$, $x\%$ is the width of the centrality class). No correction is needed with MB since we will give the normalization factor in 0-90 %.

Finally, since the centrality distribution of MSL and MSH is not flat, we continue to correct the normalization factor, except for minimum-bias collisions by a factor: $\frac{N_{\mathrm{event}}^{\mathrm{MSL}}(x\%)}{N_{\mathrm{event}}^{\mathrm{MSL}}(0-90\%)}$ and $\frac{N_{\mathrm{event}}^{\mathrm{MSH}}(x\%)}{N_{\mathrm{event}}^{\mathrm{MSH}}(0-90\%)}$ for MSL and MSH, respectively. We use $x = 8$ for semi-central triggered events, $x = 35$ for central triggered events.

Normalization Factor The normalization factors after all corrections for muon single low (MSL) and muon single high (MSH) triggered events obtained with the method just discussed are summarized in Tab. 4.8 and 4.9.

The central value of the normalization factor which will be used is the average between the three triggers. The systematic uncertainty is the deviation of the maximum and minimum values with respect to the average. The normalization factors for MSL and MSH are: $F_{\mathrm{norm}}^{\mathrm{Trigger}}(MSL, 0-90\%) = 4.9 \pm 0.12\%(\mathrm{stat.}) \pm 0.4\%(\mathrm{syst.})$ and $F_{\mathrm{norm}}^{\mathrm{Trigger}}(MSH, 0-90\%) = 26.06 \pm 0.25\%(\mathrm{stat.}) \pm 1.6\%(\mathrm{syst.})$, respectively.

The inelastic Pb-Pb cross section in Pb–Pb collisions at $\sqrt{s_{\mathrm{NN}}} = 2.76$ TeV: 7.57 ± 0.03 b [225]. Finally, the integrated luminosities for the MSL and MSH

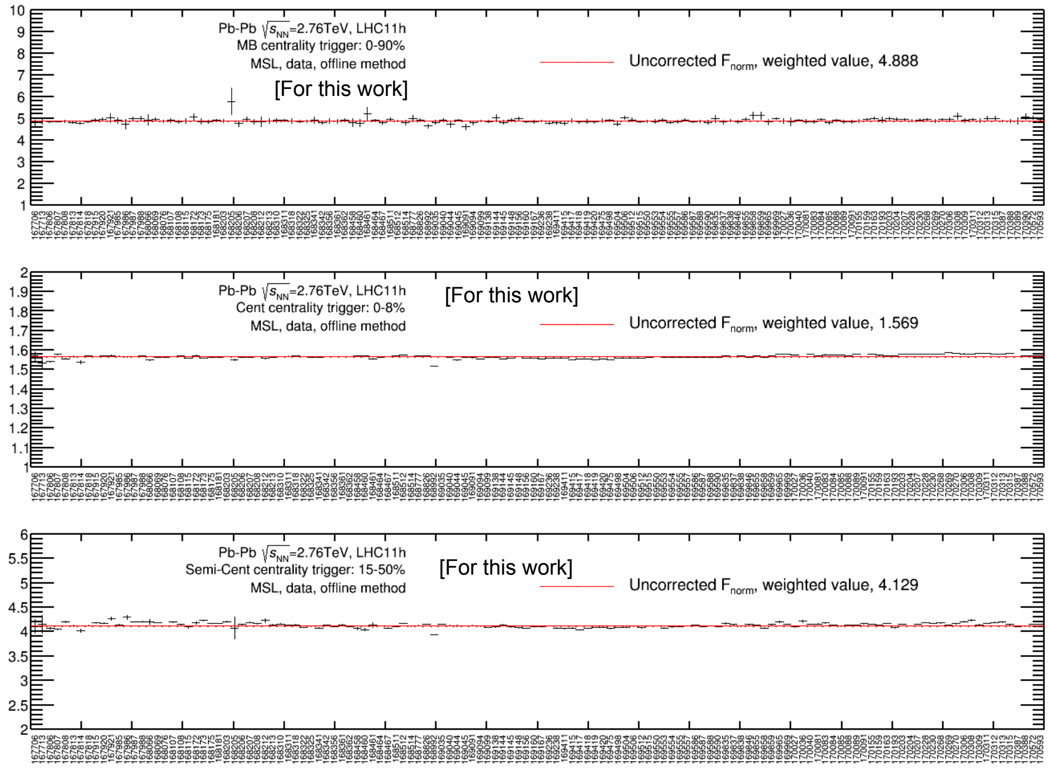

Figure 4.10: Run by run uncorrected normalization factor for MSL from MB (top), central (middle) and semi-central (bottom) triggers in Pb–Pb collisions at $\sqrt{s_{\rm NN}}$ = 2.76 TeV.

Trigger	UnCorr	binning.Corr	events.Corr	$F_{\rm norm}(MSH)$
MB	4.888	1	1	4.888
CENT	1.569	90/8	0.278	4.907
Semi-CENT	4.129	90/35	0.462	4.905

Table 4.8: Normalization factor for MSL within the centrality class 0-90% in Pb–Pb collisions at $\sqrt{s_{\rm NN}}$ = 2.76 TeV

Trigger	UnCorr	binning.Corr	events.Corr	$F_{\rm norm}(MSH)$
MB	25.643	1	1	25.643
CENT	6.335	90/8	0.3668	26.141
Semi-CENT	26.931	90/35	0.3813	26.405

Table 4.9: Normalization factor for MSH within the centrality class 0-90% in Pb–Pb collisions at $\sqrt{s_{\rm NN}}$ = 2.76 TeV.

triggers in Pb–Pb collisions at $\sqrt{s_{\rm NN}}$ = 2.76 TeV are calculated as in Pb-Pb collisions at $\sqrt{s_{\rm NN}}$ = 5.02 TeV. The results are summarized in Tab. 4.10.

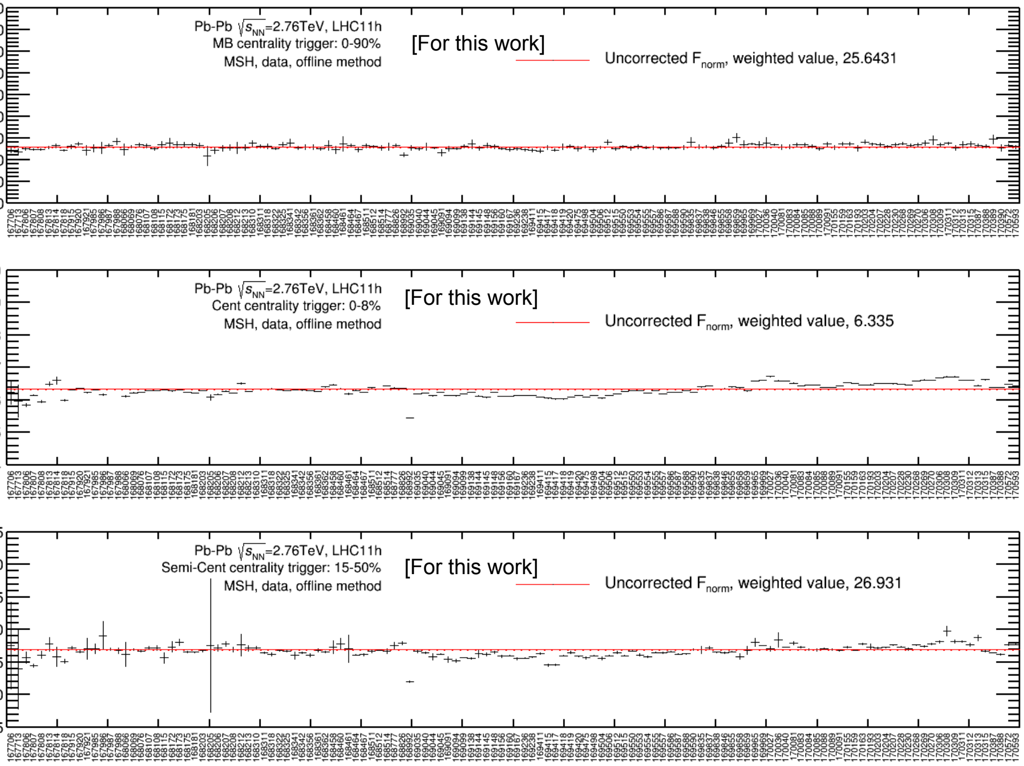

Figure 4.11: Run by run uncorrected normalization factor for MSH from MB (top), central (middle) and semi-central (bottom) triggers in Pb–Pb collisions at $\sqrt{s_{\mathrm{NN}}} = 2.76$ TeV.

Luminosity / μb	Pb-Pb
MSL	3.6
MSH	63.9

Table 4.10: Integrated luminosity for the Pb–Pb data sample at $\sqrt{s_{\mathrm{NN}}} = 2.76$ TeV with MSL and MSH triggers corresponding to the analysed statistics in the 0-90% centrality class.

4.3 Acceptance × efficiency correction

The muon yields need to be corrected for acceptance × efficiency (A×ε). This correction is estimated from realistic monte carlo simulations where muons from charm and beauty decays are generated using the p_T and y distributions predicted by FONLL calculations [2]. The p_{T} and y distributions of muons from charm and beauty decays from FONLL calculation are parameterized as: $p_1 \cdot (e^{\mathrm{p}_2(1-\mathrm{e}^{\mathrm{x}\cdot \mathrm{p}_3})} + p_4) \cdot \frac{1}{x^{p_5}} \cdot (p_6 + x \cdot p_7 + x^2 \cdot p_8)$ and $x^8 \cdot p_1 + x^6 \cdot p_2 + x^4 \cdot p_3 + x^2 \cdot p_4 + x \cdot p_5 + p_6$, respectively. The fit parameters are p_1, p_2, p_3, p_4, p_5, p_6, p_7 and p_8. The detector

---

[2] It has been checked that the correction is the same for all muons within uncertainties.

description and its response are modeled using the GEANT3 transport package. Moreover, the simulated statistics is proportional to the number of MSL (MSH) triggers in each run to account for the time evolution of $A\times\varepsilon$. Finally, an additional correction is used to consider the dependence of $A\times\varepsilon$ on detector occupancy via the embedding technique [199, 201]. This is done by embedding one muon in each MB event simulated with HIJING model [199]. The muon input shapes are obtained from the parameters just discussed.

4.3.1 Acceptance × efficiency correction at $\sqrt{s_{\rm NN}} = 5.02$ TeV

The calculation of the centrality-integrated $A \times \varepsilon$ uses the embedding production [201]. The results are weighted with $\langle N_{\rm coll}\rangle$ since the number of muons (from heavy-flavour hadron decays) depends on centrality. Most of results presented in this strategy have been extracted from [201].

Figure 4.12 shows the evolution of $A \times \varepsilon$ as a function of run number for the 0–90% centrality class, with the tracking-trigger matching with the low $p_{\rm T}$ trigger and $p_{\rm T} > 0.8$ GeV/c. One observes that $A \times \varepsilon$ is very stable over the whole period, only two runs have a lower $A\times\varepsilon$. Note that a same behaviour was also reported in the J/ψ analysis at same collision energy [199].

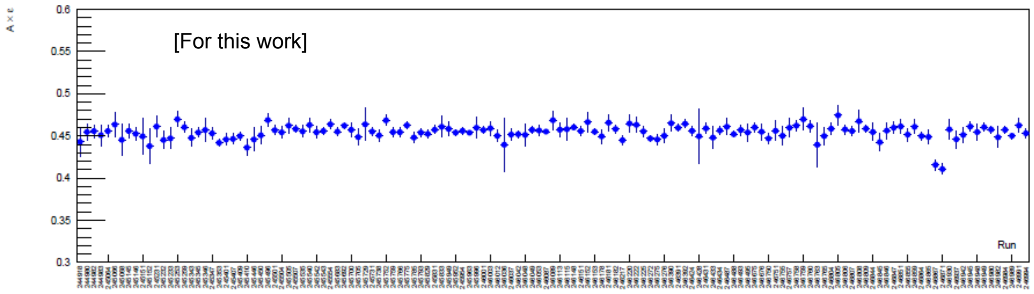

Figure 4.12: Acceptance × efficiency as a function of run number for the low $p_{\rm T}$ trigger cut in Pb–Pb collisions at $\sqrt{s_{\rm NN}} = 5.02$ TeV.

One example of the typical $p_{\rm T}$-differential $A \times \varepsilon$ is presented in Fig. 4.13 (left panel) for the 0–10% centrality class and, for the tracking-trigger matching with the low- and high-$p_{\rm T}$ trigger. The $A \times \varepsilon$ with MSL tends to saturate in the region $p_{\rm T} > 2$ GeV/c, while with MSH the plateau seems to be reached for $p_{\rm T} > 10$ GeV/c. The need of more statistics is clearly seen when looking at the results obtained for $p_{\rm T} > 10$ GeV/c. Even, with wide $p_{\rm T}$ bins, the $A\times\varepsilon$ will remain affected by statistical fluctuations.

The $A \times \varepsilon$ is also studied as a function of centrality. Figure 4.13 (right panel) shows the corresponding $A \times \varepsilon$ for the tracking-trigger matching with the low $p_{\rm T}$ trigger and for the region $2 < p_{\rm T} < 20$ GeV/c. One observes that, due to the detector occupancy, the $A \times \varepsilon$ decreases from peripheral to central collisions by about 6%. It has been observed that the $A \times \varepsilon$ is constant in narrow centrality intervals in the centrality region 60–90% [201]. A same behaviour was also reported in the J/ψ analysis [199]. Therefore the decreasing factor of $A \times \varepsilon$ from peripheral to central collisions is calculated with respect to the centrality class 60–90%.

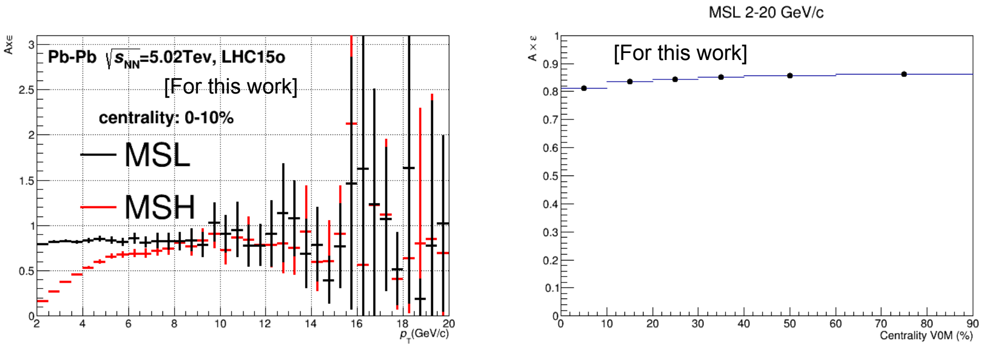

Figure 4.13: Left: acceptance × efficiency as a function of p_{T} in the 0–10% centrality class for MSL and MSH triggers in Pb–Pb collisions at $\sqrt{s_{\mathrm{NN}}} = 5.02$ TeV. Right: p_{T}-integrated ($2 < p_{\mathrm{T}} < 20$ GeV/c) acceptance × efficiency as a function of centrality for MSL trigger in Pb–Pb collisions at $\sqrt{s_{\mathrm{NN}}} = 5.02$ TeV.

Finally, it is observed that the decreasing factor from peripheral to central collisions is independent of p_{T} within uncertainties, as also observed with the unlike-sign dimuon trigger [199]. This is illustrated in Fig. 4.14 where the ratio of $A \times \varepsilon$ for MSL trigger in a given centrality class to that in the 60–90% centrality class is displayed for different p_{T} regions (i.e. as a function of a minimum p_{T}). Similar trends are also found with MSH trigger, and the decrease of $A \times \varepsilon$ with increasing centrality is compatible with that obtained with MSL within 2% at maximum. The small differences are due to statistical fluctuations and, consequently a smaller p_{T} range is used to extract this factor for MSH due to the limited statistics in the embedding production ($5 < p_{\mathrm{T}}^{\mathrm{min}} < 8$ GeV/c compared to $2 < p_{\mathrm{T}}^{\mathrm{min}} < 7$ GeV/c for MSL). The decreasing factor determined with MSL will be used in the following to correct the $A \times \varepsilon$ from a simulation of pure muon signals (see later). The values of the decreasing factor of $A \times \varepsilon$ from peripheral to central collisions for various centrality classes are reported in Tab. 6.6 for MSL and MSH triggers.

	0–10%	10–20%	20–40%	40–60%	60–90%
MSL	0.941	0.973	0.982	0.994	1
MSH	0.927	0.952	0.975	0.984	1

Table 4.11: Decreasing factor of $A \times \varepsilon$ from peripheral to central collisions in various centrality classes for MSL and MSH in Pb–Pb collisions at $\sqrt{s_{\mathrm{NN}}} = 5.02$ TeV. The uncertainty from fit is smaller than 1% (about 0.5%) for MSL and about 3%–4% for MSH.

In order to avoid statistical fluctuations in the p_{T}-differential $A \times \varepsilon$ estimation from the embedding production, a procedure based on a simulation using as input a

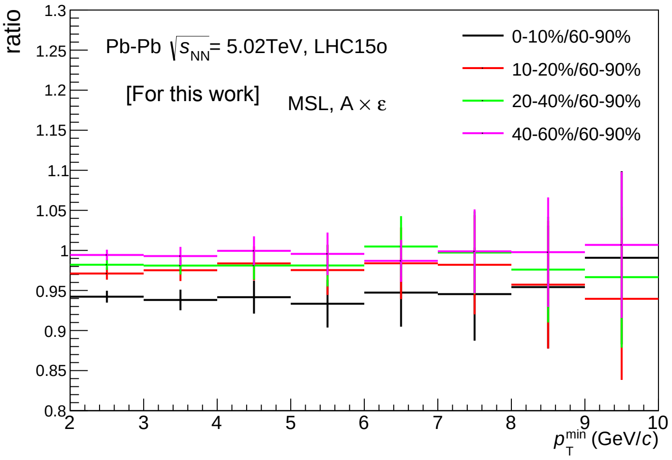

Figure 4.14: Ratio of $A\times\varepsilon$ in a given centrality class to that in the 60–90% centrality class as a function of a minimum p_{T} for MSL trigger in Pb–Pb collisions at $\sqrt{s_{\mathrm{NN}}}$ = 5.02 TeV.

parameterization of the p_{T} and y distributions of muons from heavy-flavour hadron decays from FONLL predictions is implemented. The $A \times \varepsilon$ as a function of the reconstructed p_{T} and generated p_{T} for MSL and MSH triggers is presented in left and right panel of figure 4.15, respectively. For reconstructed $p_{\mathrm{T}} > 3 - 4$ GeV/c, the $A \times \varepsilon$ tends to saturate at a value close to 90% in MSL events with a slight increase that can be seen at high p_{T}. For MSH trigger, the efficiency plateau is reached at a p_{T} value of about 13 GeV/c. As expected, the $A \times \varepsilon$ as a function of generated p_{T} becomes constant for both triggers at high p_{T} and saturate at about 90%. Note that it has been checked that a compatible efficiency value is extracted from the embedding production in the 60–90% centrality class, although affected by large fluctuations at high p_{T}.

The $A \times \varepsilon$ values further corrected by the decreasing factor from peripheral to central collisions, are used in the following for the measurement of the p_{T}-differential production cross sections and R_{AA} of muons from heavy-flavour hadron decays in various centrality classes. The measurement of the R_{CP} of muons from heavy-flavour hadron decays requires only the decreasing factor from peripheral to central collisions in various centrality classes.

Transverse momentum distributions normalized to the equivalent number of MB events and corrected for $A \times \varepsilon$

The ratio of the p_{T} distribution of inclusive muons $A\times\varepsilon$ corrected and normalized to the equivalent number of minimum-bias events in MSL triggered events to that in MSH triggered events is reported in Fig. 4.16 for the 0–90% centrality class (left) and for various centrality intervals in the range 0–90% (right). The ratio is consistent with unity within statistical uncertainties. The deviation between MSL and MSH amounts to less than 2% in the 0–90% centrality class and $7 < p_{\mathrm{T}} < 20$ GeV/c. As

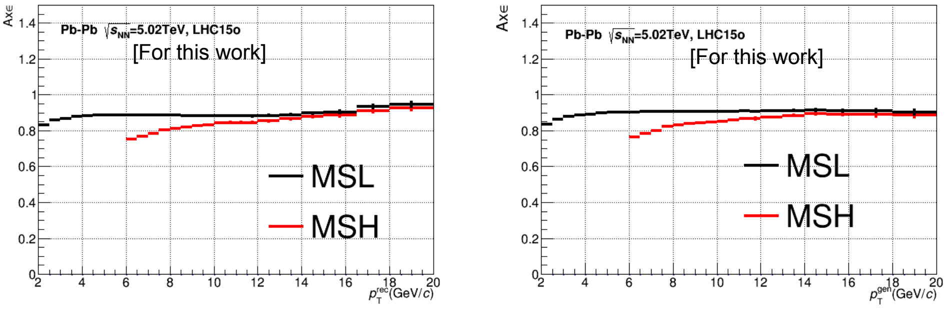

Figure 4.15: $A \times \varepsilon$ as a function of reconstructed (left) and generated (right) $p_{\rm T}$ in Pb–Pb collisions at $\sqrt{s_{\rm NN}} = 5.02$ TeV. The simulation uses as input a parameterization of $p_{\rm T}$ and y distributions from FONLL calculations.

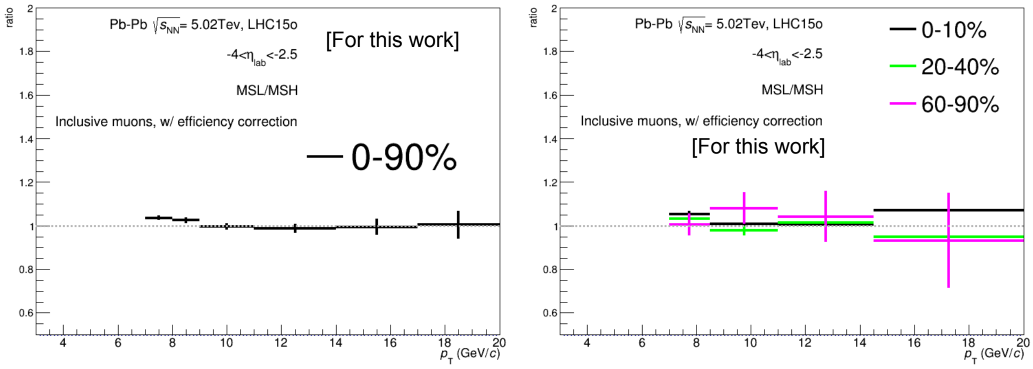

Figure 4.16: Ratio of the $p_{\rm T}$ distributions between MSL and MSH triggers after normalization to the equivalent number of minimum-bias events and after applying the $A \times \varepsilon$ correction for the 0–90% centrality class (left) and, in various centrality classes (right) in Pb–Pb collisions at $\sqrt{s_{\rm NN}} = 5.02$ TeV.

a function of centrality, the deviation remains stable within about 1.3–2.8%.

4.3.2 Acceptance × efficiency correction at $\sqrt{s_{\rm NN}} = 2.76$ TeV

Figure 4.17 shows the acceptance × efficiency as function of $p_{\rm T}$ with MSL and MSH in Pb-Pb collisions at $\sqrt{s_{\rm NN}} = 2.76$ TeV. The value acceptance × efficiency is obtained from a realistic simulation of muon from heavy flavour decays.

The strategy to determaine the acceptance × efficiency correction in Pb–Pb collisions at $\sqrt{s_{\rm NN}} = 2.76$ TeV is similar to that implemented in Pb-Pb collisions at $\sqrt{s_{\rm NN}} = 5.02$ TeV. Both a simulation of pure signals of heavy flavour decay muons and an embedding production are considered.

One can notice in particular that acceptance × efficiency is close to 80% (MSL) and that the ratio of the measured distributions between MSL and MSH is unity

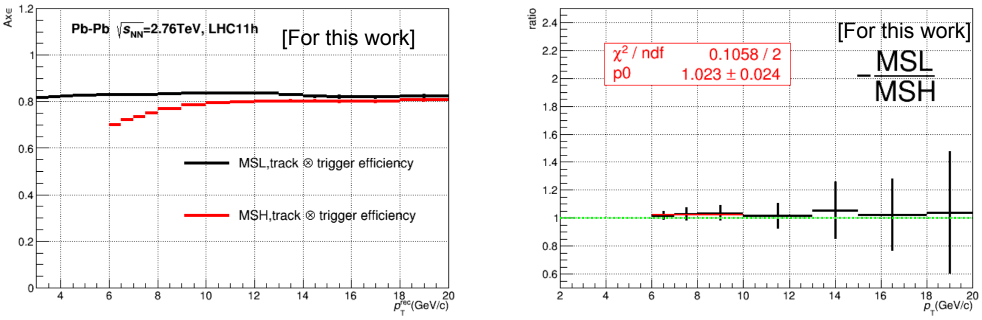

Figure 4.17: Left: Acceptance × efficency with MSL and MSH (left) as a function of p_{T} in Pb–Pb collisions at $\sqrt{s_{\mathrm{NN}}} = 2.76$ TeV. Right: ratio of the p_{T} distributions between MSL and MSH triggers after normalization to the equivalent number of MB events and after applying the acceptance × efficiency correction in Pb-Pb collisions at $\sqrt{s_{\mathrm{NN}}} = 2.76$ TeV.

within uncertainties in the region $p_{\mathrm{T}} > 6$ GeV/c. The dependence of efficiency on the centrality of the collision was evaluated by means of the embedding procedure. A decrease of the efficiency of 4% is observed in the 10% most central collisions [202]. The corresponding systematic uncertainty is 1%. The deviation betwen MSL and MSH is about 2% in $6 < p_{\mathrm{T}} < 10$ GeV/c, as shown in right panel of Fig. 4.17.

4.4 Estimation the muon-background contributions

The p_{T} distribution of muons from heavy-flavour hadron decays at forward rapidity is obtained after the subtraction of the muon background to the corrected inclusive muon yield and is expressed as:

$$\frac{dN_{\mathrm{AA}}^{\mu\leftarrow HF}}{dp_{\mathrm{T}}} = \frac{dN_{\mathrm{AA}}^{incl\ \mu}}{dp_{\mathrm{T}}} - \frac{dN_{\mathrm{AA}}^{\mu\leftarrow K,\pi}}{dp_{\mathrm{T}}} - \frac{dN_{\mathrm{AA}}^{\mu\leftarrow W,Z/\gamma^*}}{dp_{\mathrm{T}}} - \frac{dN_{\mathrm{AA}}^{\mu\leftarrow J/\psi}}{dp_{\mathrm{T}}}. \tag{4.12}$$

The main background contribution at low/intermediate p_{T} is the component of muons from primary charged pion and kaon decays, while at high p_{T} (above $p_{\mathrm{T}} > 14 - 15$ GeV/c) the main source of background is W,Z/γ^*-decay muons.

The contribution of J/ψ decay muons to the single muon p_{T} distribution is small over the whole p_{T} range, the fraction of J/ψ decay muons relative to inclusive muons being 1–4% (maximum contribution is located at $p_{\mathrm{T}} = 5$ GeV/c). The Υ contribution can be ignored according to the production cross sections, compared to J/ψ ones. The contribution of muon from secondary light-hadron decays is negligible in the region $3 < p_T < 20$ GeV/c. Therefore these two contributions will be not discussed in the following.

4.4.1 Estimation of the background contribution of muons from light-hadron decays

Primary charged π and K decay muons in Pb–Pb collisions at $\sqrt{s_{\mathrm{NN}}}$ = 5.02 TeV

The procedure being similar at $\sqrt{s_{\mathrm{NN}}} = 5.02$ TeV and 2.76 TeV, a detailed description of the procedure is provided for Pb-Pb collisions at $\sqrt{s_{\mathrm{NN}}} = 5.02$ TeV. For the Pb-Pb collisions at 2.76 TeV, only the differences will be discussed.

The procedure implemented for the estimation of the contribution of muons from primary charged pion and kaon decays to the single muon p_{T} distribution uses as inputs, the ALICE mid-rapidity charged π and K distributions measured in Pb-Pb collisions at $\sqrt{s} = 5.02$ TeV for various centrality classes [204], which are shown in Fig. 4.25.

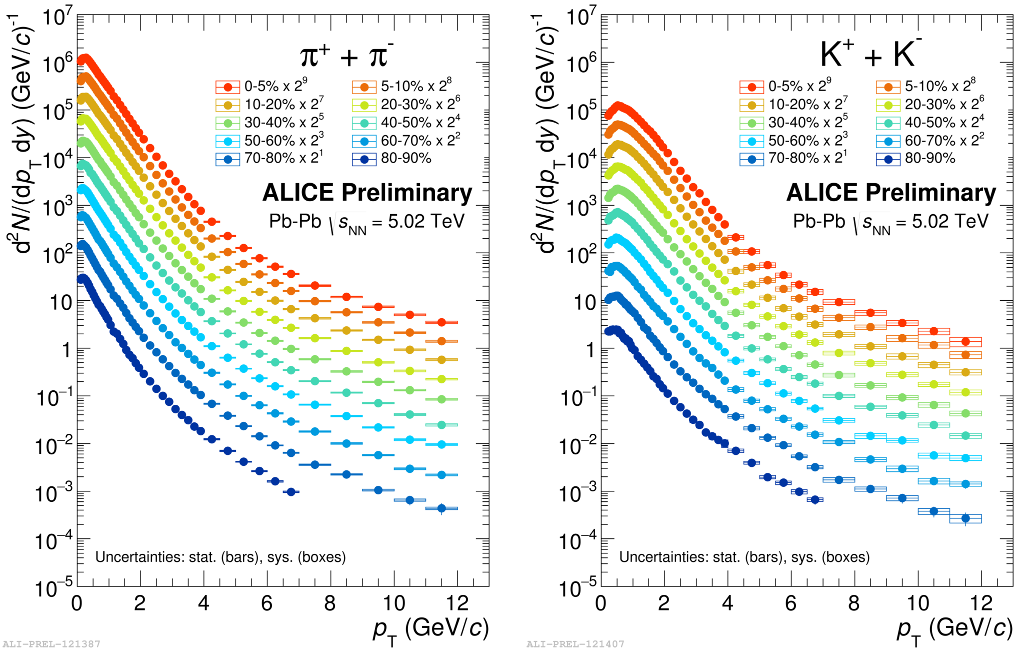

Figure 4.18: Charged pions measured at mid-rapidity (left) and charged kaons measured at mid-rapidity (right) in Pb–Pb collisions at $\sqrt{s_{\mathrm{NN}}} = 5.02$ TeV with ALICE. Figure taken from Ref. [204]

The three main steps that will be discussed in the following are:

- Transverse momentum extrapolation of mid-rapidity charged pion and kaon spectra at higher p_{T} than the measurement;
- Extrapolation towards forward rapidity of the p_{T}-extrapolated mid-rapidity charged pion and kaon spectra;

- Production of decay muons via fast detector simulations of decay kinematics and absorber effect. The absorber effect is already discussed in chapter 3.

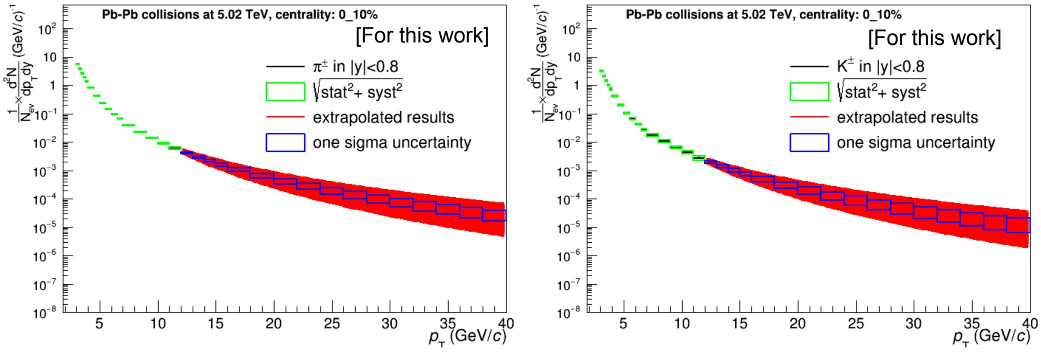

Figure 4.19: p_{T} extrapolation of charged π (left) and charged K (right) measured at mid-rapidity in Pb–Pb collisions at $\sqrt{s_{\mathrm{NN}}} = 5.02$ TeV with ALICE.

The extrapolated p_{T} distributions of mid-rapidity charged pions and kaons are shown in Fig. 4.19. They are extrapolated to higher p_{T} using a power-law fit:

$$\mathrm{f}(p_{\mathrm{T}}) = C\frac{p_{\mathrm{T}}}{(1+(p_{\mathrm{T}}/p_0)^2)^n}, \tag{4.13}$$

where p_0, C and n are free parameters.

- the spectra in $p_{\mathrm{T}} < 12$ GeV/c are filled 1000 times and the original points are Gaussian smeared (gRandom→Gaus(μ,σ)) where μ is the center value of pion and kaon spectra, and σ is the total uncertainty (the statistical and systematic uncertainty in data);
- For $p_{\mathrm{T}} > 12$ GeV/c, μ and σ are obtained from the p_{T} extrapolation intervals of pion and kaon spectra (see Fig. 4.19).

The method of extrapolation towards forward rapidity of the p_{T}-extrapolated mid-rapidity charged pion and kaon spectra can be shown as:

$$\begin{aligned}[\mathrm{d}N/\mathrm{d}p_{\mathrm{T}}]^{\pi,\mathrm{K}}_{\mathrm{PbPb,FW}} &= n_y \cdot <N_{coll}> \cdot R_{\mathrm{AA}} \cdot F(p_{\mathrm{T}}, y) \cdot [\mathrm{d}N/\mathrm{d}p_{\mathrm{T}}]^{\pi,\mathrm{K}}_{\mathrm{pp,CB}} \\ &= n_y \cdot F(p_{\mathrm{T}}, y) \cdot [\mathrm{d}N/\mathrm{d}p_{\mathrm{T}}]^{\pi,\mathrm{K}}_{\mathrm{PbPb,CB}}, \end{aligned} \tag{4.14}$$

where $F(p_{\mathrm{T}}, y)$ is the p_{T}-dependent rapidity extrapolation factor of pp spectra. n_y which accounts for unknown quenching at forward rapidity is taken equal to unity for the central value and is varied conservatively from 0.5 to 1.5 to provide a systematic uncertainty on unknown quenching at forward rapidity.

The p_T-dependent rapidity extrapolation in pp collisions is discussed in Chap. 3. In this section the results are presented with $p_T > 3$ GeV/c. Figure 4.20 presents

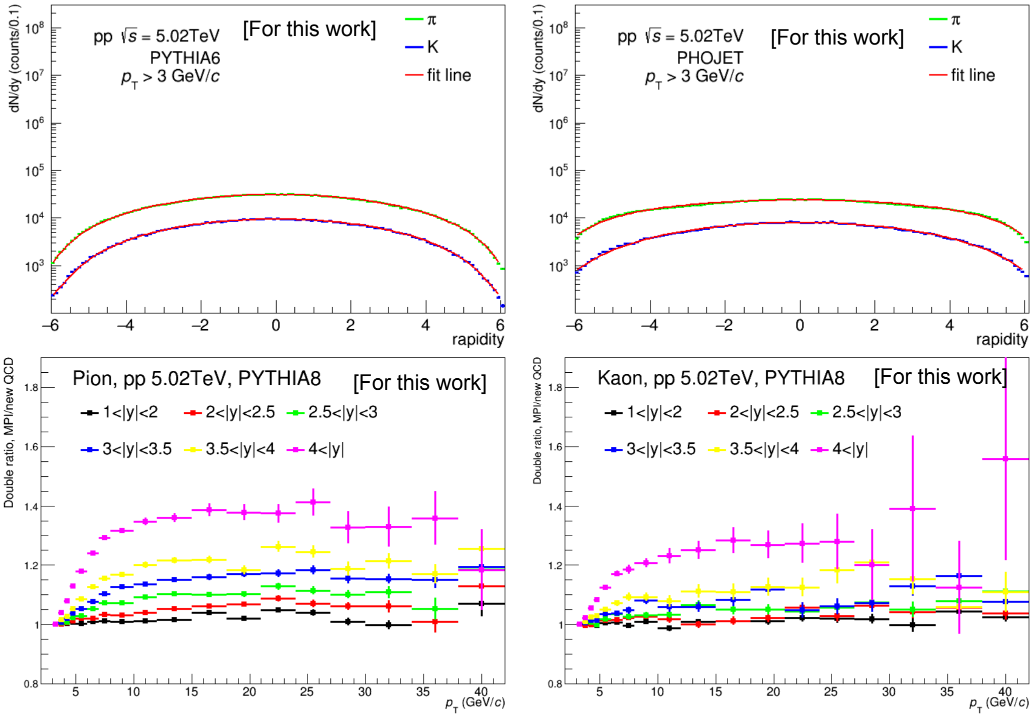

Figure 4.20: Rapidity distribution charged π and K with $p_{\mathrm{T}} > 3$ GeV/c from PYTHIA (upper, left) and PHOJET (upper, right) and corresponding polynomial fit in Pb–Pb collisions at $\sqrt{s_{\mathrm{NN}}} = 5.02$ TeV. PYTHIA8 simulation of the double ratio of the ratio of the generated p_{T} distribution in a given rapidity interval to that in $|y| < 0.8$ for colour reconnection option (CR) $= 0$ to the same ratio for CR $=1$ for charged π (bottom, left) and K (bottom, right) in pp collisions at $\sqrt{s} = 5.02$ TeV.

the rapidity distribution of charged π and K with $p_{\mathrm{T}} > 3$ GeV/c from PYTHIA6 (upper, left) and PHOJET (upper, right) and corresponding polynomial fit. The double ratio of the ratio of the generated p_{T} distribution in a given rapidity interval to that in $|y| < 0.8$ for colour reconnection (CR) [3] option in PYTHIA8: CR $= 0$ to the same ratio for CR $=1$ is shown for charged π (bottom, left) and K (bottom, right). Figure 4.21 presents a comparison of the p_{T} distribution of muons from charged π (left) and charged K (right) decays obtained using the absorber effect parameterization and the polynomial fit function of the rapidity extrapolation (see also Chap. 3). The uncertainty reaches about 9% and 6% for muons from charged π (left) and charged K (right) decays, respectively. Figure 4.22 presents a comparison of the p_{T} distributions of muons from charged π and K decays in $2.5 < y < 4$, obtained using the two strategies for the rapidity extrapolation of the mid-rapidity p_{T} distributions towards forward rapidity e.g. without and with taking into account

---

[3] The simulations were performed for various Colour Reconnection settings CR $= 0$ (MPI), 1 (new QCD), 2 (no colour reconnection).

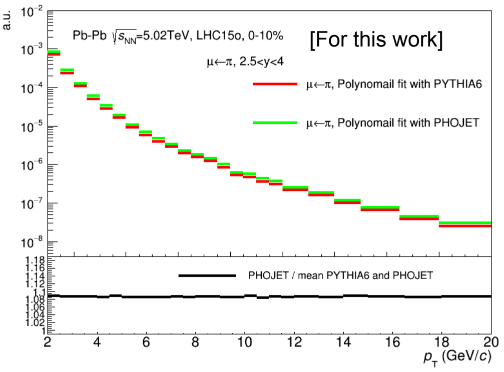

Figure 4.21: Comparison of the p_{T} distribution of muons from charged π (left) and charged K (right) decays obtained using the absorber effect parameterization and the polynomial function of the rapidity extrapolation in central(0-10%) Pb–Pb collisions at $\sqrt{s_{\mathrm{NN}}} = 5.02$ TeV.

a p_{T}-dependent correction. As expected, the differences between the two methods increase with increasing p_{T}. The background contribution becomes smaller with the improved strategy for both the absorber effect description and the rapidity extrapolation, in particular at high p_{T} and for charged K. Indeed, the differences reach about 15% and 50% for muons from charged π and K, respectively, in the high p_{T} region where this background source is small (see background fraction results, Figure 4.24).

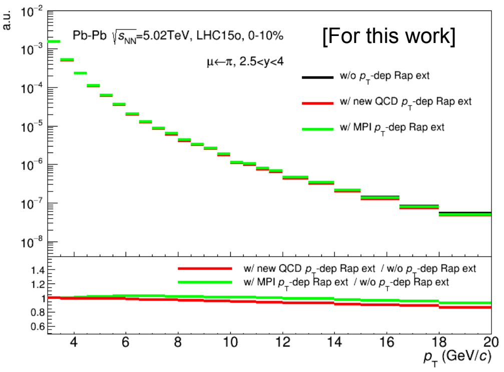

Figure 4.22: Comparison of the p_{T} distribution of muons from charged π (left) and charged K (right) decays obtained using the absorber effect parameterization and the two strategies (QCD and MPI setting) for the p_{T}-dependent rapidity extrapolation in central (0-10%) Pb–Pb collisions at $\sqrt{s_{\mathrm{NN}}} = 5.02$ TeV.

The final distributions of muons from charged π and K decays (Figure 4.23) are obtained considering for the central value the mean between the results obtained with CR options: CR = 0 and 1. The corresponding systematic uncertainty on models is derived from the difference with respect to the mean value (Fig. 4.23, bottom). This systematic uncertainty increases slightly with p_{T} and is in the range 0–5% (0–3%) for muons from charged π (K) decays.

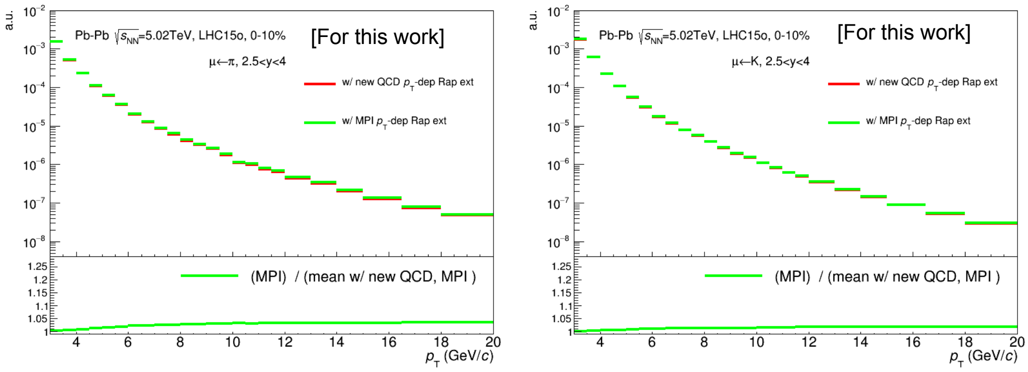

Figure 4.23: Comparison of the p_{T} distribution of muons from charged π (left) and K (right) decays using the new strategy for both absorber description and rapidity extrapolation and different model parameters in central (0-10%) Pb–Pb collisions at $\sqrt{s_{\mathrm{NN}}} = 5.02$ TeV.

Figure 4.24 presents the corresponding decay muon background fraction with respect to inclusive muons as a function of p_{T}. The fraction decreases with increasing p_{T} from about 14-20% ($p_{\mathrm{T}} = 3$ GeV/c) down to about 5-8% ($p_{\mathrm{T}} = 20$ GeV/c) depending on the centrality class. Figure 4.24 also shows the estimated p_{T} distribution for muons from charged pion decays (black) and muons from charged kaon decays (blue) in $2.5 < y < 4$ (bottom left), as well the various systematic uncertainty sources (bottom right) in central (0-10%) Pb-Pb collisions at $\sqrt{s_{\mathrm{NN}}} = 5.02$ TeV. The systematic uncertainty sources affecting the produced muons from pion and kaon decays include contributions from i) the mid-rapidity charged π and K distributions and the p_{T} extrapolation to higher p_{T} (from about 7%–8.5% ($p_{\mathrm{T}} = 2$ GeV/c) to 21–22% ($p_{\mathrm{T}} = 20$ GeV/c)), depending on the particle type, ii) the polynominal rapidity extrapolation (about 9% and 6% for muons from charged π and K decays and the p_{T}-dependent correction of about 6% (3%) for muons from charged π (K) decays) and iii) the absorber effect (about 4%). The various sources are added in quadrature. This leads to a systematic uncertainty in the range from about 12% ($p_{\mathrm{T}} = 3$ GeV/c) until 24% ($p_{\mathrm{T}} = 20$ GeV/c), before propagation to the final results i.e. production cross section of muons from heavy-flavour hadron decays.

Primary charged π and K decay muons in Pb–Pb collisions at $\sqrt{s_{\mathrm{NN}}} = 2.76$ TeV

A strategy similar to that developed for the estimation of the contribution of π and K decay muons in Pb-Pb collisions at $\sqrt{s_{\mathrm{NN}}} = 5.02$ TeV is implemented in Pb-Pb collisions at $\sqrt{s_{\mathrm{NN}}} = 2.76$ TeV.

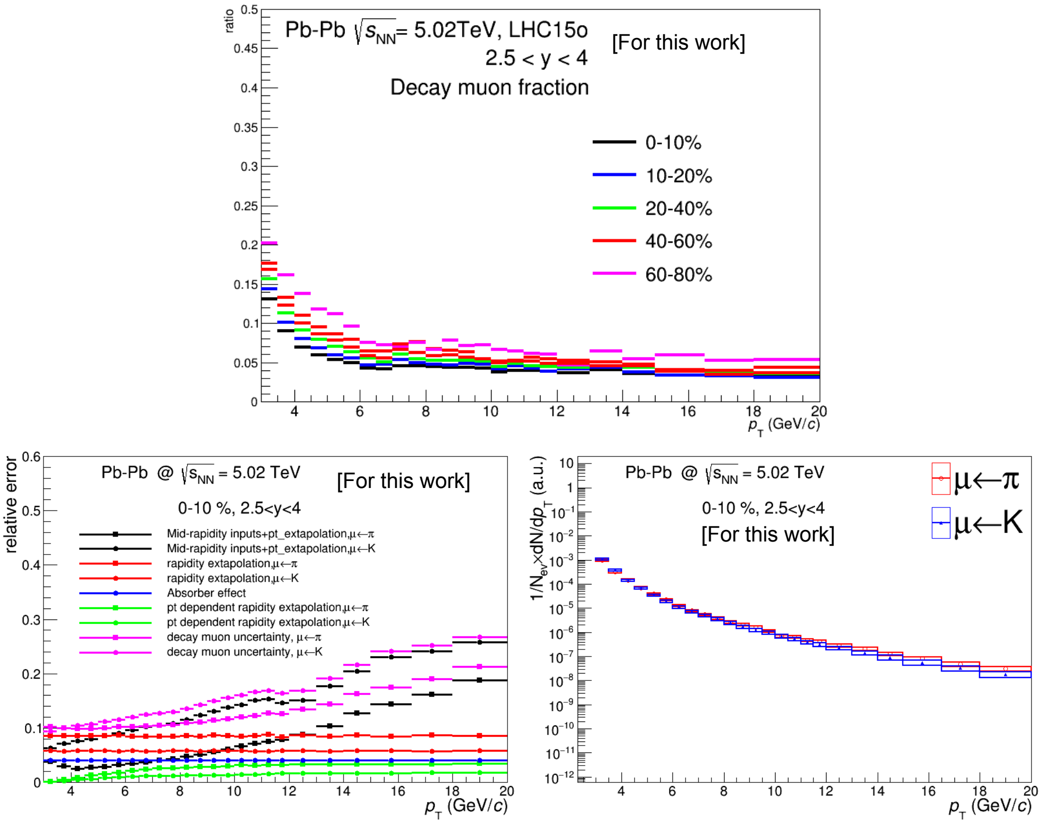

Figure 4.24: Estimated fraction of muons from charged pion and kaon decays relative to inclusive muons as a function of p_{T} for various centrality classes in Pb-Pb collisions at $\sqrt{s_{\mathrm{NN}}} = 5.02$ TeV (upper). Estimated distributions of muons from charged pion and kaon decays (bottom left) and associated systematic uncertainties (bottom right) in $2.5 < y < 4$ in central (0-10%) Pb–Pb collisions at $\sqrt{s_{\mathrm{NN}}} = 5.02$ TeV.

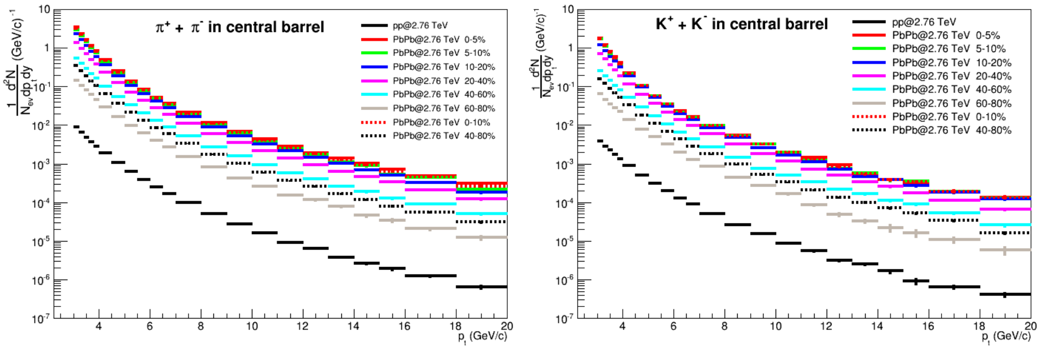

Figure 4.25: Charged pions (left) and charged kaon (right) measured at mid-rapidity with ALICE in Pb–Pb collisions at $\sqrt{s_{\mathrm{NN}}} = 2.76$ TeV [205].

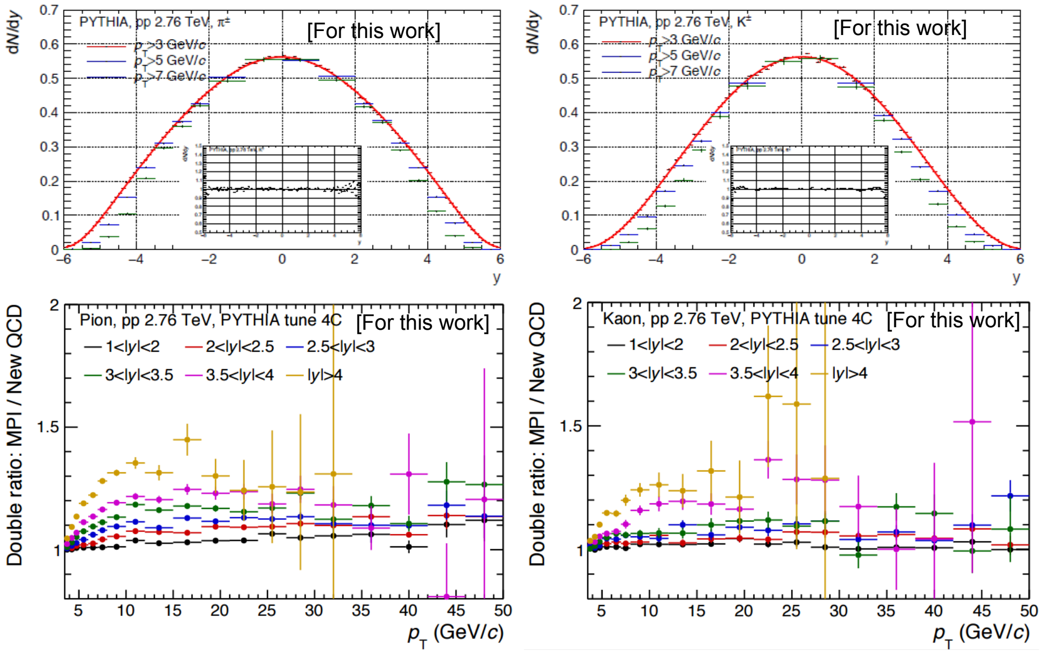

Figure 4.26: Rapidity distribution of charged π (upper, left) and K (upper, right) with $p_{\mathrm{T}} > 3$ GeV/c from PYTHIA6 and corresponding polynomial fit in pp collisions at $\sqrt{s_{\mathrm{NN}}} = 2.76$ TeV. Double ratio of the ratio of the generated p_{T} distribution in a given rapidity interval to that in $|y| < 0.8$ for CR $= 0$ to the same ratio for CR $=1$ for charged π (bottom, left) and K (bottom, right) in pp collisions at $\sqrt{s_{\mathrm{NN}}} = 2.76$ TeV with PYTHIA8 simulations.

Inputs from mid-rapidity measurements ($|y| < 0.8$). We use the mid-rapidity charged pions and kaons distributions measured in pp collisions and in various centrality classes in Pb-Pb collisions. These distributions are shown in Fig. 4.25 after normalization and combining different centralities.

p_{T} **extrapolation (pions and kaons)**. In order to estimate the p_{T} distribution of muons from heavy-flavour hadron decays up to $p_{\mathrm{T}} = 20$ GeV/c, from fast-simulation study [174], one needs to extrapolate the input π and K distributions to higher p_{T}, up to about $p_{\mathrm{T}} = 40$ GeV/c [174] (as already done in pp collisions at $\sqrt{s} = 5.02$ TeV and Pb-Pb collisions at $\sqrt{s_{\mathrm{NN}}} = 5.02$ TeV).

Charged π/K decay muons at forward rapidity. The method of extrapolation towards forward rapidity of the p_{T}-extrapolated mid-rapidity charged pion and kaon spectra is detailed for Pb-Pb collisions at $\sqrt{s_{\mathrm{NN}}} = 5.02$ TeV and is summarized though Eq. 4.14.

Figure 4.26 shows the distribution of rapidity for charged π (upper, left) and K (upper, right) with $p_{\mathrm{T}} > 3$ GeV/c from PYTHIA6 and corresponding polynomial fit. With PYTHIA8 simulations, the double ratio of the ratio of the generated p_{T} distribution in a given rapidity interval to that in $|y| < 0.8$ for CR $= 0$ to the same ratio for CR $=1$ is also presented in the same figure for charged π (bottom, left) and

K (bottom, right).

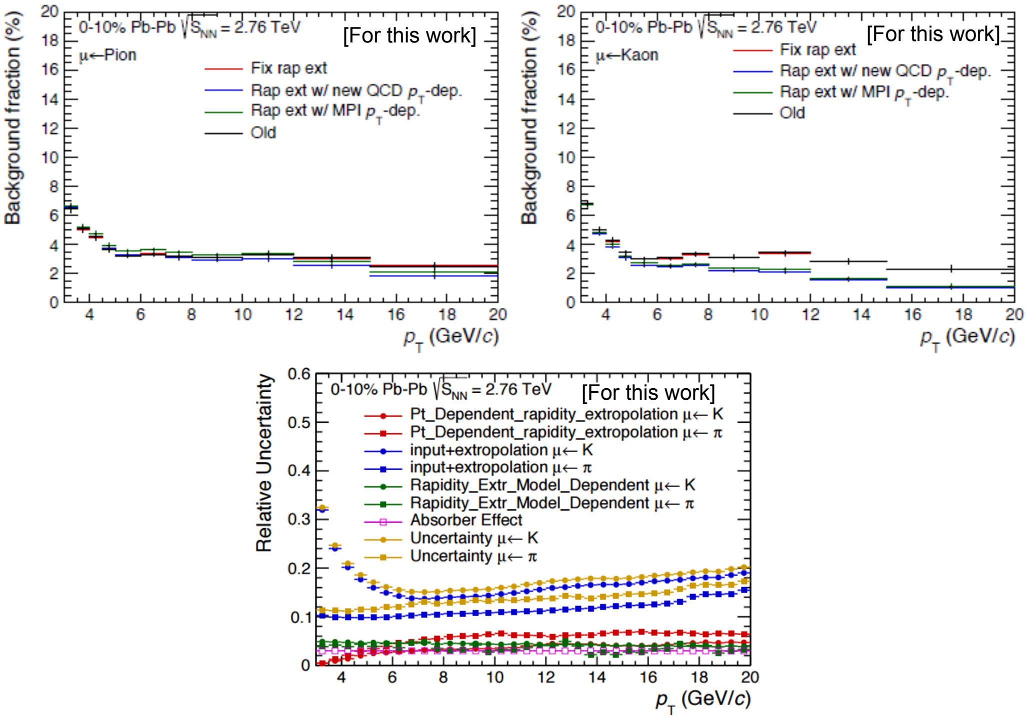

Figure 4.27: Background fraction of charged π decay muons (upper, left) and K decay muons (upper, right) with respect to inclusive muons in cental (0-10%) Pb-Pb collisions at $\sqrt{s_{\rm NN}} = 2.76$ TeV and systematic corresponding systematic uncertainties (bottom).

Figure 4.27 shows the background fraction of charged π decay muons (upper, left) and K decay muons (upper, right) and systematic uncertainties of charged π/K decay muons (bottom). The systematic uncertainty sources affecting the produced muons from pion and kaon decays include, as in Pb-Pb collisions at $\sqrt{s_{\rm NN}} = 5.02$ TeV, contributions from i) the mid-rapidity charged π and K distributions and the $p_{\rm T}$ extrapolation to higher $p_{\rm T}$ (from about 10% and 32% ($p_{\rm T} = 3$ GeV/c) to 18% and 20% ($p_{\rm T} = 20$ GeV/c), depending on the particle type, ii) the polynominal rapidity extrapolation (about 4% and 5% for muons from charged π and K decays) and the $p_{\rm T}$-dependent correction (about 6% (3%) for muons from charged π (K) decays at $p_{\rm T} = 20$ GeV/c), and iii) the absorber effect (about 4%). The various sources are added in quadrature. This leads to a total systematic uncertainty in the range from about 32% ($p_{\rm T} = 3$ GeV/c) until 20% ($p_{\rm T} = 20$ GeV/c), before propagation to the final results i.e. production cross section of muons from heavy-flavour hadron decays.

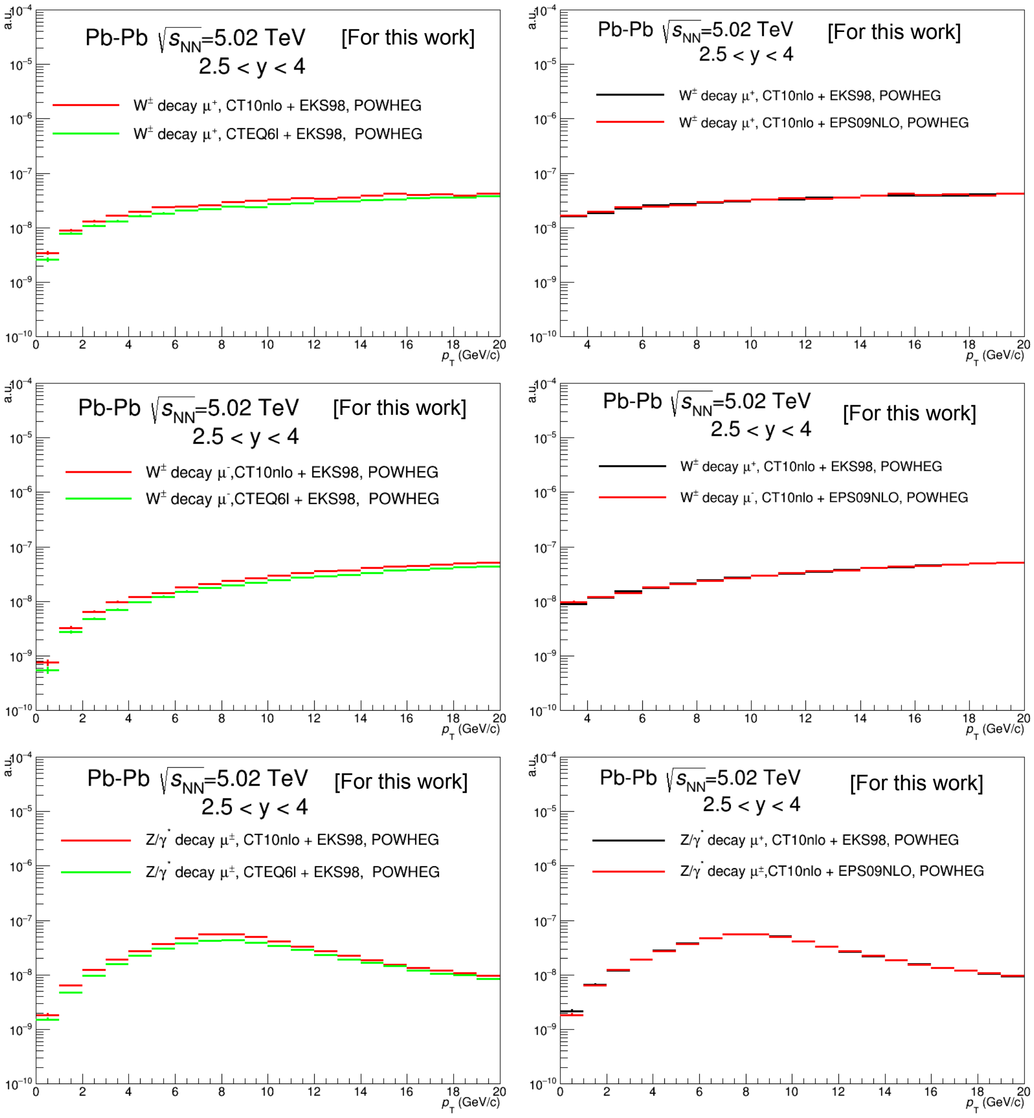

Figure 4.28: Top: W-boson decay μ^+ p_{T} distributions with CT10nlo and CTEQ6l PDF sets with EKS98 nuclear modification (left) and with CT10nlo with EKS98 and EPS09NLO nuclear modification (right). Middle: W-boson decay μ^- p_{T} distributions. Bottom: Z/γ^*-boson decay muon p_{T} distribution. All plots are simulated in rapidity interval $2.5 < y < 4$ for Pb–Pb collisions at $\sqrt{s_{\mathrm{NN}}} = 5.02$ TeV.

4.4.2 Estimation of the background contribution of W,Z/γ^* decay muons

The contribution of muons from W,Z/γ^* -boson decays in Pb–Pb collisions at $\sqrt{s_{\mathrm{NN}}} = 5.02$ and 2.76 TeV is estimated with simulations with the POWHEG event generator. The simulations are performed for pp, nn, np, pn collisions and these four systems are combined as:

$$\frac{\mathrm{d}\sigma_{\mathrm{NN}}}{\mathrm{d}p_{\mathrm{T}}} \approx \frac{Z^2}{A^2} \times \frac{\mathrm{d}\sigma_{\mathrm{pp}}}{\mathrm{d}p_{\mathrm{T}}} + \frac{(A-Z)^2}{A^2} \times \frac{\mathrm{d}\sigma_{\mathrm{nn}}}{\mathrm{d}p_{\mathrm{T}}} + \frac{Z(A-Z)}{A^2} \times (\frac{\mathrm{d}\sigma_{\mathrm{pn}}}{\mathrm{d}p_{\mathrm{T}}} + \frac{\mathrm{d}\sigma_{\mathrm{np}}}{\mathrm{d}p_{\mathrm{T}}}). \quad (4.15)$$

This procedure allows us to properly take into account the valence-quark composition of the colliding nuclei. $\frac{\mathrm{d}\sigma_{\mathrm{NN}}}{\mathrm{d}p_{\mathrm{T}}}$ is the p_{T}-differential cross section per nucleon-nucleon Pb-Pb collision and, A and Z are the mass and atomic number of the Pb nucleus. The W,Z/γ^* decay muon spectra in different centrality classes are scaled by the value of corresponding nuclear overlap function $< T_{\mathrm{AA}} >$.

W,Z/γ^* decay muons in Pb–Pb collisions at $\sqrt{s_{\mathrm{NN}}}$ = 5.02 TeV

Figure 4.28 shows the estimated W,Z/γ^* decay muons at forward rapidity in Pb-Pb collisions at $\sqrt{s_{\mathrm{NN}}} = 5.02$ TeV using KCT10nlo and kCTEQ6l PDF sets and with the EKS98 and EPS09NLO parameterization of the nuclear modification of the PDF (nPDF sets).

The yields and fractions of muons from W,Z/γ^* decays as a function of p_{T} are displayed in Fig. 4.29. They are obtained using POWHEG simulations with CT10 + EPS09NLO set. The yields of muons from W,Z/γ^* decays as a function of p_{T} are normalized per nucleon-nucleon Pb-Pb collision. The nuclear overlap function $< T_{\mathrm{AA}} >$ (Tab. 4.12) is used to get the W,Z/γ^* decay muons in different centrality classes. One observes in particular that at forward rapidity more μ^- than μ^+ from W decays are produced. One can also deduce that the contribution of W,Z/γ^*-decay muons to the inclusive muon p_{T} distribution is negligible for $p_{\mathrm{T}} < 14$ GeV/c for all centrality classes. The fraction of W,Z/γ^*-decay muons varies from about 17% (peripheral collisions) to about 34% (central collisions) in the region $18 < p_{\mathrm{T}} < 20$ GeV/c. This indicates the need to subtract this component in the high-p_{T} region.

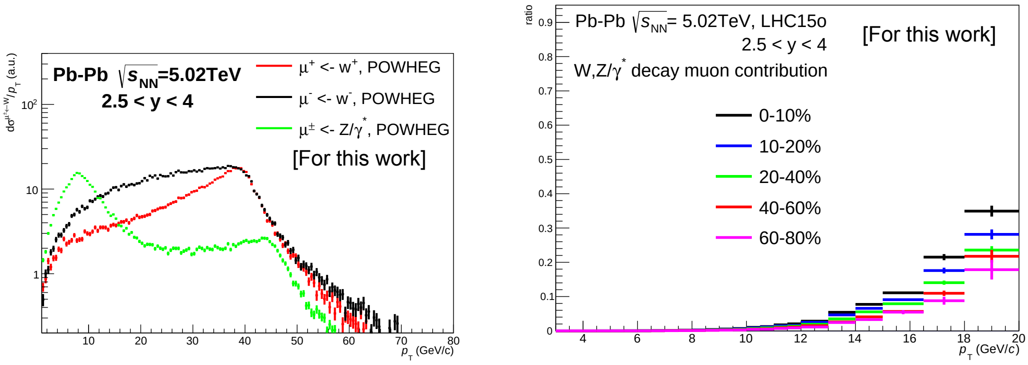

Figure 4.29: Yields and fractions of W,Z/γ^* decay muons with respect to inclusive muons as a function p_{T} at forward rapidity ($2.5 < y < 4$) in Pb-Pb collisions at $\sqrt{s_{\mathrm{NN}}} = 5.02$ TeV.

The POWHEG simulation can reproduce the data in $|y| < 2.6$ and $p_{\mathrm{T}} > 25$ GeV/c with CMS [206], the systematic uncertainty of W,Z/γ^* decay muon is obtained POWHEG simulation with various PDF and nPDF. The results are shown in Fig. 4.30. The systematic uncertainty is 8% (7%) for W (Z/γ^*) decay muons.

This systematic uncertainty is not yet propagated to the muon yield from heavy-flavour hadron decays. Therefore the background fraction comes as an additional factor, reducing this systematic uncertainty.

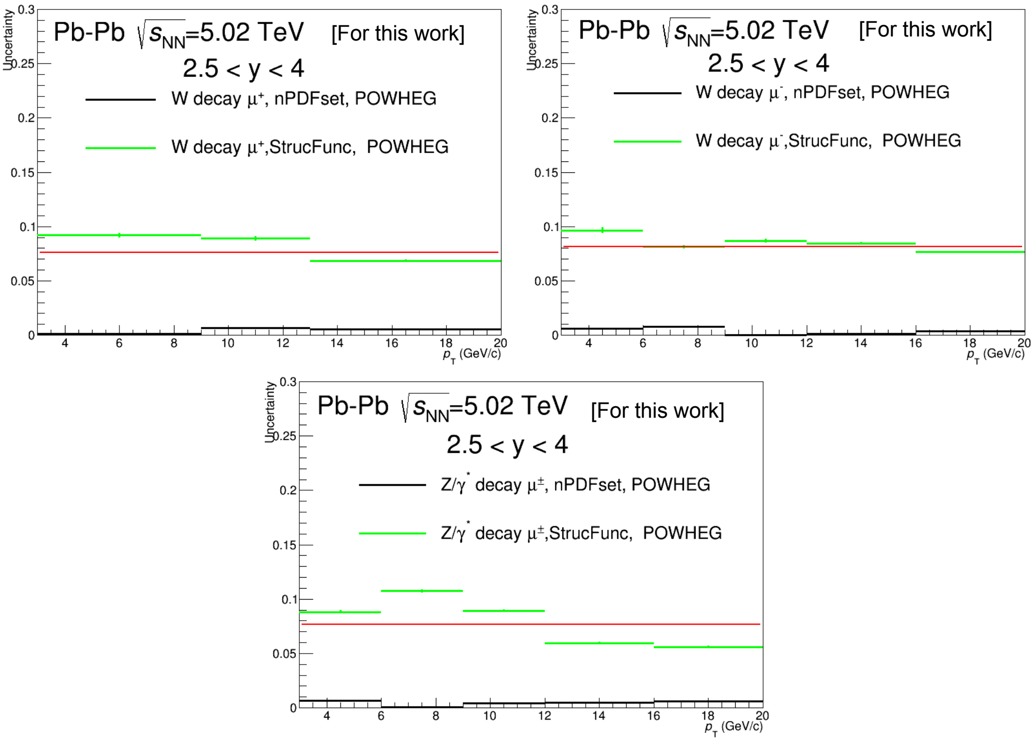

Figure 4.30: Top: systematic uncertainty on W^+ (left) and W^- (right) decay muons for Pb–Pb collisions at $\sqrt{s_{\mathrm{NN}}} = 5.02$ TeV. Bottom: Z/γ^* decay muon systematic uncertainty for Pb–Pb collisions at $\sqrt{s_{\mathrm{NN}}} = 5.02$ TeV.

The μ^--to-μ^+ ratio as a function of p_{T} is shown in Fig. 4.31 before (left) and after (right) the subtraction of muons from W and Z, γ^* decays in central collisions where this contribution is more important. The ratio is larger than unity (about 1.5) in the kinematic region $p_{\mathrm{T}} > 15$ GeV/c, where this background component starts to be significant. It becomes compatible with unity within statistical uncertainties after the subtraction of muons from W and Z bosons and γ^* decays over the whole p_{T} range (and is very similar to the one obtained by subtraction W-decay muons, only).

W,Z/γ^* decay muons in Pb-Pb collisions at $\sqrt{s_{\mathrm{NN}}} = 2.76$ TeV

The background fraction and systematic uncertainty of W,Z/γ^* decay muons in Pb–Pb collisions at $\sqrt{s_{\mathrm{NN}}} = 2.76$ TeV have been found similar to that just reported for Pb–Pb collisions at $\sqrt{s_{\mathrm{NN}}} = 5.02$ TeV.

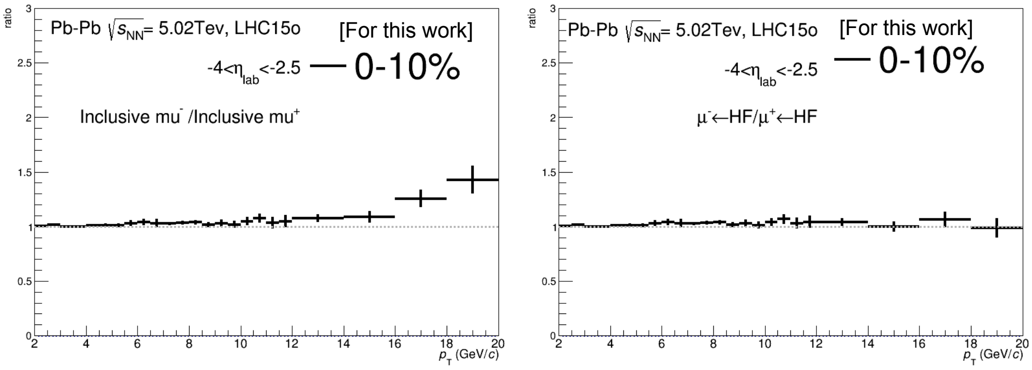

Figure 4.31: μ^-/μ^+ ratio as a function of p_T before (left) and after (right) the subtraction of muons from W and Z/γ^* decays in central Pb–Pb collisions at $\sqrt{s_{NN}}$ = 5.02 TeV.

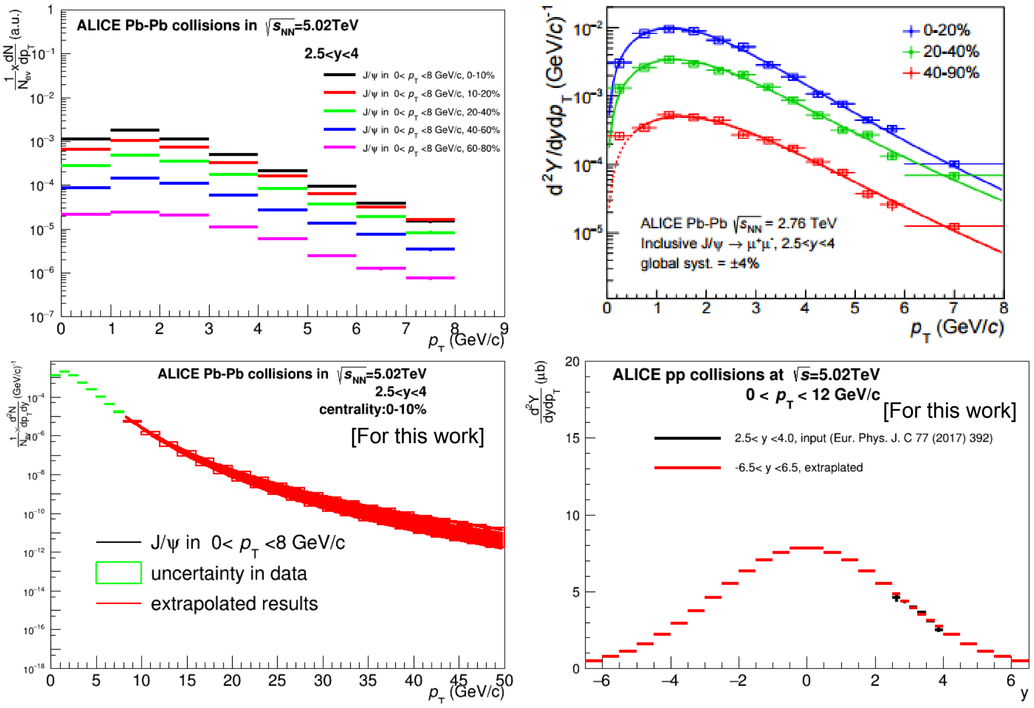

Figure 4.32: J/ψ p_T distributions measured at forward rapidity in Pb–Pb collisions at $\sqrt{s_{NN}}$ = 5.02 TeV (upper left) extrapolated to higher p_T using a power-law function (bottom left), y distributions measured at forward rapidity pp collisions at $\sqrt{s}$ = 5.02 TeV (bottom right), the J/ψ p_T distributions measured at forward rapidity in Pb–Pb collisions at $\sqrt{s_{NN}}$ = 2.76 TeV (upper right).

4.4.3 Estimation of the J/ψ decay muon contribution

The contribution of J/ψ decay muons to the inclusive muon p_{T} distribution is obtained using the strategy already implemented for pp collisions at 5.02 TeV.

The analysis procedure in Pb-Pb collisions at 5.02 TeV and 2.76 TeV uses as inputs the p_{T} and y distributions of J/ψ measured in Pb-Pb collisions at 5.02 TeV [199] and 2.76 TeV [209] (see Fig. 4.32) and includes following steps:

1. Extrapolation in a higher p_T region using the same procedure as that implemented for charged π and K (Fig. 4.32, bottom left);
2. Rapidity extrapolation with a Gaussian function to a wider acceptance with respect to the acceptance of the muon spectrometer is performed to avoid border effects;
3. The p_{T}- and y-extrapolated distributions are used as inputs of fast detector simulations where J/ψ are forced to decay in dimuons. Then the generated yields of muons from J/ψ decays are corrected for the branching ratio and converted into a cross section according to the input J/ψ distributions;
4. The systematic uncertainty is estimated including the systematic uncertainty on measurements and on the p_{T}- and y-extrapolation.

Figure 4.33 (left panels) shows the fraction of J/ψ decay muons relative to inclusive muons that has been estimated in central (0-10%) Pb-Pb collisions at $\sqrt{s_{\mathrm{NN}}}$ = 5.02 and 2.76 TeV using the J/ψ p_{T} and y measured with ALICE at forward rapidity [199, 207, 208, 209]. In the acceptance of the muon spectrometer, it varies in the range 1–3.5% both at 5.02 and 2.76 TeV in the 10% most central Pb–Pb collisions, the maximum being at intermediate p_{T} around 5 GeV/c. The corrsponding systematic uncertainty of J/ψ decay muons increases with increasing p_{T} from 8% to 32% and 4% to 42% in central (0-10%) Pb-Pb collisions at 5.02 and 2.76 TeV.

4.5 Estimation of the systematic uncertainty sources

$$R_{\mathrm{AA}}(p_{\mathrm{T}}) = \frac{\mathrm{d}^2 N_{\mathrm{AA}}/\mathrm{d}p_{\mathrm{T}}\mathrm{d}y}{< \mathrm{T}_{\mathrm{AA}} > \mathrm{d}^2\sigma_{\mathrm{pp}}/\mathrm{d}p_{\mathrm{T}}\mathrm{d}y} \tag{4.16}$$

Several sources of systematic uncertainty affect the heavy-flavour hadron decay muon nuclear modification factor R_{AA} (Eq. 4.16) . These are the systematic uncertainties on the inclusive muon yields, the estimated background, the pp reference cross section and the normalization.

4.5.1 Systematic uncertainty on detector response at $\sqrt{s_{\mathrm{NN}}}$ = 5.02 and 2.76 TeV

Uncertainty on muon tracking efficiency at $\sqrt{s_{\mathrm{NN}}}$ = 5.02 and 2.76 TeV. This systematic uncertainty is estimated by comparing the single-muon tracking

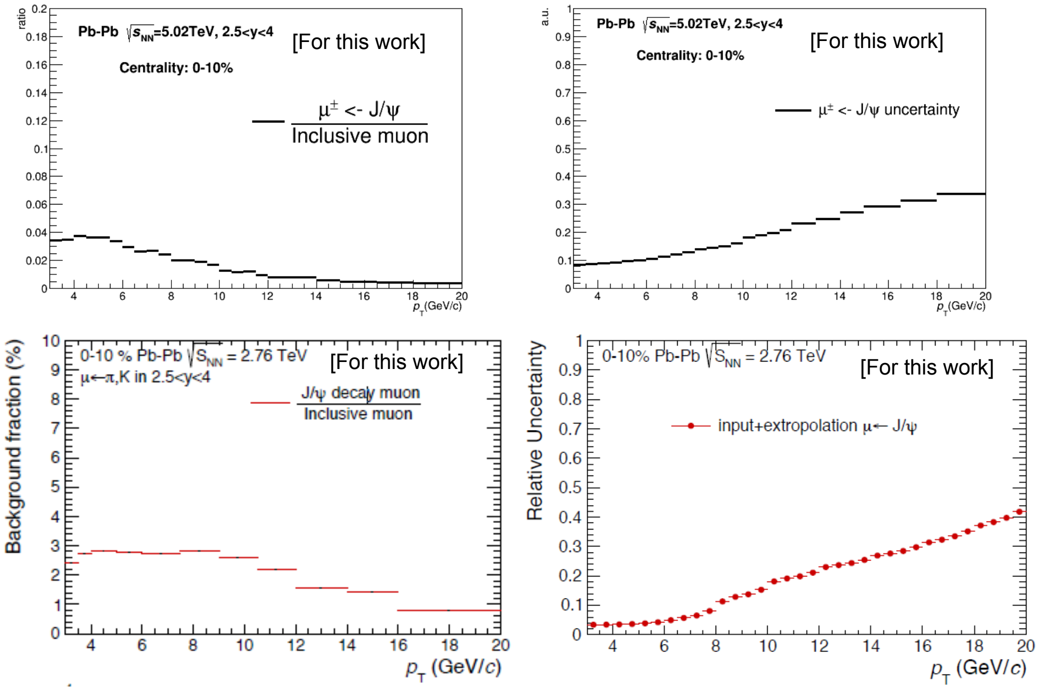

Figure 4.33: Fraction of J/ψ decay muons with respect to inclusive muons as a function $p_{\rm T}$ and corresponding systematic uncertainty in central (0-10%) Pb-Pb collisions at $\sqrt{s_{\rm NN}}$ = 5.02 TeV (top) and 2.76 TeV (bottom).

efficiency in data and simulation. The uncertainty on muon tracking efficiency at $\sqrt{s_{\rm NN}}$ = 5.02 and 2.76 TeV are 1.5% and 2.5%, respectively. These results are discussed in [133, 199]. This systematic uncertainty is correlated as a function of centrality and there is no dependence on $p_{\rm T}$ distribution.

Systematic uncertainty on muon trigger efficiency at $\sqrt{s_{\rm NN}}$ = 5.02 and 2.76 TeV. The systematic uncertainty on the trigger efficiency includes the uncertainty on the intrinsic trigger efficiency and the trigger response (for detail, see chapter 3). Finally these two sources are added in quadrature to get the final systematic uncertainty on trigger efficiency. It amounts to 1.2% (3%) for MSL (MSH) triggers in Pb-Pb collisions at $\sqrt{s_{\rm NN}}$ = 5.02 TeV, and it is 1.4% (2.3%) for MSL (MSH) triggers in Pb-Pb collisions at $\sqrt{s_{\rm NN}}$ = 2.76 TeV (see Ref. [133, 199]). These systematic uncertainties are correlated with centrality.

Systematic uncertainty on muon trigger-tracking matching at $\sqrt{s_{\rm NN}}$ = 5.02 and 2.76 TeV. This systematic uncertainty is related to the choice of the χ^2 cut used in defining the matching between the reconstructed tracks in the tracking chambers and the trigger tracklets [133, 207]. This systematic uncertainty amounts to 0.5% for single muons at both $\sqrt{s_{\rm NN}}$ = 5.02 and 2.76 TeV and is correlated as a function of centrality.

Systematic uncertainty on track resolution and mis-alignment at $\sqrt{s_{\rm NN}}$

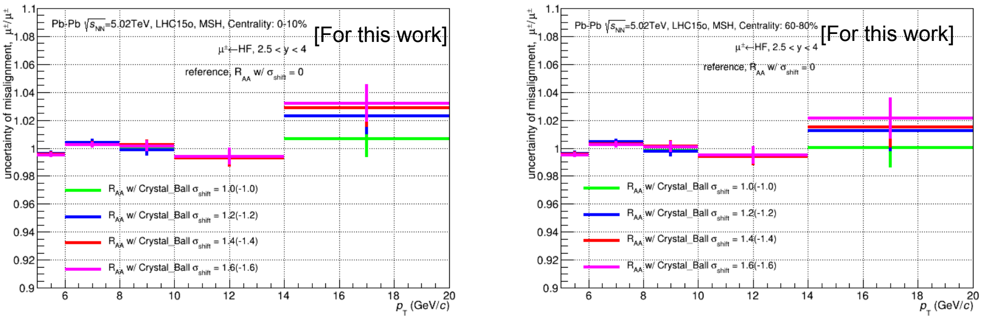

Figure 4.34: Uncertainty on track resolution affecting the R_{AA} of heavy-flavour decay muons for 0-10% and 60-80% centrality classes in Pb-Pb collisions at $\sqrt{s_{\mathrm{NN}}}$ = 5.02 TeV.

= **5.02 and 2.76 TeV**. The strategy to estimate the systematic uncertainty on track resolution and mis-alignment **in Pb-Pb collisions at $\sqrt{s_{\mathrm{NN}}}$ = 5.02 TeV** includes several steps: i)first the smearing parameters are tuned to reproduce the efficiency in full simulations; ii)then the parameters are smeared to reproduce the mis-alignment in full simulations; iii)finally, the uncertainty on track resolution is obtained by comparing the p_{T} spectra corrected for efficiency by reproducing mis-alignment and reproducing efficiency in full simulations.

The track resolution and mis-alignment uncertainty of heavy flavour decay muons is given by:

$$\frac{Pb-Pb_{reproducing-mis-alignment}/pp_{reproducing-mis-alignment}}{Pb-Pb_{reproducing-efficiency}/pp_{reproducing-efficiency}}, \tag{4.17}$$

where the $Pb-Pb_{reproducing-mis-alignment}$ is the p_{T} spectra corrected for efficiency by reproducing mis-alignment, the $Pb-Pb_{reproducing-efficiency}$ is the p_{T} spectra corrected for efficiency by reproducing efficiency in full simulations.

Figure 4.34 shows that the systematic uncertainty on track resolution and mis-alignment affecting the R_{AA} measurement is negligible at low and intermediate p_{T} and the maximum at high p_{T} (14-20 GeV/c) is 3% in 0-10% centrality collisions.

Moreover, the comparison of the ratio of the muon p_{T} distribution of μ^+ to that for μ^- shows that the ratio becomes compatible with unity within uncertainties after the W/Z-boson and γ^* decay muons are subtracted. This is also an indication that the mis-alignment in the 2015 Pb–Pb heavy-ion run is not an issue up at least to $p_{\mathrm{T}} = 20$ GeV/c.

The strategy used to determine the systematic uncertainty on mis-alignment **in Pb-Pb collisions at $\sqrt{s_{\mathrm{NN}}}$ = 2.76 TeV**: 1%×p_{T} (GeV/c), following same strategy as in the Run-1 analysis and published paper [133].

4.5.2 Centrality-dependent systematic uncertainty at $\sqrt{s_{\mathrm{NN}}} = 5.02$ and 2.76 TeV

A systematic uncertainty arising from the decrease of tracking efficiency with increasing centrality as the detector occupancy increases, has to be considered. This systematic uncertainty is evaluated by comparing the muon tracking efficiency versus centrality in data and embedding simulation. Note that it has been checked that the efficiency drop depends little of the muon kinematics ([133, 199, 210]. The corresponding systematic uncertainty varies within 0% (60-80%)-0.5% (0-10%) for single muons in Pb-Pb collisions at $\sqrt{s_{\mathrm{NN}}} = 5.02$ TeV, and it varies within 0% (60-80%)-1% (0-10%) for single muons in Pb-Pb collisions at $\sqrt{s_{\mathrm{NN}}} = 2.76$ TeV.

4.5.3 Systematic uncertainty on muon background subtraction at $\sqrt{s_{\mathrm{NN}}} = 5.02$ and 2.76 TeV

These uncertainties have been discussed when estimating the background sources.

4.5.4 Systematic uncertainty on the pp reference

The systematic uncertainty on the measured p_{T}-differential cross section of muons from heavy-flavour hadron decays in pp collisions at $\sqrt{s} = 5.02$ TeV varies in the range 3%–15% in the region $2 < p_{\mathrm{T}} < 20$ GeV/c (see chapter 3). In pp collisions at $\sqrt{s} = 2.76$ TeV, the systematic uncertainty on the p_{T}-differential cross section of muons from heavy-flavour hadron decays varies in the range 15%–20% in the region $2 < p_{\mathrm{T}} < 10$ GeV/c where the measurement at $\sqrt{s} = 2.76$ TeV is used. At higher p_{T}, ths systematic uncertainty amounts to 23%–25% (see chapter 3).

4.5.5 Systematic uncertainty on normalization

The systematic uncertainty on normalization includes the systematic uncertainty on the normalization factor and $\langle T_{\mathrm{AA}} \rangle$. The systematic uncertainty on $\langle N_{\mathrm{part}} \rangle$ is also used when studying R_{AA} versus centrality by means of $\langle N_{\mathrm{part}} \rangle$. The systematic uncertainty on N_{MB} of 0.3% (0.7%) for MSL (MSH) Pb-Pb data samples at 5.02 TeV and 0.5% (1.6%) for MSL (MSH) in Pb-Pb data samples at 2.76 TeV reflects the difference between the normalization factor (F_{norm}) obtained with the approaches described in Sec. 4.2. This global systematic uncertainty is correlated with p_{T} and centrality. The values and systematic uncertainties of $\langle T_{\mathrm{AA}} \rangle$ and $\langle N_{\mathrm{part}} \rangle$ in Pb-Pb collisions at 2.76 and 5.02 TeV are obtained from a Glauber calculation and extracted from [133, 211]. The systematic uncertainty on $\langle T_{\mathrm{AA}} \rangle$ varies from 3.3% (0–10%) to 6.0% (60–80%) and 4.1% (0–10%) to 7.0% (60–80%) in Pb-Pb collisions 5.02 TeV and 2.76 TeV, respectively. They are correlated with p_{T}.

The $\langle N_{\mathrm{part}} \rangle$ and $\langle T_{\mathrm{AA}} \rangle$ values and systematic uncertainties are summarized in Tab. 4.12 and Tab. 4.13 for Pb-Pb collisions at 5.02 TeV and 2.76 TeV, respectively.

On the other hand, the systematic uncertainties on normalization in pp collisions (needed for R_{AA}) at 2.76 and 5.02 TeV are 3.5% and 2.1%, respectively.

Centrality	$\langle N_{\rm part} \rangle$	$\langle T_{\rm AA} \rangle$
0–10%	359 ± 3.0	23.4 ± 0.78
10–20%	263 ± 3.6	14.3 ± 0.46
20–40%	159.6 ± 2.6	6.754 ± 0.22
40–60%	69.97 ± 1.4	1.949 ± 0.081
60–80%	23 ± 0.61	0.401 ± 0.024

Table 4.12: $\langle N_{\rm part} \rangle$ and $\langle T_{\rm AA} \rangle$, and associated systematic uncertainties in Pb-Pb collisions at $\sqrt{s_{\rm NN}} = 5.02$ TeV. Extracted from [211].

Centrality	$\langle N_{\rm part} \rangle$	$\langle T_{\rm AA} \rangle$
0–10%	357 ± 4	23.48 ± 0.97
10–20%	261 ± 4	14.43 ± 0.57
20–40%	157 ± 3	6.85 ± 0.28
40–60%	69 ± 2	2.00 ± 0.11
60–80%	23 ± 1	0.42 ± 0.03

Table 4.13: $\langle N_{\rm part} \rangle$ and $\langle T_{\rm AA} \rangle$, and associated systematic uncertainties in Pb-Pb collisions at $\sqrt{s_{\rm NN}} = 2.76$ TeV. Extracted from [133].

4.5.6 Summary of systematic uncertainties

A summary of the various systematic uncertainties considered in Pb-Pb collisions at $\sqrt{s_{\rm NN}} = 5.02$ and 2.76 TeV are presented in Tab. 4.14 and 4.15, respectively. All the listed systematic uncertainties are then propagated to the various measurements. Note that we vary the mis-alignment uncertainty in pp and Pb-Pb collisions at $= 5.02$ TeV simultaneously and use a $1\% \times p_{\rm T}$ systematic uncertainty in Pb-Pb collisions $\sqrt{s_{\rm NN}} = 2.76$ TeV to calculate total uncertainty on $R_{\rm AA}$. The $n_{\rm y}$ parameter (Eq. 4.14) which is varied conservatively from 0.5 to 1.5 to provide a systematic uncertainty on unknown quenching at forward rapidity at both $\sqrt{s_{\rm NN}} = 5.02$ and 2.76 TeV Pb-Pb collisions. All systematic uncertainties entering in the measurement of the $R_{\rm AA}$ affect the normalized $p_{\rm T}$-differential yields with the exception of the contribution from the pp reference and $< T_{\rm AA} >$. These $p_{\rm T}$-differential yields and $R_{\rm AA}$ results are discussed in Chap. 5.

Figure 4.35 shows the various systematic uncertainty sources affecting the $R_{\rm AA}$ measurement in the 0–10% centrality class which are combined in Pb-Pb collisions at $\sqrt{s_{\rm NN}} = 5.02$ TeV.

Tracking efficiency	1.5%
Trigger efficiency	1.2% (MSL), 3% (MSH)
Matching efficiency	0.5%
Mis-alignment	0-1% (60-80%) - 0-3% (0-10%)
Embedding	0 (60-80%) - 0.5% (0-10%)
W,Z/γ^* decay muons (dominant at high p_{T})	4.2% (1.5%) in 0-10% (60-80%)
π, K decay muons (dominant at low p_{T})	1.6% (2.5%) in 0-10% (60-80%)
J/ψ decay muons	<0.4%
F_{norm}	0.3% (MSL), 0.7% (MSH)
$\langle T_{\mathrm{AA}} \rangle$	3.3% (6%) in 0-10% (60-80%)
pp reference	2%–4% (without Mis-alignment))
n_{y}	4% (6%) in 0-10% (60-80%), $p_{\mathrm{T}} = 3$ GeV/c

Table 4.14: Systematic uncertainties considered in the measurement of muons from heavy-flavour hadron decays in Pb-Pb collisions at $\sqrt{s_{\mathrm{NN}}} = 5.02$ TeV.

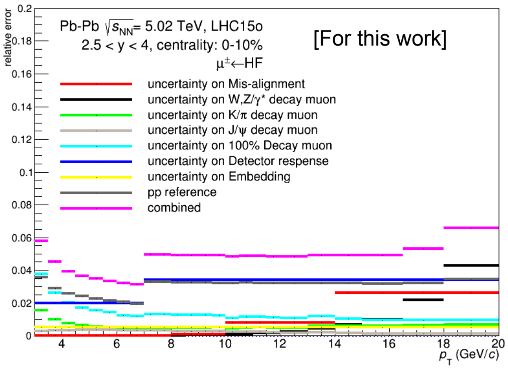

Figure 4.35: Various systematic uncertainty sources affecting the R_{AA} measurement in the 0–10% centrality class which are combined (Uncertainty on track resolution (misalignment) is not considered) in Pb-Pb collisions at $\sqrt{s_{\mathrm{NN}}} = 5.02$ TeV.

Tracking efficiency	2.5%
Trigger efficiency	1.4% (MSL), 2.3% (MSH)
Matching efficiency	0.5%
Mis-alignment	1%×p_{T}
Embedding	0 (60-80%) - 1% (0-10%)
W,Z/γ^* decay muons (dominant at high p_{T})	4.4% (1.6%) in 0-10% (60-80%)
π, K decay muons (dominant at low p_{T})	3.4% (4.5%) in 0-10% (60-80%)
J/ψ decay muons	<0.3%
F_{norm}	0.4% (MSL), 1.6% (MSH)
$\langle T_{\mathrm{AA}} \rangle$	4.1% (7%) in 0-10% (60-80%)
pp reference (data)	15%–20% ($3 < p_{\mathrm{T}} < 10$ GeV/c)
pp reference (FONLL)	23%–25% ($10 < p_{\mathrm{T}} < 20$ GeV/c)
n_{y}	4% (6%) in 0-10% (60-80%), $p_{\mathrm{T}} = 3$ GeV/c

Table 4.15: Systematic uncertainties considered in the measurement of muons from heavy-flavour hadron decays in Pb-Pb collisions at $\sqrt{s_{\mathrm{NN}}} = 2.76$ TeV.

Chapter 5

Open heavy-flavour hadron decay muon measurement results in Pb–Pb collisions at $\sqrt{s_{\mathrm{NN}}} = 5.02$ and 2.76 TeV

In this chapter, we focus on the open heavy-flavour hadron decay muon measurement results in Pb–Pb collisions at $\sqrt{s_{\mathrm{NN}}} = 5.02$ and 2.76 TeV with a particular emphasis on the results at $\sqrt{s_{\mathrm{NN}}} = 5.02$ TeV in Sec. 5.1, 5.2 and 5.3. This allows us to study also the dependence on the collision system. The results are discussed and compared with other ALICE measurements obtained in a different kinematic region and with measurements of other LHC experiments in Sec. 5.4. The comparisons with model predictions are presented in Sec. 5.5. The conclusion of this chapter is shown in Sec. 5.6.

5.1 Open heavy-flavour hadron decay muon measurement results in Pb–Pb collisions at $\sqrt{s_{\mathrm{NN}}} = 5.02$ TeV

All the results concerning the Pb–Pb collisions at $\sqrt{s_{\mathrm{NN}}} = 5.02$ TeV are obtained using muon-triggered events i.e. MSL- and MSH-triggered events in $2 < p < 7$ GeV/c and $7 < p < 20$ GeV/c, respectively.

5.1.1 Normalized p_{T}-differential yields of muons from heavy-flavour hadron decays

Figure 5.1 presents the corrected p_{T}-differential normalized yields in various centrality intervals in the range 0–80% for muons from heavy-flavour hadron decays at forward rapidity ($2.5 < y < 4$) in Pb–Pb collisions at $\sqrt{s_{\mathrm{NN}}} = 5.02$ TeV. The vertical bars are the statistical uncertainties and the open boxes represent the systematic uncertainties. The statistics collected with MSH allows us to perform the measurement over a wide p_{T} interval, up to $p_{\mathrm{T}} = 20$ GeV/c, even in peripheral collisions (60–80%). One observes that the yields increase by more than one order of magnitude from peripheral to central collisions.

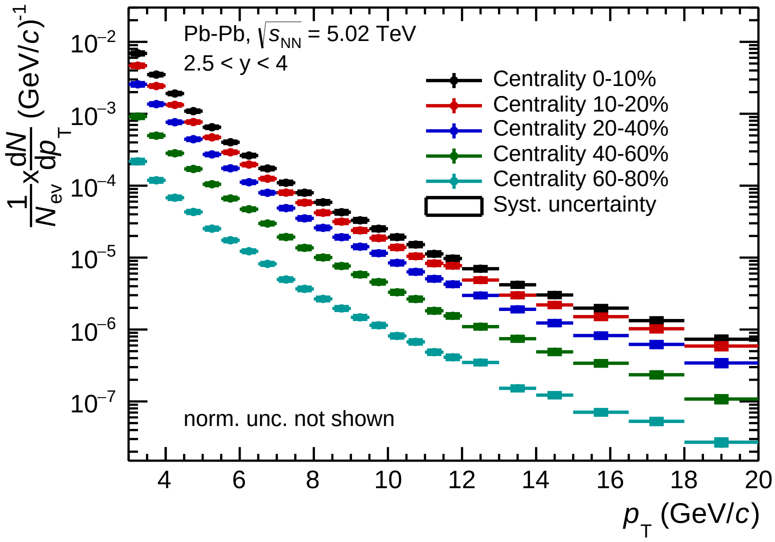

Figure 5.1: Normalized and corrected p_T-differential yields of muons from heavy-flavour hadron decays in Pb–Pb collisions at $\sqrt{s_{NN}} = 5.02$ TeV. The distributions are shown in various centrality inervals mentioned in the figure.

5.1.2 The p_T-differential R_{AA} of muons from heavy-flavour hadron decays

Figure 5.2 shows the p_T-differential nuclear modification factor of muons from heavy-flavour hadron decays in several centrality intervals in the range 0–80% in Pb–Pb collisions at $\sqrt{s_{NN}} = 5.02$ TeV. The vertical bars are the statistical uncertainties. The systematic uncertainties are displayed by the open boxes and include all contributions discussed in chapter 4. The normalization uncertainty is displayed at R_{AA} =1. The results are provided in wide p_T interval from $p_T = 3$ GeV/c to p_T $= 20$ GeV/c for all centrality classes. The pp reference needed to compute the R_{AA} is discussed in chapter 3.

One observes a clear increase of the suppression with increasing centrality which reaches a factor of about 3 at intermediate p_T ($7 < p_T < 14$ GeV/c) in the 10% most central collisions. The suppression decreases towards the low p_T region. There is also a tendency of slightly less suppression in the high-p_T region where beauty dominates over charm according to FONLL predictions (see Chap. 3). Therefore, the results provide a precise measurement of beauty suppression at high p_T. As it will be discussed later, the suppression in all centrality classes is related to in-medium energy loss effect induced by the hot and dense medium. The effect is more visible in central collisions than in peripheral collisions.

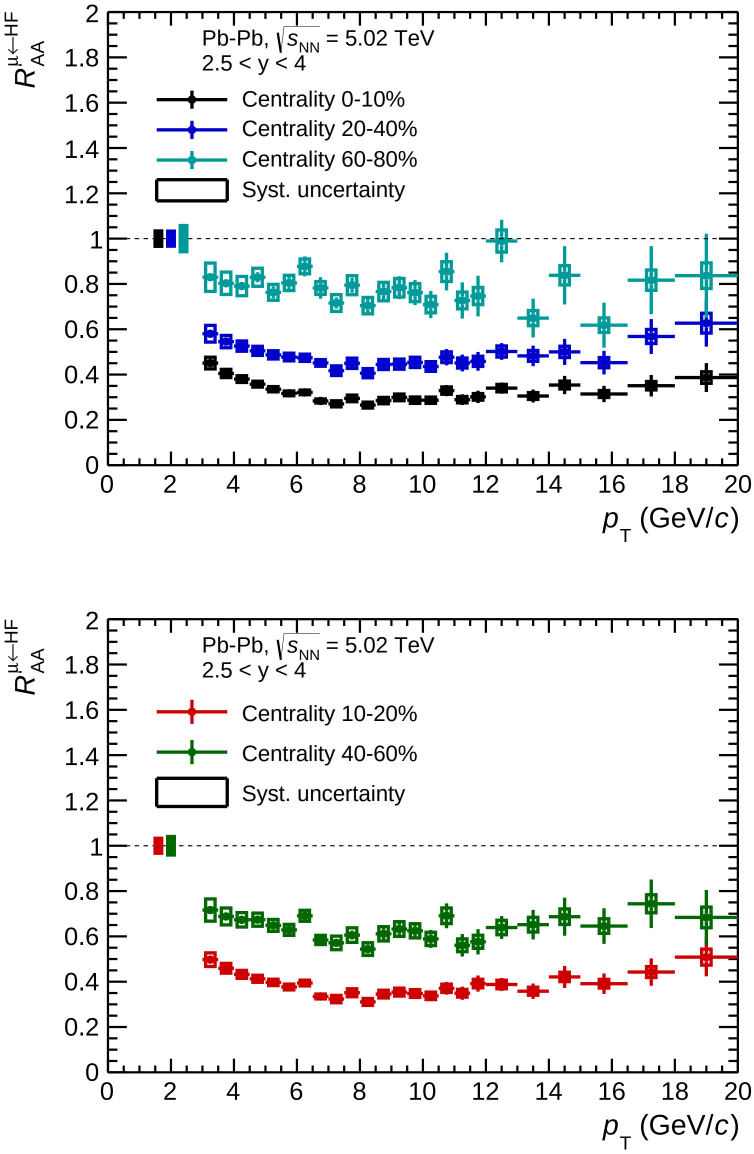

Figure 5.2: R_{AA} of muons from heavy-flavour hadron decays in various centrality classes in the range 0–80% for Pb–Pb collisions at $\sqrt{s_{\mathrm{NN}}} = 5.02$ TeV. Vertical bars are the statistical uncertainties. Open boxes represent the systematic uncertainties, except the systemactic uncertainty on normalization which is shown in full boxes at $R_{\mathrm{AA}} = 1$.

5.1.3 Comparison with R_{pPb} results in p-Pb collisions at 5.02 TeV

In p-Pb collisions, where the formation of a hot and dense medium (the so-called Quark-Gluon Plasma, QGP) is not expected, the suppression of heavy-flavour decay muon yields with respect to pp collisions is not observed [167]. Figure 5.3 shows

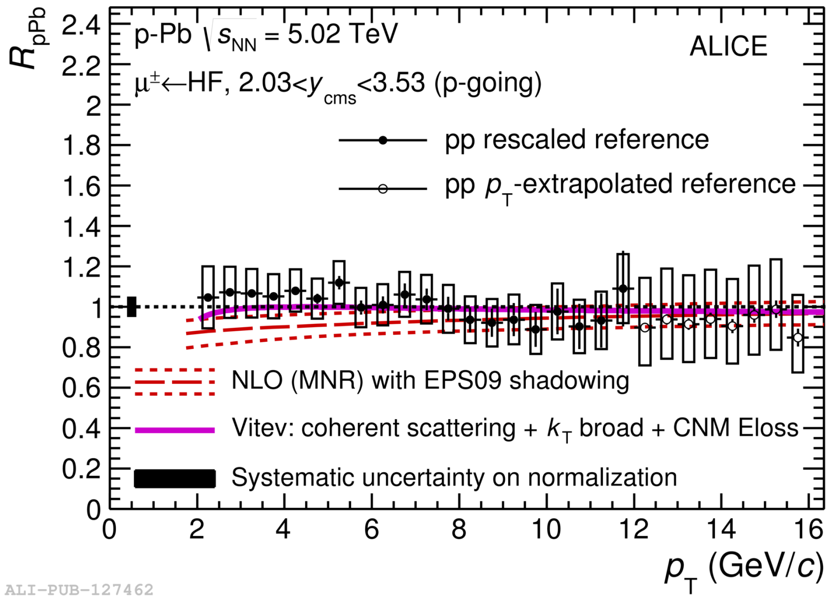

Figure 5.3: Nuclear modification factor of muons from heavy-flavour hadron decays as a function of p_T for p-Pb collisions at $\sqrt{s_{NN}} = 5.02$ TeV at forward rapidity (2.03 $< y_{cms} <$ 3.53) compared to model predictions [186, 212, 218]. Figure taken from Ref. [214].

the heavy-flavour decay muon nuclear modification factor R_{pPb} as a function of p_T in p-Pb collisions at $\sqrt{s_{NN}} = 5.02$ TeV at forward rapidity ($2.03 < y_{cms} < 3.53$) compared with model predictions [186, 212, 218]. The p_T-differential heavy-flavour decay muon nuclear modification factor R_{pPb} at forward rapidity is compatible with unity within uncertainties over the whole p_T range. Therefore, we can conclude that cold nuclear matter (CNM) effects are small and that the strong suppression of the yields of muons from heavy-flavour hadron decays observed in the 10% most central Pb-Pb collisions should result from final-state effects related to the heavy-quark in-medium energy loss.

5.1.4 The p_T-integrated R_{AA} of muons from heavy-flavour hadron decays

The centrality dependence of R_{AA} of muons from heavy-flavour hadron decays is investigated via the mean number of participant nucleons $\langle N_{part}\rangle$ in various p_T intervals in the high-p_T region where the beauty contribution dominates over charm. The systematic uncertainties which are fully correlated between centrality classes (pp reference, normalization) are shown as full boxes. The remaining systematic uncertainties which are fully uncorrelated are shown as open boxes. The results presented in Fig. 5.4 confirm the trends evidenced in Fig. 5.2 with the p_T-differential R_{AA} of muons from heavy-flavour hadron decays, namely a decrease of R_{AA} from peripheral to central collisions for the three p_T intervals in the region $7 < p_T <$

20 GeV/c, with a slight increase of $R_{\rm AA}$ with increasing $p_{\rm T}$.

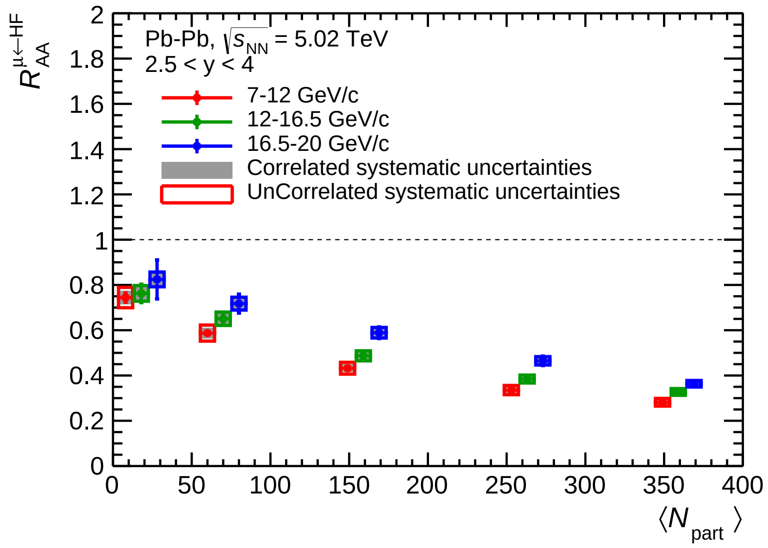

Figure 5.4: $R_{\rm AA}$ as a function of $\langle N_{\rm part}\rangle$ for muons from heavy-flavour hadron decays in Pb–Pb collisions at $\sqrt{s_{\rm NN}} = 5.02$ TeV. The distributions are shown in various $p_{\rm T}$ intervals mentioned in the figure. For each centrality class, the set of points for the different $p_{\rm T}$ intervals are displaced horizontally for better visibility.

5.2 Results in Pb–Pb collisions at $\sqrt{s_{\rm NN}} = 2.76$ TeV

In Pb–Pb collisions at $\sqrt{s_{\rm NN}} = 2.76$ TeV the results are also obtained by combining MSL- and MSH-triggered events, as at $\sqrt{s_{\rm NN}} = 5.02$ TeV.

Figure 5.5 presents the $R_{\rm AA}$ of muons from heavy-flavour decays in $2.5 < y < 4$, as a function of $p_{\rm T}$ in central and peripheral collisions. The vertical bars are the statistical uncertainties. The $p_{\rm T}$-dependent systematic uncertainties are displayed by the open boxes and include all the contributions previously discussed in chapter 4, except the normalization uncertainty that is displayed at $R_{\rm AA} = 1$. A large suppression is observed which reaches a factor of about 3 in the 10% most centrality collisions for the interval $7 < p_{\rm T} < 14$ GeV/c. Note that $R_{\rm AA}$ results can reach 20 GeV/c only in the 10% most centrality collisions. The suppression is smaller in peripheral collisions (60-80% centrality class). At higher $p_{\rm T}$, there is a tendency of a smaller suppression.

The resulting $R_{\rm AA}$ is displayed as function of $\langle N_{\rm part}\rangle$ in Fig. 5.6 in the $p_{\rm T}$ region $6 < p_{\rm T} < 12$ GeV/c where the beauty contribution to heavy-flavour decay muons is dominant according to FONLL simulations (see Chap. 3). The contribution to the total systematic uncertainty which is fully correlated between centrality classes (filled boxes), including the pp reference and normalization, is displayed separately

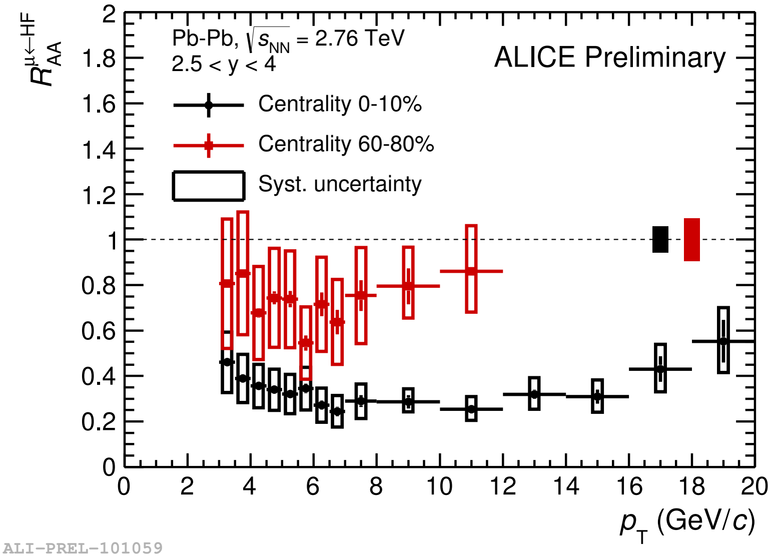

Figure 5.5: R_{AA} of muons from heavy-flavour hadron decays in various centrality classes in the range 0–10% and 60-80% for Pb–Pb collisions at $\sqrt{s_{NN}} = 2.76$ TeV.

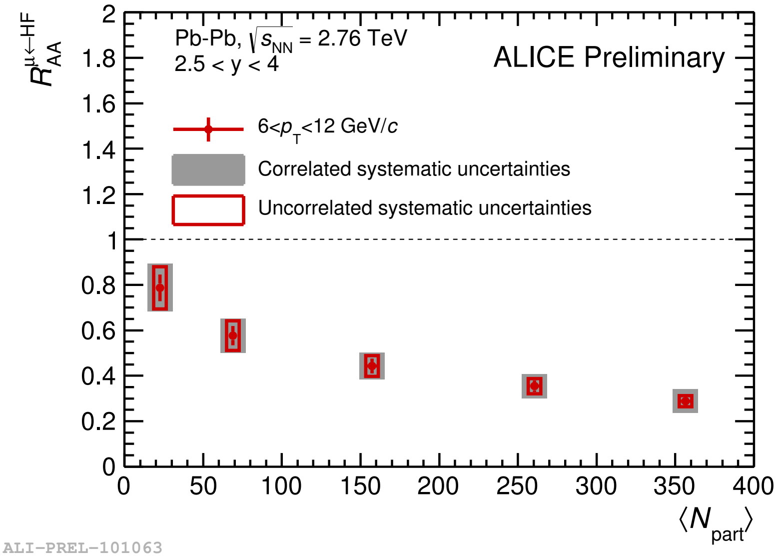

Figure 5.6: R_{AA} as a function of $\langle N_{\mathrm{part}} \rangle$ for muons from heavy-flavour hadron decays in Pb-Pb collisions at $\sqrt{s_{NN}} = 2.76$ TeV. The distributions is shown in $6 < p_T < 12$ GeV/c.

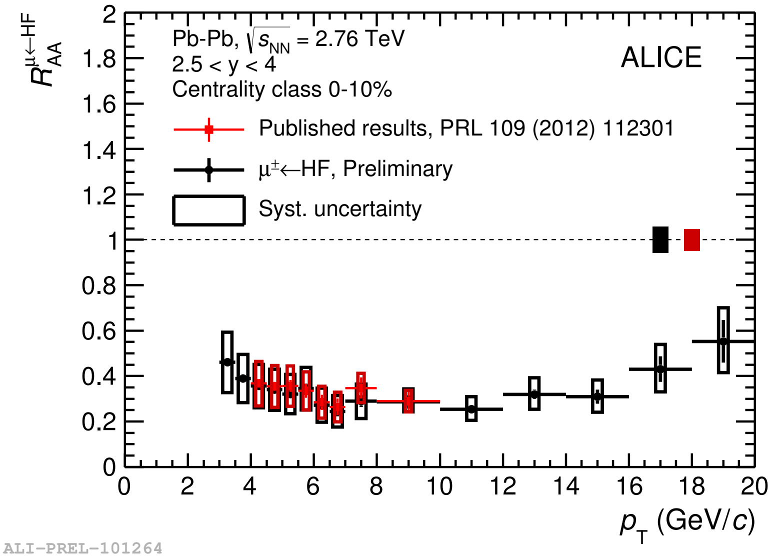

Figure 5.7: Comparison of the R_{AA} of heavy-flavour decay muons based on the analysis of MSL(MSH) trigger events collected during the 2011 run, with the published heavy-flavour decay muon R_{AA} based on the analysis of minimum-bias trigger events that were collected during the 2010 run of Pb-Pb collisions at $\sqrt{s_{NN}} = 2.76$ TeV.

from the remaining uncorrelated systematic uncertainty (open boxes). The R_{AA} of muons from heavy-flavour decays at forward rapidity decreases with increasing centrality, the suppression reaching a factor of 3-4 in the 10% most central collisions.

Figure 5.7 shows that compatible results are obtained in the overlap p_T range ($4 < p_T < 10$ GeV/c) with the published results (taken from Ref. [133]). The published results used the Pb-Pb data collected during the 2010 run and are based on the analysis of minimum-bias (MB) trigger events.

5.3 Comparison of results at $\sqrt{s_{NN}} = 5.02$ and 2.76 TeV in Pb-Pb collisions

A comparison between results obtained in Pb–Pb collisions at $\sqrt{s_{NN}} = 2.76$ TeV and 5.02 TeV is presented in Fig. 5.8 for central (0–10%) and peripheral (60%–80%) collisions. A similar suppression is measured at both beam energies within uncertainties. This similar suppression effect can be explained by a model [215] which considers two effects, the harder spectra and denser medium, that counterbalance.

Moreover, one can notice that at $\sqrt{s_{NN}} = 2.76$ TeV the systematic uncertainties are larger than the ones estimated at $\sqrt{s_{NN}} = 5.02$ TeV. This is mainly due to the larger systematic uncertainties on the pp reference (see chapter 3) and mis-alignment (1% × p_T) at the lower beam energy. Finally, the statistical uncertainties are also large at $\sqrt{s_{NN}} = 2.76$ TeV. Also the new data-driven strategy for the estimation of the contribution of muons from charged π (K) decays in Pb-Pb collisions at $\sqrt{s_{\mathrm{NN}}}$ = 5.02 TeV has improved significant the uncertainties in the low/intemediate p_{T} region.

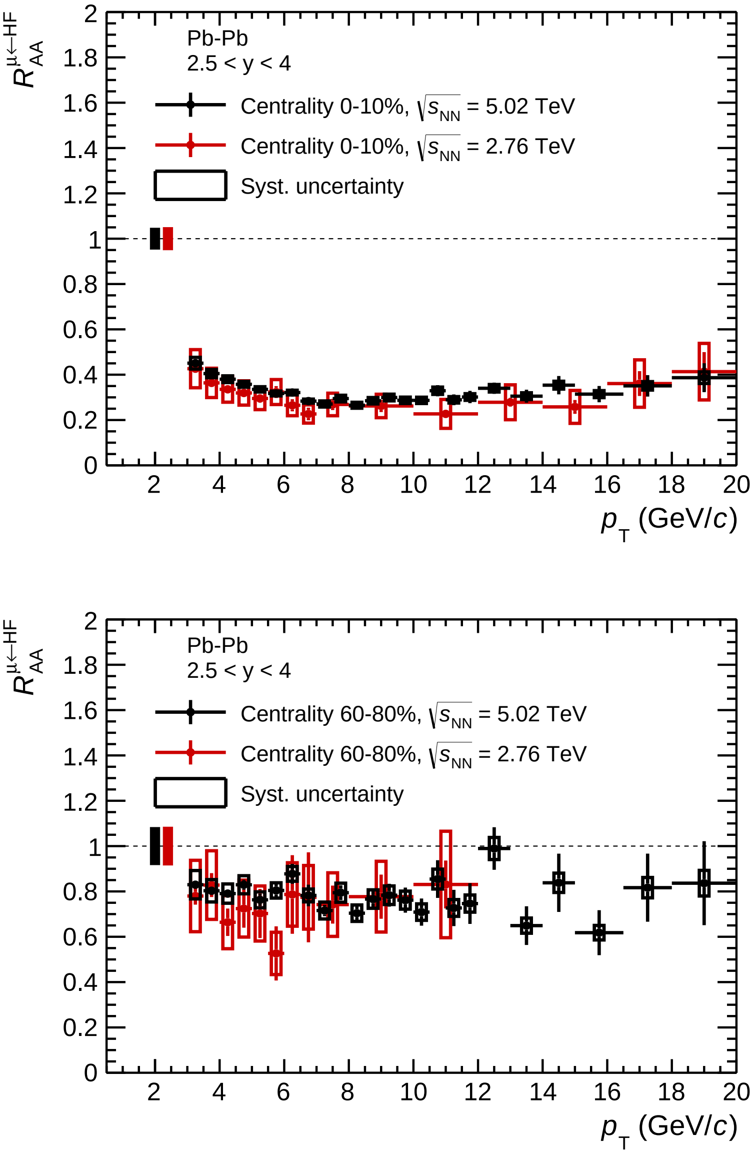

Figure 5.8: Comparison of the p_{T}-differential R_{AA} of muons from heavy-flavour hadron decays in Pb–Pb collisions at $\sqrt{s_{\mathrm{NN}}} = 5.02$ TeV with that obtained at $\sqrt{s_{\mathrm{NN}}}$ = 2.76 TeV for central collisions (top) and peripheral collisions (bottom).

5.4 Comparison with other experiment results

5.4.1 Comparison with heavy-flavour hadron decay electron R_{AA} results in Pb-Pb collisions at 5.02 TeV with ALICE

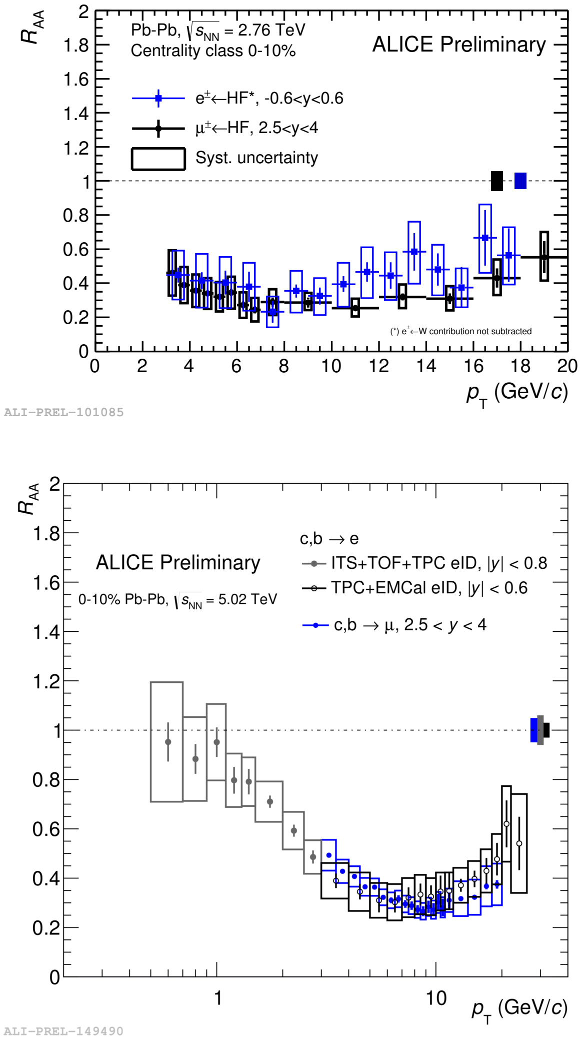

Figure 5.9: Upper: comparison of R_{AA} of heavy-flavour decay muons at forward rapidity and heavy-flavour decay electrons at mid-rapidity in Pb-Pb collisions at $\sqrt{s_{\mathrm{NN}}} = 2.76$ TeV. Bottom: comparison of R_{AA} of heavy-flavour decay muons at forward rapidity and heavy-flavour decay electrons at mid-rapidity in Pb-Pb collisions at $\sqrt{s_{\mathrm{NN}}} = 5.02$ TeV.

The R_{AA} of heavy-flavour decay muons at forward rapidity is similar to that of heavy-flavour decay electrons at mid-rapidity at both $\sqrt{s_{\mathrm{NN}}} = 2.76$ TeV and $\sqrt{s_{\mathrm{NN}}} = 5.02$ TeV Pb-Pb collisions (Fig. 5.9). These results indicate that heavy quarks suffer a strong in-medium energy loss in a wide rapidity internal. Note that for heavy-flavour decay electrons in Pb-Pb collisions at $\sqrt{s_{\rm NN}}$ = 2.76 TeV, the W,Z/γ^* contribution is not subtracted.

5.4.2 Comparison with heavy-flavour hadron decay muon $R_{\rm AA}$ measurement in Pb-Pb collisions at 2.76 TeV with ATLAS

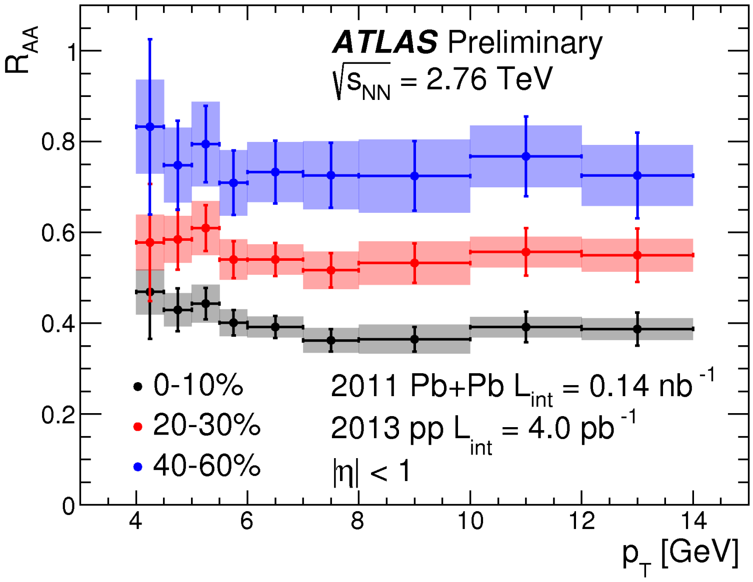

Figure 5.10: Nuclear modification factor of muons from heavy-flavour hadron decays as a function of $p_{\rm T}$ for Pb-Pb collisions at $\sqrt{s_{\rm NN}}$ = 2.76 TeV at mid-rapidity (-1 < y < 1) from ATLAS. Figure taken from Ref. [216]

.

Figure 5.10 shows a comparable measurement of the nuclear modification factor of muons from heavy-flavour hadron decays as a function of $p_{\rm T}$ for Pb-Pb collisions at $\sqrt{s_{\rm NN}}$ = 2.76 TeV at mid-rapidity (-1 < y < 1) done by ATLAS [216]. The result from ATLAS are comparable within uncertainty with those obtained with ALICE for the same decay channel at forward rapidity (see Fig. 5.8). This comparison confirms that heavy quarks suffer a strong interaction in a wide rapidity internal.

5.5 Comparison with model calculations

In this section, comparisons with model predictions including charm and beauty quark interactions with a QGP medium and models based on pQCD calculated of high-$p_{\rm T}$ parton energy loss are discussed. These models differ in statement of initial condition, medium properties, dynamics of the medium evolution, interaction of heavy quarks with the medium and implementation of the hadronization.

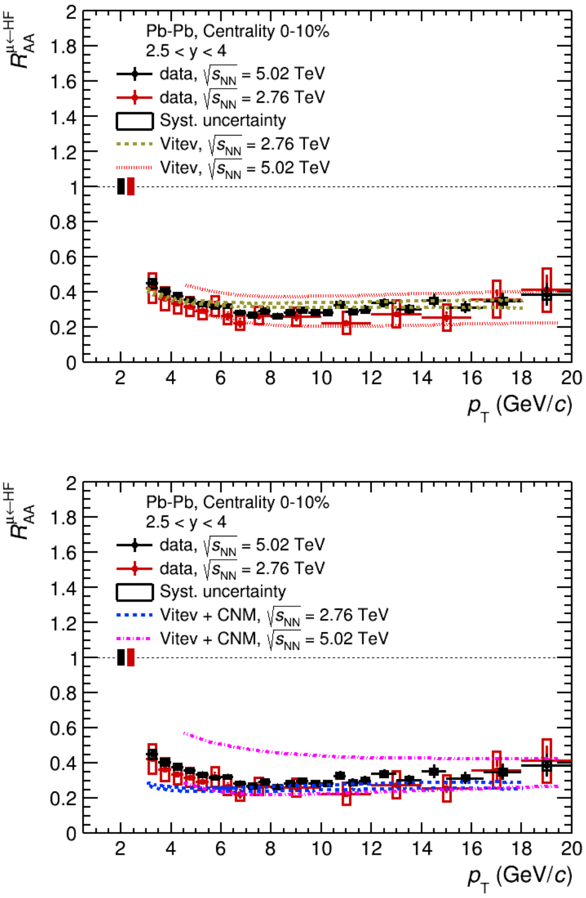

Figure 5.11: p_T-differential of the R_{AA} of muons from heavy-flavour hadron decays in 10% most centrality class at $\sqrt{s_{NN}}$ = 2.76 TeV and $\sqrt{s_{NN}}$ = 5.02 TeV compared with SCET (Vitev) model [218]. SCET predictions are shown without cold nuclear effect (upper panel) and with cold nuclear effect (bottom panel), separately.

Table 5.1 presents the list of heavy-quark transport and pQCD energy loss models, which are used for comparison with results of muons from heavy-flavour hadron decays in Pb-Pb collisions at $\sqrt{s_{NN}}$ = 5.02 and 2.76 TeV. Transport models in Tab. 5.1 includes TAMU model [217] in which the interactions are only described by collisional (i.e. elastic) processes, MC@sHQ+EPOS2 [221, 222] and PHSD [221, 222] in which also energy loss from medium-induced gluon radiation is considered, in addition to collisional process. In the following a pQCD energy loss model is also used. This is the SCET model [218] which implements in-medium meson dissociation. The TAMU, MC@sHQ+EPOS2 and PHSD models include a contribution of hydrodynamics, nuclear PDF (nPDF) and hadronisation via quark recombination, in addition to independent fragmentation. The SCET model includes a contribution of nPDF and hadronisation via quark fragmentation.

Figure 5.11 displays the p_{T}-differential R_{AA} of muons from heavy-flavour hadron decays in the 10% most centrality class at $\sqrt{s_{\mathrm{NN}}} = 2.76$ TeV and $\sqrt{s_{\mathrm{NN}}} = 5.02$ TeV compared with SCET model. One can notice that this model which includes the collisional and in-medium meson dissociation energy loss processes describes the data at both $\sqrt{s_{\mathrm{NN}}} = 2.76$ TeV and 5.02 TeV within uncertainties.

Figure 5.12 displays the p_{T}-differential R_{AA} of muons from heavy-flavour hadron decays at $\sqrt{s_{\mathrm{NN}}} = 2.76$ TeV and $\sqrt{s_{\mathrm{NN}}} = 5.02$ TeV compared with PHSD, TAMU and MC@sHQ + EPOS2 model predictions (μ←c and μ←b are shown in model predictions, separately). The comparisons are also shown for the 10% most central Pb-Pb collisions.

The upper panel in Fig. 5.12 displays the p_{T}-differential R_{AA} of muons from heavy-flavour hadron decays in the 10% most central Pb-Pb collisions at $\sqrt{s_{\mathrm{NN}}} = 2.76$ TeV and $\sqrt{s_{\mathrm{NN}}} = 5.02$ TeV compared with PHSD model predictions. One can notice that this model which includes both collisional and radiative energy loss processes can describe the data at $4 < p_T < 9$ GeV/c with μ←c predictions within uncertainties.

The middle panel in Fig. 5.12 displays the p_{T}-differential R_{AA} of muons from heavy-flavour hadron decays in 10% most central collisions at $\sqrt{s_{\mathrm{NN}}} = 2.76$ TeV and $\sqrt{s_{\mathrm{NN}}} = 5.02$ TeV and comparisons with TAMU model [217]. One can notice that this model which includes only the collisional energy loss processes overestimates the data for $p_{\mathrm{T}} > 7$ GeV/c with μ←b predictions, while for $3 < p_{\mathrm{T}} < 7$ GeV/c, model with μ←c predictions can describe the data within uncertainties.

A similar comparison is also presented in bottom panel of Fig. 5.12 with MC@sHQ + EPOS2 model. The MC@sHQ + EPOS2 model describes well the measurement over the whole p_{T} range. Moreover the data at high p_{T} are very close to the model predictions for μ←b. The model shows that the R_{AA} of μ←b is about 2 times larger than the R_{AA} of μ←c.

With respect to TAMU model which includes collisional energy loss processes, the MC@sHQ + EPOS2 model includes both collisional and radiative energy loss processes can estimate data at both low p_{T} and high p_{T} within uncertainties.

Figure 5.13 shows a comparison with the SCET model [218] predictions including cold nuclear effects (upper panel) and with MC@sHQ + EPOS2 model [221, 222] (bottom panel). The upper curves of MC@sHQ + EPOS2 model only include collisional energy loss processes and the lower curves include both collisional and radiative energy loss processes . One can notice these models can describe the data within uncertainties in central, semi-central and peripheral centrality classes.

Figure 5.14 shows comparison with MC@sHQ + EPOS2 prediction for μ←c, μ←b, μ←c+b in central (0-10%), semi-central (20-40%) and peripheral(60-80%) collisions. The model predictions for μ←b reproduce well the data at high p_{T} for all centralities within uncertainties

In summary, the measurements of the production of muons from heavy-flavour hadron decays in Pb-Pb collisions at 5.02 TeV via the nuclear modification factor R_{AA} with an improved precision compared to 2.76 TeV results provide new constraints on energy loss models.

5.6 Conclusion

The measurement of the production of single muons from heavy-flavour hadron decays at forward rapidity in Pb-Pb collisions at $\sqrt{s_{\rm NN}} = 5.02$ TeV has been presented as a function of transverse momentum ($p_{\rm T}$) and collision centrality. A strong suppression of the yields is observed in the most central collisions compared to the binary-scaled expectation from pp collisions at the same energy. The $p_{\rm T}$-integrated nuclear modification factor as function of the number of participating nucleons confirms the trends observed with the $p_{\rm T}$-differential results, namely an increase of the suppression from peripheral to central collisions.

Cold nuclear matter effects on heavy-flavour production has been assessed at forward and backward rapidity via the nuclear modification factor $R_{\rm pPb}$ of muons from heavy-flavour hadron decays measured in p-Pb collisions. Models implementing initial-state effects describe the data within uncertainties. The $p_{\rm T}$-differential of the heavy-flavour decay muons nuclear modification factor $R_{\rm pPb}$ at forward rapidity is compatible with unity within uncertainties over the whole $p_{\rm T}$ range. This confirms that CNM effect are small and the suppression measured in central Pb-Pb collisions results from medium effects.

The $R_{\rm AA}$ of heavy-flavour decay muons at forward rapidity is similar to that of heavy-flavour decay electrons from ALICE at mid-rapidity for both $\sqrt{s_{\rm NN}} = 2.76$ TeV and $\sqrt{s_{\rm NN}} = 5.02$ TeV Pb-Pb collisions. The $R_{\rm AA}$ of heavy-flavour decay muons at forward rapidity also is similar to that of heavy-flavour decay muons from ATLAS at mid-rapidity for $\sqrt{s_{\rm NN}} = 2.76$ TeV Pb-Pb collisions. These results indicate that heavy quarks suffer a strong interaction in a wide rapidity internal.

Comparisons with the results for Pb-Pb collisions at $\sqrt{s_{\rm NN}} = 2.76$ TeV and with model predictions are investigated. A similar suppression is measured at both $\sqrt{s_{\rm NN}} = 2.76$ TeV and 5.02 TeV. The results available from $p_{\rm T} = 3$ GeV/c up to $p_{\rm T} = 20$ GeV/c, provide new constraints on transport model ingredients and new insights on the understanding of the evolution of the hot and dense matter formed in ultra-relativistic heavy-ion collisions.

Transport models	**Heavy quark interactions**	**Hadronization**	**hydrodynamics**	**nPDF**
TAMU	Collisional	Fragmentation+Recombination	√	√
PHSD	Collisional+Radiative energy loss	Fragmentation+Recombination	√	√
MC@sHQ+EPOS2	Collisional+Radiative energy loss	Fragmentation+Recombination	√	√
pQCD Eloss models	**Heavy quark interactions**	**Hadronization**	**hydrodynamics**	**nPDF**
SCET	Collisional+In-medium meson dissociation	Fragmentation	×	√

Table 5.1: Transport and perturbative QCD (pQCD) energy loss models used for comparison with results of muons from heavy-flavour hadron decays in Pb-Pb collisions at $\sqrt{s_{\mathrm{NN}}} = 5.02$ and 2.76 TeV. The information on models is taken from Ref. [213]

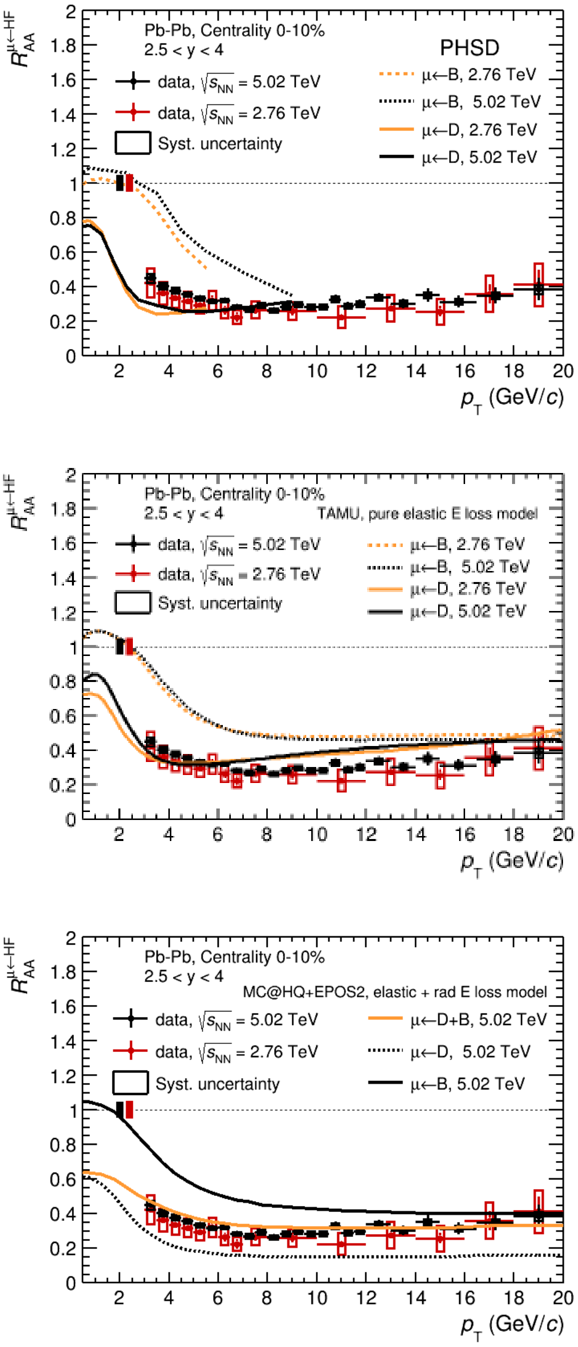

Figure 5.12: p_T-differential R_{AA} of heavy flavour decay muon compared with PHSD [219, 220] (upper) and TAMU model [217] (middle), and with MC@sHQ + EPOS2 model [221, 222] (bottom) model predictions. Note that the p_T-differential R_{AA} of muons from heavy-flavour hadron decays is measured in the 10% most centrality Pb-Pb collisions at $\sqrt{s_{NN}} = 2.76$ TeV and $\sqrt{s_{NN}} = 5.02$ TeV. Model predictions are also shown for $\mu\leftarrow$c and $\mu\leftarrow$b, separately

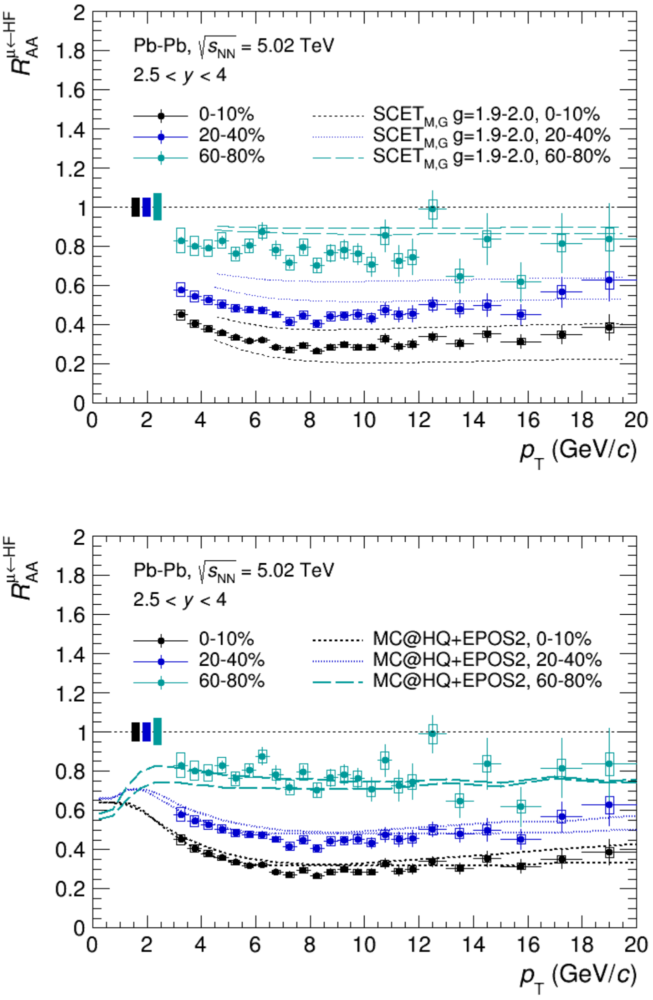

Figure 5.13: p_T-differential R_{AA} of muons from heavy-flavour hadron decays in 0-10%, 20-40%, 60-80% centrality classes at $\sqrt{s_{NN}} = 5.02$ TeV compared with models. SCET model [218] predictions include cold nuclear effects (upper panel). The upper curves of MC@sHQ + EPOS2 model [221, 222] predictions include collisional energy loss processes while the lower curves include both collisional and radiative energy loss processes (bottom panel).

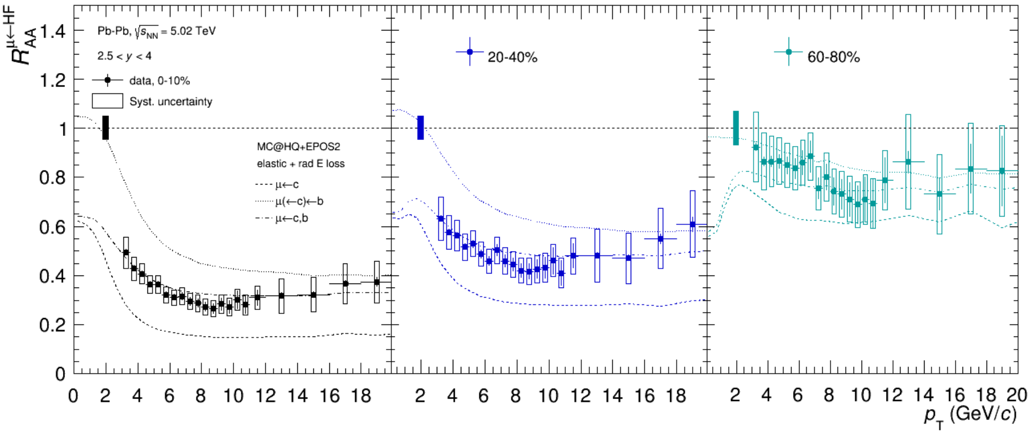

Figure 5.14: p_{T}-differential R_{AA} of muons from heavy-flavour hadron decays in 0-10%, 20-40%, 60-80% centrality classes at $\sqrt{s_{\mathrm{NN}}} = 5.02$ TeV compared with MC@sHQ + EPOS2 model [221, 222]. The model predictions are presented for $\mu \leftarrow$b,c and $\mu \leftarrow$b and $\mu \leftarrow$c.

Chapter 6

Production of muons from open heavy-flavour hadron decays in Xe-Xe collisions at $\sqrt{s_{\mathrm{NN}}}$=5.44 TeV

In this chapter, we focus on the measurement of the nuclear modification factor R_{AA} of muons from open heavy-flavour hadron decays in Xe–Xe collisions at $\sqrt{s_{\mathrm{NN}}} =$ 5.44 TeV. This allows us to study the dependence on the collision system size where Xe-Xe collisions bridge the gap between data from pp, p-Pb and Pb-Pb collisions. The analysis of Xe-Xe collisions uses the LHC17n data sample collected end of 2017 during a pilot run of about six hours (see Sec. 6.1). The analysis details will be described. This includes following steps: event and track selection, normalization, corrections, background subtraction, pp reference and estimation of systematics in Sec. 6.2. The results are discussed and compared with other measurements and model predictions in Sec. 6.3.

6.1 Data sample and muon selection

The Xe–Xe analysis is based on the AODs of the pass2 muon reconstruction (AOD) and is performed with the AliRoot version vAN-20171222. Xe–Xe collisions have been collected at $\sqrt{s_{\mathrm{NN}}}$ = 5.44 TeV with minimum-bias (MB) trigger and muon-triggered events corresponding to Muon Single Low (MSL) with a p_{T} trigger threshold of about 0.5 GeV/c. The following runs have been selected after the Quality Assurance (QA) checks [223].

- LHC17n, muon_pass2, AOD, 2 runs: 280234, 280235

The classification of events according to their centrality is performed through a Glauber fit of the V0 signal amplitude and the 0–90% interval is selected in the following (MB trigger fully efficient for these events). Figure 6.1 displays the centrality distribution of MB and MSL trigger events. The MB trigger exhibits a uniform behaviour which, as expected, is not the case of MSL-triggered events.

The event and track selection is the standard one used in previous single muon analyses. An offline event selection (Physics Selection) is applied and a reconstructed vertex within ±10 cm along the beam axis is required. Moreover, as just mentioned

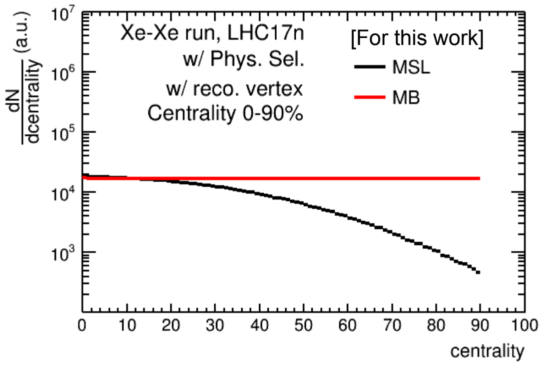

Figure 6.1: Centrality distribution with MB, MSL triggers.

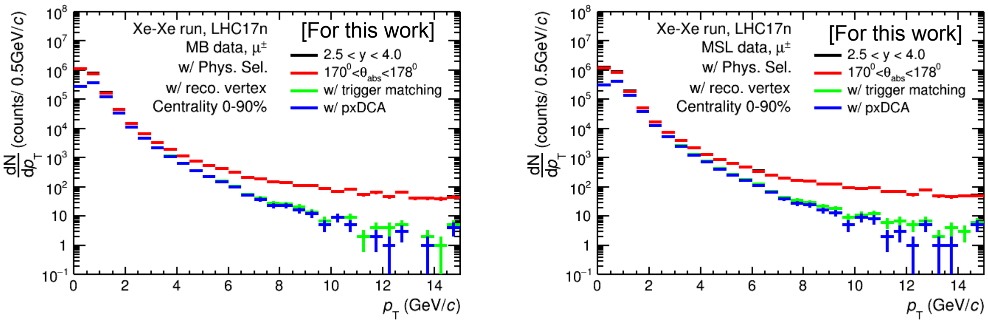

Figure 6.2: Transverse momentum distributions of inclusive muons with different selection cuts at event and track level in Xe-Xe collisions (centrality class: 0–90%) for MB (left) and MSL-triggered (right) events.

the 0–90% centrality interval is selected. The following cuts are applied for track selection. Tracks are required to be reconstructed within the acceptance of the muon spectrometer ($-4 < \eta_{\rm lab} < -2.5$) and to have a polar angle at the end of the absorber ($\theta_{\rm abs}$) from 170 to 178 degrees. The first cut removes particles at the edge of the muon spectrometer acceptance and the second one rejects muons crossing the high-density region of the front absorber which undergoes scatterings. One also requires that the track candidate in the tracking system matches the track reconstructed in the trigger system. Finally, the $p \times$ DCA cut within 6σ was applied in order to remove beam-induced background and particles produced in the absorber. The effect of the cuts on the measured $p_{\rm T}$ distributions of inclusive muons is illustrated in Fig. 6.2 for MB (CINT7ZAC-B-NOPF-CENT) and MSL-triggered events in the centrality interval 0–90%, and tables 6.1 and 6.2 give the number of events and tracks for the different triggers after the event and track selections.

From the $p_{\rm T}$ distribution of inclusive muons after selection cuts are applied (Fig. 6.3), the collected statistics allows us to investigate $R_{\rm AA}$ up to about $p_{\rm T}$ = 6 GeV/c in all centrality classes. In the 10% most central collisions, one can even

		N_{evt} (After Phys.Sel)	+ Rec.Vertex	+ cent(0-90%)	N_{evt}
LHC17n	MB	$1.66 \cdot 10^6$	0.6 %	8.5%	$1.51 \cdot 10^6$
	MSL	$7.74 \cdot 10^5$	0.1%	0.4%	$7.70 \cdot 10^5$

Table 6.1: Number of events in the centrality class 0–90% after the event selection conditions are applied (Physics selection and reconstructed vertex, percentages of rejected tracks by each cut).

		n_{trk}(+ event cuts)	$+\ \eta$	$+\ \theta_{\mathrm{abs}}$	+ TrM	+ p×DCA	N_{trk}
LHC17	MB	$2.59 \cdot 10^6$	16.98%	2.79%	60.29%	0.36%	$8.28 \cdot 10^5$
	MSL	$2.89 \cdot 10^6$	16.95%	2.50%	59.95%	0.43%	$9.33 \cdot 10^5$

Table 6.2: Number of tracks after event selection and with the various analysis cuts for the centrality interval 0–90% (percentages of rejected tracks by each cut).

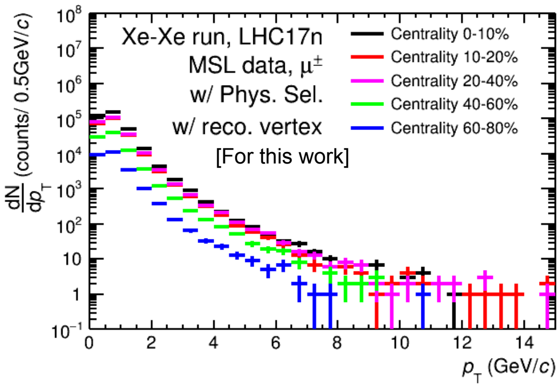

Figure 6.3: Inclusive muon p_{T} distribution with MSL trigger after selection cuts in various centrality classes in Xe–Xe collisions.

perform the measurement of the p_{T}-differential production cross section up to about $p_{\mathrm{T}} = 8$ GeV/c (28% statistical uncertainty in 7-8 GeV/c).

6.2 Analysis procedure

In this section, we will discuss the various analysis steps except the pp reference which was discussed in Chap. 3.

6.2.1 Normalization to equivalent number of Minimum-Bias events

In order to get the integrated luminosity corresponding to the MSL-triggered data sample, one needs to determine the normalization factor ($F^{\mathrm{MSL}}_{\mathrm{norm}}$) needed to derive the equivalent number of MB events. The strategy is the same as the one used in all analysis based on muon triggered events and in the J/ψ analysis for the same system

[224], where both offline and scaler methods have been implemented. As described hereafter, in the offline method one applies the muon trigger condition on minimum-bias events, while in the online method one uses the trigger rates. Once this factor is determined, the equivalent number of minimum-bias events ($N_{\text{MB}}^{\text{eq}}$) is calculated as $N_{\text{MB}}^{\text{eq}} = F_{\text{norm}}^{\text{MSL}} \times N_{\text{MSL}}$. The MB trigger which is used to get the normalization factor is CINT7ZAC-B-NOPF-CENT (one advantage of using the CINT7ZAC-B-NOPF-CENT trigger is that the number of minimum-bias events with CINT7ZAC-B-NOPF-CENT trigger is larger than with CINT7-B-NOPF-MUFAST trigger).

Offline method

The normalization factor for MSL ($F_{\text{norm}}^{\text{MSL}}$) triggered events is calculated in the centrality class 0–90% on a run by run basis according to:

$$F_{\text{norm}}^{\text{i}}(\text{MSL}) = \frac{N_{\text{MB}}^{\text{i}} \times F_{\text{pile-up}}^{\text{i}}}{N_{(\text{MB\&\&0MSL})}^{\text{i}}} \tag{6.1}$$

N_{MB} and N_{MSL} are the number of MB and MSL triggers after the offline selection. $N_{(\text{MB\&\&0MSL})}$ is the sample of MB events containing a 0MSL input. 0MSL (= 20) is the ID of the Central Trigger Processor (CTP) trigger input for MSL trigger. The pile-up being negligible in the 2017 Xe–Xe run, no pile-up correction is needed ($F_{\text{pile-up}} = 1$). The final value is the weighted average, using the relative statistical uncertainty as a weight (Eq. 6.2).

$$F_{\text{norm}}^{\text{MSL}} = \frac{\sum_i F_{\text{norm}}^{\text{MSL}}/(\sigma^2)_{\text{stat}}^{\text{MSL}}}{\sum_i 1/(\sigma^2)_{\text{stat}}^{\text{MSL}}} \tag{6.2}$$

The statistical uncertainty is calculated as:

$$[\Delta F_{\text{norm}}^{\text{MSL}}]_{\text{stat}} = \sqrt{\frac{1}{\sum 1/(\sigma^2)_{\text{stat}}^{\text{MSL}}}} \tag{6.3}$$

run	N_{MB}	$N_{\text{MB\&\&0MSL}}$	$F_{\text{norm}}(0-90\%)$
280234	89825	40761	2.20
280235	1420176	643032	2.21

Table 6.3: Normalization factor with offline method.

Table 6.3 presents the normalization factor values for MSL trigger events as a function of run number. One can notice that almost all the statistics collected in the Xe–Xe run is contained in run 280235 (16 times more statistics than in run 280234). In the following the online method has been also implemented to get the systematic uncertainty on the normalization factor.

Online method

This method relies on the L0b counting rates (scalers) taken from the Offline Conditions Database (OCDB). The normalization factor is computed run by run as:

$$F^{\mathrm{i}}_{\mathrm{norm-onl}}(\mathrm{MSL}) = \frac{L0b^{\mathrm{i}}_{\mathrm{MB}} \times PS^{\mathrm{i}}_{\mathrm{MB}} \times F_{\mathrm{pile-up}}}{L0b^{\mathrm{i}}_{\mathrm{MSL}} \times PS^{\mathrm{i}}_{\mathrm{MSL}}} \tag{6.4}$$

where $L0b_{\mathrm{MB}}$, $L0b_{\mathrm{MSL}}$ are the scaler values (rates) recorded for MB (CINT7ZAC-B-NOPF-CENT), MSL triggers, respectively. The variable $PS_{\mathrm{MB(MSL)}}$ (or purity) is the fraction of accepted MB (MSL) triggered events that pass the offline event selection in the centrality range 0-90%. $F_{\mathrm{pile-up}}$ is the pile-up correction factor for minimum-bias events that is neglected ($F_{\mathrm{pile-up}} = 1$). Note that since the MB trigger named CINT7ZAC-B-NOPF-CENT is a level L1 trigger, the equivalent L0b level trigger is computed as $L0b_{\mathrm{MB}} = (L1b_{\mathrm{INT7ZAC}}\ /\ L0a_{\mathrm{INT7ZAC}}) * L0b_{\mathrm{INT7ZAC}}$. The $L1b_{\mathrm{INT7ZAC}}$, $L0a_{\mathrm{INT7ZAC}}$ and $L0b_{\mathrm{INT7ZAC}}$ are the rates of CINT7ZAC-B-NOPF-CENT trigger events recorded at L1b, L0a and L0b level, respectively. The quantities entering in Eq. 6.4 are listed in Tab. 6.4.

run	$L0b_{\mathrm{MB}}$ rate	$L0b_{\mathrm{MSL}}$ rate	PS_{MB}	PS_{MSL}	$F_{\mathrm{norm}}(0-90\%))$
280234	117.9	51.0	0.907	0.995	2.11
280235	91.8	37.9	0.907	0.995	2.21

Table 6.4: Various quantities used to compute the normalization factor with the online method.

The final value of the normalization factor with the online method is obtained using the same procedure as with the offline method (see Eqs 6.2-6.3). This leads to: $F^{\mathrm{MSL}}_{\mathrm{norm-onl}} = 2.21 \pm 0.05\%$ (stat.) $\pm 1\%$ (syst.). The systematic uncertainty of about 1% reflects the difference between offline and online methods.

Final results

Finally, the normalization factor used to get the equivalent number of minimum-bias events in MSL-triggered events for the 0–90% centrality class is: $F^{\mathrm{MSL}}_{\mathrm{norm-onl}} = 2.21 \pm 0.05\%$ (stat.) $\pm 1\%$ (syst.).

As a function of centrality, the normalization factor in 0–90% is scaled with the fraction of the inelastic cross section of a given centrality class with respect to the 0–90% centrality class (e.g. 10/90 for the 0–10% centrality class, 20/90 for the 20–40% centrality class). Therefore, the equivalent number of minimum-bias events in a given centrality class c is given by:

$$N^{\mathrm{c}}_{\mathrm{MB}} = F_{\mathrm{norm}}(0-90\%) \cdot C^{\mathrm{c}} \cdot N_{\mathrm{MSL}}(0-90\%), \tag{6.5}$$

C^{c} being the scaling factor in a given centrality class c.

The equivalent number of minimum-bias events in the 0–100% centrality class and the integrated luminosity for MSL trigger are listed in Tab. 6.5. The latter is obtained using an inelastic Xe–Xe cross section of 5.61 ± 0.03 b [225].

	N_{evt} (equivalent MB events) in 0–100%	$L_{\mathrm{int}}(\mu\mathrm{b}^{-1})$
MSL	$1.891 \cdot 10^6$	0.337

Table 6.5: Equivalent number of minimum-bias events in the MSL data sample and integrated luminosity in 0–100% centrality class.

6.2.2 Acceptance × efficiency correction

Strategy and results

The procedure to estimate the p_{T}-differential $A \times \varepsilon$ is similar to the one developed for Pb–Pb collisions at $\sqrt{s_{\mathrm{NN}}} = 5.02$ TeV and consists in two steps. First a procedure based on a full simulation using as input a parameterization of the p_{T} and y distributions of muons from heavy-flavour hadron decays from FONLL predictions depicted in figure 6.4, is implemented. The detector description and its response are modeled using the GEANT3 transport package. The simulation is performed for each run and the statistics is proportional to the number of MSL-triggered events in order to reproduce the detector conditions during data taking. The $A \times \varepsilon$ as a function of the reconstructed p_{T} for MSL is presented in Fig. 6.5. The resulting $A \times \varepsilon$ as function of p_{T} tends to saturate at about 90%.

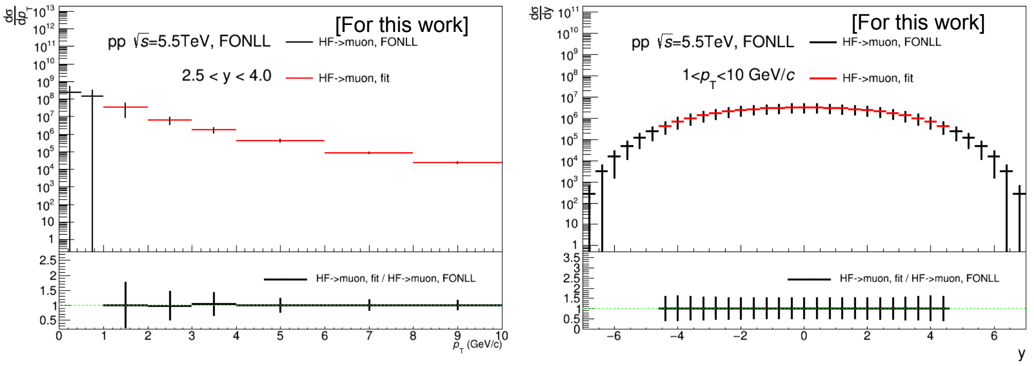

Figure 6.4: Parameterization of p_{T} and y distributions from FONLL predictions used as inPuts of simulations for the estimation of $A \times \varepsilon$.

Then, the dependence of $A \times \varepsilon$ on the collision centrality, due to the occupancy of the tracking chambers of the muon spectrometer needs to be considered. The factors are derived from those calculated for Pb–Pb collisions at $\sqrt{s_{\mathrm{NN}}}$ =5.02 TeV via the embedding technique (see [226] and chapter 4 for details). We remind here that the decreasing factor of $A \times \varepsilon$ in Pb-Pb collisions as a function of a minimum p_{T} shown in Fig. 6.6 exhibits no p_{T} dependence. The obtained values in Pb–Pb collisions at 5.02 TeV are also summarized in 6.6.

In order to obtain the decreasing factor of $A \times \varepsilon$ from peripheral to central collisions in Xe–Xe collisions, one needs to determine the equivalent centrality in

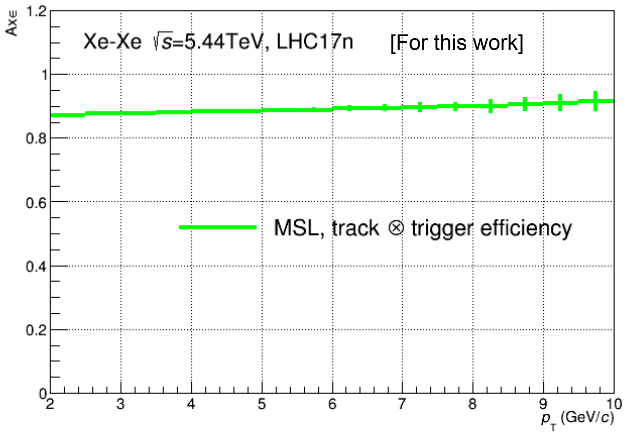

Figure 6.5: $A \times \varepsilon$ as a function of reconstructed p_{T} from a simulation using as input a parameterization of p_{T} and y distributions from FONLL.

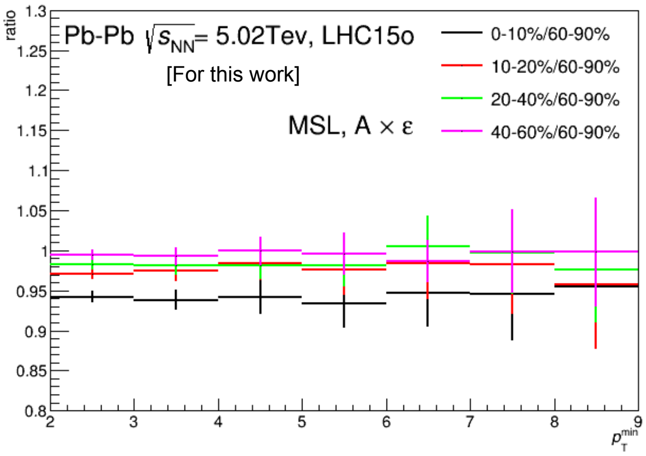

Figure 6.6: Ratio of $A \times \varepsilon$ in a given centrality class to that in the 60–90% centrality class as a function of a minimum p_{T} for MSL trigger.

	0–10%	10–20%	20–40%	40–60%	60–90%
MSL	0.941	0.973	0.982	0.994	1

Table 6.6: Decreasing factor of $A \times \varepsilon$ from peripheral to central collisions in various centrality classes for MSL events.

Xe–Xe collisions based on the comparison of $\langle N_{\mathrm{part}} \rangle$ ($\langle N_{\mathrm{part}} \rangle$ in central (0-10%) Xe-Xe collisions is close to that in 10-20% Pb-Pb collisions at forward rapidity). Table 6.7 summarizes the $\langle N_{\mathrm{part}} \rangle$ values for different centrality classes in Pb–Pb and

Xe–Xe collisions (extracted from [227, 228]). Note that one can also determine the equivalent centrality in Xe-Xe collisions based on $\langle \mathrm{d}N_{\mathrm{ch}}/\mathrm{d}\eta \rangle$ at forward rapidity. Tab. 6.8 summarizes the corresponding $\langle \mathrm{d}N_{\mathrm{ch}}/\mathrm{d}\eta \rangle$ values for 0-10% and 10-20% centrality classes in Pb–Pb and Xe–Xe collisions (extracted from [229])

	0–10%	10–20%	20–40%	40–60%	60–80%
Pb–Pb	359 ± 3.0	263 ± 3.6	159.6 ± 2.6	69.97 ± 1.4	17.86 ± 0.45
Xe–Xe	221.2 ± 2.2	164.8 ± 2.8	100.3 ± 3.8	44.32 ± 3.3	15.11 ± 1.6

Table 6.7: $\langle N_{\mathrm{part}} \rangle$ in various centrality classes for Pb–Pb and Xe–Xe collisions. The values are extracted from [227, 228].

.

	0–10%	10–20%
Pb–Pb	2252 + 125 - 126	1548 + 80 - 81
Xe–Xe	1388 + 91 - 95	955 + 63 - 65

Table 6.8: $\langle \mathrm{d}N_{\mathrm{ch}}/\mathrm{d}\eta \rangle$ at forward rapidity in 0-10% and 10-20% centrality classes for Pb-Pb and Xe-Xe collisions. The values are extracted from [229].

.

Consequently, the values of the decreasing factor of $A \times \varepsilon$ from peripheral to central collisions in Xe–Xe collisions using Pb-Pb collisions results are summarized in Tab. 6.9.

	0–10%	10–20%	20–40%	40–60%	60–90%
MSL	0.973	0.982	0.994	0.994	1

Table 6.9: Decreasing factor of $A \times \varepsilon$ from peripheral to central Xe–Xe collisions in various centrality classes for MSL events.

Transverse momentum distributions normalized to the equivalent number of MB events and corrected for $A \times \varepsilon$

The p_{T} distributions of inclusive muons corrected for $A \times \varepsilon$ and normalized to the equivalent number of minimum-bias events in MSL triggered events and MB triggered events are reported in Fig. 6.7 for the 0–90% centrality class (left) and the ratio between these distributions is presented in the right panel. The ratio is consistent with unity within statistical uncertainties. The deviation between MB and MSL amounts to less than 2% in the 0–90% centrality class for the interval $3 < p_{\mathrm{T}} < 10$ GeV/c.

6.2.3 Estimation the muon-background contributions

The p_{T} distribution of muons from heavy-flavour hadron decays at forward rapidity is obtained after the subtraction of the muon background to the corrected inclusive muon yield and is expressed as:

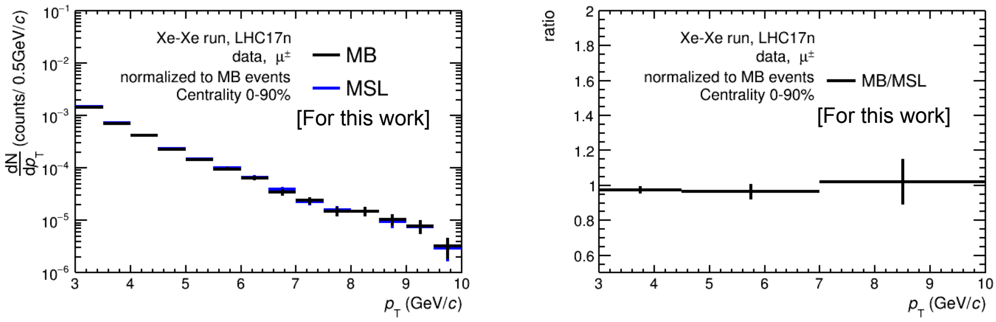

Figure 6.7: Left: p_{T} distributions of inclusive muons with MB and MSL triggers after normalization to the equivalent number of minimum-bias events and after applying the $A \times \varepsilon$ correction for the 0–90% centrality class. Right: ratio between the two distributiions.

$$\frac{dN_{\mathrm{AA}}^{\mu\leftarrow HF}}{dp_{\mathrm{T}}} = \frac{dN_{\mathrm{AA}}^{incl\ \mu}}{dp_{\mathrm{T}}} - \frac{dN_{\mathrm{AA}}^{\mu\leftarrow K,\pi}}{dp_{\mathrm{T}}} - \frac{dN_{\mathrm{AA}}^{\mu\leftarrow J/\psi}}{dp_{\mathrm{T}}} - \frac{dN_{\mathrm{AA}}^{\mu\leftarrow W,Z/\gamma^*}}{dp_{\mathrm{T}}}. \tag{6.6}$$

The main background contribution at low/intermediate p_{T} is the component of muons from primary charged pion and kaon decays. A smaller contribution of muons from J/ψ decays is also considered. The background contribution of W,Z/γ^*-decay muons relevant at high p_{T} (for $p_{\mathrm{T}} > 12 - 14$ GeV/c) is negligible in the p_{T} interval accessible with the present statistics.

A strategy similar to that developed for Pb-Pb collisions at $\sqrt{s_{\mathrm{NN}}} = 5.02$ TeV (see [226] and Chap. 4) is implemented. It uses the charged pion and kaon spectra measured at mid-rapidity with ALICE (Fig. 6.8).

The three main steps that will be discussed in the following are:

- Transverse momentum extrapolation of mid-rapidity charged pion and kaon spectra at higher p_{T};
- Extrapolation towards forward rapidity of the p_{T}-extrapolated mid-rapidity charged pion and kaon spectra with its p_{T} dependence;
- Production of decay muons via fast detector simulations of decay kinematics and absorber effect.

The extrapolated p_{T} distributions of mid-rapidity charged pions and kaons are performed as in Pb-Pb collisions (see Chap. 4), using a power-law fit.

- the spectra in $p_{\mathrm{T}} < 5$ GeV/c are filled with 1000 times and the original points are Gaussian smeared (gRandom→Gaus(μ,σ)), μ is the central value of pion and kaon spectra. The σ is the total uncertainty (the statistical and systematic uncertainties in the data);

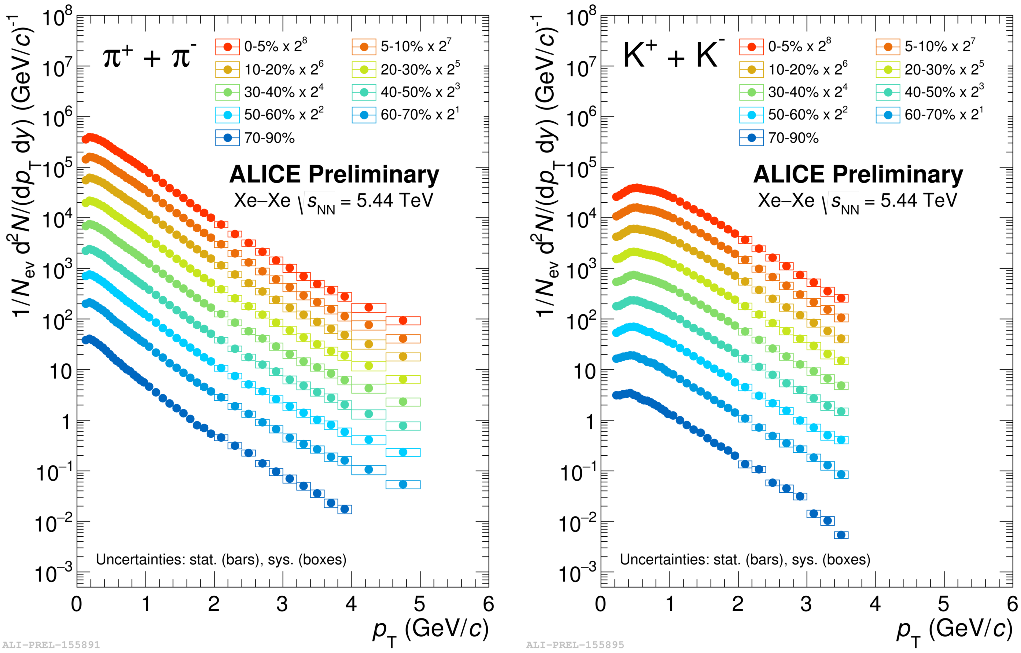

Figure 6.8: Mid-rapidity p_{T} distributions of charged pions and kaons measured in Xe-Xe collisions at $\sqrt{s_{\mathrm{NN}}} = 5.44$ TeV [232].

- $p_{\mathrm{T}} > 5$ GeV/c, μ and σ are from the p_{T} extrapolated intervals of pion and kaon spectra.

The method of extrapolation towards forward rapidity of the p_{T}-extrapolated mid-rapidity charged pion and kaon spectra is performed as in Pb-Pb collisions. The charged pion and kaon spectra at forward rapidity are obtained according to:

$$[\mathrm{d}N/\mathrm{d}p_{\mathrm{T}}]^{\pi,\mathrm{K}}_{\mathrm{XeXe,FW}} = n_y \cdot F(p_{\mathrm{T}}, y) \cdot [\mathrm{d}N/\mathrm{d}p_{\mathrm{T}}]^{\pi,\mathrm{K}}_{\mathrm{XeXe,CB}}. \tag{6.7}$$

$F(p_{\mathrm{T}}, y)$ is the p_{T}-dependent rapidity extrapolation factor for pp collisions. n_y which accounts for unknown quenching at forward rapidity is taken equal to unity for the central value and is varied conservatively from 0.5 to 1.5 (same value as the analysis in Pb–Pb results, see Chap. 4). After propagation to the R_{AA} of muons heavy-flavour hadron decays, the corresponding systematic uncertainty due to unknown quenching at forward rapidity varies from about 1% ($p_{\mathrm{T}} = 8$ GeV/c) to 4% ($p_{\mathrm{T}} = 3$ GeV/c) in the 10% most central collisions.

The rapidity extrapolation of charged pion and kaon distributions in pp collisions is performed using PYTHIA 6 and PHOJET models. PYTHIA 8 simulations with various colour reconnection options are employed to account for the p_{T} dependence of the rapidity extrapolation. More details about the extrapolation can be found in [231] and Chap. 4. Finally, muons from charged pion and kaon decays are generated from a fast detector simulation of decay kinematics and absorber effect which uses the extrapolated charged pion and kaon distributions as inputs (as already discussed in Chap. 4).

The systematic uncertainty on the estimated yield of muons from charged π (K) decays includes contributions from i) the measured mid-rapidity p_{T} distributions of charged π (K) in Xe-Xe collisions at $\sqrt{s_{\mathrm{NN}}} = 5.02$ TeV and their extrapolation to higher p_{T}, ii) the rapidity extrapolation for charged K (π), estimated by comparing the results with PYTHIA 6 and PHOJET generators iii) the p_{T}-dependent rapidity extrapolation obtained by comparing the results with several colour reconnection options in PYTHIA 8 and iv) the front absorber effect. The latter was estimated by comparing the p_{T} distributions of muons from charged pion and kaon decays obtained in a fast detector simulation implementing the parameterized front absorber effect and a full simulation. Figure 6.9 shows the estimated p_{T} distributions of muons from charged pion and kaon decays in the 10% most central collisions (left). The corresponding systematic uncertainties are displayed as a function of p_{T} in the 10% most central collisions in Fig. 6.9 (right). The corresponding fraction with respect to inclusive muons is presented in Fig. 6.10. The latter decreases with increasing p_{T} in the range 14-22% ($p_{\mathrm{T}} = 3$ GeV/c) down to about 5% ($p_{\mathrm{T}} = 8$ GeV/c), depending on the collision centrality.

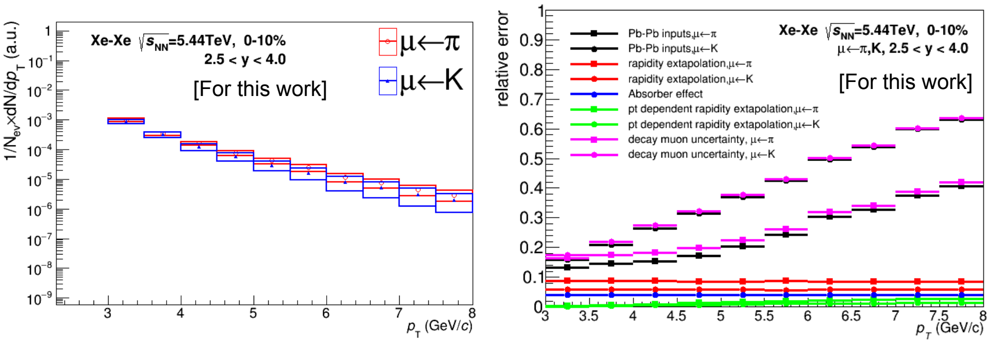

Figure 6.9: Estimated p_{T}-differential distributions of muons from charged pion and kaon decays (left) and corresponding systematic uncertainty sources (right) in central Xe–Xe collisions at $\sqrt{s_{\mathrm{NN}}} = 5.44$ TeV.

Estimation of the J/ψ contribution

Since the statistics in Xe–Xe collisions is not sufficient to perform differential measurements of the J/ψ production, the estimated yields of muons from J/ψ decays are taken from Pb–Pb results (see Chap. 4) at a centrality corresponding to an equivalent $\langle N_{\mathrm{part}} \rangle$. The systematic uncertainty on the extracted J/ψ yields originates from the measured p_{T} and y distributions in Pb–Pb collisions and their extrapolation in a wider kinematic region (the contribution of muons from J/ψ decays varies within about 1-4%, the maximum being at $p_{\mathrm{T}} \sim$ 4-6 GeV/c.). The

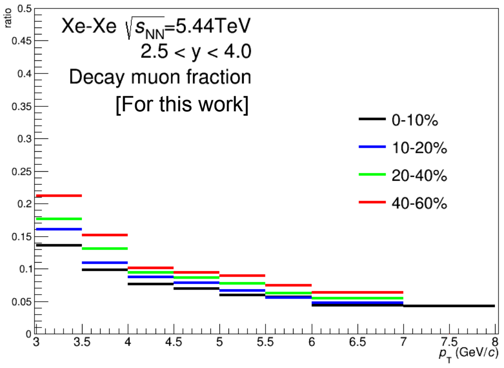

Figure 6.10: Estimated fraction of muons from charged pion and kaon decays relative to inclusive muons as a function of p_T for various centrality classes in Xe–Xe collisions at $\sqrt{s_{NN}} = 5.44$ TeV.

systematic uncertainty is smaller than 1% in all centralities after propagation to the R_{AA} measurement.

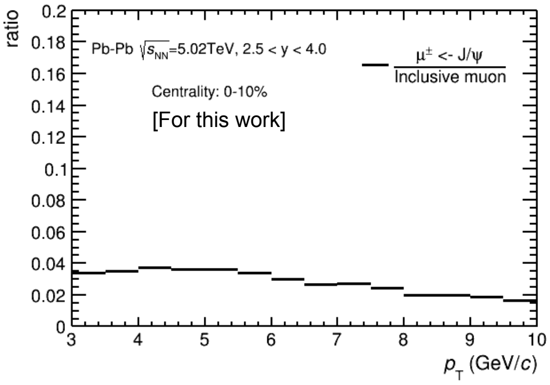

Figure 6.11: Fraction of J/ψ decay muons with respect to inclusive muons as a function p_T at forward rapidity in central Pb-Pb collisions at $\sqrt{s_{NN}} = 5.02$ TeV.

6.2.4 Estimation of systematic uncertainties

Several source of systematic uncertainty affect the measurements of muons from heavy-flavour hadron decays. These are the systematic uncertainties on the inclusive muon yield, the estimated background sources and the systematic uncertainty on normalization.

Detector response systematic uncertainties

The systematic uncertainty affecting the yield of inclusive muons contains the systematic uncertainty on the muon tracking efficiency and the systematic uncertainty associated with the muon trigger efficiency. Moreover, a systematic uncertainty due to the efficiency of the matching between tracking and trigger needs also to be considered. An other source of systematic uncertainty comes from the decrease of tracking efficiency as the collision centrality increases. A p_{T}-dependent systematic uncertainty is also assigned to take into account the track resolution and alignment effects [231]. The systematic uncertainty on the muon tracking efficiency amounts to 1% [233]. The systematic uncertainty on the trigger efficiency includes the uncertainty on the intrisinc trigger efficiency (1%) and the trigger response (2%), which leads to a total systematic uncertainty of 2.2%. The systematic uncertainty on the muon trigger-tracking matching of 0.5% is related to the choice of χ^2 cut used to define the matching between reconstructed tracks in the tracking system and trigger tracklets. The systematic uncertainty on track resolution and alignment is negligible for $p_{\mathrm{T}} < 7$ GeV/c and is 0.5% in $7 < p_{\mathrm{T}} < 8$ GeV/c. It is derived from Pb–Pb collisions since the quality of the alignment is similar. Based on the results for Pb–Pb collisions, the systematic uncertainty due to the decrease of tracking efficiency with increasing centrality is within 0–0.5%.

Systematic uncertainty on muon background subtraction

The evaluation of the systematic uncertainty sources affecting the estimation of the yield of muons from charged π and K decays and the yield of J/ψ decay muons were discussed in Sec. 6.2.3.

Systematic uncertainty on normalization

The systematic uncertainty includes the systematic uncertainty from N_{MB} (equivalent number of minimum-bias events) and $\langle T_{\mathrm{AA}}\rangle$. The systematic uncertainty on $\langle N_{\mathrm{part}}\rangle$ is also used when studying R_{AA} versus centrality by means of $\langle N_{\mathrm{part}}\rangle$. The systematic uncertainty on N_{MB} of 1% for MSL data sample reflects the difference between the normalization factor (F_{norm}) obtained with the two different approaches as described in Sec. 6.2.1. This global systematic uncertainty is correlated with p_{T} and centrality. The values and systematic uncertainties of $\langle T_{\mathrm{AA}}\rangle$ and $\langle N_{\mathrm{part}}\rangle$ are obtained from a Glauber calculation and extracted from [227]. The systematic uncertainty on $\langle T_{\mathrm{AA}}\rangle$ varies from 8.4% (0–10%) to 18.4% (60–80%) and is correlated with p_{T}. The systematic uncertainty on $\langle N_{\mathrm{part}}\rangle$ amounts to 1% and 10.6% for the centrality class 0–10% and 60–80%, respectively. The $\langle \mathrm{d}N_{\mathrm{ch}}/\mathrm{d}\eta\rangle$ values and systematic uncertainties in 0-10% and 10-20% centrality classes for Pb-Pb and Xe-Xe collisions have been already summarized in Tab. 6.8. The $\langle N_{\mathrm{part}}\rangle$ and $\langle T_{\mathrm{AA}}\rangle$ values and systematic uncertainties are summarized in Tab. 6.10.

Systematic uncertainty on the pp reference cross section

The pp reference at $\sqrt{s} = 5.44$ TeV needed for the computation of the R_{AA} of muons from heavy-flavour hadron decays is obtained by applying a pQCD-driven energy scaling to the p_{T}-differential cross section of muons from heavy-flavour hadron decays measured in pp collisions at $\sqrt{s} = 5.02$ TeV in $2 < p_{\mathrm{T}} < 20$ GeV/c [231], as

Centrality	$\langle N_{\text{part}} \rangle$	$\langle T_{\text{AA}} \rangle$
0–10%	221.2 ± 2.2	12.33 ± 1.03
10–20%	164.8 ± 2.8	7.465 ± 0.74
20–40%	100.3 ± 3.8	3.466 ± 0.49
40–60%	44.32 ± 3.3	1.008 ± 0.18
60–80%	15.11 ± 1.6	0.228 ± 0.042

Table 6.10: $\langle N_{\text{part}} \rangle$ and $\langle T_{\text{AA}} \rangle$, and associated systematic uncertainties for Xe–Xe collisions. Extracted from [227].

Tracking efficiency	1.0%
Trigger efficiency	2.2%
Matching efficiency	0.5%
Track resolution + alignment	negligible for $p_{\text{T}} < 7$ GeV/c, 0.5% in $7 < p_{\text{T}} < 8$ GeV/c
Embedding	0.5%
J/ψ decay muons	0.2%-0.5%
π, K decay muons	< 2%
F_{norm} in Xe-Xe collisions	1%
$\langle T_{\text{AA}} \rangle$	8.4%–18.4%
pp reference	2.2%–4%
F_{norm} from pp reference	0.3% (MSL), 0.7% (MSH)
n_y	1.3%–4.1%

Table 6.11: Systematic uncertainties considered in the measurement of muons from heavy-flavour hadron decays in central (0–10%) collisions. For the p_{T}-dependent uncertainties the minimum and maximum values are given.

discussed in Chap. 3. The energy scaling factor, from 5.02 TeV to 5.44 TeV, and its related systematic uncertainty are obtained using FONLL calculations with different sets of factorization and renormalization scales and quark masses, as detailed in [230] (see Chap. 3).

Therefore, the systematic uncertainty on the p_{T}-differential cross section of muons from heavy-flavour hadron decays includes the systematic uncertainty on the measured p_{T}-differential cross section of muons from heavy-flavour hadron decays in pp collisions at $\sqrt{s} = 5.02$ TeV within 2%–3.7% in the interval $3 < p_{\text{T}} < 8$ GeV/c and the systematic on energy scaling from FONLL in the range 1%–1.5%. This leads to a total systematic uncertainty of 2.2%–4%, depending on p_{T}

Summary of systematic uncertainties

A summary of the various systematic uncertainties is presented in Tab. 6.11. The systematic uncertainties entering in the measurement of the R_{AA} affect the normalized p_{T}-differential yields with the exception of the contribution from the pp reference and $< T_{AA} >$.

For the measurement of R_{AA} as function of centrality, the uncertainties which are fully correlated with centrality (pp reference, normalization) are drawn separately.

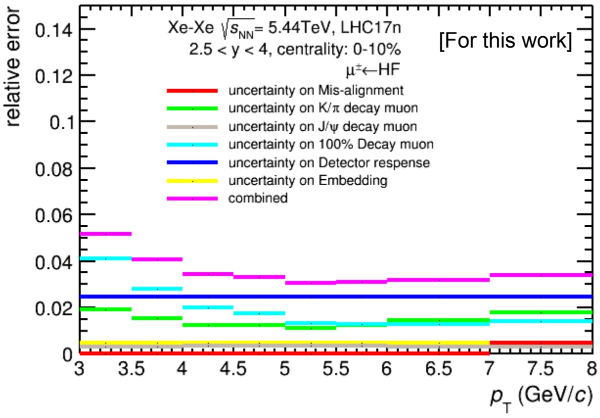

Figure 6.12: Various systematic uncertainty sources affecting the normalized p_T-differential yields of muons from heavy-flavour hadron decays in the 0–10% centrality class added in quadrature to obtain the total systematic uncertainty.

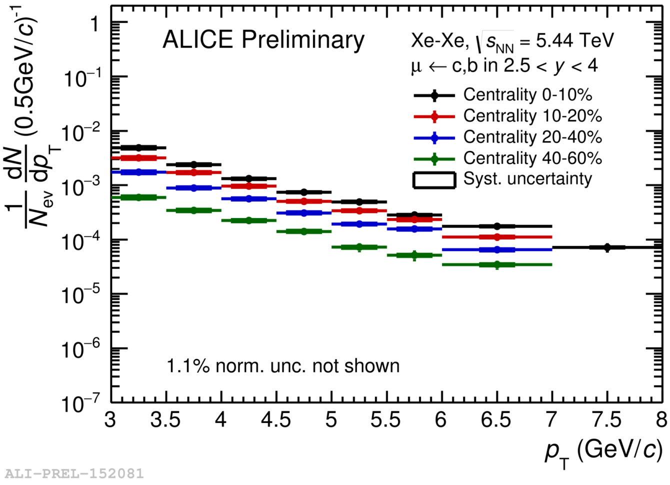

Figure 6.13: Normalized and corrected p_T-differential yields of muons from heavy-flavour hadron decays in Xe–Xe collisions at $\sqrt{s_{NN}} = 5.44$ TeV. The distributions are shown in various centrality intervals mentioned in the figure. See the text for details.

The various systematic uncertainties entering in the R_{AA} measurement are displayed as function of p_T for the 10% most central collisions in Fig. 6.12.

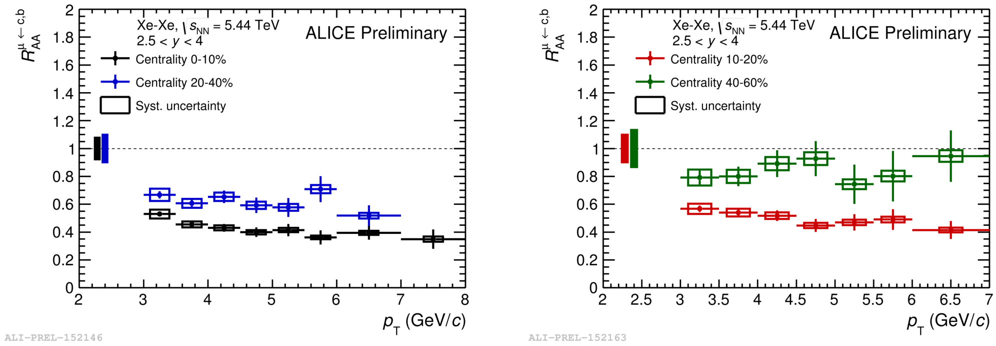

Figure 6.14: $R_{\rm AA}$ of muons from heavy-flavour hadron decays in various centrality classes in the range 0–80% for Pb–Pb collisions at $\sqrt{s_{\rm NN}} = 5.44$ TeV. Vertical bars are the statistical uncertainties. Open boxes represent the systematic uncertainties, except the systemactic uncertainty on normalization which is shown as full boxes at $R_{\rm AA} = 1$.

6.3 Results and discussion

All the results presented in the following are obtained using MSL triggered events in the interval from $p_{\rm T} = 3$ to 7 or 8 GeV/c, depending on centrality.

Normalized $p_{\rm T}$-differential yields of muons from heavy-flavour hadron decays

Figure 6.13 presents the corrected $p_{\rm T}$-differential normalized yields in various centrality intervals in the range 0–80% for muons from heavy-flavour hadron decays. The statistics collected with MSL allows us to perform the measurement over the $p_{\rm T}$ interval, up $p_{\rm T} = 7$ or 8 GeV/c, depending on centrality (40–60%, up to $p_{\rm T} = 7$ GeV/c). One observes that the yields increase by more than one order of magnitude from peripheral to central collisions.

$R_{\rm AA}$ of muons from heavy-flavour hadron decays

Figure 6.14 shows the $p_{\rm T}$-differential nuclear modification factor of muons from heavy-flavour hadron decays in several centrality intervals in the range 0–60%. The results are provided in a $p_{\rm T}$ interval from 3 to 8 GeV/c in the 0–10% centrality class. One observes a clear increase of the suppression with increasing centrality which reaches a factor of about three at intermediate $p_{\rm T}$ ($p_{\rm T} = 4$–6 GeV/c) in the 10% most central collisions. The suppression tends to decrease towards the low $p_{\rm T}$ region.

The $p_{\rm T}$-integrated $R_{\rm AA}$ of muons from heavy-flavour hadron decays

The $p_{\rm T}$-integrated $R_{\rm AA}$ as a function of $\langle N_{\rm part}\rangle$ is presented for the interval $3 < p_{\rm T} < 6$ GeV/c in Fig. 6.15. The systematic uncertainties which are fully

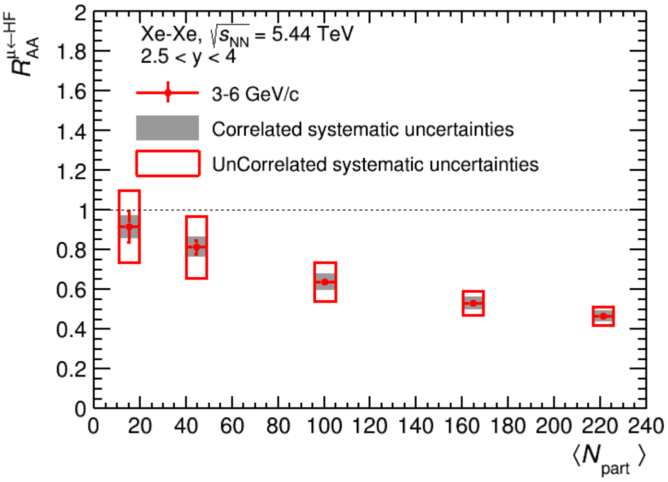

Figure 6.15: $R_{\rm AA}$ as a function of $\langle N_{\rm part}\rangle$ for muons from heavy-flavour hadron decays in Xe–Xe collisions at $\sqrt{s_{\rm NN}}$ = 5.44 TeV. The systematic uncertainties which are fully correlated between bins (pp reference, normalization) are shown as full boxes. See the text for details.

correlated between centrality bins (pp reference, normalization) are shown as full boxes. The clear increase of the suppression with increasing centrality is confirmed.

Comparison of the results in Xe-Xe and Pb-Pb collisions

A comparison of the results in the 10% most central Xe-Xe collisions with those obtained in Pb–Pb collisions at $\sqrt{s_{\rm NN}}$ = 5.02 TeV for the 0–10% and 10-20% centrality classes are presented in Fig. 6.16. One observes that the results in the 10% most central Xe–Xe collisions are compatible within uncertainties with the measured $R_{\rm AA}$ in Pb–Pb collisions for the 10–20% centrality class. Indeed the $\langle {\rm d}N_{\rm ch}/{\rm d}\eta\rangle$ at forward rapidity in the 10–20% Pb–Pb collisions is close to the one in the 10% most central Xe–Xe collisions (see Tab. 6.8). This behaviour could explained from possible interplay of geometry and path-lengh dependence of medium-induced parton energy loss [235].

Comparison with the $R_{\rm AA}$ of electrons from heavy-flavour hadron decays measured at mid-rapidity

Figure 6.17 shows a comparison with the $R_{\rm AA}$ measured at mid-rapidity for electrons from heavy-flavour hadron decays in central and semi-central collisions [234]. A similar suppression is observed at both forward and mid-rapidity within uncertainty. This is a confirmation that heavy quarks suffer a strong interaction in a wide rapidity internal.

Comparisons with models

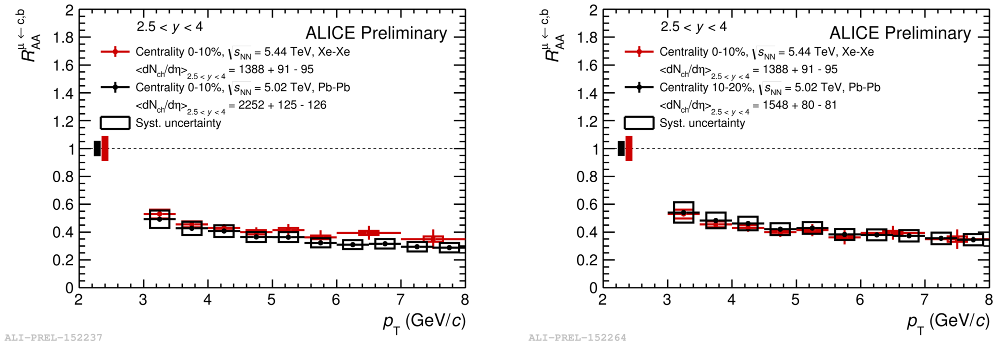

Figure 6.16: Comparison of the p_{T}-differential R_{AA} of muons from heavy-flavour hadron decays in the 10% most central Xe–Xe collisions at $\sqrt{s_{\mathrm{NN}}} = 5.44$ TeV with that obtained in Pb–Pb collisions at $\sqrt{s_{\mathrm{NN}}} = 5.02$ TeV for the centrality classes 0–10%, 10–20%.

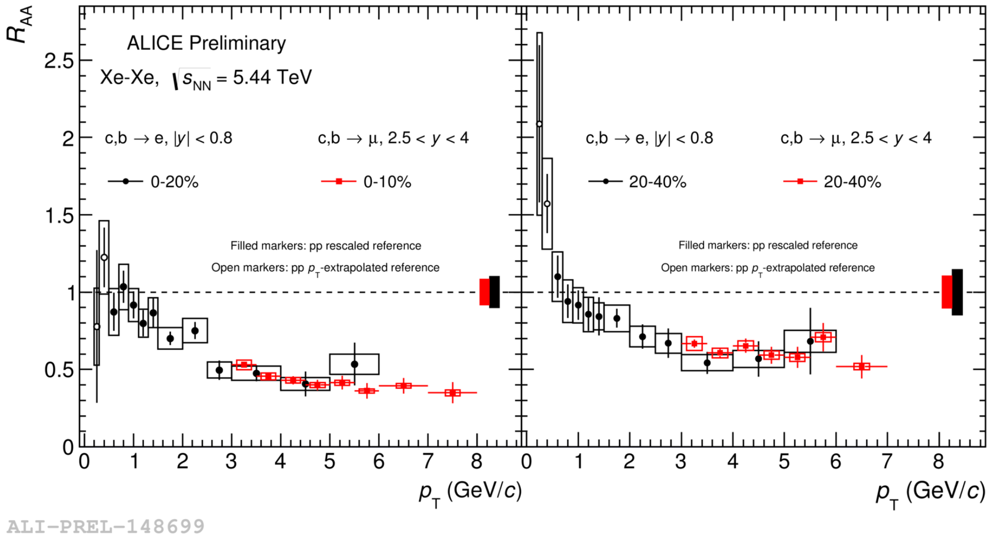

Figure 6.17: Comparison of the p_{T}-differential R_{AA} of muons from heavy-flavour hadron decays in the central and semi-central Xe–Xe collisions at $\sqrt{s_{\mathrm{NN}}} = 5.44$ TeV with that obtained at mid-rapidity for heavy-flavour hadron decay electrons.

Finally, we also show comparisons of the p_{T}-differential R_{AA} of muons from heavy-flavour hadron decays in the Xe–Xe collisions at $\sqrt{s_{\mathrm{NN}}} = 5.44$ TeV with the Parton-Hadron-String-Dynamics (PHSD) model [219, 220] predictions in Fig. 6.18. The model describes the measured R_{AA} in the 20-40% within uncertainties, while in the 0-10% and 10-20% centrality classes, it trends to overestimate the R_{AA} results. Figure 6.19 shows comparisons with PHSD model in central Xe-Xe and Pb-Pb collisions at similar $\langle \mathrm{d}N_{\mathrm{ch}}/\mathrm{d}\eta \rangle$ (in the 0-10% Xe-Xe collisions and 10–20% Pb–Pb

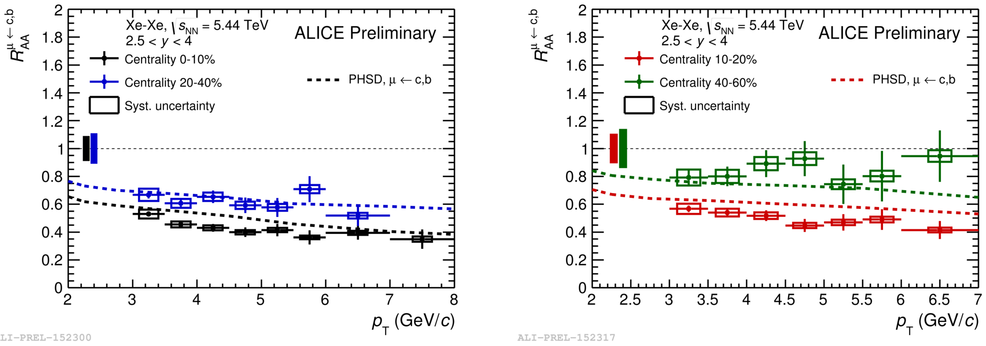

Figure 6.18: Comparison of the p_T-differential R_{AA} of muons from heavy-flavour hadron decays in Xe–Xe collisions at $\sqrt{s_{NN}} = 5.44$ TeV with predictions from PHSD model [219, 220].

collisions). The model trends to overestimate the R_{AA} measurements, in particular the Pb-Pb results. So, the R_{AA} measurements have the potential to constrain energy loss models.

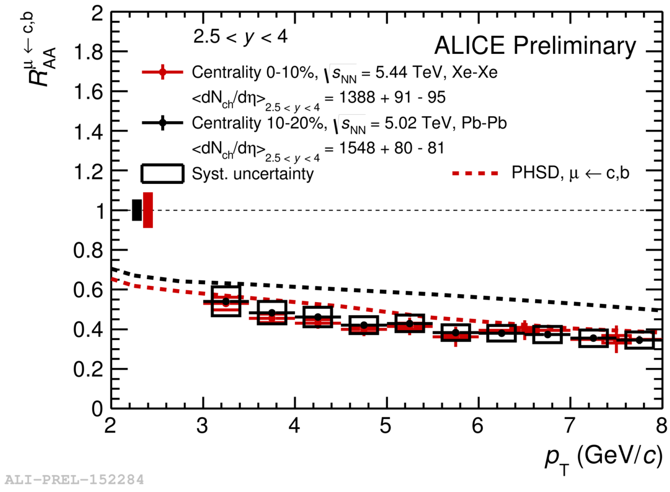

Figure 6.19: The p_T-differential R_{AA} of muons from heavy-flavour hadron decays in Xe-Xe (centrality:0-10%) collisions at 5.44 TeV in comparison with that in Pb-Pb (centrality:10-20%) collisons at 5.02 TeV. Comparisons with PHSD model are also shown.

Test of path-length dependence

The comparison of the production of muons form heavy-flavour hadron decays in Pb-Pb and Xe-Xe collisions with different sizes (atomic number is A = 208 for

Pb, while A = 129 for Xe) at a similar collision energy allow us to investigate how the energy loss depends on the length of the traversed medium e.g. the so-called path-length dependence [235]. In that purpose, a new observable has proposed in Ref. [235]. This is the path-length sensitive suppression ratio $R_{\mathrm{L}}^{\mathrm{XePb}}$ defined as:

$$R_{\mathrm{L}}^{\mathrm{XePb}} = \frac{1 - R_{\mathrm{XeXe}}}{1 - R_{\mathrm{PbPb}}}. \tag{6.8}$$

where R_{XeXe} and R_{PbPb} are the nuclear modification factor in Xe-Xe and Pb-Pb collisions for a given centrality. This observable can be approximated as $R_{\mathrm{L}}^{\mathrm{XePb}} = \left(\frac{A_{\mathrm{Xe}}}{A_{\mathrm{Pb}}}\right)^{b/3}$ [235], where A_{Xe} (A_{Pb}) are the atomic number of Xe and Pb, and b is a free parameter. Such observable depends on the system size through $A_{\mathrm{Xe}}/(A_{\mathrm{Pb}})$ and on the path-length through the parameter b. This parameter is equal to unity for a linear path-length dependence and it value is two for quadratic path-length dependence.

The p_{T}-differential $R_{\mathrm{L}}^{\mathrm{XePb}}$ of muons from heavy-flavour hadron decays in three centrality classes in the interval ranges (0-10%, 10-20%, 20-40%) for Xe-Xe and Pb-Pb collisions is depicted in Fig. 6.20. The vertical bars are statistical uncertainties and the open boxes are the systematic uncertainties. This observable does not depend on p_{T} in the interval $3 < p_{\mathrm{T}} < 8$ GeV/c and is also insensitive to the collision centrality within uncertainties, in central and semi-central collisions. The adjustment with the function $\left(\frac{A_{\mathrm{Xe}}}{A_{\mathrm{Pb}}}\right)^{b/3}$ indicates that a factor b =0.5 is favored in central collisions, while in semi-central collisions (0-40% centrality class), the data tend to be in better agreement with b = 1 within large uncertainties. Similar trends were also reported for light hadrons [235].

From these results, one can conclude that the measurement of the path-length sensitive suppression ratio is promising and provides new insights on the path-length dependence of heavy-quark in-medium energy loss and energy loss mechanisms.

In summary, the first measurement of the nuclear modification factor of open heavy flavours via single muons at forward rapidity in Xe-Xe collisions at $\sqrt{s_{\mathrm{NN}}} =$ 5.44 TeV is presented. The results indicate a strong suppression in central (0-10%) collisions, close to that measured at $\sqrt{s_{\mathrm{NN}}} = 5.02$ TeV in Pb–Pb collisions for the 10–20% centrality class. The measurement of R_{AA} in this new system could enable a test of path-length dependence of energy loss when compared to Pb-Pb results via the path-length sensitive suppression ratio. Finally, these new R_{AA} measurements have the potential to add further constrains on energy loss models.

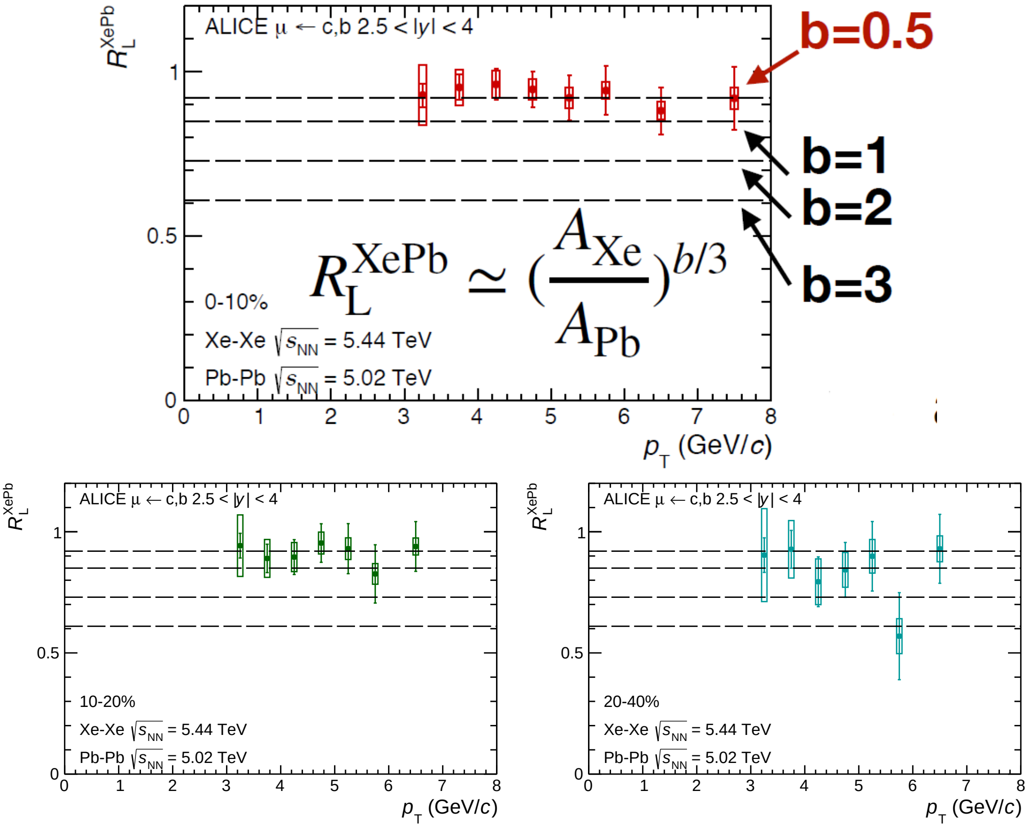

Figure 6.20: Path-length sensitive suppression ratio $R_{\rm L}^{\rm XePb}$ for the centrality class: 0-10% (top), 10-20% (bottom, left) and 20-40% (bottom, right). The dashed lines are for factor $b = 0.5$, 1, 2, and 3, respectively. see the text for details.

CHAPTER 7

Summary and Outlooks

In high-energy heavy-ion collisions, heavy quarks (charm and beauty) are regarded as efficient probes of the properties of the Quark-Gluon Plasma as they are created on a short time scale with respect to that of the QGP and experience the full evolution of the system, while losing energy in the interaction with the medium constituents. According to QCD, quarks should lose less energy than gluons when passing through the medium. This is due to the color-charge of gluons which is higher than that of quarks. In addition, heavy quarks are expected to lose less energy than light quarks due to the dead-cone effect. The parton energy loss can be studied by means of the nuclear modification factor ($R_{\rm AA}$) which compares the open heavy-flavour particle yield in heavy-ion collisions and in binary-scaled pp collisions. First measurements have been performed and published with the data taken with the ALICE detector during the LHC Run-1 [175]. In the LHC Run-2, the higher beam energy and luminosity [236] allow better precision measurements over a wider transverse momentum ($p_{\rm T}$) range.

Summary of measurements of muons from heavy-flavour hadron decays in the LHC Run-2

After a general introduction on high-energy heavy-ion collisions and QCD phase transitions and a description the ALICE apparatus in Chap. 1 and 2, respectively, measurements of the production of muons from the semi-muonic decays of charm and beauty hadrons at forward rapidity in proton-proton and nucleus-nucleus collisions collected in the LHC Run-2 have been presented in this thesis. The study of pp collisions at $\sqrt{s}$ = 5.02 TeV allowed us to provide the essential baseline for the measurements in Pb-Pb collisions at $\sqrt{s_{\rm NN}}$ = 5.02 TeV, and Xe-Xe collisions at $\sqrt{s_{\rm NN}}$ = 5.44 TeV via a energy scaling based on pQCD calculations (FONLL). The pp results provide also a stringent test of pQCD-based calculations. For comparisons with Pb-Pb measurements at lower collisions energy, the 2011 Pb-Pb data sample at $\sqrt{s_{\rm NN}}$ = 2.76 TeV has been analyzed to extend the $p_{\rm T}$ range with respect to the published results. The published pp reference at $\sqrt{s}$ = 2.76 TeV has been extrapolated to higher $p_{\rm T}$ by means of FONLL calculations. All the results have been compared with model predictions.

The statistics collected for pp collisions at $\sqrt{s} = 5.02$ TeV in the LHC Run-2 for muon-triggered events (the integrated luminosity is $L_{\rm int} = 53.7$ nb^{-1} and 104.4 nb^{-1} for MSL and MSH triggers) allowed us to perform $p_{\rm T}$- and y-differential measurements of the production cross sections of muons from heavy-flavour hadron decays. The measurements are performed over a wide $p_{\rm T}$ interval ($2 < p_{\rm T} < 20$ GeV/c) with an improved precision compared to published Run-1 results [175]. That was a consequence of an increase of the integrated luminosity associated with the analysis of muon-triggered events (MSH, in particular) a better understanding of the detector response and new data-driven strategy for the estimation of the muon background. The results are described by pQCD-based calculations (FONLL) within uncertainties and they are the reference for the study of heavy-flavour hadron decay muons in heavy-ion collisions. The ratios of the production cross sections between different beam energies and rapidity intervals expected to be sensitive to PDFs are in good agreement with pQCD calculations (FONLL). A publication of these results is presently reviewed by the ALICE Collaboration.

Then we focused on the measurement of the nuclear modification factor $R_{\rm AA}$ of muons from open heavy-flavour hadron decays in Pb-Pb collisions at $\sqrt{s_{\rm NN}}$ = 5.02 TeV and 2.76 TeV in Chap. 4 and 5. The analysis of Pb-Pb collisions at $\sqrt{s_{\rm NN}}$ = 5.02 TeV uses the data sample collected in the LHC Run-2 in 2015 with muon triggers. The statistics collected (the integrated luminosity is $L_{\rm int}$ = 21.9 nb^{-1} and 202.3 nb^{-1} for MSL and MSH triggers) allowed us to measure the $p_{\rm T}$-differential nuclear modification factor of muons from heavy-flavour hadron decays up to $p_{\rm T}$ = 20 GeV/c in various centrality classes with an improved precision compared to published results in a $p_{\rm T}$ interval limited to 10 GeV/c [175]. The results indicate a suppression of the heavy-flavour hadron decay muon yields which increases with increasing centrality. It reaches a factor of about three in the 10% most central collisions at intermediate $p_{\rm T}$. At high $p_{\rm T}$, the contribution of muons from beauty-hadron decays dominate over charm. Therefore our results provide a precise measurement of beauty production at forward rapidity and indicate a clear suppression of this contribution.

Cold nuclear matter effects on heavy-flavour production have been assessed at forward/backward rapidity via the measurement of the nuclear modification factor in p-Pb collisions at $\sqrt{s_{\rm NN}}$ = 5.02 TeV [214]. The latter being compatible with unity at intermediate/high $p_{\rm T}$, one can conclude that cold nuclear matter effects [186, 212, 218] are small and that the measured suppression in Pb-Pb collisions is due to final-state effects related the hot and dense medium formed in these collisions. Finally, the results provide new constraints on model predictions. The results show a fair agreement with most of the transport model predictions available at forward rapidity for heavy-flavour hadron decay muons. With the current precision, the data have the potential to set important constraints on model parameters. In order to perform comparison with Pb-Pb collisions at $\sqrt{s_{\rm NN}}$ = 2.76 TeV in a similar $p_{\rm T}$ region, the Pb-Pb sample at $\sqrt{s_{\rm NN}}$ = 2.76 TeV collected in 2011 has been analyzed. The results show a similar suppression of the yields of muons from heavy-flavour hadron decays at both energies. Such trend results from the interplay between harder $p_{\rm T}$ shape and denser medium. The paper proposal of Pb–Pb results has been accepted by the ALICE Collaboration and the publication is in preparation.

The first measurement of the nuclear modification factor of open heavy flavours via single muons at forward rapidity in Xe–Xe collisions at $\sqrt{s_{\rm NN}}$ = 5.44 TeV is presented in chapter 6. Xe-Xe collisions have collected in 2017 during a short pilot run of six hours in odrer to investigate the system-size dependence on the open heavy-flavour production. With the statistics collected for muon-triggered events, the nuclear modification factor has been measured up to $p_{\mathrm{T}} = 8$ GeV/c in central collisions. The heavy-flavour decay muon yields are strongly suppressed, by a factor of about three in the 10% most central collisions. The suppression is comparable with that measured in Pb–Pb collisions $\sqrt{s_{\mathrm{NN}}} = 5.02$ TeV for the 10–20% centrality corresponding to a similar charged-particle density at forward rapidity. This comparison of Pb-Pb and Xe-Xe nuclear modification factor for a given centrality class brings insight in the path-length dependence of medium-induced parton energy loss. Finally, the new results provide additional constraints on model predictions. The results have been approved as preliminary by the ALICE collaboration and the results presented has been accepted already by the ALICE collaboration.

Outlooks with Run-3 and Run-4

The LHC Run-2 will be over end of 2018, after the second Pb–Pb run scheduled in November-December 2018. The ALICE Collaboration is preparing a major upgrade of the apparatus for the Run-3 (2021–2023) and Run-4 (2026–2029) [236] to cope with new conditions where the Pb–Pb peak interaction rate may reach 50 kHz and, to improve the precision of the measurements and to give access to new set of observables to characterize the Quark-Gluon Plasma. The goal is to accumulate an integrated luminosity of 10 nb^{-1} minimum-bias Pb–Pb collisions. The implementation of the upgrade programme includes a new Inner Tracking System (ITS) [159], the replacement of the Time Projection Chamber readout wire chambers with micro-pattern gaseous readout detectors (GEM), a new set of forward trigger detectors, a new integrated online-offline system and the Muon Forward Tracker (MFT) [158]. The installation and commissioning will be done during the second Long Shutdown (LS2). The MFT is of particular interest for open heavy-flavour measurements at forward rapidity. This is a Si-tracking detector designed to add vertexing capabilities to the muon spectrometer. This will give access to new measurements presently out of reach with the muon spectrometer alone and will improve the sensitivity of some other measurements. In particular, the MFT will contribute significantly in the heavy-flavour sector by adding the possibility to discriminate muons from charm and beauty decays down to low p_{T}.

Bibliography

[1] K. A. Olive, et al. (Particle Data Group), "Review of Particle Physics," *Chinese Physics* **C38** (2014) 9. (Cited on pages 1 and 24.)

[2] S. L. Glashow, "Partial-symmetries of weak interactions," *Phys. Lett.* **22** (1961) 579. (Cited on pages 1 and 24.)

[3] Standard Model. (Cited on pages x, 1 and 2.)

[4] ATLAS Collaboration, G. Aad, et al., "Observation of a new particle in the search for the Standard Model Higgs boson with the ATLAS detector at the LHC," *Phys. Lett.* **B716** (2012) 1-29. (Cited on pages 3 and 46.)

[5] CMS Collaboration, S. Chatrchyan, et al., "Observation of a new boson at a mass of 125 GeV with the CMS experiment at the LHC," *Phys. Lett.* **B716** (2012) 30-61. (Cited on pages 3, 19 and 46.)

[6] ATLAS Collaboration, CMS Collaboration, G. Aad, et al., "Combined Measurement of the Higgs Boson Mass in pp Collisions at 7 and 8 TeV with the ATLAS and CMS Experiments" *Phys. Rev. Lett.* **114** (2015) 191803. (Cited on pages x and 3.)

[7] G. Dissertori and G. P. Salam, Particle Data Group, "Review of Particle Physics," *J. Phys. G.* **37** (2010) 075021. (Cited on pages 3 and 33.)

[8] PDG, "Review of Particles Physics," *ChinesePhysics* **C Vol. 40, No. 10** (2016), 100001. (Cited on pages x and 5.)

[9] D. J. Gross and Frank Wilczek, "Ultraviolet Behavior of Non-Abelian Gauge Theories" *Phys. Rev. Lett.* **30** (1973), 1343-1346. (Cited on page 5.)

[10] H. D. Politzer, "Reliable Perturbative Results for Strong Interactions," *Phys. Rev. Lett.* **30** (1973), 1346-1349. (Cited on page 5.)

[11] S. Hands, "The Phase Diagram of QCD," *Contemp. Phys.*, **42** (2001), 209-225. (Cited on page 5.)

[12] J. Goldstone, A. Salam, and S. Weinberg, "Broken Symmetries," *Phys. Rev.* **127** (1962), 965 (Cited on page 6.)

[13] P. B. Munzinger and J. Stachel, "Probing the phase boundary between hadronic matter and the quark-gluon-plasma in relativistic heavy ion collisions," *Nucl. Phys.* **A606** (1996), 320-328. (Cited on page 6.)

[14] J. M. Lattimer and M. Prakash, "Neutron star observations: Prognosis for equation of state constraints," *Phys. Rept.* **442** (2007), 109-165. (Cited on page 8.)

[15] M. G. Alford *et. al.*, "Color superconductivity in dense quark matter," *Rev. Mod. Phys.* **80** (2008), 1455) (Cited on page 8.)

[16] B. J. Schaefer and M. Wagner, "On the QCD phase structure from effective models," *ProgressinParticleandNuclearPhysics.* **62** (2009), 381-385 (Cited on pages x and 6.)

[17] K. G. Wilson, "Confinement of quarks," *Phys. Rev.* **D10** (1974), 2445. (Cited on page 6.)

[18] Alexei Bazavov *etal.*, "The equation of state in (2+1)-flavor QCD," *Phys. Rev.* **D90** (2014) 094503. (Cited on pages x, 6, 7 and 12.)

[19] E. V. Shuryak, "What RHIC experiments and theory tell us about properties of quark¨Cgluon plasma ?" *Nucl. Phys.* **A750** (2005), 64-83. (Cited on page 6.)

[20] F. Karsch, "Deconfinement and quarkonium suppression," *Eur. Phys. J. C* **43** (2005), 35-43. (Cited on page 6.)

[21] The evolution of the universe. (Cited on pages x and 7.)

[22] J. P. Blaizot and A. H. Mueller, "The early stage of ultra-relativistic heavy ion collisions," *Nucl. Phys.* **B289** (1987), 847-860 (Cited on page 8.)

[23] CMS Collaboration, Serguei Chatrchyan et al., "Measurement of the elliptic anisotropy of charged particles produced in PbPb collisions at 2.76 TeV," *Phys. Rev.* **C87** (2013), 014902 (Cited on pages xi and 15.)

[24] CERN COURIER, "Participants and spectators at the heavy-ion fireball," International Journal of High-Energy Physics, Apr 26, 2013 (Cited on pages x and 8.)

[25] M. Berndt, "Investigation of Hot QCD Matter: Theoretical Aspects," arXiv:1309.7616 [nucl-th]. (Cited on pages xi and 15.)

[26] R. J. Glauber and G. Matthiae, "High-energy scattering of protons by nuclei," *Nucl. Phys.* **B21** (1970), 135. (Cited on pages 9, 28 and 29.)

[27] L. McLerranv, "Theoretical Concepts for Ultra-Relativistic Heavy Ion Collisions," arXiv:0911.2987 [hep-hp]. (Cited on pages x and 9.)

[28] A. Tawfik, "Balance Function in High-Energy Collisions," Review Article. (Cited on pages x and 9.)

[29] Hans J. Specht, "Heavy Ion Physics at the CERN SPS: Roots 1974-1984 and Key Results," CERN, September 8, 2014. (Cited on pages 8, 11 and 13.)

[30] P. Crochet for the ALICE Collaboration, "The ALICE Experiment at the LHC," Physics of Particles and Nuclei, 2008, Vol. 39, No. 7, pp. 1074-1081. (Cited on page 14.)

[31] D. J. Bjorken, "Highly relativistic nucleus-nucleus collisions: The central rapidity region," *Phys. Rev.* **D27** (1983), 140. (Cited on pages xii, 8, 11, 25 and 26.)

[32] T. Matsui and H. Satz, "J/Ψ Suppression by Quark-Gluon Plasma Formation," Phys. Lett. B **178** (1986) 416. (Cited on page 11.)

[33] NA50 Collaboration, M. c. Abreu, *et. al.*, "Evidence for deconfinement of quarks and gluons from the J/Ψ suppression pattern measured in Pb-Pb collisions at the CERN-SPS" *Phys. Lett.* **B477** (2000), 28. (Cited on pages x, 11, 12 and 13.)

[34] J. Schukraft and R. Stock, *et. al.*, "Toward the Limits of Matter: Ultra-relativistic nuclear collisions at CERN" arXiv:1505.06853 [nucl-ex]. (Cited on pages x, 11 and 12.)

[35] T. Matsui and H. Satz, "J/Ψ Suppression by Quark-Gluon Plasma Formation," *Phys. Lett.* **B178** (1986), 416. (Cited on pages 11 and 13.)

[36] B. Müller and J. Rafelski, "Strangeness Production in the Quark-Gluon Plasma," *Phys. Rev. Lett.* **48** (1982), 1006. (Cited on page 11.)

[37] NA57 Collaboration, L. Sandor, *et. al.*, "Results on hyperon production from the NA57 experiment," arXiv:0404030v1 [nucl-ex]. (Cited on page 11.)

[38] T. Peitzmann and M. H. Thoma, *et. al.*, "Direct Photons from Relativistic Heavy-Ion Collisions" arXiv:0111114v2 [hep-ph]. (Cited on pages 11 and 20.)

[39] A. Franz, *et. al.*, "RHIC Experimental Evaluations," Nuclear Physics A Volume 757, (2005) Issues 1-2. (Cited on pages 8, 14 and 19.)

[40] A New Area of Physics. (Cited on page 19.)

[41] K. Adcox, *et. al.*, "Measurement of the midrapidity transverse energy distribution from $\sqrt{s_{\rm NN}}$ = 130 GeV Au-Au collisions at RHIC," Phys. Rev. Lett. **87** (2001) 052301. (Cited on page 14.)

[42] J. Cleymans, H. Oeschler, K.Redlich, and S. Wheaton, "Status of chemical freeze-out," J. Phys. G **32** (2006) S165.. (Cited on pages xi and 14.)

[43] C. Blume, *et. al.*, "Strange hadron production in heavy ion collisions from SPS to RHIC," arXiv:1105.2798v2 [nucl-ex]. (Cited on pages xi and 14.)

[44] M. J. Tannenbaum, "Results from PHENIX at RHIC with Implications for LHC," arXiv:1406.0830v1 [nucl-ex]. (Cited on pages xi, 14, 16 and 17.)

[45] R. Rapp, H. v. Hees, "Heavy Quark Diffusion as a Probe of the Quark-Gluon Plasma," arXiv:0803.0901 [hep-ph]. (Cited on pages xi, 14, 16, 17 and 19.)

[46] S. Cao, *et. al.*, "Heavy and light flavor jet quenching at RHIC and LHC energies," arXiv:1703.00822v1 [nucl-ex]. (Cited on pages xi, 14 and 17.)

[47] STAR Collaboration, J. Adams, *et. al.*, "Experimental and Theoretical Challenges in the Search for the Quark Gluon Plasma: The STAR Collaboration's Critical Assessment of the Evidence from RHIC Collisions," *Nucl. Phys.* **A757** (2005), 102-183. (Cited on pages xi, 14 and 18.)

[48] S. Campbell, "Thermal and direct photons in PHENIX," Conference Series **422** (2013) 012020. (Cited on page 14.)

[49] R. Nouicer, "Open Heavy Flavor and Quarkonia Results at RHIC," EPJ Web of Conferences 164, (2017) 06003. (Cited on page 14.)

[50] J. Adam, et al., "Measurement of transverse energy at midrapidity in Pb-Pb collisions at $\sqrt{s_{\mathrm{NN}}} = 2.76$," arXiv:1603.04775 [nucl-ex]. (Cited on pages xi and 19.)

[51] B. Donigus, et al., "Particle Yields, Ratios and Thermal Model Fits," ALI-PREL-148739. (Cited on page 20.)

[52] J. Adam, et al., "Direct photon production in Pb-Pb collisions at $\sqrt{s_{\mathrm{NN}}} = 2.76$," arXiv:1509.07324v2 [nucl-ex]. (Cited on pages xi and 20.)

[53] S. Chatrchyan, et al., "Centrality dependence of dihadron correlations and azimuthal anisotropy harmonics in Pb-Pb collisions at $\sqrt{s_{\mathrm{NN}}} = 2.76$ TeV," *Eur. Phys. J.* **C72** (2012), 2012. (Cited on pages xi and 22.)

[54] J. Adam, et al., "Anisotropic flow of charged particles in Pb-Pb collisions at $\sqrt{s_{\mathrm{NN}}} = 5.02$ TeV," *Phys. Rev. Lett.* **116** (2016), 132302. (Cited on pages xi and 22.)

[55] S. A. Voloshin, et al., "Collective phenomena in non-central nuclear collisions," arXiv:0809.2949 [nucl-ex]. (Cited on pages xi and 22.)

[56] S. A. Voloshin, et al., "Centrality and pseudorapidity dependence of the charged-particle multiplicity density in Xe-Xe collisions at $\sqrt{s_{\mathrm{NN}}} = 5.44$ TeV," arXiv:1805.04432 [nucl-ex]. (Cited on pages xi and 21.)

[57] B. Alver, et al., "High transverse momentum triggered correlations over a large pseudorapidity acceptance in Au-Au collisions at $\sqrt{s_{\mathrm{NN}}} = 200$ GeV," *Phys. Rev. Lett.* **104** (2010), 062301. (Cited on page 22.)

[58] B. I. Abelev, et al., "Long range rapidity correlations and jet production in high energy nuclear collisions," *Phys. Rev.* **C80** (2009), 064912. (Cited on page 22.)

[59] K. Aamodt, et al., "Harmonic decomposition of two-particle angular correlations in Pb-Pb collisions at $\sqrt{s_{\mathrm{NN}}} = 2.76$ TeV," *Phys. Lett.* **B708** (2012), 249-264. (Cited on page 22.)

[60] S. Chatrchyan, et al., "Long-range and short-range dihadron angular correlations in central PbPb collisions at a nucleon-nucleon center of mass energy of 2.76 TeV," *JHEP* **07** (2011), 076. (Cited on page 22.)

[61] K. Aamodt, et al., "Elliptic flow of charged particles in Pb-Pb collisions at 2.76 TeV," *Phys. Rev. Lett.* **105** (2010), 252302. (Cited on page 22.)

[62] K. H. Ackermann, et al., "Elliptic flow in Au-Au collisions at $\sqrt{s_{\rm NN}} = 130$ GeV," *Phys. Rev. Lett.* **86** (2001), 402-407. (Cited on page 22.)

[63] M. Luzum, P. Romatschke, "Viscous Hydrodynamic Predictions for Nuclear Collisions at the LHC," *Phys. Rev. Lett.* **103** (2009), 262302. (Cited on page 22.)

[64] S. Chatrchyan, et al., "Study of high-$p_{\rm T}$ charged particle suppression in Pb-Pb compared to pp collisions at $\sqrt{s_{\rm NN}} = 2.76$ TeV," *Eur. Phys. J.* **C72** (2012), 1945. (Cited on pages xi, 22 and 23.)

[65] K. Aamodt, et al., "Suppression of Charged Particle Production at Large Transverse Momentum in Central Pb-Pb Collisions at $\sqrt{s_{\rm NN}} = 2.76$ TeV," *Phys. Lett.* **B696** (2011), 30-39. (Cited on pages xi, 22 and 23.)

[66] A. Dainese, C. Loizides, and G. Paic, "Leading-particle suppression in high energy nucleus-nucleus collisions," Eur. Phys. J. C **38** (2005) 461. (Cited on pages xi and 23.)

[67] I. Vitev and M. Gyulassy, "High $p_{\rm T}$ tomography of d-Au and Au-Au at SPS, RHIC, and LHC," Phys. Rev. Lett. **89** (2002) 252301. (Cited on pages xi and 23.)

[68] I. Vitev, "Jet tomography," , J. Phys. G **30** (2004) S791. (Cited on pages xi and 23.)

[69] C. A. Salgado and U. A. Wiedemann, "Calculating quenching weights," Phys. Rev. D **68** (2003) 014008. (Cited on pages xi and 23.)

[70] K. Adcox, et al., "Suppression of hadrons with large transverse momentum in central Au+Au collisions at $\sqrt{s_{\rm NN}} = 130$ GeV," *Phys. Rev. Lett.* **88** (2002), 022301. (Cited on page 23.)

[71] C. Adler, et al., "Centrality dependence of high p_T hadron suppression in Au+Au collisions at $\sqrt{s}_{\rm NN} = 130$ GeV," *Phys. Rev. Lett.* 89 (2002), 202301. (Cited on page 23.)

[72] J. Schukraft, "Heavy ions at the LHC: Physics perspectives and experimental program," Nucl. Phys. A **698**, 287 (2002). (Cited on pages xxvi and 10.)

[73] P. Foka, M. A. Janik, "An overview of experimental results from ultra-relativistic heavy-ion collisions at the CERN LHC: bulk properties and dynamical evolution," arXiv:1702.07233 [hep-ex]. (Cited on pages 20 and 24.)

[74] P. Foka, M. A. Janik, "An overview of experimental results from ultra-relativistic heavy-ion collisions at the CERN LHC: hard probes," arXiv:1702.07231 [hep-ex]. (Cited on page 24.)

[75] J. C. Collins, *et. al.*, "Heavy Particle Production in High-Energy Hadron Collisions," *Nucl. Phys.* **B263** (1986), 37. (Cited on page 25.)

[76] N. Carrer and A. Dainese, "Charm and beauty production at LHC," arxiv:0311225 [hep-ph]. (Cited on pages xii and 26.)

[77] N. Kidonakis, *et. al.*, "Sudakov Resummation and Finite Order Expansions of Heavy Quark Hadroproduction Cross Sections," *Phys. Rev.* **D64** (2001), 114001. (Cited on page 27.)

[78] M. Cacciari, M. Greco, P. Nason, "The p_T spectrum in heavy flavor hadroproduction," *JHEP* 9805 (1998), 007. (Cited on page 27.)

[79] A. H. Mueller, "Cut vertices and their renormalization: A generalization of the Wilson expansion," *Phys. Rev.* **D18** (1978), 3705. (Cited on page 27.)

[80] J. C. Collins, *et. al.*, "Soft Gluons and Factorization," *Nucl. Phys.* **B308** (1988), 833. (Cited on page 27.)

[81] J. D. Bjorken, "Properties of hadron distributions in reactions containing very heavy quarks," *Phys. Rev.* **D17** (1978), 171-173. (Cited on page 28.)

[82] S. Mahiko, "Fragmentation of hadrons from heavy quark partons," *Phys. Lett.* **B71** (1977), 139-141. (Cited on page 28.)

[83] M. L. Miller, *et. al.*, "Glauber Modeling in High-Energy Nuclear Collisions," *Annu. Rev. Nucl. Part. Sci.* **57** (2007), 205-243 (Cited on pages xii and 28.)

[84] R. D. Woods, D. S. Saxon, "Diffuse surface optical model for nucleon-nuclei scattering," *Physical Review* **95** (1954), 577-578. (Cited on page 28.)

[85] R. Vogt, "Relation of hard and total cross sections to centrality," arXiv:9903051 [nucl-th]. (Cited on page 28.)

[86] K. J. Eskola, R. Vogt, X. N. Wang, "Nuclear overlap functions," *Int. J. Mod. Phys.* **A10** (1995), 3087-3090. (Cited on page 28.)

[87] A. Michele, "Nuclear effects in structure functions," *Phys. Rept.* **240** (1994), 301-393. (Cited on page 30.)

[88] A. Bodek, J. L. Ritchie, "Fermi Motion Effects in Deep Inelastic Lepton Scattering from Nuclear Targets," *Phys. Rev.* **D23** (1981), 1070. (Cited on page 30.)

[89] P. R. Norton, "The EMC effect," *Rept. Prog. Phys.* **66** (2003), 1253-1297. (Cited on page 30.)

[90] K. J. Eskola, *et. al.*, "The scale dependent nuclear effects in parton distributions for practical applications," *Eur. Phys. J.* **C9** (1999), 61-68. (Cited on pages xii, 30 and 31.)

[91] K. J. Eskola, H. Paukkunen, C. A. Salgado, "An improved global analysis of nuclear parton distribution functions including RHIC data," arXiv:0802.0139v2 [hep-ph]. (Cited on pages xii, 30 and 31.)

[92] D. de Florian, R. Sassot, "Nuclear parton distributions at next to leading order," arXiv:0311227 [hep-ph]. (Cited on pages xii, 30 and 31.)

[93] K. Eskola, et al, "EPS09 - a New Generation of NLO and LO Nuclear Parton Distribution Functions," *JHEP* 0904 (2009), 065. (Cited on pages xii, 30 and 31.)

[94] H.Fujii and K.Watanabe, "Heavy quark pair production in high energy pA collisions: Quarkonium," Nucl. Phys. **A915**(2013) 1. (Cited on page 29.)

[95] I. Vitev, "Non-Abelian energy loss in cold nuclear matter," *Phys. Rev.* **C75** (2007) 064906. (Cited on page 29.)

[96] T. Ochiai, *et. al.*, "EMC Effect and Hadron Production off Nuclei at Large Transverse Momentum," *Prog. Theor. Phys.* **75**, (1986), 288. (Cited on page 31.)

[97] X. N. Wang, "Systematic Study of High p_T Hadron Spectra in pp, pA and AA Collisions from SPS to RHIC Energies," *Phys. Rev.* **C61** (2000) 064910. (Cited on pages xii and 31.)

[98] X. N. Wang, "Jet Quenching," arXiv:0209038 [hep-ph]. (Cited on pages xii, 32 and 34.)

[99] R. Baier, *et. al.*, "Radiative energy loss of high energy quarks and gluons in a finite-volume quark-gluon plasma," *Nucl. Phys.* **B483** (1997), 291. (Cited on pages 29 and 33.)

[100] R. Baier, *et. al.*, "Angular Dependence of the Radiative Gluon Spectrum and the Energy Loss of Hard Jets in QCD Media," *Phys. Rev.* **C60** (1999), 064902. (Cited on page 33.)

[101] Y. L. Dokshitzer, D. E. Kharzeev, "Heavy quark colorimetry of QCD matter," *Phys. Lett.* **B519** (2001), 199-206. (Cited on page 33.)

[102] G. Y. Qin, *et. al.*, "Radiative and Collisional Jet Energy Loss in the Quark-Gluon Plasma at the BNL Relativistic Heavy Ion Collider," *Phys.Rev.Lett.* **100** (2008), 072301. (Cited on pages xii and 34.)

[103] S. Wick, *et. al.*, "Elastic, Inelastic, and Path Length Fluctuations in Jet Tomography," arXiv:0512076 [nucl-th]. (Cited on pages xii and 34.)

[104] M. Djordjevic, "Theoretical formalism of radiative jet energy loss in a finite size dynamical QCD medium," Phys. Rev. C **80**, 064909. (Cited on pages xii and 34.)

[105] S. Wick, *et. al.*, "Heavy-flavour and quarkonium production in the LHC era: from proton¨Cproton to heavy-ion collisions," Eur. Phys. J. C (2016) 76:107. (Cited on pages xii, 10, 24, 27, 31 and 34.)

[106] X. Zhao, R. Rapp, "Medium Modifications and Production of Charmonia at LHC," Nucl. Phys. **A859** (2011) 114-125. (Cited on pages xii, 35 and 36.)

[107] X. Du, R. Rapp, "Sequential Regeneration of Charmonia in Heavy-Ion Collisions," Nucl. Phys. **A943** (2015) 147-158. (Cited on pages xii, 35 and 36.)

[108] X. Du, R. Rapp, M. He, "Color Screening and Regeneration of Bottomonia in High-Energy Heavy-Ion Collisions," arXiv:1706.08670 [hep-ph]. (Cited on pages xii, 36 and 37.)

[109] K. Zhou, N. Xu, P. Zhuang, "Υ Production in Heavy Ion Collisions at LHC," arXiv:1408.3900 [hep-ph]. (Cited on pages xii, 36 and 37.)

[110] B. Krouppa, A. Rothkopf, M. Strickland, "Bottomonium suppression using a lattice QCD vetted potential," arXiv:1710.02319 [hep-ph]. (Cited on pages xii, 36 and 37.)

[111] J. Adam, et al., "Quarkonium measurements in nucleus-nucleus collisions with ALICE," arXiv:1807.07757v1 [hep-ex]. (Cited on pages xii and 36.)

[112] Z. Conesa del Valle, "Heavy-flavor suppression and azimuthal anisotropy in Pb-Pb collisions at $\sqrt(s_{\rm NN}) = 2.76$ TeV with the ALICE detector," *Nucl. Phys.* **A904-905** (2013), 178c-185c. (Cited on page 37.)

[113] J. Adam, et al., "Transverse momentum dependence of D-meson production in Pb-Pb collisions at $\sqrt{s_{\rm NN}} = 2.76$ TeV," arXiv:1509.06888 [nucl-ex]. (Cited on pages xiii, 37 and 38.)

[114] J. Adam, et al., "Measurement of D_s^+ production and nuclear modification factor in Pb-Pb collisions at $\sqrt{s_{\rm NN}} = 2.76$ TeV," arXiv:1509.07287 [nucl-ex]. (Cited on page 37.)

[115] B. Abelev, et al., "Measurement of prompt D-meson production in p-Pb collisions at $\sqrt{s_{\rm NN}} = 5.02$ TeV," *Phys. Rev. Lett.* **113** (2014), 232301. (Cited on page 38.)

[116] S. Acharya, et al., "Measurement of D^0, D^+, D^{*+} and D_s^+ production in Pb-Pb collisions at $\sqrt{s_{\rm NN}} = 5.02$ TeV," arXiv:1804.09083 [nucl-ex]. (Cited on pages xii and 37.)

[117] S. Chatrchyan, et al., "Suppression of non-prompt J/Ψ , prompt J/Ψ , and Y(1S) in Pb-Pb collisions at $\sqrt{s_{\rm NN}} = 2.76$ TeV," *JHEP* **05** (2012), 063. (Cited on page 38.)

[118] J. Adam, et al., Inclusive, prompt and non-prompt J/Ψ production at mid-rapidity in Pb-Pb collisions at $\sqrt{s_{\rm NN}} = 2.76$ TeV, *JHEP* **07** (2015), 051. (Cited on page 38.)

[119] B. Abelev, et al., "Production of charged pions, kaons and protons at large transverse momenta in pp and Pb-Pb collisions at $\sqrt{s_{\rm NN}}$ =2.76 TeV," *Phys. Lett.* **B736** (2014), 196-207. (Cited on pages xiii and 38.)

[120] J. Adam, et al., "Centrality dependence of high-p_T D meson suppression in Pb-Pb collisions at $\sqrt{s_{\rm NN}} = 2.76$ TeV," *JHEP* **11** (2015), 205. (Cited on pages xiii and 38.)

[121] CMS Collaboration, "J/Ψ results from CMS in Pb-Pb collisions, with 150μb^{-1} data," Tech. Rep. CMS-PAS-HIN-12-014, CERN, Geneva (2012). (Cited on pages xiii and 38.)

[122] S. Acharya, et al., "D-meson azimuthal anisotropy in mid-central Pb-Pb collisions at $\sqrt{s_{\rm NN}} = 5.02$ TeV," Phys. Rev. Lett. **120** (2018), 102301. (Cited on pages xiii and 40.)

[123] S. Acharya, et al., "Preliminary Physics Summary: Measurement of D^0, D^+, D^{*+} and D_s^+ production in Pb-Pb collisions at $\sqrt{s_{\rm NN}} = 5.02$ TeV," ALICE-PUBLIC-2017-003. (Cited on pages xiii and 40.)

[124] W. Horowitz, M. Gyulassy, "The Surprising Transparency of the sQGP at LHC," *Nucl. Phys.* **A872** (2011), 265-285. (Cited on pages xiii and 40.)

[125] M. Nahrgang, et al., "Influence of hadronic bound states above $T_{\rm c}$ on heavy-quark observables in Pb-Pb collisions at LHC," arXiv:1305.6544 [hep-ph]. (Cited on pages xiii and 40.)

[126] M. He, et al., "Heavy Flavor at the Large Hadron Collider in a Strong Coupling Approach," *Phys. Lett.* **B735** (2014), 445-450. (Cited on pages xiii and 40.)

[127] W. M. Alberico, et al., "Heavy-flavour spectra in high energy nucleus-nucleus collisions," *Eur. Phys. J.* **C71** (2011), 1666. (Cited on pages xiii and 40.)

[128] J. Uphoff, et al., "Open Heavy Flavor in Pb+Pb Collisions at $\sqrt{s} = 2.76$ TeV within a Transport Model," *Phys. Lett.* **B717** (2012), 430-435. (Cited on pages xiii and 40.)

[129] T. Lang, et al, "Heavy quark transport in heavy ion collisions at energies available at the BNL Relativistic Heavy Ion Collider and at the CERN Large Hadron Collider within the UrQMD hybrid model," *Phys. Rev.* **C93** (2016), 014901. (Cited on pages xiii and 40.)

[130] S. Cao, et al, "Heavy-quark dynamics and hadronization in ultrarelativistic heavy-ion collisions: Collisional versus radiative energy loss," *Phys. Rev.* **C88** (2013), 044907. (Cited on pages xiii and 40.)

[131] N. Armesto, E. Scomparin, "Heavy-ion collisions at the Large Hadron Collider: a review of the results from Run 1," arXiv:1511.02151 [nucl-ex]. (Not cited.)

[132] B. Abelev, et al, "Heavy flavour decay muon production at forward rapidity in proton-proton collisions at $\sqrt{s}$ =7 TeV," arXiv:1201.3791 [hep-ex]. (Cited on pages xiii, 41 and 42.)

[133] B. Abelev, et al, "Production of muons from heavy flavour decays at forward rapidity in pp and Pb-Pb collisions at $\sqrt{s_{\rm NN}} = 2.76$ TeV," arXiv:1205.6443 [hep-ex]. (Cited on pages xiii, xxvii, 39, 41, 42, 43, 150, 151, 152, 153 and 163.)

[134] The Large Hadron Collider. (Cited on pages xiii, 8, 19, 45 and 46.)

[135] ATLAS home page. (Cited on pages 3 and 46.)

[136] CMS home page. (Cited on pages 3, 19 and 46.)

[137] LHCb home page. (Cited on page 46.)

[138] ALICE home page. (Cited on pages 19 and 47.)

[139] TOTEM home page. (Cited on page 47.)

[140] MoEDAL home page. (Cited on page 47.)

[141] LHCf home page. (Cited on page 47.)

[142] ALICE Collaboration, "ALICE Technical Design Report of the Inner Tracking System," CERN-LHCC-99-12, (1999). (Cited on pages xiv, 47, 53 and 54.)

[143] ALICE Collaboration, "ALICE Technical Design Report of the Time Projection Chamber," CERN-LHCC-2000-001, (2000). (Cited on pages xiv, 47, 53, 54 and 55.)

[144] ALICE Collaboration, "ALICE Technical Design Report of the Transition Radiation Detector," CERN-LHCC-2001-021, (2001). (Cited on pages 47 and 55.)

[145] ALICE Collaboration, "Addendum to the Technical Design Report of the Time of Flight System ," CERN-LHCC-2002-016, (2002). (Cited on pages 50 and 55.)

[146] ALICE Collaboration, "ALICE Technical Design Report of the High Momentum Particle Identification Detector," CERN-LHCC-98-19, (1998). (Cited on pages 50 and 55.)

[147] ALICE Collaboration, "ALICE Technical Design Report of the Photon Spectrometer," CERN-LHCC-99-04, (1999). (Cited on pages 50 and 55.)

[148] ALICE Collaboration, "ALICE Electromagnetic Calorimeter Technical Design Report," CERN-LHCC-2008-014, (2008). (Cited on pages 50 and 56.)

[149] ALICE Collaboration, "ALICE DCal: An Addendum to the EMCal Technical Design Report Di-Jet and Hadron-Jet correlation measurements in ALICE," CERN-LHCC-2010-011 ,ALICE-TDR-14-add-1, (2010). (Cited on page 50.)

[150] ALICE Collaboration, "ACORDE, The ALICE cosmic ray detector," Proceedings of the 30th International Cosmic Ray Conference, (2008) Vol. 5 (HE part 2), pages 1201-1204. (Cited on pages 50 and 56.)

[151] K. Aamodt, et al. , "The ALICE experiment at the CERN LHC," *JINST* 3 (2008) , S08002. (Cited on pages xiii, xxvi, 48, 49, 50 and 58.)

[152] B. B. Abelev et al., "Performance of the ALICE Experiment at the CERN LHC," arXiv:1402.4476 [nucl-ex]. (Cited on page 50.)

[153] K. Aamodt, et al. , "Technical Proposal A Large Ion Collider Experiment CERN LHC," CERN/LHCC (1995), 95-71. (Cited on page 50.)

[154] ALICE Collaboration, "ALICE Technical Design Report on Forward Detectors: FMD, T0 and V0," CERN-LHCC-2004-025, (2004). (Cited on pages xiii, 50, 51 and 52.)

[155] ALICE Collaboration, "ALICE Technical Design Report: Photon Multiplicity Detector," CERN-LHCC-99-32, (1999). (Cited on pages 50 and 53.)

[156] ALICE Collaboration, "ALICE Technical Design Report of the Zero Degree Calorimeter," CERN-LHCC-99-05, (1999). (Cited on pages 50 and 52.)

[157] J. Adam et al.,"Centrality dependence of the charged-particle multiplicity density at mid-rapidity in Pb-Pb collisions at $\sqrt{s_{\rm NN}} = 5.02$ TeV," *Phys. Rev. Lett.* **116** (2016) 222302. (Cited on pages xiii and 52.)

[158] ALICE Collaboration, "Technical Design Report for the Muon Forward Tracker," CERN-LHCC-2015-001, (2015). (Cited on pages xiv, 56, 57, 60, 61 and 198.)

[159] ALICE Collaboration, "Upgrade of the ALICE Inner Tracking System," arXiv:1607.01171 [physics.ins-det]. (Cited on pages xiv, 59 and 198.)

[160] ALICE Collaboration, "ALICE trigger data-acquisition high-level trigger and control system: Technical Design Report," CERN-LHCC-2003-062, (2004). (Cited on page 62.)

[161] Environment of ROOT. (Cited on page 64.)

[162] R. Brun, et al.„ "GEANT Detector Description and Simulation Tool," CERN Program Library Long Writeup W5013, (1994). (Cited on page 65.)

[163] J. Allison, *et. al.*, "Geant4 developments and applications," IEEE Transactions on Nuclear Science **53** No. 1 (2006) 270-278. (Cited on page 65.)

[164] A. Fasso, et al., "FLUKA : A multi-particle transport code (program version 2005)," CERN-2005-10 (2005). (Cited on page 65.)

[165] ALICE Collaboration, "The ALICE Offline Bible," AliRoot Documentation. (Cited on pages xiv, 64, 65, 66 and 67.)

[166] X. Zhang, "Study of Heavy Flavours from Muons Measured with the ALICE Detector in Proton-Proton and Heavy-Ion Collisions at the CERN-LHC," PHD Thesis. (Cited on pages xiv and 68.)

[167] J. Adam et *al.*, "Production of muons from heavy-flavour hadron decays in p-Pb collisions at $\sqrt{s_{\mathrm{NN}}} = 5.02$ TeV," Phys. Lett. **B 770** (2017) 459-472 (Cited on pages 43, 70 and 159.)

[168] Z Zhang et *al.*, "Production of muons from heavy-flavour hadron decays at forward rapidity in Pb–Pb collisions at $\sqrt{s_{\mathrm{NN}}} = 5.02$ TeV," https://aliceinfo.cern.ch/Notes/node/519 (Cited on pages 71, 73, 99 and 106.)

[169] S. Acharya et *al.*, "Energy dependence of forward-rapidity J/ψ and ψ(2S) production in pp collisions at the LHC," arXiv:1702.00557 [hep-ex]. (Cited on pages 73, 95, 98 and 99.)

[170] M. Gagliardi, "PWG-PP Run Conditions meeting, 23 Oct. 2015," https://indico.cern.ch/event/456763. (Cited on page 73.)

[171] Z. Zhang, "PAG-HFM, PAG meeting, April 27$^{\mathrm{th}}$, 2016," https://indico.cern.ch/event/524572. (Cited on page 73.)

[172] J. Adam et *al.*, "ALICE luminosity determination for pp collisions at $\sqrt{s} = 5$ TeV," ALICE-PUBLIC-2016-005. (Cited on pages 76 and 78.)

[173] J. Adam et *al.*, "Multiplicity dependence of charged pion, kaon, and (anti)proton production at large transverse momentum in p-Pb collisions at $\sqrt{s_{\mathrm{NN}}}$ $= 5.02$ TeV," Phys. Lett. B **760** (2016) 720. (Cited on pages xv and 82.)

[174] Z. Zhang, *al.*,"Production of muons from heavy-flavour hadron decays at forward rapidity in Pb-Pb collisions at 2.76 TeV," https://aliceinfo.cern.ch/Notes/node/418. (Cited on pages 83 and 143.)

[175] B. Abelev et *al.*, "Production of Muons from Heavy Flavor Decays at Forward Rapidity in pp and Pb-Pb Collisions at $\sqrt{s_{\mathrm{NN}}} = 2.76$ TeV," Phys. Rev. Lett. **109** (2012) 112301. (Cited on pages 105, 108, 115, 196 and 197.)

[176] X. Zhang et *al.*, "Study of absorber effects on decay muon production," https://indico.cern.ch/event/632785. (Cited on page 86.)

[177] X. Zhang et *al.*, "New study of absorber effects on decay muon production," https://indico.cern.ch/event/634736. (Cited on page 86.)

[178] S. Tang et *al.*, "Update on absorber effects on decay muon production," https://indico.cern.ch/event/638435 (Cited on page 86.)

[179] X. Zhang et *al.*, "Update on decay muon estimation in Pb-Pb at 2.76 TeV," https://indico.cern.ch/event/641957 (Cited on pages 85, 86 and 87.)

[180] X. Zhang, ALICE Muon workshop, "Study of decay muon background with ALICE muon spectrometer," https://indico.cern.ch/event/614004 (Cited on pages 85, 86 and 87.)

[181] S. Chatrchyan et *al.*, "Study of W boson production in Pb-Pb and pp collisions at $\sqrt{s_{\rm NN}} = 2.76$ TeV," Phys. Lett. B **715** (2012) 66. (Cited on pages 94 and 146.)

[182] B. Abelev et *al.*, "Heavy flavour decay muon production at forward rapidity in proton-proton collisions at $\sqrt{s} = 7$ TeV," Phys. Lett. B **708** (2012) 265. (Cited on pages 71, 105 and 108.)

[183] T. Sjostrand, S. Mrenna, and P. Z. Skands, "PYTHIA 6.4 Physics and Manual," arXiv:hep-ph/0603175 [hep-ph]. (Cited on page 91.)

[184] R. Brun et *al.*, "GEANT Detector Description and Simulation Tool," CERN Program Library Long Writeup W5013. (Cited on page 91.)

[185] FONLL, http://www.lpthe.jussieu.fr/ cacciari/fonll/fonllform.html (Cited on page 105.)

[186] M. L. Mangano, P. Nason, G. Ridolfi, "Heavy quark correlations in hadron collisions at next-to-leading order," Nucl. Phys. B **373** (1992) 295-345. (Cited on pages xxii, 104, 160 and 197.)

[187] S. Acharya et *al.*, "Measurement of D-meson production at mid-rapidity in pp collisions at $\sqrt{s} = 7$ TeV," arXiv:1702.00766 [hep-ex]. (Cited on page 108.)

[188] B. Abelev et *al.*, "production at central rapidity in proton-proton collisions at $\sqrt{s} = 7$ TeV," JHEP **01** (2012) 128. (Cited on page 108.)

[189] B. Abelev et *al.*, "Measurement of electrons from semileptonic heavy-flavor hadron decays in pp collisions at $\sqrt{s} = 2.76$ TeV," Phys. Rev. D **91** (2015) 012001. (Cited on page 108.)

[190] B. Abelev et *al.*, "Beauty production in pp collisions at $\sqrt{s} = 2.76$ TeV measured via semi-electronic decays," Phys. Lett. B **738** (2014) 97. (Cited on page 108.)

[191] B. Abelev et *al.*, "Measurement of electrons from beauty hadron decays in pp collisions at $\sqrt{s} = 7$ TeV" Phys. Lett. B **721** (2013) 13-23. (Cited on page 108.)

[192] B. Abelev et *al.*, "Measurement of electrons from semileptonic heavy-flavor hadron decays in pp collisions at $\sqrt{s} = 7$ TeV," Phys. Rev. D **86**, 112007 (2012). (Cited on page 108.)

[193] M. Cacciari et al., "Gluon PDF constraints from the ratio of forward heavy-quark production at the LHC at at $\sqrt{s} = 7$ and 13 TeV," Eur. Phys. J. C **75** (2015) 610. (Cited on pages 108 and 109.)

[194] R. Averbeck et al., "Reference heavy flavour cross sections in pp collisions at $\sqrt{s}$ = 2.76 TeV, using a pQCD-driven sqrt(s)-scaling of ALICE measurements at $\sqrt{s}$ = 7 TeV" arXiv:1107.3243 [hep-ex]. (Cited on pages 104, 112, 115 and 187.)

[195] https://twiki.cern.ch/twiki/bin/view/ALICE/MuonPbPbQA2015. (Cited on page 117.)

[196] https://twiki.cern.ch/twiki/bin/viewauth/ALICE/MuonpPbQA2013. (Cited on page 118.)

[197] Z. Zhang, "Production of muons from heavy-flavour hadron decays in Pb-Pb and pp collisions at 5.02 TeV," PWG-HF meeting, July 19th, 2016. (Cited on page 121.)

[198] D. Stocco et al., "Production of muons from W boson decays at forward rapidity in p-Pb collisions at 5.02 TeV," https://aliceinfo.cern.ch/Notes/node/237 (Cited on pages 120 and 121.)

[199] R. Arnaldi et al., "J/ψ production in Pb–Pb collisions at $\sqrt{s_{\rm NN}}$ = 5.02 TeV," https://aliceinfo.cern.ch/Notes/node/486 (Cited on pages 125, 132, 133, 149, 150 and 152.)

[200] Z. Zhang et al., "Production of muons from heavy-flavour hadron decays at forward rapidity in Pb-Pb collisions at $\sqrt{s_{\rm NN}}$ = 2.76 TeV," https://aliceinfo.cern.ch/Notes/node/418 (Cited on page 127.)

[201] M. Marchisone, "Cross section at 8 TeV and analysis of the embedding production," PAG-HFM meeting on 15 June 2016. (Cited on pages 132 and 133.)

[202] B. Abelev, et al, "Production of muons from heavy flavour decays at forward rapidity in pp and Pb-Pb collisions at $\sqrt{s_{\rm NN}}$ = 2.76 TeV," arXiv:1205.6443 [hep-ex]. (Cited on page 136.)

[203] Z. Conesa Del Valle, "Performance of the ALICE muon spectrometer. Weak boson production and measurement in heavy-ion collisions at LHC," PhD thesis, CERN-THESIS-2007-102. (Not cited.)

[204] Ivan Ravasenga, et al, "Production of pi/K/p in pp and Pb-Pb collisions at $\sqrt{s_{\rm NN}}$ = 5.02TeV," https://aliceinfo.cern.ch/Notes/node/589. (Cited on pages xx and 137.)

[205] ALICE Collaboration, "Elliptic flow of muons from heavy-flavour hadron decays at forward rapidity in Pb-Pb collisions at $\sqrt{s_{\rm NN}}$ = 2.76TeV," arXiv:1507.03134 [nucl-ex]. (Cited on pages xx and 142.)

[206] CMS Collaboration, "Study of W boson production in PbPb and pp collisions at 2.76 TeV," Phys. Lett. B **715** (2012) 66. (Cited on pages 94 and 146.)

[207] B. Audurier et al., "J/ψ production in pp collisions at $\sqrt{s}$ = 5.02 TeV," https://aliceinfo.cern.ch/Notes/node/500. (Cited on pages 149 and 150.)

[208] Z.Zhang, "Updates of muons from open heavy-flavour hadron decays analysis in RUN-II," PAG-HFM, June 22, 2016. (Cited on page 149.)

[209] ALICE Collaboration, "Energy dependence of forward-rapidity J/ψ and ψ(2S) production in pp collisions at the LHC," Eur. Phys. J. C **77** (2017) 392. (Cited on page 149.)

[210] J. Castillo, "Embedding results," PAG-JPsimumu, March 18, 2016. (Cited on page 152.)

[211] https://twiki.cern.ch/twiki/bin/view/ALICE/CentralityCodeSnippets. (Cited on pages xxvii, 152 and 153.)

[212] Z. B. Kang et *al.*, "Multiple scattering effects on heavy meson production in p+A collisions at backward rapidity," arXiv:1409.2494 [hep-ph]. (Cited on pages xxii, 160 and 197.)

[213] S. Acharya et *al.*, "Measurement of D^0, D^+, D^{*+} and D_s^+ production in Pb-Pb collisions at $\sqrt{s_{NN}}$ =5.02 TeV," arXiv:1804.09083 [nucl-ex]. (Cited on pages xxvii and 170.)

[214] S. Acharya et *al.*, "Production of muons from heavy-flavour hadron decays in p-Pb collisions at $\sqrt{s_{NN}} = 5.02$ TeV with the ATLAS detector," Phys. Lett. B **770** (2017) 459-472. (Cited on pages xxii, 160 and 197.)

[215] M. Djordjevic, M. Djordjevic, "Heavy flavor suppression predictions at 5.1 TeV Pb-Pb collisions at LHC," Phys. Rev. C **92** (2015) 024918. (Cited on page 163.)

[216] A. Milov for the ATLAS Collaboration, "The R_{AA} and v_2 of muons from heavy-quark decays in Pb+Pb collisions at $\sqrt{s_{NN}} = 2.76$ TeV with the ATLAS detector," Nuclear Physics A **956** (2016) 521¨C524. (Cited on pages xxii and 166.)

[217] R. Sharma et *al.*, "Heavy flavor at the large hadron collider in a strong coupling approach," Phys. Lett. B **735** (2014) 445. (Cited on pages xxiii, 167, 168 and 171.)

[218] R. Sharma et *al.*, "Light-cone wave function approach to open heavy flavor dynamics in QCD matter," Phys. Rev. C **80** (2009) 054902. (Cited on pages xxii, xxiii, 160, 167, 168, 172 and 197.)

[219] T. Song et *al.*, "Open charm and dileptons from relativistic heavy-ion collisions," arXiv:1803.02698 [nucl-th]. (Cited on pages xxiii, xxiv, 171, 191 and 192.)

[220] T. Song et *al.*, "Single electrons from heavy-flavor mesons in relativistic heavy-ion collisions," Phys.Rev. C**96** (2017) no.1, 014905. (Cited on pages xxiii, xxiv, 171, 191 and 192.)

[221] M. Nahrgang et *al.*, "Influence of hadronic boundstates above Tc on heavy-quark observables in Pb-Pb collisions at the CERN Large Hadron Collider," Phys. Rev. C **89** (1) (2014) 014905, arXiv:1305.6544 [hep-ph]. (Cited on pages xxiii, 167, 168, 171, 172 and 173.)

[222] K. Werner et *al.*, "Event-by-event simulation of the three-dimensional hydrodynamic evolution from flux tube initial conditions in ultra-relativistic heavy ion collisions," Phys. Rev. C **82** (2010)044904, arXiv:1004.0805 [nucl-th]. (Cited on pages xxiii, 167, 168, 171, 172 and 173.)

[223] https://twiki.cern.ch/twiki/bin/view/ALICE/MuonPbPbQA2015. (Cited on page 174.)

[224] S. Acharya et *al.*, "Inclusive J/ψ production in Xe-Xe collisions at $\sqrt{s_{\rm NN}}$ = 5.44 TeV," arXiv:1805.04383 [nucl-ex]. (Cited on page 177.)

[225] C. Loizides et *al.*, "Precision Monte Carlo Glauber predictions at present and future nuclear colliders," arXiv:1710.07098 [nucl-ex]. (Cited on pages 128, 129 and 178.)

[226] Z. Zhang et *al.*, "Production of muons from heavy-flavour hadron decays at forward rapidity in Pb–Pb collisions and pp collisions at 5.02 TeV," https://aliceinfo.cern.ch/Notes/node/519. (Cited on pages 179 and 182.)

[227] https://twiki.cern.ch/twiki/bin/view/ALICE/XeXeCentStudies. (Cited on pages xxviii, 181, 186 and 187.)

[228] https://twiki.cern.ch/twiki/bin/view/ALICE/CentralityCodeSnippets. (Cited on pages xxviii and 181.)

[229] https://twiki.cern.ch/twiki/bin/view/ALICE/ReferenceMultCentrality. (Cited on pages xxviii and 181.)

[230] R. Averbeck et *al.*, "Reference heavy flavour cross sections in pp collisions at $\sqrt(s)$ = 2.76 TeV, using a pQCD-driven $\sqrt(s)$-scaling of ALICE measurements at $\sqrt{s}$ = 7 TeV," arXiv:1107.3243 [hep-ph]. (Cited on pages 104, 112, 115 and 187.)

[231] Z. Zhang et *al.*, "Production of muons from heavy-flavour hadron decays in pp collisions at $\sqrt{s}$ = 5.02 TeV," https://aliceinfo.cern.ch/Notes/node/671. (Cited on pages 183 and 186.)

[232] N. Jacazio et *al.*, "Production of pi/K/p in Xe-Xe collisions at $\sqrt{s_{\rm NN}}$ = 5.44 TeV," https://aliceinfo.cern.ch/Notes/node/771. (Cited on pages xxiii and 183.)

[233] R. Arnaldi et *al.*, "Forward-rapidity production of inclusive J/Ψ in Xe-Xe collisions at $\sqrt{s_{\rm NN}}$ = 5.44 TeV," https://aliceinfo.cern.ch/Notes/node/718. (Cited on page 186.)

[234] A. Dubla et *al.*, "Nuclear modification factor of electrons from of heavy-flavour hadron decays in Xe-Xe collision at $\sqrt{s_{\mathrm{NN}}} = 5.44$ TeV," https://alice-notes.web.cern.ch/node/730. (Cited on page 190.)

[235] M. Djordjevic et *al.*, "How to test path-length dependence in energy loss mechanisms: analysis leading to a new observable," arXiv:1805.04030 [nucl-th]. (Cited on pages 190 and 193.)

[236] F. Noferini, "ALICE results from Run-1 and Run-2 and perspectives for Run-3 and Run-4," Journal of Physics: Conf. Series **1014** (2018) 012010 . (Cited on pages xxvi, 62, 196 and 198.)

Publication list

1. Z. Zhang, et al, Production of muons from heavy-flavour hadron decays in p-Pb collisions at 5.02 TeV, Published in Phys.Lett. B770 (2017) 459-472
2. Z. Zhang (for the ALICE collaboration), Production of muons from heavy-flavour hadron decays at forward rapidity in Pb-Pb collisions at 5.02 TeV, Published in Nucl.Part.Phys.Proc. 289-290 (2017) 405-408
3. Z. Zhang, et al, Elliptic flow of muons from heavy-flavour hadron decays at forward rapidity in Pb-Pb collisions at 2.76 TeV, Published in Phys. Lett. B 753 (2016) 41-56
4. Z. Zhang, et al, Production of muons from heavy-flavour hadron decays at forward rapidity in pp collisions at 5.02 TeV, paper proposal in August 25, 2017(https://aliceinfo.cern.ch/ArtSubmission/node/4120)
5. Z. Zhang, et al, Production of muons from heavy-flavour hadron decays at forward rapidity in Pb-Pb collisions at 5.02 TeV , including the comparison with Pb-Pb results at 2.76 TeV, paper proposal in November 24, 2017 (https://aliceinfo.cern.ch/ArtSubmission/node/4121)
6. As a member of the ALICE collaboration (∼70)

The Analysis note

1. Z. Zhang, et al, Production of muons from heavy-flavour hadron decays in p-Pb collisions at $\sqrt{s_{\rm NN}}$=5.02 TeV
2. Z. Zhang, et al, Production of muons from heavy-flavour hadron decays at forward rapidity in Pb-Pb collisions at $\sqrt{s_{\rm NN}}$=2.76 TeV
3. Z. Zhang, et al, Production of muons from heavy-flavour hadron decays at forward rapidity in Pb-Pb collisions at $\sqrt{s_{\rm NN}}$= 5.02 TeV
4. Z. Zhang, et al, Production of muons from heavy-flavour decays in pp collisions at $\sqrt{s}$=5.02 TeV
5. Z. Zhang, et al, Production of heavy-flavour decay muons in Xe-Xe collisions at $\sqrt{s_{\rm NN}}$= 5.44 TeV with ALICE

Presentations list

1. Z. Zhang (for the ALICE collaboration), "Measurement of muons from heavy-flavour hadron decays in Pb-Pb collisions at $\sqrt{s_{\mathrm{NN}}} = 2.76$ TeV with ALICE at the LHC", QM2015, KOBE , Japan, September, 2015 (poster)

2. Z. Zhang (for the ALICE collaboration), "Measurement of muons from heavy-flavour hadron decays in Pb-Pb collisions at 2.76 TeV with ALICE at the LHC", FCPPL2016, Strasbourg, France, March, 2016

3. Z. Zhang (for the ALICE collaboration), "Measurement of muons from heavy-flavour hadron decays in pp and Pb-Pb collisions at 5.02 TeV with ALICE at the LHC", ALICE muon meeting 2016, Pornichet, France, May, 2016

4. Z. Zhang (for the ALICE collaboration), "Muons from Open Heavy-flavour Decays in Pb-Pb collisions at $\sqrt{s_{\mathrm{NN}}} = 5.02$ TeV in Run 2 with ALICE", Hard Probes 2016, Wuhan, China, September, 2016

5. Z. Zhang (for the ALICE collaboration), "Muons from Open Heavy-flavour Decays in Pb-Pb collisions at $\sqrt{s_{\mathrm{NN}}} = 5.02$ TeV with ALICE", Rencontres QGP-France, Etretat, France, October, 2016

6. Z. Zhang (for the ALICE collaboration), "Production of muons from heavy-flavour decays in Pb-Pb collisions at $\sqrt{s_{\mathrm{NN}}} = 5.02$ TeV", Physics Forum, CERN, Switzerland, January, 2017

7. Z. Zhang (for the ALICE collaboration), "Measurement of muons from heavy-flavour hadron decays in Pb-Pb collisions at $\sqrt{s_{\mathrm{NN}}} = 5.02$ TeV with ALICE at the LHC", LHCC2017, CERN, Switzerland, February, 2017 (poster)

8. Z. Zhang (for the ALICE collaboration), "Measurement of muons from heavy-flavour hadron decays in pp collisions at $\sqrt{s} = 5.02$ TeV with ALICE at the LHC", ALICE muon meeting 2017, Grotta Giusti, Italy, May, 2017

9. Z. Zhang (for the ALICE collaboration), "Muons from Open Heavy-flavour Decays in Pb-Pb collisions at 5.02 TeV with ALICE", France China Particle Physics Laboratory 2017, Beijing, China, March, 2017

10. Z. Zhang (for the ALICE collaboration), "Muons from Open Heavy-flavour Decays in Pb-Pb and pp at 5.02 TeV collisions with ALICE", Rencontres QGP-France, Etretat, France, October, 2017

11. Z. Zhang (for the ALICE collaboration), "Open Heavy-flavour Decay muons in Pb-Pb and pp collisions at 5.02 TeV with ALICE", ALICE Physics Week, Amsterdam, Netherlands, December 2017

12. Z. Zhang (for the ALICE collaboration), "Measurement of muons from heavy-flavour hadron decays in Pb-Pb collisions at $\sqrt{s_{\mathrm{NN}}} = 5.02$ TeV with ALICE at the LHC", LHCC2018, CERN, Switzerland, February, 2018 (poster)
13. Z. Zhang (for the ALICE collaboration), "Measurement of muons from heavy-flavour hadron decays in Xe-Xe collisions at $\sqrt{s} = 5.44$ TeV with ALICE at the LHC", ALICE muon meeting 2018, Aligarh Muslim University, India, February, 2018
14. Z. Zhang (for the ALICE collaboration), "Measurements of muons from heavy-flavour hadron decays with ALICE", France China Particle Physics Laboratory 2018, Marseille, France, May, 2018
15. Z. Zhang (for the ALICE collaboration), "Open heavy flavours in heavy-ion collisions with ALICE", Opportunities and Challenges with Jets at LHC and beyond, Central China Normal University, Wuhan, China, June, 2018
16. Z. Zhang (for the ALICE collaboration), "Muons from Open Heavy-flavour decays in nucleus-nucleus collisions with ALICE", Rencontres QGP-France, Etretat, France, July, 2018
17. Z. Zhang (for the ALICE collaboration), "Measurements of heavy-flavor decay lepton production in Pb-Pb and Xe-Xe collisions with ALICE at the LHC", Hard Probe, Aix-Les-Bains, France, October, 2018
18. Presentations in meetings of the ALICE Collaboration ($\sim$60)

Acknowledgments

It is my great pleasure to thank all these people who have helped me during the past three years of my PHD study in CCNU/LPC, though it is difficult to express my gratitude to all of them individually.

First of all, I would specially like to thank my supervisors Prof. Zhou Daicui and Prof. Zhang Xiaoming at CCNU in China who led me to the fascinating world of high energy particle physics and I feel fortunate to work under their kind guidance and support. Also, I would like to thank Prof. Yin Zhongbao, Prof. Pei Hua, Prof. Mao Yaxian, and Prof. Paolo Bartalini for their discussions in our Wuhan ALICE work group. Then I would like to thank the PhD committee members of Prof. ALBERTO Baldisseri, Prof. BASTID Nicole, Associate Prof. ALESSANDRO Grelli, Prof. CROCHET Philippe, Prof. MA Yugang, Prof. Li Xiaomei, Prof. YIN Zhongbao, Associate Prof.ZHANG Xiaoming, Prof. ZHOU Daicui.

I would also specially like to thank my supervisors Nicole Bastid and Philippe Crochet at LPC Clermont-Ferrand in France, who gave me the support, guidance and availability deserve my deepest gratitude. Their experience and personal qualities have been of great influence for me both on professional and personal aspects.

I would like also to thank Prof. Cai Xu, Prof. Liu Feng, Prof. Yang Chunbin, Prof. Liu Fuming, Prof. Hou Defu, Prof. Zhang Beiwei, Prof. Chen Shaolong and Prof. Zhou Daimei for their teaching and helps during my studies.

Thanks to the ALICE Group at LPC for the discussion and support, in particular to Crochet Philippe, Pascal Dupieux, Nicole Bastid, Valerie Ramillien, Lopez Xavier, Vulpescu Bogdan, Philippe Rosnet, Sarah Porteboeuf, Alain Baldit, Franck Manso, Tasnuva Chowdhury for useful suggestions and discussions

It is my pleasure to thank all members from the Institute of Particle Physics (IOPP) at CCNU for their effort to make our institute and laboratory warm and enjoyable, just like a big family. I appreciate the hele of my colleagues of ALICE Wuhan Group: Ren Xiaowen, Peng Xinye, Zhu Ya, Li Xinlong, Xu Ran, Chang Wan, Ding Yanchun, Fan Feng, Cui Pengyao, Cai Mengke, Tang Siyu, Zhang Biao, Zhou Yingjie, Hou Yongzhen, Zhang Wenjing, Qiao Qi, Guo Wenda, Ceng Shuxin, Yuan Qi, Jiang Xiuxiu, Dang Yuxing, Tan Yalei, Cheng Tiantian, Liu Donghai, Wang Ruiqin and so on. Especially, I really appreciate the patient guidance and help of Nicole Bastid, Zhang Xiaoming and Li Shuang in my analysis work.

Finally, last but least in my thoughts, I want to express my heartfelt gratitude to my parents, my sister and my wife, for their understanding and encouragement in these years.

Zuman Zhang
CCNU, Wuhan, China
October 1th, 2018

Abstract

The study of ultra-relativistic heavy-ion collisions aims at investigating a state of strongly-interacting matter at high energy density and temperature, the Quark-Gluon Plasma (QGP). Heavy quarks (charm and beauty) are predominantly produced in initial hard scattering processes during the early stage of the collisions and experience the full evolution of the medium. Therefore, the measurement of open heavy flavours should provide essential information on the QGP properties. Similar measurements in small systems are also essential for a comprehensible understanding of the QGP properties. The study of open heavy flavours in proton-proton (pp) collisions provides the mandatory reference for measurements in heavy-ion collisions. This thesis presents measurements of the production of muons from heavy-flavour hadron decays at forward rapidity ($2.5 < y < 4$) in pp collisions at $\sqrt{s} = 5.02$ TeV, Pb-Pb collisions at $\sqrt{s_{\mathrm{NN}}} = 2.76$ and 5.02 TeV and Xe-Xe collisions at $\sqrt{s_{\mathrm{NN}}} = 5.44$ TeV collected with the ALICE detector at the CERN-LHC. The differential production cross sections of muons from heavy-flavour hadron decays in pp collisions at $\sqrt{s} = 5.02$ TeV are obtained in a wide transverse momentum interval, $2 < p_{\mathrm{T}} < 20$ GeV/c, and with an improved precision compared to the previously published measurements at $\sqrt{s} = 2.76$ and 7 TeV. The measurements are described within uncertainties by predictions based on perturbative QCD. A strong suppression of the yield of muons from heavy-flavour decays is observed in the 10% most central Pb-Pb collisions at both $\sqrt{s_{\mathrm{NN}}} = 2.76$ and 5.02 TeV. This suppression is due to final-state effects induced by the hot and dense medium. The suppression in Xe-Xe collisions is similar to that observed with Pb-Pb collisions. The comparison in the two colliding systems provides insight in the path-length dependence of medium-induced parton energy loss. The results constrain model calculations.

Keywords: Quark-Gluon Plasma (QGP); ALICE; LHC; pp and heavy-ion collisions; open heavy-flavour production via single muons; nuclear modification factor (R_{AA}); perturbative QCD; transport models

Résumé

Les collisions d'ions lourds ultra-relativistes ont pour objectif l'étude d'un état de matière en interaction forte dans des conditions extrêmes de densité d'énergie et température, le plasma de quarks et gluons (QGP). Les saveurs lourdes (charme et beauté) sont produites principalement lors de processus durs aux premiers instants de la collision et participent aux différentes étapes de la collision. Par conséquent, la mesure des saveurs lourdes ouvertes devrait permettre d'extraire des informations importantes concernant le système créé aux premiers instants de la collision. L'étude des collisions proton-proton (pp) fournit la référence indispensable pour la mesure des saveurs lourdes dans les systèmes lourds. Cette thèse est dédiée à l'étude de la production des muons de décroissance des hadrons charmés et beaux aux rapidités avant ($2.5 < y < 4$) dans les collisions pp $\sqrt{s} = 5.02$ TeV, Pb-Pb à $\sqrt{s_{\mathrm{NN}}} = 2.76$ et 5.02 TeV et Xe-Xe à $\sqrt{s_{\mathrm{NN}}} = 5.44$ TeV enregistrées avec le détecteur ALICE au LHC-CERN. La mesure des sections efficaces différentielles de production des muons de décroissance des hadrons charmés et beaux dans les collisions pp à $\sqrt{s} = 5.02$ TeV couvre un grand domaine en impulsion transverse, de 2 à 20 GeV/c et ont une meilleure précision par rapport aux résultats publiés à $\sqrt{s} = 2.76$ et 7 TeV. Les résultats sont en bon accord avec les calculs perturbatifs de QCD. Une importante suppression de la production des muons de décroissance des hadrons charmés et beaux est observée dans les collisions centrales (0-10%) Pb-Pb à $\sqrt{s_{\mathrm{NN}}} = 2.76$ et 5.02 TeV. Cette suppression est attribuée au milieu dense et chaud formé dans ces collisions. L'influence de la taille de la taille du système est étudiée avec le système Xe-Xe à $\sqrt{s_{\mathrm{NN}}} = 5.44$ TeV. La suppression est similaire à celle mesurée dans les collisions Pb-Pb. Les résultats obtenus dans les collisions Pb-Pb et Xe-Xe apportent des contraintes fortes aux paramètres des modèles.

Mots clés: Plasma de Quarks et Gluons(QGP); ALICE; LHC; collisions pp; collisions d'ions lourds; production des saveurs lourdes ouvertes via les muons; facteur de modification nucléaire (R_{AA}); calculs perturbatifs QCD; modèles de transport.